Ion Implantation and Synthesis of Materials

M. Nastasi J.W. Mayer

Ion Implantation and Synthesis of Materials

With 131 Figures and 10 Tables

Springer

Michael Nastasi, PhD
Laboratory Fellow and Team Leader
Ion-Solid Interaction and Interface Engineering Team
Los Alamos National Laboratory, MS-K771
Los Alamos NM 87545, USA
E-mail: nasty@lanl.gov

James W. Mayer, PhD
Center for Solid State Science
Arizona State University
Tempe, AZ, 85287-1704, USA
E-mail: james.mayer@asu.edu

Library of Congress Control Number: 2006930120

ISBN-10 3-540-23674-0 Springer Berlin Heidelberg New York
ISBN-13 978-3-540-23674-0 Springer Berlin Heidelberg New York

This work is subject to copyright. All rights are reserved, whether the whole or part of the material is concerned, specifically the rights of translation, reprinting, reuse of illustrations, recitation, broadcasting, reproduction on microfilm or in any other way, and storage in data banks. Duplication of this publication or parts thereof is permitted only under the provisions of the German Copyright Law of September 9, 1965, in its current version, and permission for use must always be obtained from Springer. Violations are liable to prosecution under the German Copyright Law.

Springer is a part of Springer Science+Business Media.

springer.com

© Springer-Verlag Berlin Heidelberg 2006

The use of general descriptive names, registered names, trademarks, etc. in this publication does not imply, even in the absence of a specific statement, that such names are exempt from the relevant protective laws and regulations and therefore free for general use.

Typesetting by the Authors and SPi
Cover design: *design & production* GmbH, Heidelberg

Printed on acid-free paper SPIN 10864147 57/3100/SPi 5 4 3 2 1 0

To our loved ones

Preface

Ion implantation is one of the key processing steps in silicon-integrated circuit technology. Some integrated circuits require up to 35 implantation steps, and circuits are seldom processed with fewer than 10 implantation steps. Controlled doping at controlled depths is an essential feature of implantation. Ion beam processing can also be used to improve corrosion resistance, harden surfaces, reduce wear and, in general, improve materials properties. This book presents the physics and materials science of ion implantation and ion synthesis of materials with an emphasis on electronic materials. It covers ion-solid interactions used to predict ion ranges, ion straggling, and lattice damage. Also treated are the applications of ion implantation in the formation of integrated circuits and the slicing of silicon with hydrogen ion beams. Topics important for materials modification, such as ion beam-induced epitaxial growth of amorphous layers, ion-beam mixing, and sputtering, are also described.

This text is designed for undergraduate seniors and graduate students interested in electronic devices, surface engineering, reactor and nuclear engineering, and material science issues associated with irradiation effects in materials. The original course was offered by the Department of Materials Engineering. Approximately half the students came from electrical engineering or disciplines other than materials engineering. Their backgrounds and training varied. Hence, a firm grasp of the underlying concepts of ion-solid interactions in solids needed in the course could not be assumed. For this reason the first four chapters of the book are devoted to review of topics on particle interactions, binary collisions, and collision cross-sections. The purpose of these chapters is to provide sufficient coverage of the fundamentals for the subsequent chapters.

In writing this book, we have benefited immensely from the help of students in our classes. Their inquiries and responses to our lectures have strengthened the contents and organization of the book. Ms. Linda Woods is sincerely acknowledged for formatting and editing the book. We also thank Tobias Höchbauer for his contributions to Chapter 10, Lin Shao for his contributions to Chapter 14, and the ion implanter development scientists at Axcelis Technologies, Inc for their contributions to Chapter 15.

Los Alamos, Tempe *Michael Nastasi*
June 2006 *James W. Mayer*

Contents

1 General Features and Fundamental Concepts ... 1
1.1 Introduction ... 1
1.2 Range Distributions ... 2
1.3 Lattice Disorder ... 3
1.4 Atomic and Planar Densities ... 5
1.5 Energy and Particles ... 6
1.6 The Bohr Velocity and Radius ... 8
Suggested Reading ... 9
Problems ... 9

2 Particle Interactions ... 11
2.1 Introduction ... 11
2.2 Interatomic Forces ... 11
2.3 Short- and Long-Range Interatomic Forces ... 12
2.4 Interatomic Forces in Solids ... 13
2.5 Energetic Collisions of Atoms and Ions and the Screened Coulomb Potential ... 15
2.6 Screening Functions ... 16
2.7 Screening Length ... 18
References ... 20
Suggested Reading ... 20
Problems ... 21

3 Dynamics of Binary Elastic Collisions ... 23
3.1 Introduction ... 23
3.2 Classical Scattering Theory ... 24
3.3 Kinematics of Elastic Collisions ... 25
3.4 Center-of-Mass Coordinates ... 27
3.5 Motion Under a Central Force ... 30
3.5.1 Energy Conservation in a Central Force ... 31
3.5.2 Angular Orbital Momentum and the Impact Parameters ... 32
3.6 Distance of Closest Approach ... 34
References ... 35
Suggested Reading ... 35
Problems ... 35

4 Cross-Section 37
4.1 Introduction 37
4.2 Scattering Cross-Section 37
4.3 Energy-Transfer Cross-Section 42
4.4 Approximation to the Energy-Transfer Cross-Section 45
References 47
Suggested Reading 47
Problems 47

5 Ion Stopping 49
5.1 Introduction 49
5.2 The Energy-Loss Process 50
5.3 Nuclear Stopping 51
5.4 ZBL Nuclear Stopping Cross-Section 54
5.5 Electronic Stopping 56
5.5.1 High-Energy Electronic Energy Loss 57
5.5.2 Low-Energy Electronic Energy Loss 58
5.6 Stopping Calculations Using SRIM 60
References 60
Suggested Reading 60
Problems 61

6 Ion Range and Range Distribution 63
6.1 Range Concepts 63
6.2 Range Distributions 65
6.3 Calculations 67
6.3.1 Range Approximations 67
6.3.2 Projected Range 68
6.3.3 Range Straggling 70
6.3.4 Polyatomic Targets 71
6.4 Range Distributions from SRIM 72
References 74
Suggested Reading 75
Problems 75

7 Displacements and Radiation Damage 77
7.1 Introduction 77
7.2 Radiation Damage and Displacement Energy 77
7.3 Displacements Produced by a Primary Knock-on 79
7.4 Primary Knock-on Atom Damage Energy 82
7.5 Ion Damage Energy 83
7.6 Damage Production Rate and DPA 85
7.7 Replacement Collision Sequences 86
7.8 Spikes 86
7.8.1 Mean Free Path and the Displacement Spike 86
7.8.2 Thermal Spike 87

7.9 Damage Distribution from SRIM 89
References 91
Suggested Reading 91
Problems 91

8 Channeling 93
8.1 Introduction 93
8.2 General Principles 96
8.3 The Maximum Range, R_{max} 99
8.4 Dechanneling by Defects 100
References 105
Problems 106

9 Doping, Diffusion and Defects in Ion-Implanted Si 107
9.1 Junctions and Transistors 107
9.1.1 Bipolar Transistors 109
9.1.2 Metal-Oxide-Semiconductor Field-Effect Transistors 110
9.1.3 Complementary Metal Oxide Semiconductor Devices 112
9.2 Defects 114
9.2.1 Point Defects 114
9.2.2 Native Defects and Shallow Dopants 114
9.2.3 Deep Level Centers 115
9.2.4 Line Defects 116
9.2.5 Planar Defects 117
9.2.6 Volume Defects 117
9.3 Fick's First and Second Law of Diffusion 118
9.3.1 Diffusion Coefficient 119
9.3.2 Diffusion of Doping Atoms into Si 119
9.4 Diffusion Mechanisms 119
9.4.1 Interstitial Mechanism 121
9.4.2 Substitutional or Vacancy Mechanism 121
9.4.3 Interstitial–Substitutional Mechanism 121
9.4.4 Interstitialcy and the Kick-Out Mechanism 122
9.5 Transient Enhanced Diffusion of Boron 122
9.6 Irradiation–Enhanced Diffusion 124
References 125
Problems 126

10 Crystallization and Regrowth of Amorphous Si 127
10.1 Introduction 127
10.2 Epitaxial Growth of Implanted Amorphous Si 129
10.3 Ion Beam-Induced Enhanced Crystallization 137
10.4 Laser Annealing of Si 140
References 141
Problems 142

11 Si Slicing and Layer Transfer: Ion-Cut 143
11.1 Introduction 143
11.2 Formation of SOI by the Ion-Cut Process 144
11.3 The Silicon–Hydrogen System 145
11.4 The Mechanisms Behind the Ion-Cut Process 149
11.4.1 The Ion-Cut Depth 149
11.4.2 Microstructure of the Implantation Zone 153
References 157

12 Surface Erosion During Implantation: Sputtering 159
12.1 Introduction 159
12.2 Sputtering of Single-Element Targets 159
12.3 Ion Implantation and the Steady State Concentration 162
12.4 Sputtering of Alloys and Compounds 164
12.4.1 Preferential Sputtering 165
12.4.2 Compositional Changes 166
12.4.3 Composition Depth Profiles 168
12.5 High-Dose Ion Implantation 169
12.6 Concentrations of Implanted Species 171
12.6.1 Si Implanted with 45 keV Pt Ions 171
12.6.2 Pt Implanted with 45 keV Si Ions 172
12.6.3 PtSi Implanted with Si 172
12.7 Concentrations in High-Dose Ion Implantation 173
12.8 Computer Simulation 175
References 176
Suggested Reading 176
Problems 177

13 Ion-Induced Atomic Intermixing at the Interface: Ion Beam Mixing 179
13.1 Introduction 179
13.2 Ballistic Mixing 182
13.2.1 Recoil Mixing 183
13.2.2 Cascade Mixing 185
13.3 Thermodynamic Effects in Ion Mixing 187
References 191
Suggested Reading 191
Problems 192

14 Application of Ion Implantation Techniques in CMOS Fabrication 193
14.1 Introduction 193
14.2 Issues During Device Scaling 193
14.2.1 Short-Channel Effects 195
14.2.2 Hot-Electron Effect 197
14.2.3 Latchup 198
14.3 Ion Implantation in Advanced CMOS Device Fabrication 199
14.3.1 Retrograde Well Implant 202

14.3.2 Punch-Through Stop Implant 203
14.3.3 Threshold Adjust Implant 203
14.3.4 Source and Drain Implant 205
14.3.5 Halo Implant 206
14.3.6 Gate Implant 207
14.4 Issues of Ion Implantation During Device Scaling 207
14.4.1 Space Charge Effects 207
14.4.2 Energy Contamination 208
14.4.3 Beam Shadowing Effect 208
14.5 The Role of Ion Implantations in Device Fabrications 208
References 209
Suggested Reading 210
Problems 210

15 Ion implantation in CMOS Technology: Machine Challenges 213
15.1 Introduction 213
15.2 Implanters used in CMOS Processing 214
15.2.1 Beamline Architectures 215
15.2.2 Other Subsystems 221
15.3 Low Energy Productivity: Beam Transport 223
15.3.1 Space Charge Neutralization 224
15.3.2 Decel Implantation 224
15.3.3 Molecular Implantation 226
15.4 Low Energy Productivity: Beam Utilization 226
15.4.1 Beam Utilization 227
15.4.2 Implanters Commercialized in the Past 35 Years 230
15.5 Angle Control 232
15.5.1 Impact of Beam Steering Errors on Device Performance 232
15.5.2 Impact of Endstation Design and Beam Scan Mechanism 234
15.6 Conclusions and the Future of Ion Implantation in Semiconductors 236
References 237

Appendix A: Table of the Elements 239
Appendix B: Physical Constants, Conversions, and Useful Combinations 255

Index 257

1 General Features and Fundamental Concepts

1.1 Introduction

Ion beam processing of materials results from the introduction of atoms into the surface layer of a solid substrate by bombardment of the solid with ions in the electron-volt to mega-electron-volt energy range. The solid-state aspects are particularly broad because of the range of physical properties that are sensitive to the presence of a trace amount of foreign atoms. Mechanical, electrical, optical, magnetic, and superconducting properties all are affected by, and indeed may even be dominated by, the presence of such foreign atoms. The use of energetic ions affords the possibility of introducing a wide range of atomic species, independent of thermodynamic factors, thus making it possible to obtain impurity concentrations and distributions of particular interest; in many cases, these distributions would not otherwise be attainable.

Recent interest in ion beam processing has focused on studies of ion implantation, ion beam mixing, ion-induced phase transformations, and ion beam deposition. These interests have been stimulated by the possibilities of synthesizing novel materials with potential applications in the semiconductor, tribological, corrosion, and optical fields.

Ion beam processing provides an alternative and non-equilibrium method of introducing dopant atoms into the lattice. In typical applications, a beam of dopant ions is accelerated through a potential of 10–100 kV. The implantation system shown in Fig. 1.1 illustrates the basic elements required in this technique: ion source, acceleration column, mass-separator, and target chamber. With different types of ion sources available, a wide variety of beams may be produced with sufficient intensity for implantation purposes for integrated circuit technology; 10^{14}–10^{15} ions cm^{-2} (less than a 'monolayer'; see Sect. 1.4) is a representative ion dose. *Ion dose* is defined as the number of ions cm^{-2} implanted into the sample. Alternatively, the term *fluence* is used instead of dose. The ion beam current density is expressed in units of A cm^{-2}. The dose rate or flux is given in units of ions s^{-1} cm^{-2}.

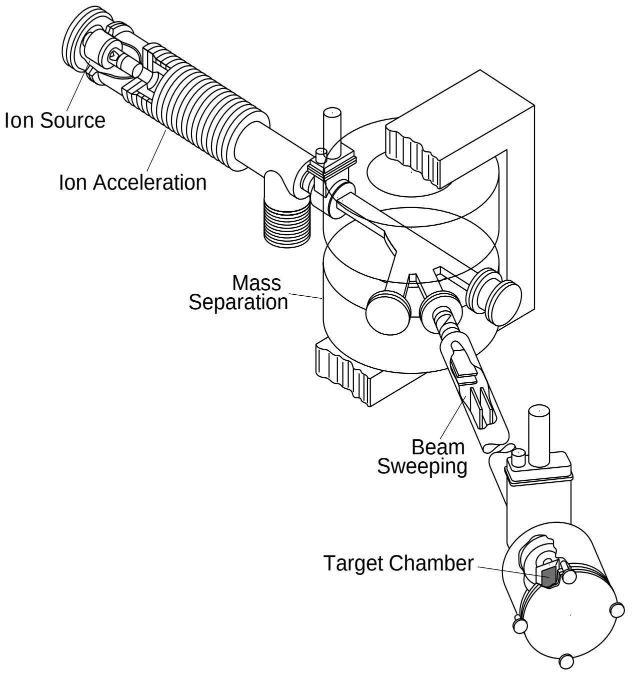

Fig. 1.1. Schematic drawing of an ion implantation system. A mass-separating magnet is used to select the ion species (elements and isotopes) of interest. Beam-sweeping facilities are required for large-area uniform implantations

1.2 Range Distributions

One of the most important considerations in any description of ion–solid interactions is the depth (range) distribution of the implanted ions. A large amount of experimental and theoretical work has been devoted to the task of understanding the energy-loss processes that govern the range distribution, and it is now possible to predict fairly accurately most of the factors involved. For example, a typical range distribution in an amorphous substrate from monoenergetic ions at moderate ion doses is approximately Gaussian in shape and may therefore be characterized by a projected range, R_p, and a straggling, ΔR_p, about this mean value, as depicted in Fig. 1.2. The notation uses Z and M for atomic number and atomic mass, respectively, with subscript 1 denoting the incident ions (Z_1, M_1) and subscript 2 denoting the ion-bombarded sample (or target). By convention, the energy of the incident ion is denoted by E_0 or by E without a subscript.

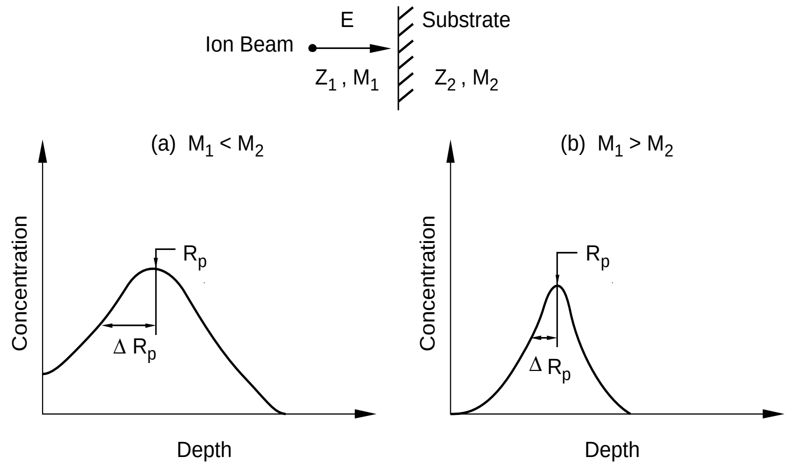

Fig. 1.2. The depth distribution of implanted atoms in an amorphous target for the cases in which the ion mass is (**a**) less than the mass of the substrate atoms or (**b**) greater than the mass of the substrate atoms. To a first approximation, the mean depth, R_p, depends on ion mass, M_1, and incident energy, E, whereas the relative width, $\Delta R_p/R_p$, of the distribution depends primarily on the ratio between ion mass and the mass of the substrate ion, M_2

1.3 Lattice Disorder

Lattice disorder and radiation-damage effects are produced in the substrate by the incident ion. As an implanted ion slows down and comes to rest, it has many violent collisions with lattice atoms, displacing them from their lattice sites. These displaced atoms can in turn displace others, and the net result is the production of a highly disordered region around the path of the ion, as shown schematically in Fig. 1.3 for the case of a heavy implanted atom at typically 10–100 keV. At sufficiently high doses, these individual disordered regions may overlap, and an amorphous or metastable crystalline layer may form.

Figure 1.4 shows the schematic atomic arrangement for a crystalline solid (a) and an amorphous solid (b). A crystalline solid has long-range atomic order; an amorphous solid has short-range order (the order among the nearest neighbors) but no long-range order. In a single-crystal, the entire sample is composed of atoms placed on well-defined planes and rows. Figure 1.5a shows a side view of a single-crystal, in which the planes of atoms are depicted by parallel pairs of lines. A polycrystalline sample is made of small single-crystal regions called crystallites, the planes and atomic rows of which are misaligned with respect to those in neighboring crystallites. A polycrystalline layer on a single-crystal substrate is shown in Fig. 1.5b.

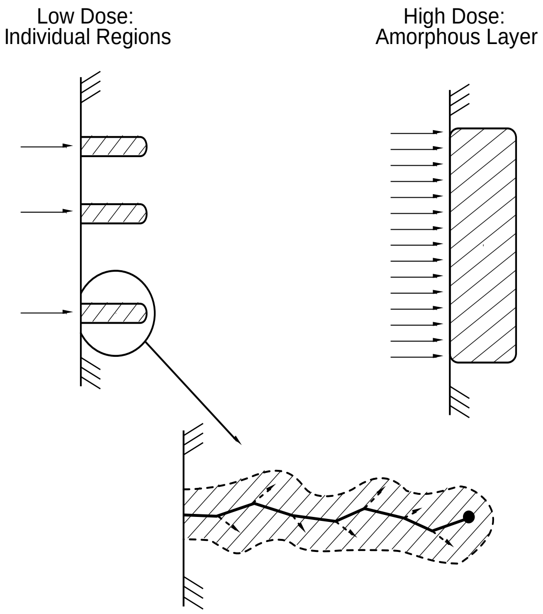

Fig. 1.3. A schematic representation of the disorder produced in room-temperature implantations of heavy ions at energies of 10–100 keV. At low doses, the highly disordered regions around the tracks of the ions are spatially separated from each other. The volume of the disordered region is determined primarily by the stopping point of the ion and the range of the displaced lattice atoms (*dashed arrows*). At high doses, the disordered regions can overlap to form an amorphous layer

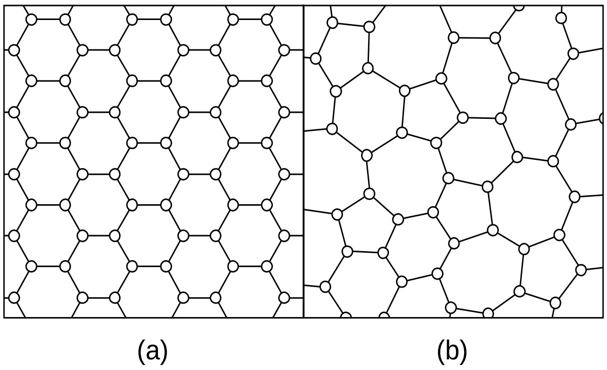

Fig. 1.4. Schematic atomic arrangement of (**a**) a crystalline solid and (**b**) an amorphous solid

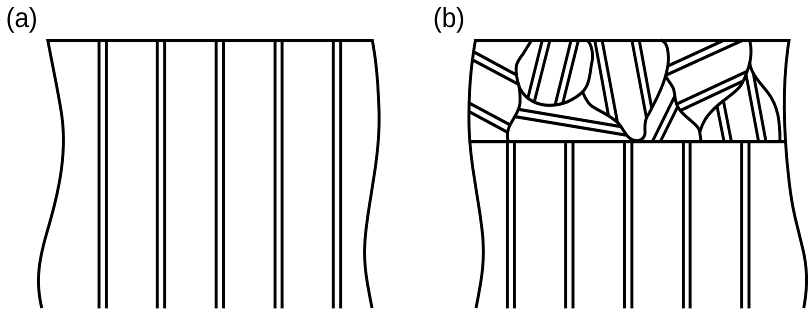

Fig. 1.5. Schematic representation for (**a**) a single-crystal with crystallographic planes perpendicular to the surface and (**b**) a polycrystalline layer on a single-crystal

1.4 Atomic and Planar Densities

To understand the description of ion implantation and ion doses, one must know the atomic density interplanar distance between planes and the number of atoms cm^{-2} on a given plane. In cubic systems with an atomic density of N atoms cm^{-3}, the crystal lattice parameter, a_c, is given by

$$a_c = \left(\frac{\text{atoms/unit cell}}{N}\right)^{1/3}, \tag{1.1}$$

where, for systems with one atom per lattice point, there are four atoms per unit cell for a face-centered-cubic lattice (Al, Ag, Au, Pd, Pt) and there are eight for the common semiconductors germanium (Ge) and silicon (Si), which have the diamond cubic structure. Aluminum has an atomic density of 6.02×10^{22} atoms cm^{-3}, so that the lattice parameter is

$$a_c = \left(\frac{4}{6.02 \times 10^{22}}\right)^{1/3} = 4.05 \times 10^{-8}\ \text{cm}. \tag{1.2}$$

The atomic volume can be calculated without the use of crystallography. The atomic density N of atoms cm^{-3} is given by

$$N = \frac{N_A}{A}\rho, \tag{1.3}$$

where N_A is Avogadro's number, ρ is the mass density in g cm^{-3}, and A is the atomic mass number. Taking Al as an example, where ρ is 2.7 g cm^{-3} and A is 27, the atomic density is $N = (6.02 \times 10^{23} \times 2.70)/27 = 6.02 \times 10^{22}$ atoms cm^{-3}. The semiconductors Ge and Si have atomic densities of about 4.4×10^{22} and 5.0×10^{22} atoms cm^{-3}, respectively. Metals such as Co, Ni, and Cu have densities of about 9×10^{22} atoms cm^{-3}. The volume Ω_V occupied by an atom is given by

$$\Omega_V = \frac{1}{N} \tag{1.4}$$

with a typical value of 20×10^{-24} cm^3.

The average areal density of a monolayer, N_s atoms cm^{-2}, also can be estimated without the use of crystallography by taking the atomic density N to the 2/3 power.

$$N_s \cong N^{2/3}. \tag{1.5}$$

Equation (1.5) gives the average areal density of one monolayer for a material with an atomic density N.

1.5 Energy and Particles

In the SI (or MKS) system of units, the joule (J) is a unit of energy, but the electron-volt (eV) is the traditional unit used in ion–solid interactions: we can define 1 eV as the kinetic energy gained by an electron accelerated through a potential difference of 1 V. The charge on the electron is 1.602×10^{-19} C, and a joule is a Coulomb-volt, so that the relationship between these units is given by

$$1\,\text{eV} = 1.602 \times 10^{-19}\,\text{J}. \tag{1.6}$$

Commonly used multiples of the electron-volt are the kilo-electron-volt (10^3 eV) and mega-electron-volt (10^6 eV).

In ion–solid interactions it is convenient to use cgs units rather than SI units in relations involving the charge on the electron. The usefulness of cgs units is clear when considering the Coulomb force between two charged particles with Z_1 and Z_2 units of electronic charge separated by a distance r

$$F = \frac{Z_1 Z_2 e^2 k_c}{r^2}, \tag{1.7}$$

where the Coulomb law constant k_c = ¼ $\pi\varepsilon_0$ = 8.988 × 10^9 m F^{-1} in the SI system (where 1 F ≡ 1 A s V^{-1}) and is equal to unity in the cgs system.

The conversion factor follows from:

$$e^2 k_c = (1.6\times10^{-19}\ \mathrm{C})^2 \times 8.988\times10^9\ \mathrm{m\,F^{-1}} = 2.3\times10^{-28}\ \mathrm{C^2\ m\,F^{-1}}.$$

The conversions 1 C ≡ 1 A s and 1 J ≡ 1 C V lead to the units of the farad:

$$1\ \mathrm{F} \equiv 1\ \mathrm{A\ s\ V^{-1}},$$

so that

$$1\mathrm{C^2\ m\,F^{-1}} \equiv 1\mathrm{C^2\ V\,m\,(A\,s)^{-1}} \equiv 1\mathrm{J\,m} \equiv 10^9\ \mathrm{J\,nm} \equiv \frac{10^9\ \mathrm{J\,nm}}{(1.6\times10^{-19}\ \mathrm{J\,eV^{-1}})} = \frac{10^{28}}{1.6}\mathrm{eV\,nm}$$

and

$$e^2 k_c = 2.31\times10^{-28}\ \mathrm{C^2\ m\,F^{-1}} = \frac{2.31}{1.6}\mathrm{eV\,nm} = 1.44\,\mathrm{eV\,nm}.$$

In this book we will follow the cgs units for e^2 with k_c = 1, so that

$$e^2 = 1.44\,\mathrm{eV\,nm}. \tag{1.8}$$

Each nucleus is characterized by a definite atomic number Z and mass number A; for clarity, we use the symbol M to denote the atomic mass in kinematic equations. The atomic number Z is the number of protons, and hence the number of electrons, in the neutral atom; it reflects the atomic properties of the atom. The mass number gives the number of nucleons (protons and neutrons); isotopes are nuclei (often called nuclides) with the same Z and different A. The current practice is to represent each nucleus by the chemical name with the mass number as a superscript, e.g., ^{12}C. The chemical atomic weight (or atomic mass) of elements as listed in the periodic table gives the average mass, i.e., the average of the stable isotopes weighted by their abundance. Carbon, for example, has an atomic weight of 12.011, which reflects the 1.1% abundance of ^{13}C.

The masses of particles may be expressed as given in Table 1.1 in terms of energy through the Einstein relation

$$E = Mc^2, \tag{1.9}$$

Table 1.1. Mass energies of particles and light nuclei

Particle	Symbol	Atomic mass (u)	Mass (10^{-27} kg)	Mass energy (MeV)
Electron	e or e^-	0.000549	9.1095×10^{-4}	0.511
Proton	p or $^1H^+$	1.007276	1.6726	938.3
Atomic mass unit (amu)	u	1.00000	1.6606	931.7
Neutron	n	1.008665	1.6747	939.6
Deuteron	D or $^2H^+$	2.01410	3.3429	1875.6
Alpha	α or $^4He^{2+}$	4.00260	6.6435	3727.4

which associates 1 J of energy with $1/c^2$ of mass, where c is the velocity of light, $c = 2.998 \times 10^8$ m s^{-1}. The mass of an electron, m_e, is 9.11×10^{-31} kg, which is equivalent to an energy

$$\begin{aligned} E &= (9.11\times10^{-31}\,\text{kg})(2.998\times10^{8}\,\text{m}\,\text{s}^{-1})^2 = 8.188\times10^{-14}\,\text{J} \\ &= 0.511\,\text{MeV}. \end{aligned} \tag{1.10}$$

The Einstein relation is also useful when calculating the velocity, v, of an ion of mass M and energy E,

$$v = \left(\frac{2E}{M}\right)^{1/2} = c\left(\frac{2E}{Mc^2}\right)^{1/2}. \tag{1.11}$$

For example, the velocity of a 2 MeV ^{4}He ion is

$$v = 3\times10^{8}\,\text{m}\,\text{s}^{-1}\left(\frac{2\times2\times10^{6}\,(\text{eV})}{3,727\times10^{6}\,(\text{eV})}\right)^{1/2} = 9.8\times10^{6}\,\text{m}\,\text{s}^{-1}.$$

1.6 The Bohr Velocity and Radius

The Bohr atom provides useful relations for simple estimates of atomic parameters. The Bohr radius is defined as the distance of the ground state electron from the nucleus in a hydrogen atom. The Bohr radius of the hydrogen atom is given by

$$a_0 = \frac{\hbar^2}{m_e e^2} = 0.5292 \times 10^{-8}\ \text{cm} = 0.05292\,\text{nm} \tag{1.12}$$

and the Bohr velocity of the electron in this orbit is

$$v_0 = \frac{\hbar}{m_e a_0} = \frac{e^2}{\hbar} = 2.188 \times 10^8\ \text{cm s}^{-1}, \tag{1.13}$$

where $\hbar = h/2\pi$ with Planck's constant $h = 4.136 \times 10^{-15}$ eV s. For comparison with the Bohr radius, the radius of a nucleus is given by the empirical formula

$$R = R_0 A^{1/3}, \tag{1.14}$$

where A is the mass number and R_0 is a constant equal to 1.4×10^{-13} cm. The nuclear radius is about four orders of magnitude smaller than the Bohr radius.

Suggested Reading

Cullity, B.D.: Elements of X-Ray Diffraction. Addison-Wesley Publishing Company, Boston, MA (1978)

Feldman, L.C., Mayer, J.W.: Fundamentals of Surface and Thin Film Analysis. North-Holland, New York (1986)

Mayer, J.W., Lau, S.S.: Electronic Materials Science. Macmillan, New York (1990)

Mayer, J.W., Eriksson, L., Davies J.A.: Ion Implantation in Semiconductors. Academic, New York (1970)

Nastasi, M., Mayer, J.W., Hirvonen, J.K.: Ion–Solid Interactions: Fundamentals and Applications. Cambridge University Press, Cambridge (1996)

Omar, M.A.: Elementary Solid-State Physics: Principles and Applications. Addison-Wesley Publishing Company, Boston, MA (1975)

Rimini, E.: Ion Implantation: Basics to Device Fabrication. Kluwer, Boston (1995)

Tu, K.N., Mayer, J.W., Feldman, L.C. Electronic Thin Film Science. MacMillan Publishing Company, New York (1992)

Weidner, R.T., Sells, R.L.: Elementary Modern Physics, 3rd edn. Allyn & Bacon, Boston, MA (1980)

Problems

1.1 Aluminum is a face-centered-cubic with a mass density of 2.70 g cm^{-3}
(a) Calculate the atomic density using (1.3)

(b) Calculate the average areal density using (1.5)
(c) What is the atomic volume?

1.2 For the canonical value of 10^{15} atoms cm^{-2} in a monolayer on a cubic crystal, estimate
(a) The bulk density
(b) The volume Ω_V occupied by an atom

1.3 Nickel is a face-centered-cubic metal with an atomic density of 9.14×10^{22} atoms cm^{-3}, an atomic weight of 8.7, and density of 8.91 g cm^{-3}
(a) What is the lattice parameter, a_c, and the atomic volume, Ω_V?

1.4 Silicon has a diamond cubic lattice structure with an atomic density of 5×10^{22} atoms cm^{-3}, an atomic weight of 28.09 and a density of 2.33 g cm^{-3}
(a) What are silicon's lattice parameter and atomic volume, Ω_V?

1.5 Calculate the energy in eV of a proton moving at the Bohr velocity. What is the velocity of a 35 keV A s ion?

2 Particle Interactions

2.1 Introduction

The manner in which the potential energy of a two-particle system varies with the distance separating the two centers determines both the equilibrium properties of an assembly of atoms and the way that energetic particles interact with a lattice of stationary atoms. The scattering probability of an ion–atom collision is intimately related to the interaction forces between atoms.

2.2 Interatomic Forces

We start our discussion with the concept that atoms are comprised of a central nucleus and orbital electrons, and we consider the forces when one atom interacts with another atom. The nucleus is effectively a solid body of diameter ~10^{-12} cm with a positive charge, Z, which is dependent on the number of protons present. If there were no orbital electrons, the force between two nuclei separated by a distance r would be Coulombic, of the form

$$F(r) = \frac{Z_1 Z_2 e^2}{r^2}, \tag{2.1}$$

where Z_1 and Z_2 are the numbers of protons contained in the nucleus, and $e^2 = 1.44$ eV nm (1.8).

For most purposes, the force between two atoms is expressed in terms of an interatomic potential, which depends primarily on the separation, r, between the atoms or other charged particles. If the dependence of the potential on other coordinates is neglected (central force approximation), then the force, $F(r)$, and the potential, $V(r)$, are related by

$$F(r) = -\frac{\mathrm{d}}{\mathrm{d}r}[V(r)]. \tag{2.2}$$

The restriction to r-dependence is usually a good approximation. Throughout this text, the variable r will define the separation distance between two interacting particles. The pairs might be atom–atom, electron–atom, electron–electron, ion–atom, etc.

The potential energy, or binding energy, of a single atom is the work done in bringing all components of the atom from infinity to their equilibrium positions in the atom. The simplest example is the semiclassical picture of the hydrogen atom. Thus, if an electron or charge, e, is brought from infinity to a distance r from the center of a proton under the attractive Coulomb field, the (negative) potential energy would be

$$V_{\mathrm{a}}(r) = \int_{\infty}^{r} \left(\frac{e^2}{r^2} \right) \mathrm{d}r = -(e^2 / r). \tag{2.3}$$

2.3 Short- and Long-Range Interatomic Forces

There are different types of forces that make up the interaction between two atoms over a large range of separation. Both experimental phenomena and theoretical considerations suggest that the forces can be categorized as *short-* and *long-range* forces.

The nature of the long-range force depends on whether the system consists of neutral atoms, charged ions, or a combination of the two. The force of greatest magnitude at large separations is the Coulomb electrostatic interaction between two charged ions, assumed to be point charges. The Coulomb potential is obtained by applying (2.2) to (2.1) to give

$$V_{\mathrm{c}}(r) = -\left(\frac{Z_1 Z_2 e^2}{r} \right). \tag{2.4}$$

where Z_1e and Z_2e are the charges of the ions. From (2.2) we see that the force $F(r)$ for a given central force field is expressed in terms of the interaction potential by

$$V_{\mathrm{c}}(r) = \int_{r}^{\infty} F(r) \mathrm{d}r. \tag{2.5}$$

If one or both of the particles are neutral, this Coulomb force is zero in the two-body approximation, and the long-range interaction is greatly reduced.

As two atoms approach each other, some degree of *merging* of the particles occurs. As the particles merge, the electron orbits from the electrons of each atom begin to overlap, and a limitation in the occupation of available electron states arises due to the Pauli Exclusion Principle. Under such circumstances, the

quantum mechanically derived short-range forces begin to govern the interaction potential, and the simple picture presented by the long-range Coulombic potential is no longer valid.

2.4 Interatomic Forces in Solids

In many applications involving the use of interatomic potentials in physics and materials science, it is not necessary to know the precise form of the force field between the interacting particles. Even if the exact functional form of the potential energy were known, its mathematical complexity would restrict it from being used in simple analytical work, finding utility only in detailed computer calculations. Empirical atomic interactions are based on a simple analytical model, which provides a mathematically tractable, analytical expression for the pairwise interaction between two atoms or ions.

A useful potential in modeling the condensed states of solids or liquids is the Lennard-Jones potential

$$V(r) = \frac{pq}{p-q}\Delta E\left[\frac{1}{p}\left(\frac{r_0}{r}\right)^p - \frac{1}{q}\left(\frac{r_0}{r}\right)^q\right], \tag{2.6}$$

where r_0 is the equilibrium interatomic separation between nearest neighbors (and is typically of the order of 10^{-8} cm), $\Delta E = V(r_0)$, and p and q are fitting constants.

Figure 2.1a schematically shows the potential energy diagram for a solid. While the exact features of this curve are model-dependent, the general shape and trends are universal for all materials. The minimum energy in this curve corresponds to the most stable configuration for atom spacing and represents the maximum energy that must be applied to pull an atom free from the crystal, i.e., the cohesive energy of the solid. The distance r_0, which is located at the minimum in the energy curve, corresponds to the equilibrium distance between atom near neighbors. The fact that such an equilibrium distance exists implies that the potential energy of the system possesses a minimum, at which point there are no net forces on the atoms. As Fig. 2.1 shows, any departure from r_0 that represents a decrease or increase in the spacing between atoms away from the equilibrium spacing results in an increase in the energy of the material (less negative) and makes the material less stable.

An alternative way to look at Fig. 2.1a is to recall that $-\mathrm{d}V/\mathrm{d}r = F$, where F is the force relationship between the atoms in the crystal. Note that under this convention, a positive force results when $\mathrm{d}r$ is negative, and a negative force results when $\mathrm{d}r$ is positive, which is opposite to the stress convention applied in materials science. We plot $F = \mathrm{d}V/\mathrm{d}r$ in Fig. 2.1b to maintain the stress convention, wherein increasing the distance between atoms produces a positive restoring force,

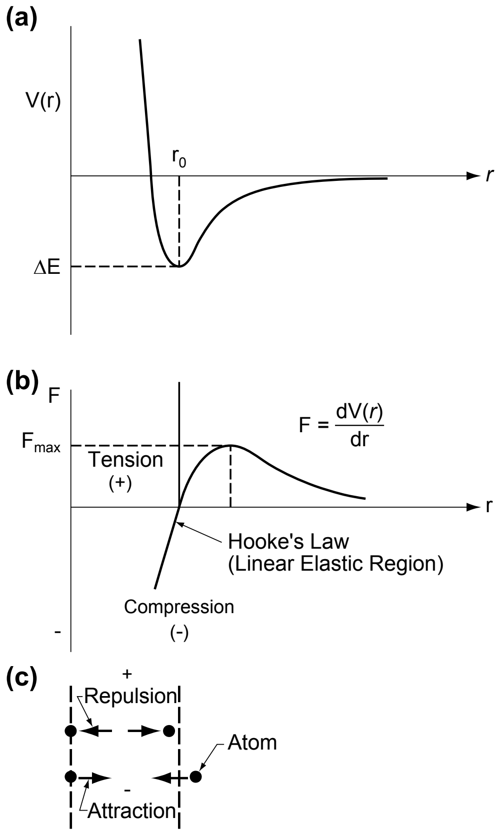

Fig. 2.1. (**a**) Interatomic potential function, $V(r)$, plotted against interatomic distance, r. (**b**) Interatomic force plotted as a function of r. (**c**) A schematic showing the force neighboring atoms experience as a function of separation (Tu et al. 1992)

and compressing the spacing produces a repulsive force. This data shows that there are no forces acting on atoms at a spacing of r_0. (The directions of the forces that an atom near the minimum experiences due to a neighboring atom located at $r = 0$ are indicated in Fig. 2.1c.) If the atoms are displaced toward each other, a repulsive force acts to increase the interatomic distance back to r_0. On the other hand, if the distance between atoms is increased, an attractive force acts to decrease the interatomic distance.

For crystalline solids, the equilibrium interatomic distance, r_0, can be estimated from knowledge of lattice site separation distances and is typically expressed as some fraction of the lattice parameter a_c. Aluminum forms a face-centered-cubic (fcc) lattice, with lattice parameter $a_c = 0.405$ nm. Since the densest packing direction is along the face diagonal, i.e., along the $\langle 110 \rangle$ direction, the equilibrium interatomic distance in Al is $\sqrt{2}a_c/2 = 0.29\text{nm}$. We can also calculate the distance approximately from the atomic volume Ω_v, where Ω_v is the reciprocal of the atomic

density N in atoms cm^{-3} ($\Omega_v = 1/N$; $\Omega_v = a^3/4$ for fcc lattices). The equilibrium distance $r_0 \cong \Omega^{1/3} = 0.26$ nm in this approximation.

2.5 Energetic Collisions of Atoms and Ions and the Screened Coulomb Potential

We now pass from the interactions between those atoms in equilibrium to the interactions between particles whose energies and velocities exceed that of thermal motion. This brings us to the range of interatomic forces at distances less than the equilibrium distance, r_0, in solids. The interaction distance, r, during the collision will depend on the relative energy of the collision. Consequently, some amount of closed-shell interpenetration and overlap will occur, which, in turn, will lead to considerable modification of the particle wave function at the moment of impact. Clearly, knowledge of the interatomic potential at small separations is crucial to the solution of problems involving ion–solid interactions and radiation damage in solids. The manner in which the potential energy of a two-particle system varies with the distance separating the two centers determines both the equilibrium properties of an assembly of atoms and the way that energetic particles interact with a lattice of stationary atoms. In the area of ion–solid interactions, knowledge of the potential energy function is necessary to determine the rate at which energetic ions lose energy as they penetrate a solid.

As an introduction to the problem of the interaction of an energetic ion with atoms in a solid, we first consider the limits of the collision. Consider two atoms with masses M_1 and M_2 and atomic numbers Z_1 and Z_2, respectively, separated by a distance r. The force is best described by a potential energy, $V(r)$, which arises from many-body interactions involving the electrons and the nuclei.

There are two useful reference points in the scale of separation. The first is the Bohr radius of the hydrogen atom, $a_0 = 0.053$ nm, which gives an indication of the extent of the atomic electron shells. The second is r_0, the spacing between neighboring atoms in the crystal (typically 0.25 nm). For the extreme condition, where $r \gg r_0$, the electrons populate the energy levels of the individual atoms, and, from the Pauli exclusion principle, there is a maximum number that can occupy any set of levels. The lowest levels, corresponding to the inner closed-shells, all will be occupied, and there will only be empty levels in the outer valence shells. As two atoms are brought together, the valence shells will begin to overlap, and there may be attractive interactions of the type that form bonds. Under these conditions the Lennard-Jones potential reasonably approximates the atomic interaction.

At the other extreme, when $r \ll a_0$, the nuclei become the closest pair of charged particles in the system, and their Coulomb potential dominates all other terms in $V(r)$. Then

$$V(r) = \frac{Z_1 Z_2 e^2}{r}, \tag{2.7}$$

where $e^2 = 1.44$ eV nm.

However, at intermediate distances, when $a_0 < r < r_0$, a positive potential energy of interaction results in a repulsive force between the two atoms. The main contributions to this potential are: (1) the electrostatic repulsion between the positively charged nuclei, and (2) the increase in energy required to maintain the electrons of nearby atoms in the same region of space without violating the Pauli exclusion principle. Since no two electrons can occupy the same position, overlapping of electrons from two atoms must be accompanied by promotion of some of the electrons to higher, unoccupied levels of the atomic structure. The energy required for this process increases as the atoms approach each other, because a large number of the orbital electrons become affected. Thus, for intermediate distances, there is a reduction of the Coulomb potential because of the electrostatic screening of the nuclear charges by the space charge of the innermost electron shells. One then refers to a *screened Coulomb potential*. This potential is given by

$$V(r) = \frac{Z_1 Z_2 e^2}{r} \chi(r), \tag{2.8}$$

where $\chi(r)$ is the screening function and is defined as the ratio of the actual atomic potential, at some radius r, to the Coulomb potential.

In ideal circumstances, $\chi(r)$ properly moderates the Coulomb potential to describe the interaction between ions and atoms at all separation distances. For large distances, $\chi(r)$ should tend to zero, while for very small distances, $\chi(r)$ should tend to unity. Such features allow a *single* interatomic potential energy function, (2.8), to describe the entire collision process.

2.6 Screening Functions

In the relatively low-velocity collision regime of most ion–solid interactions used in ion implantation and other ion surface modification experiments, the typical ion–atom distance of closest approach falls in the regime of $a_0 < r < r_0$, so that the nuclear charge is screened by the electrons. The development of a screening function requires a model of the atom as a starting point. The simplest atomic models are statistical models that allow straight forward calculation of the charge distribution of the colliding atoms. The charge distributions obtained from classical models developed by Thomas–Fermi, Bohr, Lenz–Jensen, and Moliere scale simply with atomic number and do not include any shell structure information.

Simple mathematical expressions have been developed for the Thomas–Fermi, Bohr, Lenz–Jensen, and Moliere screening functions. Several forms exist for the Thomas–Fermi model. The earliest and best known of these is the Sommerfeld asymptotic form,

$$\chi(r) = \left\{ 1 + \left(\frac{r}{12^{2/3}} \right)^{0.772} \right\}^{-3.886} . \tag{2.9}$$

Lindhard and coworkers proposed two somewhat simpler and more approximative Thomas–Fermi screening functions given by

$$\chi(r) = 1 - \frac{r}{(3 + r^2)^{1/2}} \tag{2.10}$$

and

$$\chi(r) = 1 - 1/2r. \tag{2.11}$$

The Moliere form of the screening function is composed of three exponentials:

$$\chi(r) = 7p\exp(-qr) + 11p\exp(-4qr) + 2p\exp(-20qr). \tag{2.12}$$

The screening function for a Bohr atom with $x = r/a_{TF}$ is

$$\chi_{Bohr}(x) = \exp(-x), \tag{2.13}$$

and the screening function for a Lenz–Jensen atom is

$$\chi_{LJ}(r) = [0.7466\exp(-1.038r)] + [0.2433\exp(-0.3876r)] + [0.01018\exp(-0.206r)]. \tag{2.14}$$

While classical models can be used to provide basic insight into screened interatomic potentials, the use of quantum mechanically derived charge distributions based on the Hartree–Fock atomic model create significant changes in the details of the interaction potential. In an attempt to find an analytic function that accurately predicts the interatomic potential between atoms, Ziegler, Biersack, and Littmark (ZBL; 1985) extended an earlier study made by Wilson et al. (1977), performing detailed calculations of solid-state interatomic potentials for 261 atom pairs. The details of the calculations can be found in Ziegler et al. (1985). The calculated total interaction potential was used together with the screening function, (2.8), to produce the universal screening function

$$\chi_U = 0.1818\exp(-3.2x) + 0.5099\exp(-0.9423x) + 0.2802\exp(-0.4028x) + 0.02817\exp(-0.2016), \tag{2.15}$$

where the reduced distance is given by

$$x = \frac{r}{a_U}, \tag{2.16}$$

and where a_U, the universal screening length, is defined by

$$a_U = \frac{0.8854 a_0}{\left(Z_1^{0.23} + Z_2^{0.23}\right)}. \tag{2.17}$$

The universal screening function, (2.15), is shown in Fig. 2.2 along with several of the classical screening functions given in this section.

2.7 Screening Length

In the equations given in Sect. 2.7, the screening function is always present as a function of x where x is a reduced distance defined by the particle separation distance, r, normalized by a screening length (also known as a screening radius). For example in (2.13), $x = r/a_{TF}$, where a_{TF} is the Thomas–Fermi screening length for the collision between the two atoms and is given by

$$a_{TF} = \frac{0.88534 a_0}{Z_{eff}^{1/3}}, \tag{2.18}$$

where Z_{eff} is the effective charge number in the interaction of two unlike atoms. There exist a number of approximations for Z_{eff}, but a simple description based on a mean value is

$$Z_{eff} = \left(Z_1^{1/2} + Z_2^{1/2}\right)^2. \tag{2.19}$$

The historical approach to creating classical interatomic screening functions is to use the simple atomic potentials and to adjust the definition of the screening length, a, to account for the two-atom potential. The screening length that is used to produce the reduced coordinate $x = r/a$ in interatomic potentials has been more suggested than derived. Bohr suggested a form

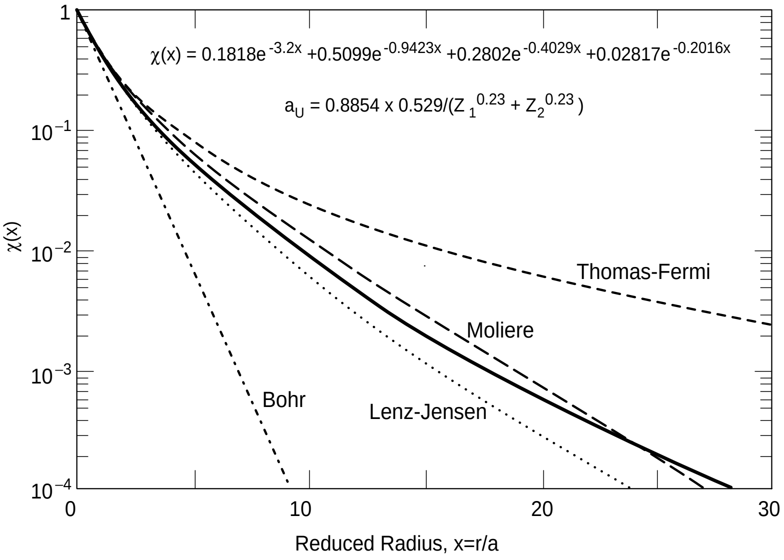

Fig. 2.2. The reduced screening functions of (2.15). This screening function is identified as χ_U, a universal screening function, with its argument, x, being defined as $x \equiv r/a_U$, where a_U is the universal screening length given in (2.17) (Ziegler et al. 1985).

$$a_B = \frac{0.8853 a_0}{\left(Z_1^{2/3} + Z_2^{2/3}\right)^{1/2}}, \tag{2.20}$$

where a_0 is the Bohr radius, 0.0529 nm, and Z_1 and Z_2 are the atomic numbers of the two atoms. Firsov suggested that the interatomic potential would be best described using a reduced distance defined by a screening length of the form

$$a_F = \frac{0.8853 a_0}{\left(Z_1^{1/2} + Z_2^{1/2}\right)^{2/3}}, \tag{2.21}$$

with the constant 0.8853 being derived from the Thomas–Fermi atom. Following Bohr, Lindhard also suggested using the atomic Thomas–Fermi screening function for the interatomic screening function, but with

$$a_L = \frac{0.8853 a_0}{\left(Z_1^{2/3} + Z_2^{2/3}\right)^{1/2}}. \tag{2.22}$$

The screening lengths presented in (2.20)–(2.22) do not differ significantly from each other. In all cases the screening lengths scale approximately with $Z^{1/3}$ of the colliding atoms.

References

Banerjea, A., Smith, J.R.: Origins of the universal binding-energy relation. Phys. Rev. B **37**, 6632 (1988)

Mayer, J.W., Lau, S.S.: Electronic Materials Science: For Integrated Circuits in Si and GaAs. Macmillan Publishing Company, New York (1990)

Rose, J.H., Smith, J.R., Ferrante, J.: Universal binding-energy curves for metals and Bimetallic interfaces. Phys. Rev. Lett. **47**, 675 (1981)

Rose, J.H., Smith, J.R., Ferrante, J.: Universal features of bonding in metals. Phys. Rev. B **28**, 1835 (1983)

Rose, J.H., Smith, J.R., Guines, F., Ferrante, J.: Universal features of the equation of state of metals. Phys. Rev. B **29**, 2963 (1984)

Torrens, I.M.: Interatomic Potentials. Academic, New York (1972)

Tu, K.-N., Mayer, J.W., Feldman, L.C.: Electronic Thin Film Science for Electrical Engineers and Materials Scientists. Macmillan Publishing Company, New York (1992)

Wilson, W.D., Haggmark, L.G., Biersack, J.P.: Calculations of nuclear stopping, range and straggling in the low-energy region. Phys. Rev. B **15**, 2458 (1977)

Ziegler, J.F., Biersack, J.P., Littmark, U.: The Stopping and Range of Ions in Solids. Pergamon Press, New York (1985)

Suggested Reading

Baker, E.B.: The application of the Fermi–Thomas statistical model to the calculation of potential distribution in positive ions. Phys. Rev. **36**, 630 (1930)

Eckstein, W.: Computer Simulation of Ion–Solid Interactions, chap. 4. Springer, Berlin Heidelberg New York (1991)

Feldman, L.C., Mayer, J.W.: Fundamentals of Surface and Thin Film Analysis. North-Holland, New York (1986)

Fermi, E.: Eine Statistische Methode zur Bestimmung einiger Eigenschaften des Atoms und ihre Anwendung auf die Theorie des periodischen Systems der Elemente. Z. Phys. **48**, 73 (1928)

Olander, D.R.: Fundamental Aspects of Nuclear Reactor Fuel Elements, chap. 17. Technical Information Center Energy Research and Development Administration, Springfield (1976)
Thomas, L.H.: The calculation of atomic fields. Proc. Cambridge Philos. Soc. **26**, 542 (1927)
Torrens, I.M.: Interatomic Potentials. Academic, New York (1972)
Ziegler, J.F., Biersack, J.P., Littmark, U.: The Stopping and Range of Ions in Solids. Pergamon Press, New York (1985)

Problems

2.1 Calculate the Universal value of the screening function for boron ($Z_1 = 15$) and arsenic ($Z_1 = 33$) ions incident on Si ($Z_2 = 14$)
2.2 Calculate the value of the Universal screening function $\chi(r/a)$ at values of $r/a_U = 1$ and 5
2.3 What are the values of a_{TF} for B and As ions incident on Si?

3 Dynamics of Binary Elastic Collisions

3.1 Introduction

In ion beam modification of materials, the energetic ions interact with the solid through atom interatomic potential. These interactions are the basis of the development of expressions for ion range and ion damage in solids. Consider the passage of an energetic ion in a solid during an ion implantation experiment (Fig. 3.1). As the ion travels through the solid, it undergoes collisions with the stationary target atoms, which deflect the ion from its initial direction. The ion also collides with electrons in the solid and loses energy in these collisions. The major changes in its flight direction are due to the ion's collision with individual lattice atoms. This chapter will focus on two-body collisions, or binary collisions, involving energetic ions and target atoms.

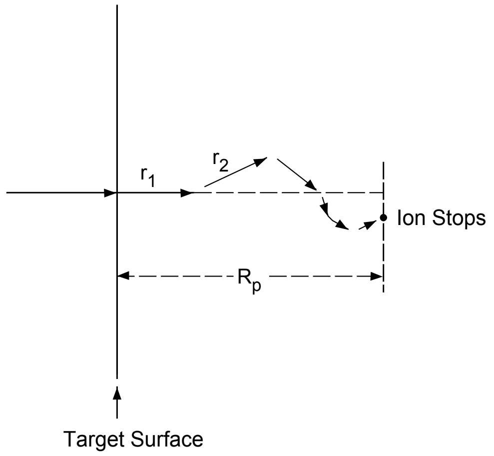

Fig. 3.1. The passage of an energetic ion in a solid during an ion implantation experiment, showing the total ion path and the projected range, R_p. As the ion travels across the solid, it undergoes collisions with stationary target atoms, which deflect the ion from its initial direction

The simplest collision event is the collision between a charged particle and the atomic nucleus. This can be treated as a two-body collision provided that the mean free path between collisions is much greater than the interatomic spacing. The chance of correlated effects, due to neighboring atoms recoiling simultaneously, is then very small. The momentum of the recoiling target atoms is the parameter that determines the amount of damage that occurs in the solid target. The momentum transferred to the recoiling atom also is responsible for a large portion of the energy-loss process of the ion.

In developing our understanding of ion–solid interactions for the purposes of ion beam modification of materials, we will first derive some general relations governing two-body collisions, considering only the asymptotic values of momentum at great distances from the collision. The principles of conservation of momentum and energy are all that are required to obtain the recoil energy as a function of recoil angle. We shall assume that collisions are elastic and, further, that velocities are small enough for nonrelativistic mechanics to apply.

3.2 Classical Scattering Theory

The following assumptions are usually made in the description of the scattering processes between energetic particles in solids:

(a) Only two-atom collisions are considered;
(b) Classical dynamics is applied;
(c) Excitation or ionization of electrons only enters as a source of energy-loss, but does not influence the collision dynamics;
(d) One of the two colliding atoms initially is at rest.

Assumption (a) is appropriate for *violent* collisions. Violent collisions between atoms of reasonably high energy range (keV) require the collision partners to approach very closely, so that the probability of a collision between three or more atoms is small. *Soft* collisions can take place at large distances and therefore can involve more than two atoms simultaneously. However, soft collisions usually can be treated by perturbation theory (the momentum or impulse approximation), in which case no restriction to binary collisions is necessary. At lower energies (below 1 keV), collective effects become increasingly important and assumption (a) starts to break down. However, the problems associated with many-body collisions in this low-energy regime can be overcome by molecular-dynamic simulations, where assumption (a) is not required.

In the limit of assumption (b), the applicability of classical mechanics is normally limited to specific quantities, one of which is the differential scattering cross-section, $\mathrm{d}\sigma(\theta_c)$, where θ_c is the center-of-mass (CM) scattering angle.

Neglecting the effect of electronic excitation on the collision dynamics, assumption (c), is justified if either the energy transferred to electrons is small compared with the exchange of kinetic energy between the atoms (so that the

scattering angle can be calculated by assuming elastic collisions) or if no appreciable deflection takes place. In either case, the electronic energy-loss enters as superimposed energy absorption.

The assumption of one collision partner being at rest initially, assumption (d), has been made in all previous work except molecular-dynamics computations. It is not fulfilled in very dense collision cascades, especially when the process of energy dissipation has proceeded to the point where most of the atoms in the cascade are in motion.

3.3 Kinematics of Elastic Collisions

The energy transfers and kinematics in elastic collisions between two isolated particles can be fully solved by applying the principles of conservation of energy and momentum. Collisions in which the kinetic energy is conserved are considered *elastic*. An *inelastic* collision does not conserve kinetic energy; an example is the promotion of electrons to higher-energy states in collisions where substantial K-shell overlap occurs. The energy lost in promoting the electrons is not available in the particle–atom kinematics after collision. In this chapter we consider only elastic processes in ion–solid interactions. In Chap. 5 we will discuss the inelastic aspects of the collision process.

For an incident energetic particle of mass M_1, the values of the velocity and energy are v_0 and E_0 ($E_0 = (1/2)M_1v_0^2$), while the target atoms of mass M_2 are at rest. After the collision, the values of the velocities v_1 and v_2 and energies E_1 and E_2 of the projectile and target atoms, respectively, are determined by the scattering angle, θ, and recoil angle, ϕ. The notation and geometry for the laboratory system of coordinates are given in Fig. 3.2. Table 3.1 lists those symbols used in kinematic expressions.

Conservation of energy and conservation of momentum parallel and perpendicular to the direction of incidence are expressed by the equations

$$E_0 = \frac{1}{2}M_1v_0^2 = \frac{1}{2}M_1v_1^2 + \frac{1}{2}M_2v_2^2, \tag{3.1}$$

$$M_1v_0 = M_1v_1\cos\theta + M_2v_2\cos\phi, \tag{3.2}$$

$$0 = M_1v_1\sin\theta - M_2v_2\sin\phi. \tag{3.3}$$

These three equations, (3.1)–(3.3), can be solved in various forms (Nastasi et al. 1996).

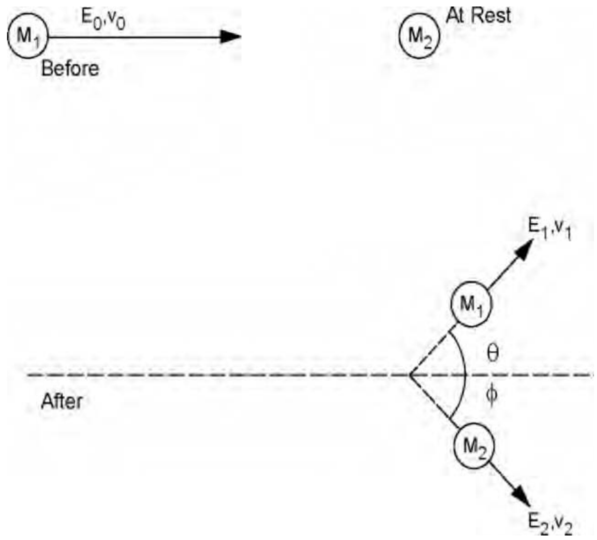

Fig. 3.2. Elastic collision diagram between two unequal masses as seen in the laboratory reference frame

Table 3.1. Definitions and symbols used in collision kinematics

Symbol	Definition
E_0	Energy of the incident projectile
E_c	Total kinetic energy in the center-of-mass system
E_1	Laboratory energy of the scattered projectile
E_2	Laboratory energy of the recoiling target
T	Energy E_2 transferred to the target atom
K	Backscattering kinematic factor E_1/E_0
M_1	Mass of the incident projectile
M_2	Mass of the target particle
M_c	Reduced mass in center-of-mass system
μ	Mass ratio M_1/M_2
V_0	Velocity of the incident projectile in laboratory coordinates
v_1	Velocity of the scattered projectile in laboratory coordinates
v_2	Velocity of the recoiling atom in laboratory coordinates
v_c	Velocity of the reduced mass in center-of-mass coordinates
v_{ion}	Velocity of the incident projectile (ion) in center-of-mass coordinates
v_{atom}	Velocity of the target atom in center-of-mass coordinates
θ	Laboratory angle of the scattered projectile
θ_c	Center-of-mass angle of the scattered projectile
θ_m	Maximum laboratory angle for M_1 scattering ($M_1 > M_2$)
ϕ	Laboratory angle of the recoiling target atom
ϕ_c	Center-of-mass angle of the recoiling target atom
π	$\pi = 180° = \theta_c + \phi_c$

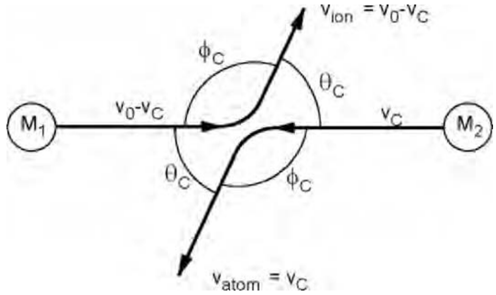

Fig. 3.3. Elastic collision diagrams between two unequal masses as seen in the CM reference frame

3.4 Center-of-Mass Coordinates

The collision and scattering problem defined by Fig. 3.2 now will be restated in terms of CM coordinates. The motivation for this transformation will be obvious when we discuss scattering in a central force field later in this chapter. Through the use of CM coordinates it will be shown that, no matter how complex the force is between the two particles, so long as it acts only along the line joining them (no transverse forces), the relative motion of the two particles can be reduced to that of a single particle moving in an interatomic potential centered at the origin of the CM coordinates. By introducing the CM system, the mutual interaction of the two colliding particles can be described by a force field, $V(r)$, which depends only on the absolute value of the interatomic separation, r. The motion of both particles is given by one equation of motion. This equation has r as the independent variable and describes a particle moving in the central force field, $V(r)$.

The CM coordinates for a two-particle system are defined in a zero-momentum reference frame in which the total force on two particles that interact only with each other is zero. We can define the total force of two interacting particles as

$$F_T = F_1 + F_2 = \frac{dp_T}{dt}, \tag{3.4}$$

where F_T is the total force, F_1 and F_2 are the individual forces on particles 1 and 2, respectively, and p_T is the total linear momentum of the two-particle system. For $F_T = 0$, $dp_T = 0$, indicating that the total momentum is unchanged or conserved during the interaction process.

One consequence associated with observing elastic collisions in the CM coordinates is that the individual particle kinetic energies are unchanged by the

collision process. Thus, the CM velocities of the two colliding particles are the same before and after the collision process. In addition, the CM scattering angle of particle 1 will equal the scattering angle of particle 2. Finally, all scattering angles in the CM system are allowed, unlike the scattering angles in the laboratory reference frame, where the allowed scattering angles depend on the ratio M_1/M_2.

For CM coordinates, Fig. 3.3, we define the system velocity, v_c, such that in this coordinate system there is no net momentum change, so that

$$M_1 v_0 = (M_1 + M_2) v_c. \tag{3.5}$$

We also define in CM coordinates a reduced mass, M_c, given by the relation

$$\frac{1}{M_c} = \frac{1}{M_1} + \frac{1}{M_2} \tag{3.6}$$

or

$$M_c = \frac{M_1 M_2}{M_1 + M_2}. \tag{3.7}$$

From (3.7) we see that, for large mass difference between M_1 and M_2, M_c approaches the value of the lower mass. For example, if $M_2 << M_1$, $M_c \cong M_2$.

We can represent the CM velocity in terms of reduced mass as

$$v_c = v_0 \frac{M_c}{M_2} = v_0 \frac{M_1}{M_1 + M_2}. \tag{3.8}$$

From the velocity vector diagram in Fig. 3.3 and (3.8), the ion and target atom velocities in the CM coordinates are:

$$v_1 = v_{\text{ion}} = v_0 - v_c = v_0 \frac{M_c}{M_1} = v_0 \frac{M_2}{M_1 + M_2}, \tag{3.9}$$

$$v_2 = v_{\text{atom}} = v_c = v_0 \frac{M_c}{M_2} = v_0 \frac{M_1}{M_1 + M_2}. \tag{3.10}$$

Equation (3.10) shows that the target atom, which has zero velocity before the collision in the laboratory reference frame, has the system velocity v_c before and after the collision in the CM reference frame.

Equations (3.9) and (3.10) show the advantage of the CM reference frame. The system velocity, v_c, and the atom and ion velocities, v_{atom} and v_{ion}, remain constant

and are independent of the final scattering angle between the two particles (Fig. 3.3b). Thus, regardless of whether the collision is elastic or inelastic, the total momentum is unchanged in a collision. In addition, from (3.9) and (3.10), we see that the ratio of the ion-to-atom velocities is inversely proportional to the ratio of their masses

$$\frac{v_{\text{ion}}}{v_{\text{atom}}} = \frac{v_0 - v_{\text{c}}}{v_{\text{c}}} = \frac{M_2}{M_1} = \frac{1}{\mu}. \tag{3.11}$$

Another advantage to the CM reference frame is that the CM total energy, E_{c}, is equal to the CM initial kinetic energy

$$E_{\text{c}} = \frac{1}{2} M_{\text{c}} v_0^2, \tag{3.12}$$

$$E_{\text{c}} = \frac{1}{2} \frac{M_1 M_2}{M_1 + M_2} v_0^2 = \frac{M_2}{M_1 + M_2} E_0 = \frac{M_{\text{c}}}{M_1} E_0, \tag{3.13}$$

where $M_1 v_0^2/2 = E_0$.

In converting the scattering angles from the laboratory system to the CM system, it can be shown that

$$\phi_{\text{c}} = 2\phi. \tag{3.14}$$

From the CM diagram, Fig. 3.3, we have $\theta_{\text{c}} + \phi_{\text{c}} = \pi$, which allows us to rewrite (3.14) in the form

$$\phi = \frac{\pi - \theta_{\text{c}}}{2}. \tag{3.15}$$

Equation (3.15) relates the target atom scattering angle in the laboratory to the CM ion scattering angle. In addition:

1. The CM angle of the scattered projectile is $\theta_{\text{c}} = \pi - 2\phi = \pi - \phi_{\text{c}}$. When $M_1 \leq M_2 \Rightarrow \mu \leq 1$, θ_{c} is defined for all $\theta \leq \pi$ and $\theta_{\text{c}} = \theta + \sin^{-1}(\mu \sin\theta)$.
2. When $M_1 > M_2 \Rightarrow \mu > 1$, θ_{c} is double valued and the laboratory scattering angle is limited to the range $\theta > \sin^{-1}(1/\mu)$. In this case, $\theta_{\text{c}} = \theta + \sin^{-1}(\mu \sin\theta)$, or $\theta_{\text{c}} = \pi + \theta - \sin^{-1}(\mu \sin\theta)$.

The transferred energy, T, can be related to the ion scattering angle, θ_{c}, by (3.15) to yield

$$T = \frac{2}{M_2}\left(v_0 M z_c \sin\frac{\theta_c}{2}\right)^2 = \frac{4E_c M_c}{M_1}\sin^2\frac{\theta_c}{2} \, . \tag{3.16}$$

From the description of reduced mass, (3.7), we rewrite (3.16) to obtain

$$T = E_0 \frac{4M_1 M_2}{(M_1 + M_2)^2}\sin^2\frac{\theta_c}{2} \tag{3.17}$$

or

$$T = T_M \sin^2\frac{\theta_c}{2}, \tag{3.18}$$

where T_M is the maximum energy transferable in a head-on collision, $\theta_c = 0$, and is given by

$$T_M = \frac{4M_1 M_2}{(M_1 + M_2)^2} E_0 = \gamma E_0, \tag{3.19}$$

where $\gamma = 4M_1 M_2/(M_1 + M_2)^2$. Examining (3.19) we see that, in an elastic collision, for the equal mass case, all the energy may be transferred, whereas for a larger mismatch in particle masses, only a fraction of the energy may be transferred.

These final relationships give the energy-loss by the ion through elastic collisions with target atoms; they will be needed in the development of the concepts of energy-loss cross-section and nuclear stopping, which will be discussed in Chaps. 4 and 5, respectively.

As an example, to determine the energy transferred in a binary collision where a 100 keV boron ($M_1 = 10$) ion is incident on Si ($M_2 = 28$) and the boron is scattered through a laboratory angle $\theta = 45°$, one first determines the corresponding CM angle, θ_c, from the expressions given under (3.15), $\theta_c = \theta + \sin^{-1}(\mu \sin\theta)$. This gives $\theta_c = 60°$. One would next calculate the ratio T/E from (3.17), which gives $T = 0.78E_0$. Finally, for $E_0 = 100$ keV, $T = 19.5$ keV.

3.5 Motion under a Central Force

In our discussions of ion–solid interactions, we restrict ourselves to central forces where the potential V is a function of r only ($V = V(r)$), so that the force is always along r. We need to consider only the problem of a single particle of mass, M_c, moving about a fixed center of force, which will be taken as the origin of the

coordinate system. Since potential-energy involves only the radial distance, the problem has spherical symmetry, indicating any rotation about a fixed axis can have no effect on the solution; i.e., if either particle is located at the origin, the force on the other is given by a central force, $F(r)$, which only depends on the separation distance, r.

In the problem examined in this section, we will assume that, in the laboratory system, one of the particles is practically at rest at the origin, O, while the other one moves with velocity v – a good approximation when the stationary particle is much heavier than the moving particle.

3.5.1 Energy Conservation in a Central Force

For conservative central forces and a defined interaction potential, $V(r)$, we can write a statement for the total mechanical energy for a particle of mass M, a distance r away from a central force F as

$$E = \frac{M}{2}\left[v_r^2 + v_\theta^2\right] + V(r), \tag{3.20}$$

where v_r and v_θ are the radial and transverse velocities, respectively. The first term on the right-hand side of (3.20) represents the kinetic energy in polar coordinates.

In addition to the total energy equation given above, we also have the condition of conservation of angular momentum,

$$\ell = Mrv_\theta \tag{3.21}$$

The quantities E and ℓ are the constants of motion, while $V(r)$ is the potential-energy for a particle of mass M in a central field. We rewrite (3.20) in the form

$$E = E(r) = \frac{Mv_r^2}{2} + \frac{\ell^2}{2Mr^2} + V(r). \tag{3.22}$$

All terms in (3.22) are a function of r only. The first term is the kinetic energy for the radial component; the term $\ell^2/2Mr^2$ is referred to as the centrifugal energy; and $V(r)$ is the interatomic potential-energy. The centrifugal energy is the portion of the kinetic energy term that is due to the particle's motion transverse to the direction of the radius vector. It is because the centrifugal energy can be described as a function of radial position r alone that we can treat the radial motion of a particle as a one-dimensional problem in r. Equation (3.22) is now simply a function of r only.

3.5.2 Angular Orbital Momentum and the Impact Parameters

Consider an interaction potential-energy, $V(r)$, which tends to zero as r approaches infinity. This situation corresponds to the condition that a moving particle has positive kinetic energy at infinity. If $V(r)$ is everywhere positive, but decreasing monotonically with r, the potential is repulsive and the radial motion of this particle in the field $V(r)$ will have no bounds or limits in its maximum value of r. However, there is a minimum in r, the distance of closest approach, $r_{\min}$, which depends on the particle's total energy and the nature of the interaction potential.

In Fig. 3.4a, the energy curves for attractive potential-energy are presented along with an arbitrarily defined centrifugal energy curve. In Fig. 3.4b, the effective potential-energy curve, given by

$$V'(r) = V(r) + \frac{\ell^2}{2Mr^2} \tag{3.23}$$

is shown. Figure 3.5 gives a schematic representation of how the effective potential-energy affects the trajectories of a particle moving with energy, $E = Mv^2/2$. The distance of closest approach is determined by the value of r that satisfies the condition $E = V'(r)$.

At large distances away from the center of force, the magnitudes of $V(r)$ and $\ell^2/2Mr^2$ will be negligible (Fig. 3.5).Under such conditions a particle with energy E travels in a straight line with a speed $v_0 = (2E/M)^{1/2}$. The particle's direction of motion is offset from a parallel line through the center of force (target atom) by a distance b that is directly related to the centrifugal energy and the angular orbital momentum. From the law of conservation of angular momentum,

$$\ell = Mr_{\min} v_\theta \tag{3.24}$$

approaches

$$\ell = Mv_0 b \tag{3.25}$$

for r approaching infinity. Since angular momentum is conserved in central force scattering, ℓ is defined by either form given by (3.24) or (3.25). The distance b is called the *impact parameter* and is very useful in characterizing a particle that approaches a center of force.

From Fig. 3.4, the distance of closest approach, $r_{\min}$, is shown to be determined from the condition $E = V'(r)$, which translates to

$$E = V(r_{\min}) + \frac{\ell^2}{2Mr_{\min}^2}. \tag{3.26}$$

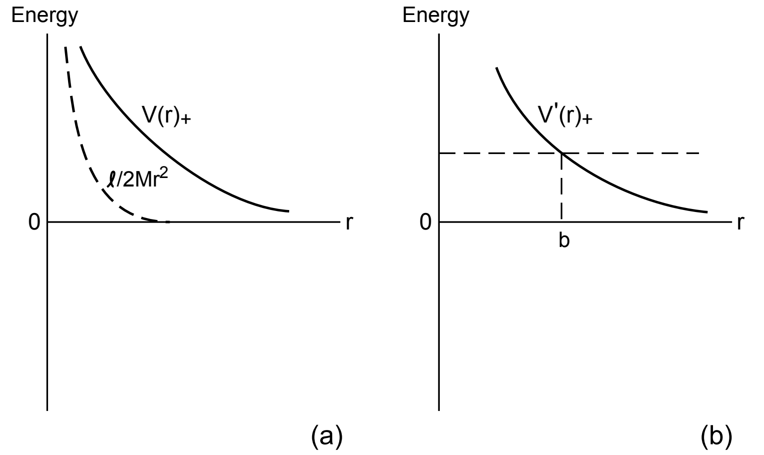

Fig. 3.4. (**a**) Centrifugal potential-energy curve (*dashed*) and a potential-energy curve that might arise from electrical interactions of like charges. (**b**) Effective potential-energy curves corresponding to the case shown in (**a**), indicating the distance of closest approach, *b*, for a given positive total energy (French, 1971)

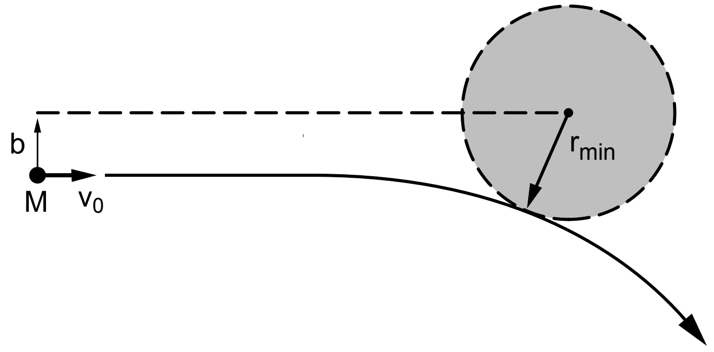

Fig. 3.5. Plan view of trajectory of a particle moving with the impact parameter *b* and with a repulsive center of force (French, 1971)

Using (3.25) to define the orbital angular momentum, we rewrite (3.26) in the form

$$0 = 1 - \frac{V(r_{\min})}{E} - \frac{b^2}{r_{\min}^2}, \tag{3.27}$$

where $E = E_c$ in the CM system. Equation (3.26) shows that $r_{\min}$ will depend on the energy of the ion and the form of the interatomic potential. Knowledge of $V(r)$ allows one to find $r_{\min}$ by applying the quadratic equation to (3.27).

3.6 Distance of Closest Approach

The distance of closest approach was defined by (3.27) and can be rewritten as

$$\frac{V(r_{\min})}{1 - b^2/r_{\min}^2} = E_c = \frac{M_2}{M_1 + M_2} E_0. \tag{3.28}$$

For a Coulomb potential and a head-on collision, $b = 0$, we can rewrite (3.28) as

$$d_c \equiv (r_{\min})_{b=0} = \frac{M_1 + M_2}{M_2 E_0} Z_1 Z_2 e^2 = \frac{Z_1 Z_2 e^2}{E_c} \tag{3.29}$$

for a head-on collision where d_c is called the collision diameter, $r_{\min} \equiv d_c$. For a given interatomic potential and ion energy, the collision diameter gives the lower limit to $r_{\min}$.

As an example, for 1 MeV He ($Z_1 = 2$) ions incident on Si ($Z_2 = 14$), the CM energy, $E_c = M_2E_0/(M_1 + M_2)$, equals 875 keV and the distance of closest approach (the collision diameter) equals $Z_1Z_2e^2/E_c = 4.6 \times 10^{-5}$ nm, which has a value much smaller than a_{TF}. It is informative to write d_c relative to the screening distance, a_{TF}, where the parameter a_{TF}/d_c is referred to as ε, the reduced energy, given by

$$\varepsilon \equiv \frac{a_{TF}}{d_c} = \frac{a_{TF} E_c}{Z_1 Z_2 e^2} = \frac{E}{Z_1 Z_2 e^2} \frac{a_{TF} M_2}{M_1 + M_2}. \tag{3.30}$$

Examining (3.30) we see that ε is a dimensionless energy unit. Physically, ε gives a measure of how energetic the collision is and how close the ion gets to the nucleus of the target atom. For example, the value of the Thomas-Fermi screening distance, a_{TF}, for He on Si is

$$a_{TF} = \frac{0.885 \times 0.053}{\left(Z_1^{1/2} + Z_2^{1/2}\right)^{2/3}} = 1.5 \times 10^{-2}\ \text{nm}.$$

The reduced energy for 1 MeV He ions is

$$\varepsilon = \frac{1.5\times10^{-2}}{4.6\times10^{-5}\ \text{nm}} = 0.34\times10^{3}.$$

This large value of ε is consistent with the very small value of the collision diameter. For calculation purposes, (3.30) can be simplified and rewritten as

$$\varepsilon = \frac{0.0326E(\text{eV})}{Z_1Z_2\left(Z_1^{1/2}+Z_2^{1/2}\right)^{2/3}}\frac{M_2}{M_1+M_2}. \tag{3.31}$$

References

French, A.P.: Newtonian Mechanics. W.W. Norton, New York (1971)

Nastasi, M., Mayer, J.W., Hirvonen, J.K.: Ion–Solid Interactions: Fundamentals and Applications, chap. 3. Cambridge University Press, Cambridge (1996)

Sigmund, P.: Collision theory of displacement damage, ion ranges and sputtering. Rev. Roum. Phys. **17**, pp. 823, 969 and 1079 (1972)

Suggested Reading

Feldman, L.C., Mayer, J.W.: Fundamentals of Surface and Thin Film Analyses. North-Holland, New York (1986)

Goldstein, H.: Classical Mechanics. Addison-Wesley, Reading, MA (1959)

Johnson, R.E.: Introduction to Atomic and Molecular Collisions. Plenum Press, New York (1982)

Olander, D.R.: Fundamental Aspects of Nuclear Reactor Fuel Elements, chap. 17. National Technical Information Service, Springfield, VA (1976)

Thompson, M.W.: Defects and Radiation Damage in Metals. Cambridge University Press, Cambridge (1969)

Torrens, I.M.: Interatomic Potentials. Academic, New York (1972)

Symon, K.R.: Mechanics. Addison-Wesley, Reading, MA (1953)

Ziegler, J.F., Biersack, J.P., Littmark, U.: The Stopping and Range of Ions in Solids. Pergamon Press, New York (1985)

Problems

3.1 Derive the expression for the laboratory energy of the recoil nucleus.

3.2 Write a simple expression for E_1/E_0 and E_2/E_0 in backscattering ($\theta = 0°$) and right angle scattering ($\theta = 90°$) for $M_1 = M_2$, $M_1 > M_2$, and $M_1 < M_2$. What are the allowed solutions?

3.3 What is the maximum energy transferred to electrons, silicon atoms, and copper atoms by incident 100 keV electrons, silicon ions, and copper ions?

3.4 In the laboratory system, we have arsenic ions at 100 keV scattered from silicon atoms at $\theta = 10°$.sdf
(a) What is v_1, v_2, ϕ, and E_2 in the laboratory system?
(b) What is v_{ion}, θ_c, and ϕ_c in the center-of-mass system?

3.5 Prove that $\ell = Mrv_\theta$ approaches $\ell = Mv_0 b$ for r approaching infinity ((3.24) and (3.25)).

3.6 Consider a 2 MeV^4 He incident on gold (pure Coulomb potential)
(a) Calculate the distance of closest approach for a head-on collision ($b = 0$)
(b) What is the value of r_{min} values of $b = 0.5a_L$ and $5a_L$, where a_L is defined in (2.22)?

3.7 Using (3.27) and assuming a pure Coulomb potential, calculate the value of r_{min} for a 100 keV boron ($Z_1 = 5$) on silicon ($Z_2 = 14$) for an impact parameter $b = 1$ nm. What is the value of ε (3.30)? What is the significance of your answers?

4 Cross-Section

4.1 Introduction

In Chap. 3 we derived equations describing the kinematics of binary elastic collisions. These equations enable us to calculate the amount of energy-transferred to a target atom in a collision when the scattering angle of the projectile or the target atom is known. Conversely, we could calculate the scattering angle if the amount of energy loss in the collision was known.

In Chap. 4 we will examine the probability of ion–solid scattering events. During ion irradiation and ion implantation experiments, many ions or energetic particles interact with many target nuclei. Due to the large number of interactions, the questions of how much energy will be transferred in a collision or what the scattering angle will be must be answered using statistics and probability. The differential cross-section is the fundamental parameter that we will develop. It gives a measure of either the probability of transferring energy T in the range between T and $T + \mathrm{d}T$ to a target atom, or of the probability of scattering a projectile into some angle between θ_c and $\theta_c + \mathrm{d}\theta_c$. The differential cross-section has units of area, typically centimeters squared. The differential cross-section integrated over all angles is the total cross-section, often referred to simply as the cross-section.

The differential cross-section will become an important parameter in describing ion ranges in solids and radiation damage, both of which will be discussed later in this book. The differential cross-section depends strongly on the form of the interatomic potential.

4.2 Scattering Cross-Section

In ion–solid interactions, it is customary to describe the number of particles scattered through different angles, θ_c, in terms of a quantity called the angular differential scattering cross-section. Imagine the experiment depicted in Fig. 4.1, where a beam of ions is incident on a thin foil and is scattered into a detector of area Δa at a polar angle between θ_c and $\theta_c + \mathrm{d}\theta_c$. Each of the ions in the incident

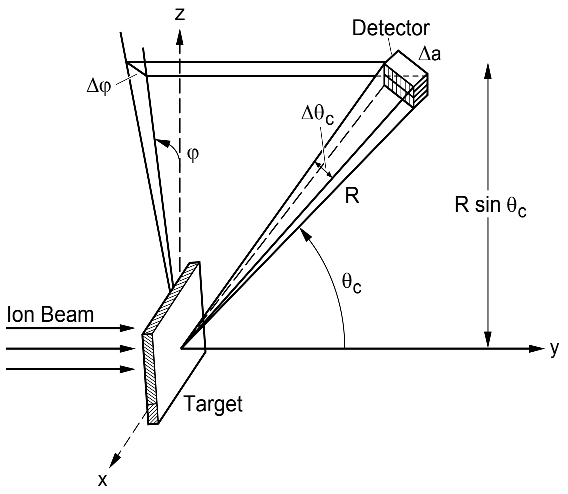

Fig. 4.1. Experiment for measuring angular differential cross-section. The detector area is $\Delta a = (R\Delta\theta_c)(R \sin \theta_c\Delta\varphi)$. By moving the detector to all angular positions for a fixed R, all the scattered particles can be counted, and the detector will have covered an area $4\pi R^2$, or a total solid angle of 4π

beam has a different impact parameter b (as described in Chap. 3) and will be scattered through a different angle. We define the differential $\mathrm{d}n_\theta$ as the number of ions scattered into the detector of area Δa, between angles θ_c and $\theta_c + \mathrm{d}\theta_c$, per unit time. We define I_0 to be the flux of incident particles, equal to the number of ions incident on the sample per unit time, per unit area (i.e., ions s^{-1} cm^{-2}). The solid angle of the detector, $\Delta\Omega$, is related to the detector area, Δa, and its distance away from the sample, R. It is given by

$$\Delta\Omega = \frac{\Delta a}{R^2} = \frac{(R\Delta\theta_c)(R\sin\theta_c\Delta\varphi)}{R^2} = \Delta\theta\,\Delta\varphi\sin\theta_c. \tag{4.1}$$

We now define $\mathrm{d}\sigma(\theta_c)$, the differential scattering cross-section, to be given by

$$\frac{\mathrm{d}\sigma(\theta_c)}{\mathrm{d}\Omega} \equiv \frac{1}{I_0}\frac{\mathrm{d}n_\theta}{\mathrm{d}\Omega}, \tag{4.2}$$

where for $\Delta a \to 0$ we have $\Delta\Omega \to \mathrm{d}\Omega$. The term $\mathrm{d}\sigma(\theta_c)/\mathrm{d}\Omega$ is the differential scattering cross-section per unit solid angle, and $\mathrm{d}n_\theta/\mathrm{d}\Omega$ is the number of particles scattered into the angular regime between θ_c and $\theta_c + \mathrm{d}\theta_c$ per unit solid angle, per

unit time. Since the solid angle Ω unit (steradian) is dimensionless, the differential scattering cross-section has units of area.

The cross-section is simply the effective target area presented by each scattering center (target nucleus) to the incident beam. At a more microscopic level, the scattering cross-section can be shown to be dependent on b, the impact parameter. In Fig. 4.2 we present the collision process in which the incident particle is scattered by a target nucleus through an angle θ_c. The projectile moves in a nearly straight line until it gets fairly close to the target nucleus, at which point it is deflected through an angle θ_c. After being deflected, the trajectory of the particle is again nearly a straight line. If there had been no interaction force between the projectile and the target nucleus, the projectile would have maintained a straight trajectory and passed the target nucleus at a distance b.

On examining Fig. 4.2, we see that all incident particles with impact parameter b are headed in a direction to strike the rim of the circle drawn around the target nucleus and will be deflected by an angle θ_c. The area of this circle is πb^2, and any particle with a trajectory that strikes anywhere within this area will be deflected by an angle greater than θ_c. The target area defined by the impact parameter is called the total cross-section, $\sigma(\theta_c)$:

$$\sigma(\theta_c) = \pi b^2. \tag{4.3}$$

For projectiles moving with small values of b, the cross-section defined by (4.3) will be small, but, due to the interaction forces, the scattering angle will be large. Thus, b is proportional to $\sigma(\theta_c)$, while b and $\sigma(\theta_c)$ are inversely related to θ_c. From this discussion we see that $b = b(\theta_c)$.

In addition to the total cross-section, there is the differential cross-section, $d\sigma(\theta_c)$, and its relationship to b. As shown in Fig. 4.3, particles incident with

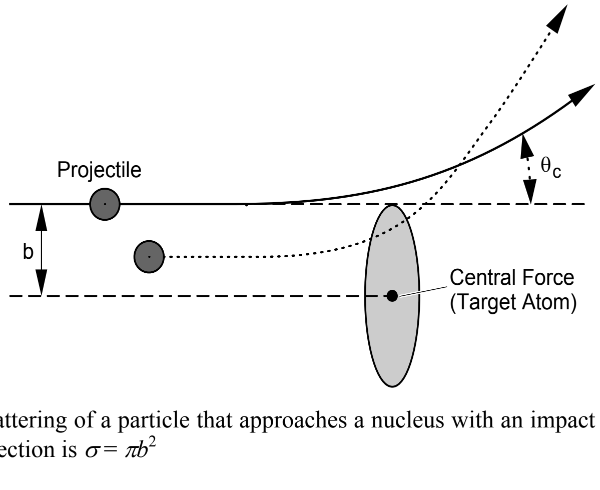

Fig. 4.2. Scattering of a particle that approaches a nucleus with an impact parameter b. The total cross-section is $\sigma = \pi b^2$

impact parameters between b and $b + \mathrm{d}b$ will be scattered through angles between θ_c and $\theta_c + \mathrm{d}\theta_c$. The differential cross-section for this process is found by taking the differential of (4.3) with respect to the impact parameter.

$$\mathrm{d}\sigma(\theta_c) = \mathrm{d}(\pi b^2) = 2\pi b\,\mathrm{d}b. \tag{4.4}$$

From the description given in (4.4) and the schematic presented in Fig. 4.3, the differential cross-section of each target nucleus is presented as a ring of radius b, a circumference $2\pi b$, and a width $\mathrm{d}b$. Any incident particles with an impact parameter within $\mathrm{d}b$ will be scattered into angles between θ_c and $\theta_c + \mathrm{d}\theta_c$.

From the examples presented in Figs. 4.2 and 4.3, we see that there is a unique connection between the value of b and the scattering angle, θ_c. To find the dependence of $\mathrm{d}\sigma(\theta_c)$ on the scattering angle, we rewrite (4.4) in the form

$$\mathrm{d}\sigma(\theta_c) = 2\pi b(\theta_c)\left|\frac{\mathrm{d}b(\theta_c)}{\mathrm{d}\theta_c}\right|\mathrm{d}\theta_c. \tag{4.5}$$

We use the absolute value of $\mathrm{d}b(\theta_c)/\mathrm{d}\theta_c$ to maintain $\mathrm{d}\sigma(\theta_c)$ as a positive value; θ_c increases as b decreases, indicating that $\mathrm{d}b(\theta_c)/\mathrm{d}\theta_c$ is negative.

To determine an expression for the differential scattering cross-section per unit solid angle, (4.1), we note that scattering experiments are performed by observing the number of incident particles that are scattered into a solid angle located at θ_c. Measurements give information in units of the number of scattering particles per element of solid angle. A schematic of this process is presented in Fig. 4.4. The annular region represents the solid angle $\mathrm{d}\Omega$ subtended between the scattering angles θ_c and $\theta_c + \mathrm{d}\theta_c$. The entire area of the sphere of radius R is $4\pi R^2$, and the total

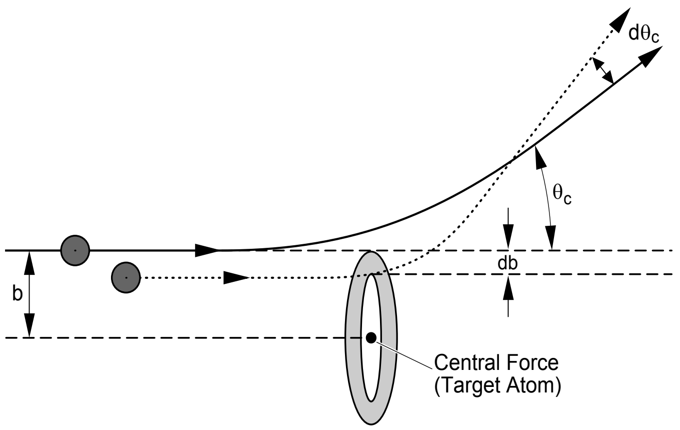

Fig. 4.3. Nuclear target area for the differential cross-section $\mathrm{d}\sigma = 2\pi b\,\mathrm{d}b$

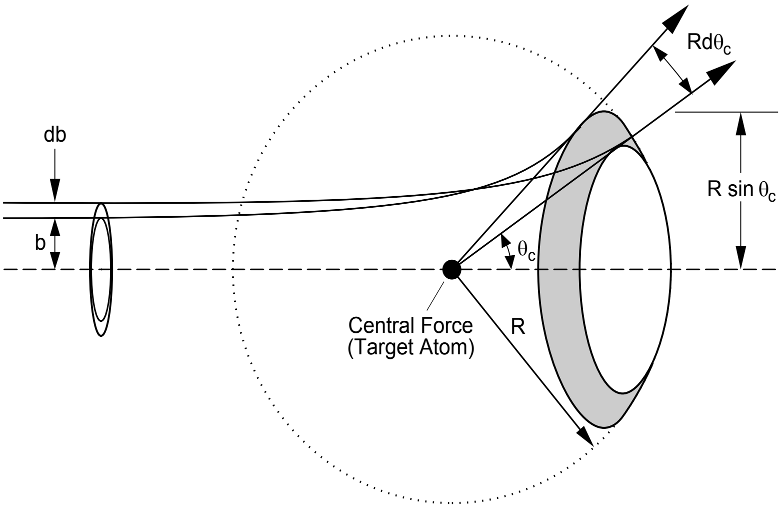

Fig. 4.4. The *solid angle* dΩ subtended at the scattering angle θ_c by the incremental angle dθ_c. By definition, d$\Omega/4\pi$ is the shaded area divided by the entire area of spherical surface; the *shaded area* is equal to $2\pi(R \sin \theta_c)(R\, d\theta_c)$. Then $d\Omega/4\pi = 2\pi R^2 \sin \theta_c\, d\theta_c/R^2$; therefore $d\Omega = 2\pi \sin \theta_c\, d\theta_c$

solid angle of the sphere is 4π. The shaded area is a ring of radius $R \sin \theta_c$, circumference $2\pi R \sin \theta_c$, and width $R\, d\theta_c$. The area of the shaded ring is therefore $(2\pi)(R \sin \theta_c)(R\, d\theta_c) = 2\pi R^2 \sin \theta_c\, d\theta_c$. By definition of solid angle, area/R^2, we obtain

$$d\Omega = 2\pi \sin\theta_c d\theta_c. \tag{4.6}$$

The result is equivalent to (4.1), where $\Delta\phi$ has been integrated over 2π. The differential scattering cross-section for scattering into a solid angle, dΩ, (4.1), is obtained by combining (4.5) and (4.6) to produce

$$\frac{d\sigma(\theta_c)}{d\Omega} = \frac{b}{\sin\theta_c}\left|\frac{db}{d\theta_c}\right|. \tag{4.7}$$

Equations (4.5) and (4.7) give the differential scattering cross-section in the center-of-mass. The equivalent expressions in the laboratory reference frame can be obtained for the scattered projectile and scattered target nucleus by using the angular relationships presented in Table 3.2.

Integration of (4.7) provides a relationship between the differential scattering cross-section and the impact parameter

$$\int_0^b b(\theta_c)\mathrm{d}b = \int_{\theta_c}^{\pi} \frac{\mathrm{d}\sigma(\theta_c)}{\mathrm{d}\Omega} \sin\theta_c \mathrm{d}\theta_c, \tag{4.8}$$

which results in the expression

$$b^2 = 2\int_{\theta_c}^{\pi} \frac{\mathrm{d}\sigma(\theta_c)}{\mathrm{d}\Omega} \sin\theta_c \mathrm{d}\theta_c, \tag{4.9}$$

where the dependence of scattering angles on the impact parameter has been omitted for brevity.

4.3 Energy-Transfer Cross-Section

In a fashion similar to the development of the angular differential scattering cross-section, we will derive an expression for the transferring of energy during a scattering event. To do so we first develop the probability functions for scattering events. Consider Fig. 4.5, where a flux of energetic incident particles traverses a thin target of thickness Δx of and unit area, containing a total of N target atoms per unit volume. Each target nucleus presents an effective scattering area, σ, to this projectile, similar to the presentation in Fig. 4.2. The thin target in Fig. 4.5 contains a total of $N\Delta x$ target nuclei per unit area. The product ($\sigma N\Delta x$) represents the total fraction of the target surface area, which acts as an effective scattering center to the incident energetic particles.

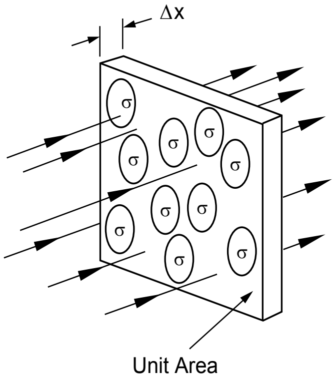

Fig. 4.5. Schematic view of a portion of a scattering foil, with each target atom presenting an effective scattering area, σ

From the above analysis of Fig. 4.5, we can define the probability of a projectile with energy E undergoing a scattering event or a collision with a target nucleus while traversing a thickness Δx as

$$P(E) = N\sigma(E)\Delta x. \tag{4.10}$$

Equation (4.10) defines the total collision cross-section, $\sigma(E)$, between an energetic particle of energy E and the target atoms. The total cross-section gives a measure of the probability for any type of collision to occur where energy-transfers are possible, for energies up to and including the maximum value $T_M = 4M_1M_2E_0/(M_1 + M_2)^2$.

In addition to the total cross-section, we also wish to consider the more restrictive types of interactions that can occur between target nuclei and particles with energy E. Consider the condition where we wish to know the probability that a projectile with energy E will transfer an amount of energy between T and $T + \mathrm{d}T$ to a target atom. Such a probability function defines the differential energy-transfer cross-section, $\mathrm{d}\sigma(E)/\mathrm{d}T$, and is obtained by differentiating (4.10)

$$P(E,T)\mathrm{d}T \equiv \frac{\mathrm{d}P(E)}{\mathrm{d}T}\mathrm{d}T = N\Delta x\frac{\mathrm{d}\sigma(E)}{\mathrm{d}T}\mathrm{d}T = \frac{1}{\sigma(E)}\frac{\mathrm{d}\sigma(E)}{\mathrm{d}T}\mathrm{d}T, \tag{4.11}$$

where $P(E, T)$ is the probability that an ion with energy E will undergo a collision producing an energy-transfer in the range T and $T + \mathrm{d}T$ while traversing a distance Δx, and is simply defined as the ratio of the differential cross-section to the total energy-transfer cross-section.

Probability functions can be constructed based on the scattering processes described by Figs. 4.2 and 4.3. The probability of a collision producing a deflection θ_c in the incident projectile's trajectory is given by

$$P(\theta_c) = \sigma(\theta_c)N\mathrm{d}x, \tag{4.12a}$$

and the probability of scattering the projectile into the angular range between θ_c and $\theta_c + \mathrm{d}\theta_c$ while it travels a distance $\mathrm{d}x$ is given by

$$P(\theta_c, b)\mathrm{d}b \equiv \frac{\mathrm{d}P(\theta_c)}{\mathrm{d}b} = N\frac{\mathrm{d}\sigma(\theta_c)}{\mathrm{d}b}\mathrm{d}b\mathrm{d}x = \frac{1}{\sigma(\theta_c)}\frac{\mathrm{d}\sigma(\theta_c)}{\mathrm{d}b}\mathrm{d}b, \tag{4.12b}$$

where $\sigma(\theta_c)$ is the total angular scattering cross-section given in (4.3), and $\mathrm{d}\sigma(\theta_c)$ is the differential angular scattering cross-section given in (4.4). An expression

similar to (4.11) can also be constructed for the differential angular scattering cross-section as a function of the impact parameter.

Following an analogous route to the development of the differential energy cross-section given in (4.11), the probability function for a particle with energy E being scattered into a solid angle $\mathrm{d}\Omega$ in the angular region between θ_c and $\theta_c + \mathrm{d}\theta_c$ is given by

$$P(E,\Omega)\mathrm{d}\Omega \equiv \frac{\mathrm{d}P(E)}{\mathrm{d}\Omega}\mathrm{d}\Omega = \frac{\mathrm{d}\sigma(E)}{\mathrm{d}\Omega}N\Delta x \mathrm{d}\Omega. \tag{4.13}$$

Equation (4.13) can be rewritten in terms of θ_c by applying (4.6), $\mathrm{d}\Omega = 2\pi \sin\,\theta_c\, \mathrm{d}\theta_c$, which allows us to write

$$P(E,\Omega)\mathrm{d}\Omega = N\Delta x \frac{\mathrm{d}\sigma(E)}{\mathrm{d}\Omega}\mathrm{d}\Omega = 2\pi \sin\theta_c N\Delta x \frac{\mathrm{d}\sigma(\theta_c)}{\mathrm{d}\Omega}\mathrm{d}\theta_c. \tag{4.14}$$

The relationship between energy-transfer, T, and the scattering angle, θ_c, or the solid angle, Ω, can be found by setting the probability functions given by (4.11) and (4.14) equal to each other, so that

$$P(E,T)\mathrm{d}T = P(E,\Omega)\mathrm{d}\Omega,$$

which is equivalent to

$$\frac{\mathrm{d}\sigma(E)}{\mathrm{d}T}\mathrm{d}T = 2\pi \sin\theta_c \mathrm{d}\theta_c \frac{\mathrm{d}\sigma(\theta_c)}{\mathrm{d}\Omega} \tag{4.15}$$

or

$$\frac{\mathrm{d}\sigma(E)}{\mathrm{d}T} = 2\pi \sin\theta_c \left|\frac{\mathrm{d}\theta_c}{\mathrm{d}T}\right| \frac{\mathrm{d}\sigma(\theta_c)}{\mathrm{d}\Omega}. \tag{4.16}$$

The transferred energy, T, is given in (3.26) as

$$T = T_M \sin^2(\theta_c/2) = \frac{1}{2}T_M(1-\cos\theta_c),$$

and the differential angular cross-section for scattering into a solid angle $\mathrm{d}\Omega$ is given by (4.7) as

$$\frac{\mathrm{d}\sigma(\theta_c)}{\mathrm{d}\Omega} = \frac{b}{\sin\theta_c}\left|\frac{\mathrm{d}b}{\mathrm{d}\theta_c}\right|.$$

This allows us to rewrite (4.16) in the form

$$\frac{\mathrm{d}\sigma(E)}{\mathrm{d}T} = \frac{4\pi}{T_M}\frac{\mathrm{d}\sigma(\theta_c)}{\mathrm{d}\Omega} = \frac{4\pi}{T_M}\frac{b}{\sin\theta_c}\left|\frac{\mathrm{d}b}{\mathrm{d}\theta_c}\right|. \tag{4.17}$$

This final expression is extremely useful since it allows us to determine the differential energy-transfer cross-section if the angular differential cross-section is known, or if the center-of-mass scattering angle and impact parameter are known.

The total cross-section for a scattering process is determined by setting the probability functions described by (4.11) and (4.12b) equal to unity. This leads to

$$\sigma(E) = \int_{T_{\min}}^{T_M} \frac{\mathrm{d}\sigma(E)}{\mathrm{d}T}\mathrm{d}T \tag{4.18a}$$

and

$$\sigma(\theta_c) = \int_{b_{\max}}^{0} \frac{\mathrm{d}\sigma(\theta_c)}{\mathrm{d}b}\mathrm{d}b = \int_{b_{\max}}^{0} 2\pi b\,\mathrm{d}b, \tag{4.18b}$$

where T_M is the maximum transferred energy (given by (3.27)), $T_{\min}$ is a lower limit to the energy-transfer process, and $b_{\max}$ is the maximum impact parameter. The total cross-sections given by (4.18a) and (4.18b) are equivalent, i.e., $\sigma(E) = \sigma(\theta_c)$. That is, integrating the energy-transfer differential cross-section over all energy-transfers from $T_{\min}$ to T_M is the same as integrating over the range of impact parameters from $b_{\max}$ to zero. This equality between the total cross-sections provides a means for passing between the energy-transfer differential cross-section and the impact parameter.

4.4 Approximation to the Energy-Transfer Cross-Section

Approximate values of the energy-transfer differential cross-section can be obtained using a power-law approximation to the potential (Winterbon et al. 1970; Nastasi et al. 1996). The power-law energy-transfer differential cross-section has the form

$$d\sigma(E) = \frac{C_m}{E^m T^{1+m}} dT, \tag{4.19}$$

where m is a variable that is dependent on the reduced energy, ε, and the constant C_m is given by

$$C_m = \frac{\pi}{2} \lambda_m a_{TF}^2 \left(\frac{2Z_1 Z_2 e^2}{a_{TF}} \right)^{2m} \left(\frac{M_1}{M_2} \right)^m , \tag{4.20}$$

where λ_m is an additional fitting variable.

If $\chi(r)$ is taken as the Thomas-Fermi screening function, Winterbon et al. (1970) have shown

$$\lambda_{1/3} = 1.309; \quad \lambda_{1/2} = 0.327; \quad \lambda_1 = 0.5. \tag{4.21}$$

Winterbon et al. (1970) recommend the following values of m for various regions of ε:

$m = 1/3$ for $\varepsilon \leq 0.2$,
$m = 1/2$ for $0.08 \leq \varepsilon \leq 2$,
$m = 1$ (Rutherford scattering) for $\varepsilon \geq 10$.

As an example, consider the case of 100 keV As implanted into Si ($Z_1 = 33$; $Z_2 = 14$; $M_1 = 75$; $M_2 = 28$). For this case, $a_{TF} = 0.105$ nm and $\varepsilon = 1.37$. For this value of reduced energy, $m = ½$ and $C_m = 1.74 \times 10^{-7}$. Applying these values to (4.19), with energy in eV units, the energy-transfer cross-section for transferring an energy $T = T_M = 44.6 \times 10^3$ eV is $d\sigma/dT = 5.8 \times 10^{-17}$ cm^2 eV^{-1}.

The probability of transferring energy between $T_M + dT$ is given by

$$P(T) = \left| \frac{d\sigma(E)}{\sigma} \right|, \tag{4.22}$$

where σ can be derived from (4.19) using (4.18a) and assuming a constant value of m ($m = 1/2$) over the energy interval between T_{min} and T_M. Applying (4.22) to our example of 100 keV As implanted into Si, taking $dT = 1$ eV and $T_{min} = 1$ eV, the probability for transferring an energy of $T = T_M = 44.6 \times 10^3$ eV is 5×10^{-8}.

References

Nastasi, M., Mayer, J.W., Hirvonen, J.K.: Ion–Solid Interactions Fundamentals and Applications. Cambridge University Press, Cambridge (1996)
Winterbon, K.B., Sigmund, P., Sanders, J.B.: Spacial distribution of energy deposited by atomic particles in elastic collisions. Mat. Fys. Medd. Dan. Vidensk. Selsk. **37**(14) (1970)

Suggested Reading

French, A.P.: Newtonian Mechanics. W.W. Norton, New York (1971)
Goldstein, H.: Classical Mechanics. Addison-Wesley, Reading, MA (1959)
Johnson, R.E.: Introduction to Atomic and Molecular Collisions. Plenum Press, New York (1982)
Sigmund, P.: Collision theory of displacement damage, ion ranges and sputtering. Rev. Roum. Phys. **17**, pp. 823, 969 and 1079 (1972)
Symon, K.R.: Mechanics. Addison-Wesley, Reading, MA (1953)
Torrens, I.M.: Interatomic Potentials. Academic, New York (1972)
Weidner, R.T., Sells, R.L.: Elementary Modern Physics, 3rd edn. Allyn & Bacon, Boston (1980)

Problems

4.1 Derive the formula for the total cross-section, $\sigma(E)$, using the power-law approximation to energy-transfer differential cross-section.

4.2 Using the formula derived in problem 4.1, calculate the probability $P(E)$, (4.10), for 50 and 100 keV B incident on a Si film of thickness 10 and 100 nm. (Are there two films of varying thickness? If yes, use Si films.)

4.3 Using the formula derived in problem 4.1, calculate the probability $P(E, T)$, (4.11) for 50 and 100 keV B incident on a Si film of thickness 10 and 100 nm.

4.4 If the projectile and target atoms interact like colliding billiard balls (elastic hard-spheres), the interatomic potential that represents this condition is called a *hard-sphere* potential. For a hard-sphere potential, the power-law cross-section parameter m in (4.19) is equal to 0. Derive the total cross-section, $\sigma(E)$, for a hard-sphere potential.

4.5 Using the formula derived in problem 4.4, calculate the probability, $P(E)$, (4.10), for 50 and 100 keV B incident on a Si film of thickness 10 and 100 nm. Compare your results to those obtained in problem 4.2.

4.6 Using the formula derived in problem 4.4 calculate the probability, $P(E, T)$, (4.11), for 50 and 100 keV B incident on a Si film of thickness 10 and 100 nm. Compare your results to those obtained in problem 4.2.

4.7 In Rutherford scattering, the potential is unscreened Coulomb. The power parameter for this potential is $m = 1$. Derive the Coulomb differential cross-section using the power-law approximation and compare to the Rutherford cross-section given by

$$\frac{\mathrm{d}\sigma(\theta_{\mathrm{c}})}{\mathrm{d}\Omega} = \left(\frac{\alpha}{4E_{\mathrm{c}}}\right)^2 \frac{1}{\sin^4(\theta_{\mathrm{c}}/2)}.$$

5 Ion Stopping

5.1 Introduction

When an energetic ion penetrates a solid, it undergoes a series of collisions with the atoms and electrons in the target. In these collisions the incident particle loses energy at a rate of dE/dx of a few to 100 eV nm^{-1}, depending on the energy, mass, and atomic number of the ion as well as on the mass, atomic number, and density of the substrate material. The energy-loss mechanisms are discussed in the next section, as we are concerned here with the penetration depth, or range, R, of the ions (Fig. 3.1). The range R is determined by the rate of energy-loss along the path of the ion

$$R = \int_{E_0}^{0} \frac{1}{\mathrm{d}E / \mathrm{d}x} \mathrm{d}E, \tag{5.1}$$

where E_0 is the incident energy of the ion as it penetrates the solid. The sign of dE/dx is negative, as it represents the energy-*loss* per increment of path, although tabulated values are given as positive quantities.

The main parameters governing the range or energy-loss rate are the energy, E_0, and atomic number, Z_1, of the ion and the atomic number, Z_2, of the substrate if we exclude the effect of the orientation of the crystal lattice. As the incident ion penetrates the solid, undergoing collisions with atoms and electrons, the distance traveled between collisions and the amount of energy lost per collision are random processes. Hence all ions of a given type and incident energy do not have the same range. Instead there is a broad distribution in the depths to which individual ions penetrate. This distribution in ranges is referred to as the *range distribution* or *range straggling*. Further, in ion implantation it is *not* the total distance R traveled by the ion that is of interest but the projection of R normal to the surface, i.e., the penetration depth or projected range R_p (Fig. 3.1).

5.2 The Energy-Loss Process

The energy-loss rate, dE/dx, of an energetic ion moving through a solid is determined by screened Coulomb interactions with the substrate atoms and electrons. It is customary to distinguish two different mechanisms of energy-loss: (1) nuclear collisions, in which energy is transmitted as translatory motion to a target-atom as a whole, and (2) electronic collisions, in which the moving particle excites or ejects atomic electrons. For most purposes, this separation is a convenient one and, although not strictly true, it is a good approximation. The energy-loss rate, dE/dx, can be expressed as

$$\frac{\mathrm{d}E}{\mathrm{d}x} = \left.\frac{\mathrm{d}E}{\mathrm{d}x}\right|_{\mathrm{n}} + \left.\frac{\mathrm{d}E}{\mathrm{d}x}\right|_{\mathrm{e}}, \tag{5.2}$$

where the subscripts n and e denote nuclear and electronic collisions, respectively.

Nuclear collisions can involve large discrete energy-losses and significant angular deflection of the trajectory of the ion (Fig. 5.1). This process is responsible for the production of lattice disorder by the displacement of atoms from their positions in the lattice. Electronic collisions involve much smaller energy-losses per collision, negligible deflection of the ion trajectory, and negligible lattice disorder. The relative importance of the two energy-loss mechanisms changes rapidly with the energy E and atomic number Z_1 of the particle: nuclear stopping predominates for low E and high Z_1, whereas electronic stopping takes over for high E and low Z_1. Typical units for the energy-loss rate are electron-volt per nanometer or

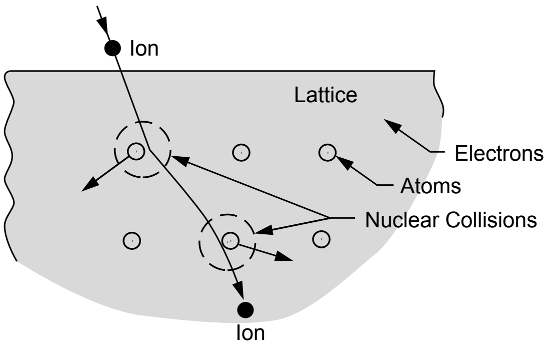

Fig. 5.1. An ion incident on a crystal lattice is deflected in nuclear collisions with the lattice atoms and also loses energy in collisions with electrons

MeV mg^{-1} cm^{-2}. In addition to the energy-loss rate, it is also customary to speak of the stopping cross-section, S, which is defined as

$$S \equiv \frac{\mathrm{d}E/\mathrm{d}x}{N}, \tag{5.3}$$

where N is the atomic density. The stopping cross-section can be thought of as the energy-loss rate per scattering center. The stopping cross-section has typical units of

$$\frac{\mathrm{d}E/\mathrm{d}x}{N} \quad \left(\text{units:} \frac{(\mathrm{eV\,cm^{-1}})}{(\mathrm{atoms\ cm^{-3}})} = \left(\frac{\mathrm{eV\,cm^2}}{\mathrm{atom}} \right) \right).$$

The nomenclature of stopping cross-section comes from the unit of area in the numerator.

A proper understanding of the mechanisms of energy-loss is important not only in controlling the depth profile of implanted dopant atoms, but also in determining the nature of the lattice disorder produced during ion implantation or ion irradiation of the solid. In the process of slowing down in the substrate, the implanted ions undergo violent collisions with some of the lattice atoms, thereby displacing them from lattice sites.

This problem of lattice disorder is a vital one in most ion beam modification work, and we will return to it again in Chap. 7. The basic principles are, however, treated in the present chapter, since ranges and lattice disorder both involve the same energy-loss mechanisms. Other secondary effects accompanying ion implantation and ion irradiation of solids, such as sputtering of target-atoms, also depend strongly on the relative importance of nuclear and electronic stopping.

5.3 Nuclear Stopping

In nuclear stopping we are concerned with the average energy-loss that results from *elastic* collisions with target-atoms. The nuclear stopping power or nuclear energy-loss rate is the energy lost by a moving particle due to elastic collisions per unit length traveled in the target. In Chap. 4 we defined the probability of a particle with energy E undergoing a collision while traveling a distance dx, which results in an energy-loss between T and $T + \mathrm{d}T$. From (4.11) we have

$$\frac{\mathrm{d}P(E)}{\mathrm{d}T}\mathrm{d}T = N\mathrm{d}x\frac{\mathrm{d}\sigma(E)}{\mathrm{d}T}\mathrm{d}T,$$

where E is the energy of the moving particle and T is the recoil or transfer energy. The average energy-loss by the moving particle in the distance dx is obtained by multiplying (4.11) by the transfer energy T and integrating over all possible values of T.

$$\langle \mathrm{d}E \rangle = \int T \frac{\mathrm{d}P(E)}{\mathrm{d}T} \mathrm{d}T = N \int_{T_{\min}}^{T_{\mathrm{M}}} T \frac{\mathrm{d}\sigma(E)}{\mathrm{d}T} \mathrm{d}T \mathrm{d}x. \tag{5.4}$$

For infinitesimal dx, omitting the averaging symbol on dE, we have

$$\left.\frac{\mathrm{d}E}{\mathrm{d}x}\right|_{\mathrm{n}} = N \int_{T_{\min}}^{T_{\mathrm{M}}} T \frac{\mathrm{d}\sigma(E)}{\mathrm{d}T} \mathrm{d}T, \tag{5.5}$$

where $\mathrm{d}E/\mathrm{d}x|_{\mathrm{n}}$ is the nuclear stopping power. The lower limit in the integration $T_{\min}$ is the minimum energy-transferred and need not be zero. One value used for $T_{\min}$ is the energy needed to displace an atom from its lattice site, approximately 20–30 eV. Atomic displacement processes will be discussed in Chap. 7. The upper limit, T_{M}, is the maximum transfer energy given by $T_{\mathrm{M}} = 4M_1M_2E/(M_1 + M_2)^2$.

In (5.3) we defined the stopping cross-section. The nuclear stopping cross-section for an ion of energy E is given by

$$S_{\mathrm{n}}(E) = \frac{1}{N} \left.\frac{\mathrm{d}E}{\mathrm{d}x}\right|_{\mathrm{n}} = \int_{T_{\min}}^{T_{\mathrm{M}}} T \frac{\mathrm{d}\sigma(E)}{\mathrm{d}T} \mathrm{d}T, \tag{5.6}$$

where $\mathrm{d}\sigma(E)/\mathrm{d}T$ is the energy-transfer differential cross-section. The nuclear stopping cross-section can be evaluated using the power representation of the energy-transfer differential cross-section given in (4.19)

$$\frac{\mathrm{d}\sigma(E)}{\mathrm{d}T} = \frac{C_m}{E^m T^{1+m}},$$

where the constant C_m is defined in (4.20). Taking $T_{\min} = 0$, the nuclear stopping cross-section is now given by

$$S_{\mathrm{n}}(E) = \frac{C_m}{E^m} \int_0^{T_{\mathrm{M}}} T^{-m} \mathrm{d}T = \left.\frac{C_m E^{-m} T^{1-m}}{1-m}\right|_0^{T_{\mathrm{M}}}$$

or

$$S_\mathrm{n}(E) = \frac{C_m E^{1-2m}}{1-m}\left[\frac{4M_1M_2}{(M_1+M_2)^2}\right]^{1-m}. \tag{5.7}$$

Equation (5.7) provides a means for calculating stopping cross-sections based on the Thomas-Fermi atom with an accuracy of ~20%. The ranges of validity for values of m are

$$\begin{aligned} m &= 1/3 \quad \text{for } \varepsilon \le 0.2, \\ m &= 1/2 \quad \text{for } 0.08 \le \varepsilon \le 2, \end{aligned} \tag{5.8}$$

where ε is the reduced energy introduced in (3.30):

$$\varepsilon = \frac{M_2}{M_1+M_2}\frac{a_\mathrm{TF}}{Z_1Z_2e^2}E. \tag{5.9}$$

Equation (5.9) gives the reduced energy in terms of the laboratory ion energy, E, where a_TF is the Thomas-Fermi screening radius. For the condition $m = 1/2$ the combination of (5.3) and (5.7)–(5.9) gives

$$\begin{aligned} \left.\frac{\mathrm{d}E}{\mathrm{d}x}\right|_\mathrm{n} &= 1.308\pi a_\mathrm{TF} N Z_1 Z_2 e^2 \frac{M_1}{M_1+M_2}, \\ \left.\frac{\mathrm{d}E}{\mathrm{d}x}\right|_\mathrm{n} &= 0.28(\mathrm{eV\,nm^2})\frac{NZ_1Z_2}{\left(Z_1^{1/2}+Z_2^{1/2}\right)^{2/3}}\frac{M_1}{M_1+M_2}, \end{aligned} \tag{5.10}$$

where N is in atoms nm^{-3}. This result shows that the stopping power is energy-independent in the regime of $m = 1/2$.

Equation (5.10) is a reasonable approximation through most of the keV energy region. For example, for Ar ($Z_1 = 18$, $M_1 = 40$) on Si ($Z_2 = 14$, $M_2 = 28$, $N = 50$ atoms nm^{-3})

$$\left.\frac{\mathrm{d}E}{\mathrm{d}x}\right|_\mathrm{n} = 520 \text{ eV nm}^{-1}$$

and for Ar on Cu ($Z_2 = 29$, $M_2 = 64$, $N = 85$ atoms nm^{-3})

$$\left.\frac{\mathrm{d}E}{\mathrm{d}x}\right|_\mathrm{n} = 1{,}060 \text{ eV nm}^{-1}.$$

5.4 ZBL Nuclear Stopping Cross-Section

While the Thomas-Fermi screening function is a reasonable approximation for calculating stopping powers and cross-sections, a higher level of accuracy and a wider range of reduced energy, ε, are obtained using the Ziegler, Biersack, and Littmark (ZBL; 1985) universal screening function (2.15). The ZBL cross-section is presented in Fig. 5.2 along the stopping curves from four classical atom screening functions. The small filled circles in the plot represent the numerical solutions, and the solid line represents an analytical fit to the points. The expression for the fit is given by

$$S_n(\varepsilon) = \frac{0.5\ln(1+1.1383\varepsilon)}{(\varepsilon + 0.01321\varepsilon^{0.21226} + 0.19593\varepsilon^{0.5})} \tag{5.11}$$

for $\varepsilon \leq 30$. For example, $S_n(\varepsilon) = 0.164$ for $\varepsilon = 10^{-2}$ and $S_n(\varepsilon) = 0.118$ for $\varepsilon = 10$. In the high-energy regime,

$$S_n(\varepsilon) = \frac{\ln(\varepsilon)}{2\varepsilon} \tag{5.12}$$

for $\varepsilon > 30$. For example, for $\varepsilon = 470$, $S_n(\varepsilon) = 6.55 \times 10^{-3}$.

Equation (5.12) is the high-energy reduced nuclear stopping cross-section for unscreened (Coulomb) nuclear stopping. Figure 5.2 shows that the reduced nuclear stopping cross-section is identical for all screening functions for $\varepsilon > 10$. However, considerable differences exist for lower values of ε.

For practical calculations, the ZBL universal nuclear stopping for an ion with energy E_0 is

$$S_n(E_0) = \frac{8.462 \times 10^{-15} Z_1 Z_2 M_1 S_n(\varepsilon)}{(M_1 + M_2)\left(Z_1^{0.23} + Z_2^{0.23}\right)} \ (\text{eV cm}^2)\ \text{atom}^{-1}, \tag{5.13}$$

where the reduced nuclear stopping cross-section is calculated using (5.11) and (5.12). For example, for As ($Z_1 = 33$, $M_1 = 75$) incident on Si ($Z_2 = 14$, $M_2 = 28$), the ratio of $S_n(E_0)/S_n(\varepsilon) = 6.99 \times 10^{-13}$ (eV cm^2). For $\varepsilon = 470$ ($E_0 = 100$ keV),

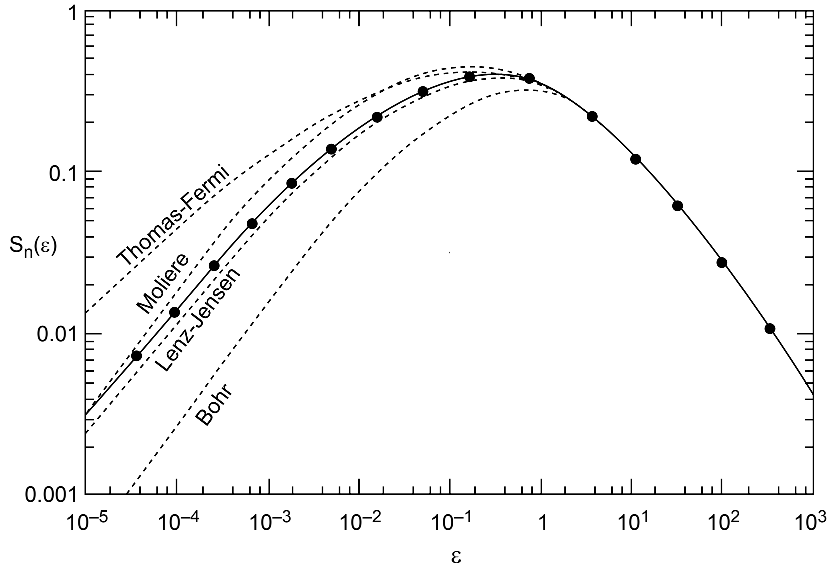

Fig. 5.2. The universal screening function, Fig. 2.3, can be used to calculate the nuclear stopping power using (5.13). The result is shown in reduced coordinates. Also shown are the nuclear stopping calculations based on the four classical atomic models (Ziegler et al. 1985)

$S_n(\varepsilon) = 6.55 \times 10^{-3}$, so that $S_n(E_0) = 4.58 \times 10^{-14}$ (eV cm^2) atom^{-1}. The atomic density of Si is 5.0×10^{22} atoms cm^{-3} so that

$$\left.\frac{\mathrm{d}E}{\mathrm{d}x}\right|_{\mathrm{n}} = NS_{\mathrm{n}}(E_0) = 22.9 \ \mathrm{eV\,nm}^{-1}.$$

The reduced energy, ε, in (5.11) and (5.12), is calculated using the universal screening length, a_{U}, given in (2.17). For calculation purposes, the form of the ZBL reduced energy is

$$\varepsilon = \frac{32.53 M_2 E_0}{Z_1 Z_2 (M_1 + M_2)\left(Z_1^{0.23} + Z_2^{0.23}\right)}, \tag{5.14}$$

where E_0 is in keV. For As incident on Si, the ratio of $\varepsilon/E_0 = 4.70 \times 10^{-3}$. For $E_0 = 100$ keV, $\varepsilon = 470$.

5.5 Electronic Stopping

As we discussed in Sect. 5.2, the energy-loss rate of ions in solids is divided into two different mechanisms of energy-loss: the energy-transferred by the ion to the target nuclei (called nuclear stopping) and the energy-transferred by the ion to the target electrons (called electronic stopping). The relative importance of the various interaction processes between the ion and the target medium depends mostly on the ion velocity and on the charges of the ion and target-atoms.

A comparison of the nuclear and electronic stopping cross-sections expressed in reduced notation is shown in Fig. 5.3. Recall that ε is proportional to ion energy and that $(\varepsilon)^{1/2}$ is proportional to ion velocity.

At higher velocities, the charge state of the ion increases and ultimately becomes fully stripped of all its electrons at $v \geq v_0 Z_1^{2/3}$. At this point, the ion can be viewed as a positive point charge Z_1, moving with a velocity greater than the mean orbital velocity of the atomic electrons in the shells or subshells of the target-atoms. When the projectile velocity v is much greater than that of an orbital electron (fast-collision case), the influence of the incident particle on an atom may be regarded as a sudden, small external perturbation. This picture leads to Bohr's theory of stopping power. The collision produces a sudden transfer of energy from the projectile to the target electron. The energy-loss from a fast particle to a stationary nucleus or electron can be calculated from scattering in a central force field. The stopping cross-section decreases with increasing velocity because the particle spends less time in the vicinity of the atom. In this high-energy, fast-collision regime, the values of electronic stopping are proportional to $(Z_1/v)^2$.

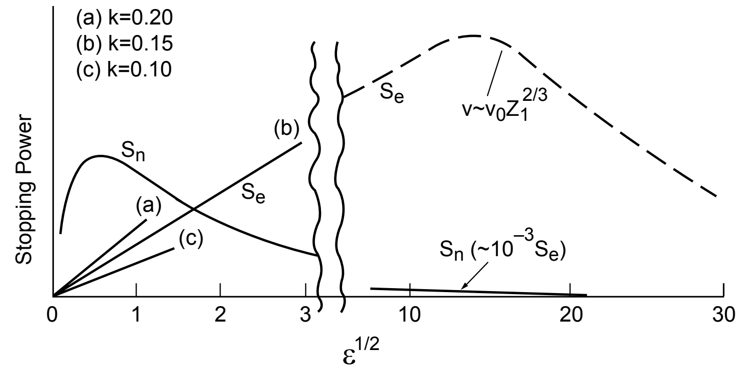

Fig. 5.3. The reduced nuclear and electronic stopping cross-sections as a function of $\varepsilon^{1/2}$. The electronic stopping power variable, k, is dependent on the mass and atomic number of the ion and target

5.5.1 High-Energy Electronic Energy-Loss

In this section we will consider the case where the ion velocity is greater than $v_0 Z_1^{2/3}$. At higher velocities, the charge state of the ion increases and ultimately becomes fully stripped of all its electrons at $v \geq v_0 Z_1^{2/3}$. At this point, the ion can be viewed as a positive point charge Z_1, moving with a velocity greater than the mean orbital velocity of the atomic electrons in the shells or subshells of the target-atoms. When the projectile velocity v is much greater than that of an orbital electron (fast-collision case), the influence of the incident particle on an atom may be regarded as a sudden, small external perturbation. This picture leads to Bohr's theory of stopping power. The collision produces a sudden transfer of energy from the projectile to the target electron. The energy-loss from a fast particle to a stationary nucleus or electron can be calculated from scattering in a central force field. The stopping cross-section decreases with increasing velocity because the particle spends less time in the vicinity of the atom. For this condition, the ion is a bare nuclei, and its interactions with target electrons can be accurately described by a pure Coulomb interaction potential.

In 1913, Bohr derived an expression for the rate of energy-loss of a charged particle on the basis of classical considerations. He considered a heavy particle, such as an α particle or a proton, of charge $Z_1 e$, mass M, and velocity v passing a target-atom electron of mass m_e at a distance b. As the heavy particle passes, the Coulomb force acting on the electron changes direction continuously. If the electron moves negligibly during the passage of the heavy particle, then the impulse parallel to the path, the integral of $F\,\mathrm{d}t$, is zero by symmetry, since, for each position of the incident particle in the $-x$ direction, there is a corresponding position in the $+x$ direction, which makes an equal and opposite contribution to the x component of the momentum. However, throughout the passage, there is a force in the y direction, and momentum Δp is transferred to the electron. The energy-loss is given in Nastasi et al. (1996) as

$$-\left.\frac{\mathrm{d}E}{\mathrm{d}x}\right|_{\mathrm{e}} = \frac{2\pi Z_1^2 e^4}{E} N Z_2 \left(\frac{M_1}{m_\mathrm{e}}\right) \ln \frac{2 m_\mathrm{e} v^2}{I}, \tag{5.15}$$

with N given by the atomic density in the stopping medium.

The average excitation energy, I, in electron-volts, for most elements is roughly

$$I \cong 10 Z_2, \tag{5.16}$$

where Z_2 is the atomic number of the stopping atoms. The description of stopping power so far ignores the shell structure of the atoms and variations in electron binding. Experimentally, these effects show up as small derivations (except for the very light elements) from the approximation given by (5.16).

The complete energy-loss formula (often referred to as the Bethe formula) contains corrections that include relativistic terms as high-velocities and corrections for the nonparticipation of the strongly bound inner shell electrons. For ions with $Z \geq 2$ in the energy regime of a few mega-electron-volts, relativistic effects are negligible, and nearly all the target electrons participate in the stopping process ($I_e = NZ_2$). Consequently, (5.15) can be used to estimate values of $dE/dx|_e$.

For example, the electronic energy-loss of 2 MeV ^{4}He ions in Si has a value (calculated from (5.15)) of 273 eV nm^{-1} using values of $n_e = NZ_2 = 700$ nm^{-3} and $I = 10Z_2 = 140$ eV. Experiments give a value of $dE/dx|_e = 246$ eV nm^{-1}. Thus, the first-order treatment gives values to within 10% of the experimental values.

A fully stripped, high-energy ion can also transfer energy to the nuclei of the solid as well as to target electrons. From Fig. 5.3, we see that the nuclear stopping cross-section is approximately equal to $10^{-3}\,S_e(\varepsilon)$ for ions with energies $\varepsilon > 30$. To confirm this, one could calculate $S_n(E)$ using (5.13).

5.5.2 Low-Energy Electronic Energy-Loss

In the projectile velocity range $v < v_0$, the Bethe theory of stopping expressed by (5.15) breaks down, and a different approach to electronic stopping theory is needed. Three major models of electronic stopping in this velocity regime have been developed over the years, all of which give the result that the stopping cross-section is proportional to the projectile velocity.

Fermi and Teller analyzed the stopping of energetic particles in a Fermi gas at velocities $v = v_F$, where v_F is the Fermi velocity. Since Fermi velocities in solids typically fall in the range of 0.7 to $1.3v_0$, the Fermi–Teller analysis corresponds to projectile ions that are not fully stripped. From Fig. 5.3 we would anticipate that electronic stopping in this velocity regime would be proportional to the projectile velocity. While the Fermi–Teller model of stopping shows that the electronic energy-loss is proportional to the projectile velocity, its quantitative abilities are questionable.

For energetic projectiles moving with velocities $v < v_0 Z_1^{2/3}$, the majority of the target electrons are moving much faster than the ions. For ions moving in this velocity regime, the electrons cannot pick up energy by direct collisions with the ion as was possible when the ion velocities were greater than $v_0 Z_1^{2/3}$. In a model proposed by Firsov (1959), electronic stopping in the velocity regime $v < v_0 Z_1^{2/3}$ arises from the work involved in the transfer of momentum that occurs when target electrons are picked up or captured by the projectile. Since the captured electron has to be accelerated up to the ion velocity, v, the ion loses a small amount of momentum proportional to $m_e v$.

The other well-known model of electronic stopping in the velocity-proportional regime is credited to Lindhard and Scharff. While the Lindhard–Scharff formula has found wide-scale use, Lindhard and Scharff have never published a derivation of their formula. The Lindhard–Scharff form for electronic stopping can be obtained following the procedure of Firsov. The primary difference between the

Table 5.1. SRIM stopping data for As ion in Si

Ion energy (KeV)	[dE/dx]$_e$ (eV nm^{-1})	[dE/dx]$_n$ (eV nm^{-1})
10.00	63.86	942.9
11.00	66.98	965.3
12.00	69.96	985.3
13.00	72.81	1,003.0
14.00	75.56	1,020.0
15.00	78.22	1,035.0
16.00	80.78	1,049.0
17.00	83.27	1,061.0
18.00	85.68	1,073.0
20.00	90.32	1,093.0
22.50	95.79	1,115.0
25.00	101.00	1,133.0
27.50	105.90	1,149.0
30.00	110.60	1,162.0
32.50	11.510	1,173.0
35.00	119.50	1,182.0
37.50	123.70	1,191.0
40.00	127.70	1,197.0
45.00	135.50	1,208.0
50.00	142.80	1,216.0
55.00	149.80	1,221.0
60.00	156.40	1,224.0
65.00	162.80	1,226.0
70.00	169.00	1,226.0
80.00	180.60	1,224.0
90.00	191.60	1,219.0
100.00	202.00	1,212.0

development of the Firsov and Lindhard–Scharff models is found in the choice of interatomic potential.

For calculational purposes, the Lindhard–Scharff stopping cross-section can be expressed as

$$S_e(E) = 3.83 \frac{Z_1^{7/6} Z_2}{\left(Z_1^{2/3} + Z_2^{2/3}\right)^{3/2}} \left(\frac{E}{M_1}\right)^{1/2} = K_L E^{1/2}, \tag{5.17}$$

where

$$K_L = 3.83 \frac{Z_1^{7/6} Z_2}{M_1^{1/2} \left(Z_1^{2/3} + Z_2^{2/3}\right)^{3/2}} \tag{5.18}$$

and $S_e(E)$ will be given in units of 10^{-15} eV cm^2 atom^{-1} for ion energies E given in kilo-electron-volts and M_1 in atomic mass units. As an example, consider a 100 keV As ion on Si. Using $Z_1 = 33$, $Z_2 = 14$, and $M_1 = 75$, we obtain $K_L = 5.64$ and $S_e(E = 100\text{ keV}) = 56.42 \times 10^{-15}$ eV cm^2 atom^{-1}. The atomic density for Si is $N = 5 \times 10^{22}$ atoms cm^{-3}, which gives an electronic energy-loss rate of 282 eV nm^{-1}.

5.6 Stopping Calculations Using SRIM

The energy-loss rate, dE/dx, can calculated using the computer program The Stopping and Ion Ranges in Matter (SRIM; http://www.srim.org/). Examples of the stopping data provided by SRIM are provided in Table 5.1 for As ions in Si at energies ranging between 10 and 100 keV.

References

Lindhard, J., Nielsen, V., Scharff, M.: Approximation method in classical scattering by screened coulomb fields (notes on atomic collisions I). Mat. Fys. Medd. Dan. Vidensk. Selsk. **36**(10) (1968)

Nastasi, M., Mayer, J.W., Hirvonen, J.K.: Ion–Solid Interactions: Fundamentals and Applications. Cambridge University Press, Cambridge (1996)

Ziegler, J.F., Biersack, J.P., Littmark, U.: The Stopping and Range of Ions in Solids. Pergamon Press, New York (1985)

Suggested Reading

Fermi, E., Teller, E.: The capture of negative mesotrons in matter. Phys. Rev. **72**, 399 (1947)

Firsov, O.B.: A qualitative interpretation of the mean electron excitation energy in atomic collisions. Sov. Phys. JETP **36**, 1076 (1959)

Gotz, G., Gartner, K. (eds.): High-Energy Ion Beam Analysis of Solids, chap. 1. Academie Verlag, Berlin (1988)

Lindhard, J., Scharff, M., Schiott, H.E.: Range concepts and heavy ion ranges (notes on atomic collisions II). Mat. Fys. Medd. Dan. Vidensk. Selsk. **33**(14), 3 (1963)

Mayer, J.W., Eriksson, L., Davies, J.A.: Ion Implantation in Semiconductors. Academic, New York (1970)

Sugiyama, H.: Electronic stopping power formula for intermediate energies. Radiat. Eff. **56**, 205 (1956)

Ziegler, J.F. (ed.): Handbook of Ion Implantation Technology. North-Holland, New York (1992)

Problems

5.1 Calculate the velocity, v, the Thomas-Fermi (Firsov) screening length, a_{TF}, the universal screening length, a_U, and the reduced energy, ε, for 1, 10, and 100 keV B ions ($Z_1 = 5$, $M_1 = 11$) incident on Si ($Z_2 = 14$, $M_2 = 28$) and the reduced ε, for 1, 10, and 100 keV B ions ($Z_1 = 5$, $M_1 = 11$) incident on Si ($Z_2 = 14$, $M_2 = 28$).

5.2 Show that, for a proton of velocity v in a direct head-on collision with an electron, the maximum change in velocity of the electron is $2v$. What is the change in velocity of the target proton for a head-on collision with an incident proton?

5.3 Calculate the nuclear stopping cross-section, (5.7), and $dE/dx|_n$ for Cu in Ni for $\varepsilon = 0.1$ and 1.

5.4 Calculate the ZBL nuclear stopping cross-section, (5.13) for Ar in Cu for $\varepsilon = 0.1$ and 1.

5.5 In the electronic stopping high-velocity regime, what is the value of $dE/dx|_e$ for 10 MeV Ar in Cu? Use (5.17).

5.6 Calculate the electronic energy-loss factor, $dE/dx|_e$, for 1 keV Ar incident on Cu using (5.17).

This page intentionally blank

6 Ion Range and Range Distribution

6.1 Range Concepts

As discussed in Chap. 5, the implanted ion loses energy by means of both nuclear and electronic interactions with the substrate atoms. The former interaction consists of individual elastic collisions between the ion and target-atom nuclei, whereas the electronic interactions can be viewed more as a continuous viscous drag phenomenon between the injected ions and the sea of electrons surrounding the target nuclei. For the energy regime normally used in heavy-ion implantation (i.e., tens to hundreds of kilo-electron-volts), the nuclear contribution to the stopping process normally dominates, and this is reflected in the particular ion trajectories as the ion comes to rest within the solid.

In Fig. 6.1 we see a two-dimensional schematic view of an individual ion's path in the ion implantation process as it comes to rest in a material. As this figure shows, the ion does not travel to its resting place in a straight path due to collisions with target atoms The actual integrated distance traveled by the ion is called the *range*, R. The ion's net penetration into the material, measured along the vector of the ion's incident trajectory, which is perpendicular to the surface in this example, is called the *projected range*, R_p.

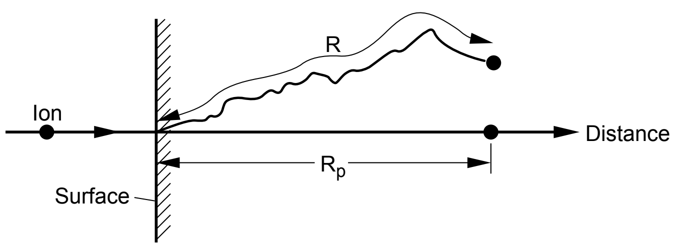

Fig. 6.1. An ion incident on a semiconductor penetrates with a total path length R, which gives a projected range R_p, along the direction parallel to that of the incident ion (Mayer et al. 1970)

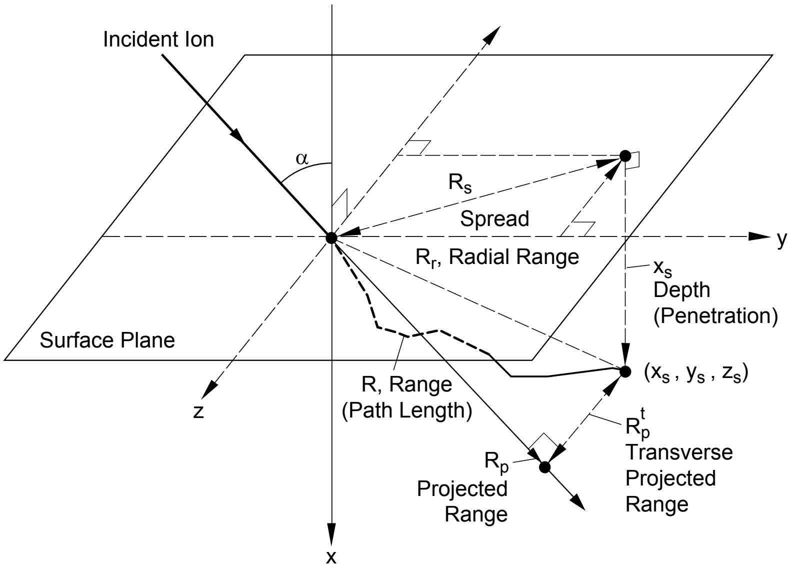

Fig. 6.2. Schematic drawing for the definition of depth, spread, radial range, longitudinal projected range, transverse projected range, and path length (Eckstein 1991)

In Fig. 6.2, a more general three-dimensional presentation of the penetration of a projectile into a solid is shown. In this schematic, an energetic projectile enters the sample surface at the point (0, 0, 0), at a angle α to the surface normal. The projectile is stopped at the point (x_s, y_s, z_s). For this presentation of an ion's penetration into a solid, we define the range, R, and the projected range, R_p, consistent with the definitions used in Fig. 6.1. However, since the incident ion is not parallel to the surface normal, the depth of penetration, x_s, which is defined as the perpendicular distance below the surface of which the projectile comes to rest, is not equal to the projected range. If $\alpha = 0$, these two quantities would be equal. The *radial range*, R_r, is the distance from the surface at the point of entrance, (0, 0, 0), to the point where the projectile comes to rest, (x_s, y_s, z_s). The *spreading range*, R_s, is the distance between the point where the projectile enters the surface and the projection of the projectile's final resting place onto the surface plane. The *transverse projected range*, R_p^t, is the vector connecting the radial range and the projected range. For a single projectile coming to rest at the point (x_s, y_s, z_s), we have the following mathematical descriptions for the quantities defined in Fig. 6.2:

1. the range spread

$$R_s = \left(y_s^2 + z_s^2\right)^{1/2}, \tag{6.1}$$

2. the radial range

$$R_{\mathrm{r}} = \left(x_{\mathrm{s}}^2 + y_{\mathrm{s}}^2 + z_{\mathrm{s}}^2\right)^{1/2}, \tag{6.2}$$

3. the transverse projected range

$$R_{\mathrm{p}}^{\mathrm{t}} = \left[(x_{\mathrm{s}} \sin\alpha - y_{\mathrm{s}} \cos\alpha)^2 + z_{\mathrm{s}}^2\right]^{1/2}, \tag{6.3}$$

4. the longitudinal projected range

$$R_{\mathrm{p}} = \left[(R_{\mathrm{r}})^2 + \left(R_{\mathrm{p}}^{\mathrm{t}}\right)^2\right]^{1/2}. \tag{6.4}$$

For normal-incidence projectiles, the range spreading is equal to the transverse projected range.

6.2 Range Distributions

Because the stopping of an ion is a stochastic (random) process, the collision sequence, the subsequent ion deflection, and the ion's total path length in coming to rest vary randomly from ion to ion. As a result, ions with the same energy, incident with the same angle onto the sample surface, and into the same material, do not necessarily come to rest in the same place. Hence, all ions of a given type and incident energy do not necessarily have the same range. Instead, if we were to examine the range history of many ions, a statistically broad distribution in the depths to which ions penetrate would be observed, similar to that shown in Fig. 6.3. The distribution in projected ranges is referred to as the range distribution or range straggling, with the most probable projected range referred to as the average or mean projected range. A statistical distribution would also be observed for all the quantities defined in Fig. 6.2.

The depth distribution, $N(x)$, of implanted ions, normalized for an ion implantation dose ϕ_{i}, is given by the expression

$$N(x) = \frac{\phi_{\mathrm{i}}}{\Delta R_{\mathrm{p}}(2\pi)^{1/2}} \exp\left[-\frac{1}{2}\left(\frac{x - R_{\mathrm{p}}}{\Delta R_{\mathrm{p}}}\right)^2\right], \tag{6.5}$$

where R_{p} is the projected range (mean depth of the distribution) and ΔR_{p} is the projected range straggling (standard deviation of the distribution). Assuming that

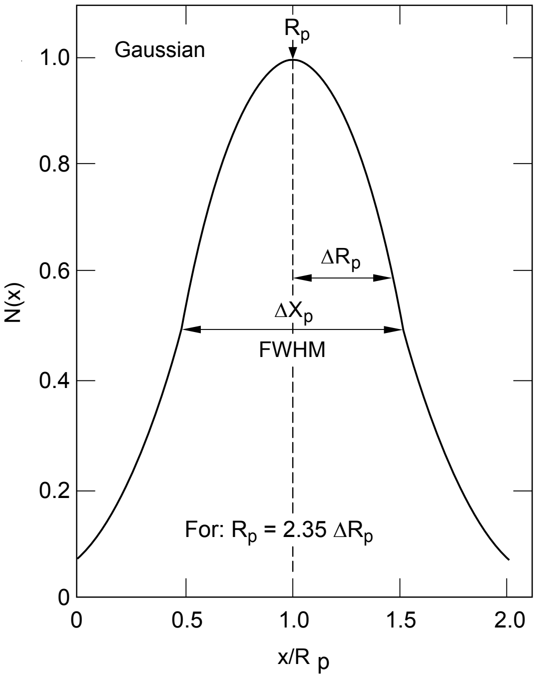

Fig. 6.3. Gaussian range distribution for implanted ions with $R_p = 2.35\Delta R_p$ and a full width of half-maximum (FWHM) of ΔX_p

all implanted ions are retained, the dose is related to the ion depth distribution by

$$\phi_i = \int_{-\infty}^{\infty} N(x)\mathrm{d}x \ . \tag{6.6}$$

The expression for peak atomic density in the ion implantation distribution is obtained by setting $x = R_p$ in (6.5)

$$N(R_p) \equiv N_p = \frac{\phi_i}{\Delta R_p (2\pi)^{1/2}} \cong \frac{0.4\phi_i}{\Delta R_p}, \tag{6.7}$$

where N_p is in units of atoms cm^{-3} for ϕ_i in units of atoms cm^{-2} and ΔR_p in centimeters. Consider a 100 keV B implantation into Si, where $R_p = 318$ nm and $\Delta R_p = 89$ nm. For an implantation dose of 1×10^{15} atoms cm^{-2}, the peak atomic density of B will be

$$N_p = 0.4 \times 10^{15} \text{ (atoms cm}^{-2}\text{)}/89 \times 10^{-7} \text{ (cm)} = 1.82 \times 10^{21} \text{ (atoms cm}^{-3}\text{)}.$$

To obtain the atomic concentration resulting from this peak number of implanted ions requires knowing N, the atomic density of the substrate. The general relation for the concentration of the implanted species at the peak of the distribution is given by

$$C_p = \frac{N_p}{N_p + N}. \tag{6.8}$$

For the example above, the atomic density of Si is 5×10^{22} atoms cm^{-3}, and the concentration of B in Si is 0.18/(0.18 + 5.00) = 0.035 = 3.5 atomic%.

6.3 Calculations

In the previous sections of this chapter we introduced the concepts of range and range distribution and their associated quantities. To proceed, we must be able to calculate quantities for range, projected range, and projected range straggling. In range theory, the range distribution is regarded as a transport problem describing the slowing down of energetic ions in matter. Two general methods for obtaining range quantities, one using simulations and the other employing analytical methods, have been developed over the years.

The analytical approach used to obtain range quantities was pioneered by Lindhard, Scharff, and Schiott (1963), and is commonly referred to as LSS theory. While not precisely accurate, the LSS approach allows one to calculated range values with an accuracy of about 20%, which is quite acceptable for most purposes. We will utilize the LSS formulation throughout this chapter. A more exact transport calculation is available using the Projected Range Algorithm (PRAL) code developed by Biersack (1981) and Ziegler et al. (1985). PRAL is part of the SRIM software package (The Stopping Ions and Ranges in Matter). Both LSS and PRAL theory assume that the target is amorphous and hence crystal orientation effects are ignored.

6.3.1 Range Approximations

Simple estimates of range can be obtained using the power law description of nuclear stopping (Sect. 5.3) and ignoring electronic stopping. Nuclear stopping is the more important process at low energies, reaching a maximum around $\varepsilon = 0.35$ and then falling off with increasing ε. Electronic stopping, however, increases linearly with ion velocity and becomes the dominant process for energies greater than $\varepsilon \cong 3$. For heavy ions in light targets, nuclear stopping remains the dominant mode of energy loss for ion energies up to several hundred kilo-electron-volts (i.e., up to $\varepsilon \cong 3$).

In the case where nuclear stopping predominates, the range can be estimated by ignoring the contributions from electronic stopping:

$$R = \int_{E_0}^{0} \frac{\mathrm{d}E}{NS_\mathrm{n}(E)} \, . \tag{6.9}$$

A power law-based estimate of the nuclear stopping cross-section, $S_\mathrm{n}(E)$, given in (5.7), results in an approximate expression for R, which is given by

$$R(E_0) = \left(\frac{1-m}{2m}\right)\frac{\gamma^{m-1}}{NC_m}E_0^{2m} \tag{6.10}$$

in which the parameters m and C_m have been defined in Chap. 4, and $\gamma = 4M_1M_2/(M_1 + M_2)^2$. A 20% accuracy in nuclear stopping and path length can be obtained using the power law approximation over the same ranges of validity

$$m = 1/3 \text{ for} = \varepsilon \le 0.2,$$

$$m = 1/2 \text{ for } 0.08 \le \varepsilon \le 2.$$

A rather useful rule-of-thumb equation for predicting heavy-ion ranges ($m = 1/2$), usually with an accuracy of ~30–40%, is given by

$$R(\mathrm{nm}) = \frac{13E(\mathrm{keV})}{\rho(\mathrm{g cm^{-3}})} \frac{1 + M_2/M_1}{Z_1^{2/3}} \, . \tag{6.11}$$

As an example, consider 50 keV As in Si where $Z_1 = 33$, $M_1 = 75$, $M_2 = 28$, and $\rho_{\mathrm{Si}} = 2.33$. Applying these values to (6.11) gives $R = 37.6$ nm.

6.3.2 Projected Range

The range, R, is the total distance that the projectile travels in coming to rest. However, in many applications of energetic ions in surface modification, the projected range, R_p, is the quantity of interest. The projected range is defined as the total path length of the projectile measured along the direction of incidence. Figure 6.1 contrasts the difference between R and R_p.

An approximate measure of the projected range can be found using the theory of Lindhard et al. (1963), which gives

$$\frac{R}{R_\mathrm{p}} \approx 1 + B\frac{M_2}{M_1} \, , \tag{6.12}$$

where B is a slowly varying function of E and R. In the energy region where nuclear stopping dominates and $M_1 > M_2$, $B = 1/3$. Increased electronic stopping at higher energies leads to smaller values of B. For the case of $M_1 < M_2$, large-angle scattering makes the correction between R_p and R somewhat larger than the value given by the above rule-of-thumb expression. On the other hand, electronic stopping is usually appreciable in such cases, and this partially offsets the increase in the correction term. Thus, $B = 1/3$ is a reasonable approximation for a wide range of implant conditions, allowing us to write

$$R_p \cong \frac{R}{1 + (M_2/3M_1)}. \tag{6.13}$$

For 50 keV As in Si, (6.13) gives $R_p = 33.4$ nm, which is within 14% of the value calculated by SRIM, 38.8 nm.

A more exact relation between range and projected range was calculated using power law-based LSS theory by Winterbon, Sigmund, and Sanders (WSS; 1970). Plots of R_p/R as a function of M_2/M_1 for the power law conditions of $m = 1/3$ and 1/2, are presented in Fig. 6.4.

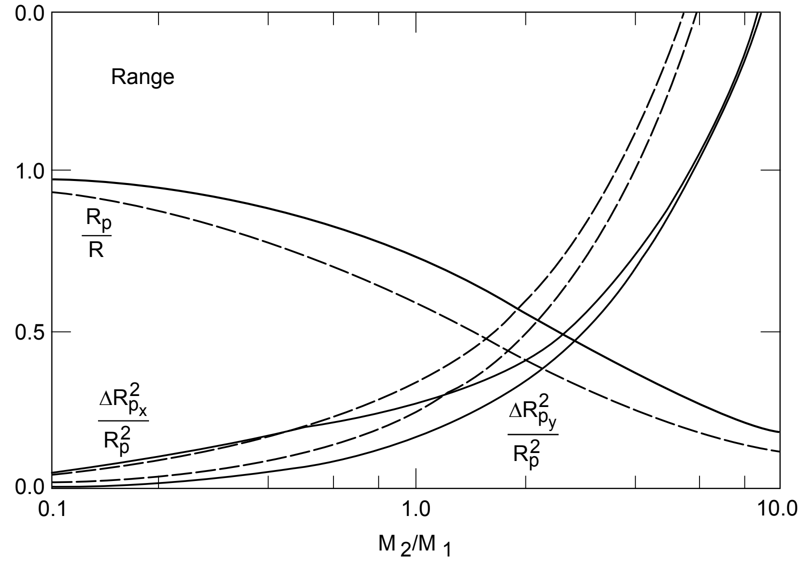

Fig. 6.4. Relationship between range, R, projected range, R_p, and range straggling, ΔR_p, as functions of mass ratio, M_2/M_1. The range straggling, ΔR_{px}, is in the direction of the incident ion, and ΔR_{py} is perpendicular to the incident ion. *Dashed lines*, $m = 1/3$; *solid lines*, $m = 1/2$ (Winterbon et al. 1970)

6.3.3 Range Straggling

Ion implantation is a stochastic (random) process. The mean projected range represents the *most probable* location for an ion to come to rest. The uncertainty in the scattering process as the ion travels through the target gives rise to ions coming to rest at distances less than and greater than the projected range. The average fluctuation (standard derivation from the mean) in the projected range is called range straggling, ΔR_p.

The influence of ion mass, M_1, and target mass, M_2, on the range straggling is schematically shown in Fig. 1.2 (also see Fig. 6.4). As can be seen, the trajectories of the lighter species in a heavier substrate exhibit larger deviations of their implant trajectories relative to those of the heavy ions in relatively lighter substrates. This behavior is influenced by the same conservation of momentum and energy physics that applies the scattering of macroscopic hard spheres, e.g., shooting marbles into a collection of billiard balls versus the opposite case of shooting a billiard ball into a collection of marbles. In the former case, the marble projectile will be more easily deflected from its incident course while in the latter case the billiard ball will plow ahead without as much lateral deviation. These differences in (elastic) nuclear scattering properties will influence the extremes in stopping locations and the width of the ion distribution in the solid. For the same physical reasons, a wider depth distribution is expected for M_1 (ion) < M_2 (substrate atom) relative to the depth distribution for $M_1 > M_2$.

The range straggling can be calculated using the theory of Lindhard et al. for the condition where nuclear stopping dominates from

$$\Delta R_p \cong R_p / 2.5. \tag{6.14}$$

As an example of (6.14), we will estimate the mean projected range straggling for the two cases, 13 keV B in Si and 35 keV As in Si, which produces an R_p of 50 nm for both ions. The PRAL code gives 28.0 and 20.9 nm for ΔR_p, for B and As, respectively. Therefore $R_p/\Delta R_p = 1.8$ and 2.4 for B and As, respectively, in reasonable agreement with (6.14).

A general relationship between projected range straggling and the mean projected range, for the mass conditions $0.1 \le M_2/M_1 \le 10$, has been developed by WSS and is plotted in Fig. 6.4. The value ΔR_{px} is the range straggling in the direction of the incident ion, and ΔR_{py} is the range straggling in the direction perpendicular to the incident ion.

6.3.4 Polyatomic Targets

The accurate treatment of ion ranges in compound targets requires extensive calculations, as performed in the PRAL code. However, estimates can be made using

two simple techniques. For different atomic species that are sufficiently close in atomic number, e.g., Fe–Ti (iron–titanium) alloys, we can substitute the mean atomic number and mass into the LSS equations and proceed as for a monatomic target. If the atomic numbers are appreciably different, a first-order of estimate may be obtained for an alloy A_xB_y using the expression

$$R_\mathrm{p}(A_xB_y) \cong N_\mathrm{alloy}\left[\frac{(R_\mathrm{p}(A)/N_A)(R_\mathrm{p}(B)/N_B)}{(yR_\mathrm{p}(A)/N_A)+(xR_\mathrm{p}(B)/N_B)}\right], \tag{6.15}$$

where $x+y=1$, N_A and N_B are the projected ranges and the atomic densities in pure substrates A and B, respectively, and N_alloy is the atomic density of the alloy. Consider, for example, the case of implanting 100 keV Kr ions into the intermetallic compound Fe_2Al. (The compound Fe_2Al is fictitious. However, for illustrative purposes, we will assume that it exists with a mass density of 6.36 g cm^{-3}.) The projected ranges of 100 keV Kr in Al and Fe are 50 and 23 nm, respectively. The atomic densities are $N_\mathrm{Al} = 6.02\times10^{22}$ atoms cm^{-3} and $N_\mathrm{Fe} = 8.50\times10^{22}$ atoms cm^{-3}. We shall assume that the intermetallic compound Fe_2Al has a mass density of 6.36 g cm^{-3}, which gives an atomic density of 8.29×10^{22} atoms cm^{-3}. Using this data and (6.15) gives $R_\mathrm{p}(\mathrm{Fe_2Al}) = 29$ nm, which is in good agreement with the PRAL calculation, which gives $R_\mathrm{p} = 28.6$ nm.

An estimate of the range straggling in alloys can be made using the empirical expression developed by Kido and Kawamoto (1986)

$$\frac{\Delta R_\mathrm{p}}{R_\mathrm{p}} = 0.27 + \frac{0.38}{\varepsilon_\mathrm{av}+2.0}, \tag{6.16}$$

where the average alloy reduced energy, ε_av, is defined by

$$\varepsilon_\mathrm{av} = \sum_{i=1}^{n} C_i\varepsilon_i, \tag{6.17}$$

where C_i (i = 1, 2,…, n) is the elemental composition of the ith element and ε_i is the elemental reduced energy defined by (5.9). Applying (6.16) and (6.17) to the problem of range straggling in 100 keV Kr in Fe_2Al, we obtain an average reduced energy of 0.38 and a ratio of $\Delta R_\mathrm{p}/R_\mathrm{p} = 0.43$. The projected range, calculated using (6.15), was 29 nm, which results in a projected range straggling of $\Delta R_\mathrm{p} = 12.5$ nm, which is within 18% of the PRAL calculated value of 10.6 nm.

6.4 Range Distributions from SRIM

The stopping and range of ions in matter can be calculated in a comprehensive computer program, entitled SRIM, which is co-authored by Ziegler and Biersack (http://www.srim.org/). Stopping/range tables obtained from analytical calculations and Monte Carlo calculations of the transport and range of ions in matter (TRIM) are all given. Background information, instructions, tutorials, and legal notices are included.

As an example, Fig. 6.5 gives the SRIM output for analytically derived values for an As ion implanted into Si at an implant energy of 50 keV. The output lists ion energy, $dE/dx|_e$ (14.28 eV Å^{-1}), $dE/dx|_n$ (121.6 eV Å^{-1}), projected range (388 Å), longitudinal straggling (124 Å), and lateral straggling (96 Å). Only one ion energy was chosen in this case, and a complete range of energies also could have been tabulated.

```
                          Arsenic in Silicon
==================================================================
              Calculation using SRIM-2003
              SRIM version ---> SRIM-2003.20
              Calc. date   ---> September 29, 2003
==================================================================

Disk File Name = SRIM Outputs\Arsenic in Silicon

Ion = Arsenic [33] , Mass = 74.92 amu

Target Density =  2.3212E+00 g/cm3 = 4.9770E+22 atoms/cm3
======= Target  Composition ========
   Atom   Atom   Atomic    Mass
   Name   Numb   Percent   Percent
   ----   ----   -------   -------
    Si     14    100.00    100.00
====================================
Bragg Correction = 0.00%
Stopping Units =   eV / Angstrom
See bottom of Table for other Stopping units

   Ion        dE/dx      dE/dx     Projected  Longitudinal   Lateral
  Energy      Elec.      Nuclear     Range     Straggling   Straggling
-----------  ---------- ---------- ----------  ----------  ----------
 50.00 keV   1.428E+01  1.216E+02    388 A       124 A         96 A
-----------------------------------------------------------------
Multiply Stopping by         for Stopping Units
-------------------          -------------------
 1.0000E+00                   eV / Angstrom
 1.0000E+01                  keV / micron
 1.0000E+01                  MeV / mm
 4.3083E-02                  keV / (ug/cm2)
 4.3083E-02                  MeV / (mg/cm2)
 4.3083E+01                  keV / (mg/cm2)
 2.0093E+00                   eV / (1E15 atoms/cm2)
 2.8352E-03                  L.S.S. reduced units
==================================================================
(C) 1984,1989,1992,1998,2003 by J.P. Biersack and J.F. Ziegler
```

Fig. 6.5. SRIM output for analytical-derived values for an As ion implanted into Si at an implant energy of 50 keV

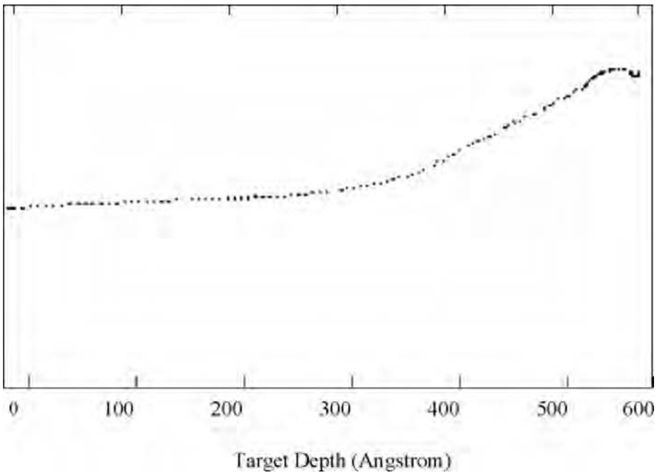

Fig. 6.6. The ion trajectory for a single 50 keV As ion in Si. Results from SRIM Monte Carlo calculations

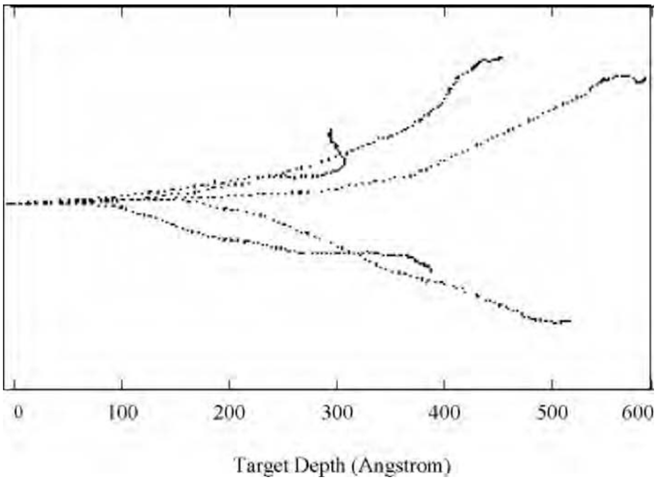

Fig. 6.7. The ion trajectory for of five 50 keV AS ions in Si. Results from SRIM Monte Carlo calculations

Figure 6.6 shows one ion track and Fig. 6.7 shows five superimposed ion tracks from SRIM Monte Carlo calculations for 50 keV As in Si. These figures illustrate the irregular nature of the ion tracks and reflect the collisions between As and Si

that cause defections in the arsenic's flight path. Figure 6.8 shows the ion distribution obtained from the statistics of 20×10^3 ion histories. Note that the Monte Carlo calculation gives a projected range of 398 Å and a longitudinal range straggling of 139 Å in good agreement with the analytical results presented in Fig. 6.5. Note that the y-axis is in units of atoms cm^{-3} $ions^{-1}$ cm^{-2}, which is atomic density normalized by dose. For example, the number of As ions in the peak of the distribution is roughly 28×10^4 atoms cm^{-3} $ions^{-1}$ cm^{-2} which, for a dose of 1×10^{14} As ions cm^{-2}, converts to

$$(28 \times 10^4) \times (1 \times 10^{14}) = 2.8 \times 10^{19} \text{ As cm}^{-3}.$$

Using (6.8) and $N_{Si} = 5 \times 10^{22}$ atoms cm^{-3}, the peak concentration of As in Si for a dose of 1×10^{14} As ions cm^{-2} is 0.06 atomic%.

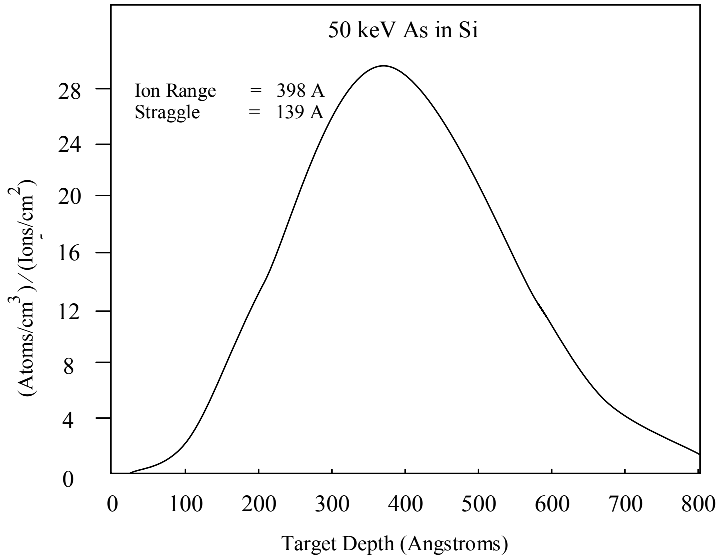

Fig. 6.8. The ion implantation distribution for 50 keV As implanted into Si calculated with the SRIM Monte Carlo simulation. Units of the y-axis are As atomic density normalized by As ion dose

References

Biersack, J.P.: Calculation of projected ranges in analytical solutions and a simple general algorithm. Nucl. Instrum. Meth. **182/183**, 199 (1981)

Eckstein, W.: Computer Simulation of Ion–Solid Interactions. Springer, Berlin Heidelberg New York (1991)

Kido, Y., Kawamoto, J.: Universal expressions of projected range and damage distributions. Appl. Phys. Lett. **48**, 257 (1986)
Lindhard, J., Scharff, M., Schiott, H.E.: Range concepts and heavy-ion ranges (notes on atomic collisions II). Mat. Fys. Medd. Dan. Vidensk. Selsk. **33**(14), 3 (1963)
Mayer, J.W., Eriksson, L., Davies, J.A.: Ion Implantation in Semiconductors. Academic, New York (1970)
Winterbon, K.B., Sigmund, P., Sanders, J.B.: Spatial distribution of energy deposited by atomic particles in elastic collisions. Mat. Fys. Medd. Dan. Vidensk. Selsk. **37**(14), 5. (1970)
Ziegler, J.F., Biersack, J.P., Littmark, U.: The Stopping and Range of Ions in Solids. Pergamon Press, New York (1985)

Suggested Reading

Nastasi, M., Mayer, J.W., Hirvonen, J.K.: Ion–Solid Interactions: Fundamentals and Applications. Cambridge University Press, Cambridge (1996)
Simonton, R., Tasch, A.F.: Channeling effects in ion implantation. In: Ziegler, J.F. (ed.) Handbook of Ion Implantation Technology, p. 119. North-Holland, New York (1992)

Problems

6.1 For 100 keV implantation of As ions (singly ionized As) into Si at current of 1 mA over an area of 200 cm^2 for 10 min
  (a) What is the number of implanted ions cm^{-2}?
  (b) What is the value of the projected range, R_p, and range straggling, ΔR_p?
  (c) What is the concentration of implanted As (cm^{-3}) at $x = R_p$?
  (d) At what depth would the As concentration drop to 10^{-2} of its value at $x = R_p$?

6.2 For 100 keV implantation of ions (singly ionized molecules): what is the velocity of the molecules? If the molecule breaks into two As ions when it hits the Si, what is the projected range of the As ions?

6.3 In the case where nuclear stopping predominates, the range can be estimated by ignoring the contributions from electronic stopping

$$R = \int_{E_0}^{0} \frac{\mathrm{d}E}{NS_n(E)}.$$

Derive the range expression in the laboratory using the energy-independent nuclear stopping expression

$$\frac{dE}{dx} = 1.308\pi a_{TF} N Z_1 Z_2 e^2 \frac{M_1}{M_1 + M_2}.$$

6.4 Using Fig. 6.4, determine R_p and ΔR_{px} for 50 keV As in Si. Compare your results to (6.13) and (6.14) and with values calculated by SRIM.

7 Displacements and Radiation Damage

7.1 Introduction

As we have shown in the preceding chapters, collisions between ions and target atoms result in the slowing down of the ion, and the energy loss resulting from nuclear stopping contributes significantly to determining the ion's range. In our discussion of range theory we have to consider how the nuclear energy losses contribute to the energy dissipation of the ion. From our discussion of elastic collisions we know that the energy loss by the ion is transferred to lattice atoms. In these collisions, sufficient energy may be transferred from the ion to displace an atom from its lattice site. Lattice atoms that are displaced by incident ions are called *primary knock-on atoms* or PKAs. The PKAs can in turn displace other atoms, i.e., secondary knock-on atoms, tertiary knock-ons, etc., thus creating a cascade of atomic collisions. This leads to a distribution of vacancies, interstitial atoms and other types of lattice disorder in the region around the ion track. As the number of ions incident on the crystal increases, the individual disordered regions begin to overlap. At some point, a heavily damaged layer is formed. The total amount of disorder and the distribution in depth depend on ion species, temperature, energy, total dose and channeling effects.

7.2 Radiation Damage and Displacement Energy

Radiation damage theories are based on the assumption that a lattice atom struck by an energetic ion or recoiling target atom must receive a minimum amount of energy in the collision to be displaced from its lattice site. The energy required to displace the lattice atom represents the displacement threshold and is called the *displacement energy*, E_d. If in the collision process the energy transfer to the lattice atom, T, is less than E_d, the struck atom undergoes large amplitude vibrations without leaving its lattice position. The vibrational energy of the struck atom is quickly shared with nearest neighbors and appears as a localized source of heat. If, however, T is greater than E_d, the struck atom is able to move out of the

potential well that represents its stable lattice site and move off into the lattice as a displaced atom. In the simplest case, the displaced atom leaves a vacancy and occupies an interstitial site in the lattice. This vacancy-interstitial defect is referred to as a *Frenkel pair* or *Frenkel defect*. A Frenkel defect is defined as a lattice vacancy created by removing an atom from its site and placing it at an interstitial position within the lattice. Thus a Frenkel pair is a vacancy and an interstitial.

The displacement energy, E_d, is the energy that a target atom has to receive in order to leave its lattice site and form a stable interstitial. This energy depends on the direction of the momentum of the target atom. Therefore, a range of displacement energies exists for the creation of a Frenkel pair. The threshold energy for atomic displacement can be determined experimentally by monitoring changes in the material's electrical resistivity using electron irradiation at liquid helium temperatures. Measurements are typically made on single crystal material as a function of both the electron's accelerating voltage and the orientation of the crystal with respect to the electron beam.

Since the recoil direction of the struck atom is determined by the dynamics of the collision, it will be a random variable during real experiments. The directional dependence of E_d, coupled with the randomness of the initial directions of the struck atom, imply that the notion of a sharp displacement threshold is oversimplified. In reality, there is a range of displacement energies for which a displacement may occur. A weighted average over the displacement directions leads to an average displacement energy, which is the value most typically used as E_d. Typical values of E_d are 16 eV for Si, 29 eV for Cu and 43 eV for Au.

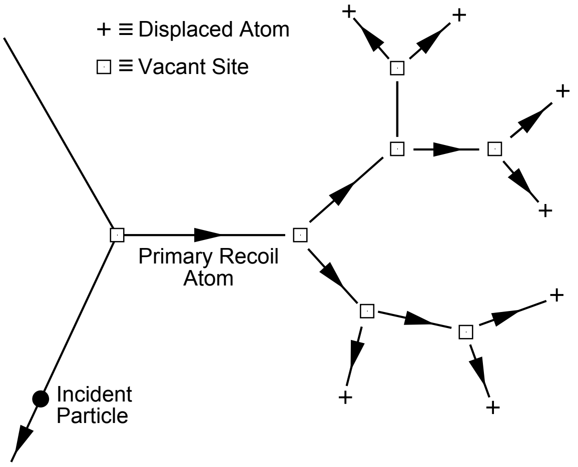

Fig. 7.1. Schematic of the formation of collision cascade by a primary knock-on atom (after Thompson 1969)

7.3 Displacements Produced by a Primary Knock-on

In this section we will examine the production of displaced atoms from a single PKA of energy E. As shown in Fig. 7.1, a primary recoil atom is produced when an energetic incident particle (ion) undergoes a collision with a lattice atom. If the energy transferred to the PKA is large enough, $E \gg E_d$, the PKA can continue the knock-on atom processes, producing secondary recoil atom displacements, which in turn can displace additional atoms. Such an event will result in many collision and displacement events occurring in near proximity to each other. The multiple displacement sequence of collision events is commonly referred to as a *collision* or *displacement cascade*. The *average number* of displaced atoms in a cascade produced by a PKA of energy E will be denoted by $\langle N_d(E) \rangle$, also known as the *displacement damage function*.

The simplest calculation of the damage function, $\langle N_d(E) \rangle$, is based on the hard-sphere model of Kinchin and Pease (1955). The following assumptions are made in the Kinchin and Pease model:

1. Collisions are between like atoms, i.e., $M_1 = M_2$;
2. The probability of transferring energy during the collision process is determined by a hard sphere cross-section, i.e.;

$$P(E,T)\mathrm{d}T \cong \frac{\mathrm{d}T}{\gamma E} = \frac{\mathrm{d}T}{E}$$

   where $\gamma = 1$ for $M_1 = M_2$;
3. The cascade is created by a sequence of two-body collisions;
4. All collisions are elastic, only consider nuclear processes, ignoring electronic stopping;
5. The energy consumed in displacing an atom, E_d, is neglected in the energy balance of the binary collision that transfers kinetic energy to the struck atom;
6. The arrangement of the atoms in the solid is random, and effects due to the crystal structure are neglected;
7. A lattice atom receiving less than a critical energy E_d is not displaced. Similarly, if a knock-on atom emerges from a collision with $E < E_d$, it does not contribute further to the cascade. Also, atoms receiving energy between E_d and $2E_d$ are displaced but cannot themselves further increase the total number of displacements.

From Assumption 7 we obtain the following conditions:

$$\begin{aligned} \langle N_d(E) \rangle &= 0, \quad (\text{for } E < E_d) \\ \langle N_d(E) \rangle &= 1, \quad (\text{for } E_d \le E \le 2E_d) \end{aligned} \tag{7.1}$$

There are two possibilities for the second statement in (7.1). Consider a PKA born with an energy between E_d and $2E_d$. Now consider the sequence of events as the PKA undergoes a collision with a lattice atom. If the energy transferred by the PKA to the lattice atom is greater than E_d, but less than $2E_d$, the lattice atom will be displaced, but the initial PKA is left with energy less than E_d. In this situation the struck atom moves off its lattice site, but the PKA falls into the vacated site, dissipating its remaining kinetic energy as heat. This process represents a *replacement collision.* Alternatively, if the PKA transfers less than E_d to the lattice atom, the struck atom will not be displaced, leaving the PKA as the only displaced atom with insufficient energy left to displace another lattice atom. In either of the above two possibilities, the PKA collision results in only one moving atom, which has an energy less than the original PKA. Therefore, a PKA with kinetic energy between E_d and $2E_d$ produces only one displaced atom.

We must now determine the functional form of the damage function $\langle N_d(E)\rangle$ for $E > 2E_d$. This can be accomplished by calculating the average energy recoil energy, $\langle T\rangle$ produced by a PKA of energy E. From the definition of an average value, the mean recoil energy is given by

$$\langle T\rangle = \int_0^{T_M} T P(E,T)\,\mathrm{d}T = \frac{1}{T_M}\int_0^{T_M} T\,\mathrm{d}T = \frac{E}{2}$$

where we have again used the hard-sphere probability function. Since the minimum energy needed to produce one displacement is E_d, the average number of displacements produced by a mean recoil energy of $\langle T\rangle$ is simply $\langle T\rangle/E_d$ or $E/2E_d$.

Kinchin and Pease defined a critical energy, E_c, to accommodate electron energy losses by the PKA. Values of E_c are taken as M_2 keV, for example $E_c(\mathrm{Cu}) = 64$ keV. For PKAs generated with energy greater than E_c, the number of displacements is assumed to be

$$\langle N_d(E)\rangle = \frac{E_c}{2E_d} \quad (\text{for } E > E_c) \tag{7.2}$$

The total Kinchin–Pease PKA damage function now can be constructed

$$\langle N_d(E)\rangle = \begin{cases} 0 & (\text{if } E < E_d) \\ 1 & (\text{if } E_d < E < 2E_d) \\ E/2E_d & (\text{if } 2E_d < E < E_c) \\ E_c/2E_d & (\text{if } E > E_c) \end{cases} \tag{7.3}$$

and is shown in Fig. 7.2.

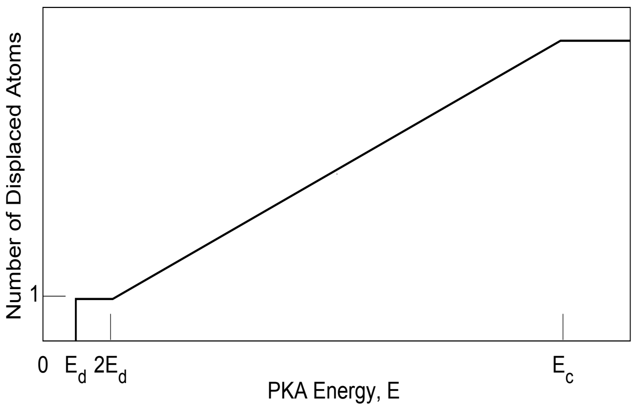

Fig. 7.2. A graphical representation of the number of displaced atoms in the cascade as a function of PKA energy according to the model of Kinchen and Pease, (7.3)

The second and fourth Kinchin–Pease assumptions, which treat the colliding particles as hard-spheres (Assumption 2) and ignore electronic stopping (Assumption 4) result in an overestimate of $\langle N_d(E)\rangle$ by (7.3). By correctly accounting for electronic stopping and using a realistic interatomic potential to describe the atomic interactions, the Kinchin–Pease damage function is modified to

$$\langle N_\mathrm{d}(E)\rangle = \frac{\xi\nu(E)}{2E_\mathrm{d}} \tag{7.4}$$

where $\xi < 1$ and depends on atomic interactions (i.e., the interaction potential), and $\nu(E)$ is the amount of PKA energy *not* lost to electronic excitation, commonly referred to as the *damage energy*. The damage energy will be discussed in detail in Sect. 7.4. Both analytical theory and computer simulations suggest a value near $\xi = 0.8$. The total *modified Kinchin–Pease displacement damage function* is given by

$$\langle N_\mathrm{d}(E)\rangle = \begin{cases} 0 & (\text{for } E < E_\mathrm{d}) \\ 1 & (\text{for } E_\mathrm{d} < E < 2E_\mathrm{d}/\xi) \\ \dfrac{\xi\nu(E)}{2E_d} & (\text{for } 2E_\mathrm{d}/\xi \le E < \infty) \end{cases} \tag{7.5}$$

7.4 Primary Knock-on-Atom Damage Energy

A PKA loses energy in both electronic and nuclear collisions as it slows down and comes to rest in a crystal. Only the latter process creates lattice disorder around the ion track and is responsible for radiation-damage effects. Therefore, in considering the disorder created by a PKA, one must first determine the partition of energy between electronic and nuclear processes. A similar procedure was used in determining the range distribution of implanted atoms in Chap. 6. The difference between range and disorder calculations is that, in the latter case, the energy partition of the displaced atoms must be considered as well. As in the case of ion-range distributions, the crystal structure can influence the amount of energy lost in nuclear collisions. For example, a well-channeled particle loses more of its energy in electronic processes, and so creates less disorder, than a particle whose initial direction direction of motion is not aligned with any low-order lattice axis or plane. However, for the moment, we will exclude consideration of the influence of channeling effects.

As a theoretical treatment for the distribution of energy between electronic and nuclear processes for both the primary and the secondary knocked-on particles, consider η as the sum total of the energy given to electrons, ν as the total energy ending up in atomic motion, and $\eta + \nu = E \equiv$ *the energy of the incoming particle*. Figure 7.3 shows ν/E, the fraction of PKA energy deposited in the solid in the form of atomic collision, as a function of PKA energy for several monatomic materials for the case $M_1 = M_2$.

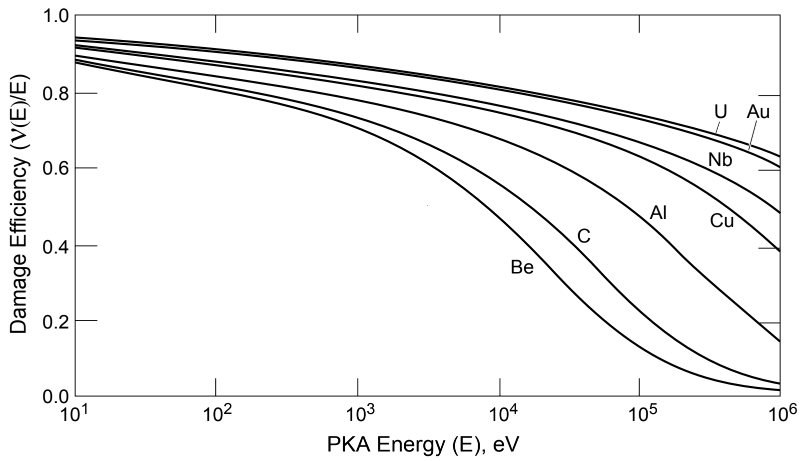

Fig. 7.3. The fraction of the PKA energy deposited in atomic collisions (damage efficiency, $\nu(E)/E$) as a function of PKA energy and self-ion type. Here we define the PKA energy as E (after Robinson 1965)

It should be noted that the damage energy of a PKA with energy E, $\nu(E)$, is closely related to the PKA's total nuclear stopping. This can be expressed as

$$\int^R S_n(E)\mathrm{d}x$$

where R is the PKA range. In general, the PKA damage energy is always approximately 20–30% smaller than the total nuclear stopping. This difference arises because the PKA loses some of its kinetic energy to electronic excitations while traveling to the end of its range.

7.5 Ion Damage Energy

In radiation damage experiments, the damage density deposited in the target is controlled by the ion's energy and mass. The calculated reduced damage energy, $\nu_p(\varepsilon)$, resulting from energetic ions in silicon and germanium is presented in Fig. 7.4, along with experimental data as a function of reduced energy. The dashed line corresponds to the situation in which all the incident energy is assumed to be going into nonionizing (nuclear) processes. The data indicates that the calculated $\nu_p(\varepsilon)$ relation derived for $M_1 = M_2$ holds approximately for $M_1 \neq M_2$. Note that below $\varepsilon \approx 3$ and for $M_1 \geq M_2$, more than half the incident energy is available for displacement processes. From Fig. 7.4, the damage energy in reduced notation can be approximated as

$$\nu_p(\varepsilon) \cong 0.8\varepsilon \quad \text{for}\, \varepsilon < 1 \quad \text{and} \quad Z_1 > 5 \tag{7.6}$$

To convert to $\nu_p(\varepsilon)$ values into laboratory damage energy $\nu_p(E)$, we will make use of the relationship

$$\nu_p(\varepsilon)/\varepsilon = \nu_p(E)/E$$

which allows us to rewrite (7.6) as

$$\nu_p(E) \cong 0.8E \tag{7.7}$$

Table 7.1 gives calculated values for the total amount of energy, $\nu_p(E_0)$, lost in nuclear collisions by energetic Group IV ions incident on silicon and germanium.

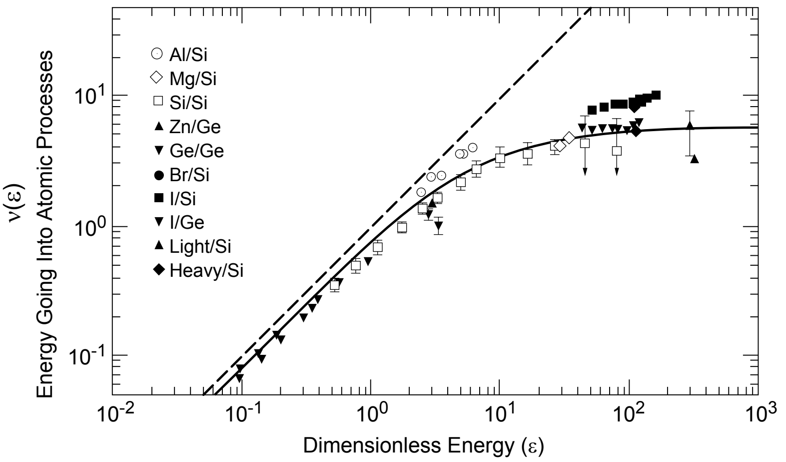

Fig. 7.4. Energy lost in atomic collisions ν versus particle energy (ε). The *dashed line* represents the limit where all energy is lost in nonionizing events. The *solid line* is the calculated value (after Haines and Whitehead 1966)

Table 7.1. Total amount of energy available for nuclear collisions, $\nu_p(E_0)$

Incident ion	E_0, incident energy (keV)						
	1	3	10	30	100	300	1,000
in silicon							
C	0.80	2.2	5.9	14	27	41	54
Si	0.83	2.4	7.3	19	51	100	170
Ge	0.84	2.5	7.7	21	63	160	370
Sn	0.85	2.5	7.9	22	68	180	460
Pb	0.86	2.5	8.0	23	70	190	530
in germanium							
C	0.74	2.0	5.8	14	30	48	65
Si	0.80	2.3	7.2	20	54	110	200
Ge	0.85	2.5	7.9	23	69	175	440
Sn	0.86	2.5	8.1	24	72	195	530
Pb	0.87	2.6	8.2	24	74	210	580

After Mayer et al., *Ion Implantation in Semiconductors*, (Academic Press, New York, 1970). Data supplied by P.V. Thomsen (Aarhus University)

These energy-loss values include the nuclear-collision contributions from the whole cascade, taking into account the electronic losses suffered by the knock-on atoms. These values of $\nu_p(E_0)$ for Group IV elements can be used for the adjacent Group III of V elements without introducing significant errors.

7.6 Damage Production Rate and DPA

A commonly used measure of irradiation damage is *displacements per atom* (dpa). A unit of 1 dpa means that, on average, every atom in the irradiated volume has been displaced once from its equilibrium lattice site.

A simple approximation for dpa(x) per unit dose can be made by assuming that $N_d(x)$, the number of displacements per unit volume at a depth x, can be expressed by a modified Kinchin–Pease expression of the form

$$N_d(x) = \frac{0.8F_D(x)}{2E_d}\phi \tag{7.8}$$

where $F_D(x)$ has units of energy per unit length. The dependence of dpa versus depth for a given dose, ϕ, can then be estimated by

$$\mathrm{dpa}(x) = \frac{N_d(x)}{N} \approx \frac{0.4F_D(x)}{NE_d}\phi \tag{7.9}$$

In many instances it is useful to calculate the total number of dpa produced over the range of the ion. The exact calculation requires integrating (7.9) over the ion's energy as it comes to rest (E_0 to E_d). An estimate of the total dpa can be made for $\varepsilon < 1$ and $Z_1 > 5$ and calculating $N_d(\nu_p(\varepsilon))$, assuming $\nu_p(\varepsilon) \cong 0.8\varepsilon$. For an ion dose ϕ (ions cm^{-2}) and an ion range R, the approximated dpa in the implanted region is given by

$$\mathrm{dpa} \cong \frac{N_d(\nu_p(\varepsilon))}{NR}\phi \cong \frac{0.4\nu(0.8\varepsilon)}{NRE_d}\phi \tag{7.10}$$

where $N_d(\nu_p(\varepsilon))$ is the modified Kinchin–Pease damage function given by (7.4) and calculated for a damage energy given by 0.8ε.

Consider, for example, 50 keV As on Si. We find $E_d = 16$ eV for Si, $N = 5.0 \times 10^{22}$ Si atoms cm^{-3}, and $R = 37$ nm. From (7.7) we have $\nu_p(E) \cong 0.8E$, which gives a damage energy of $\nu_p(E) \approx 40$ keV. The mean number of displacements is $\langle N_d(E)\rangle = 0.8 \times 40 \times 10^3/(2 \times 16) = 1 \times 10^3$. The dpa per unit dose, dpa/ϕ, is equal to $10^3/(5 \times 10^{22} \times 37 \times 10^{-7}) = 5.4 \times 10^{-15}$ dpa ion^{-1} cm^{-2}. Thus, for an ion dose of 1×10^{14} As cm^{-2}, the Si target will experience a dpa of 0.54.

7.7 Replacement Collision Sequences

In Sect. 7.2 the concept of a *replacement collision* was introduced. A replacement collision was possible if a PKA had sufficient energy to displace an atom from its lattice site but was left with energy less than E_d and fell into the vacated site it just created. Early computer simulations of the irradiation process showed that the number of such replacement events greatly exceeded the number of permanent displacements left in the lattice. While such events have little influence on monatomic materials, replacement collisions can produce considerable disorder in ordered polyatomic materials.

In addition to simple replacement collisions, computer simulations have also shown that a chain of displacement–replacement collisions, often called a *replace-ement collision sequence* or a *focused replacement sequence*, can occur when a target atom is displaced with a trajectory directed along the row of neighboring atoms. Estimates and measurements of the lengths of replacement collision sequences range from 5 to 100 nm, with values for the number of replacements produced per displacement ranging between 15 and 60. The amount of disordering produced by a replacement collision sequence will depend on the length of the replacement collision sequence and its direction.

7.8 Spikes

In this section we introduce the concept of a *spike* in irradiated materials. While several different definitions of a spike exist, for our purposes we will define a spike as a *high density cascade that possesses a limited volume in which the majority of atoms are temporarily in motion* (Seitz and Koehler 1956; Sigmund 1974).

7.8.1 Mean Free Path and the Displacement Spike

Earlier in this chapter we considered the average radiation damage imparted to a solid during ion irradiation. We now will consider the spatial distribution of point defects that are generated as an ion or a PKA slows down to rest. An important quantity in determining the spatial distribution of irradiation damage is the average distance or *mean free path*, λ_d, traveled by an energetic particle with energy E between displacement collisions with target atoms. Equation (7.11) shows that the probability of a projectile with energy E undergoing a collision with a target atom, transferring an energy greater than E_d while traversing a thickness dx, is given by

$$P(E) = N\sigma(E)\mathrm{d}x \tag{7.11}$$

where N is the atomic density of the target and $\sigma(E)$ is the total collision cross-section given by (4.18a). Setting $P(E) = 1$ and replacing dx with λ_d, the average path length per collision, or the mean free path of a particle with energy E, is given by

$$\lambda_d = \frac{1}{N\sigma(E)}. \tag{7.12}$$

Equation (7.12) can be used to calculate the mean spacing between defects for a projectile of energy E.

Brinkman (1956) has investigated the details of damage distribution in a cascade as a function of λ_d. He has suggested that as λ_d approaches the atomic spacing of the target atoms, a highly damaged region is formed where every displaced atom is forced away from the ion or PKA path, producing a volume of material composed of a core of vacancies surrounded by a shell of interstitial atoms (see Fig. 7.5). This highly damaged volume of material is referred to as a *displacement spike*. The displacement spike forms in a time equivalent to the time it takes the ion or PKA with energy E to come to rest at the end of its range (Sigmund 1974).

$$t = \int_0^E \frac{dE}{vNS_n(E)} \cong \frac{R(E)}{1/2v} \tag{7.13}$$

where $v = (2E/M)^{1/2}$ is the ion velocity, $S_n(E)$ is the nuclear stopping cross-section, and $R(E)$ is the total ion range. The simple form of (7.13) is the result of a power-law approximation for the power parameter $m = 1/2$. A simple linear estimate of the time, t, needed for a 100 keV Xe ion with mass, $M = 131$ amu to stop with range $R = 20$ nm is 10^{-13} s, of the order of a lattice vibration time.

7.8.2 Thermal Spike

As the formation of the displacement spike comes to an end, all the moving displaced atoms reach a point where they have insufficient energy to cause further displacement. Energy transfers will be at subthreshold levels. At this point the energy will be shared between neighboring atoms and will be dissipated as lattice vibrations or "heat." After approximately 10^{-12} s, a state of dynamic equilibrium may be obtained where the vibrational energy distribution begins to approximate a Maxwell–Boltzmann function. This period of lattice heating is know as the *thermal spike* phase of the collision cascade and may exist for several picoseconds before being quenched to ambient temperature. Once such a dynamic equilibrium is established, the concepts of local heating and temperature become reasonable. For a Maxwell–Boltzmann distribution of energy, the temperature is related to the

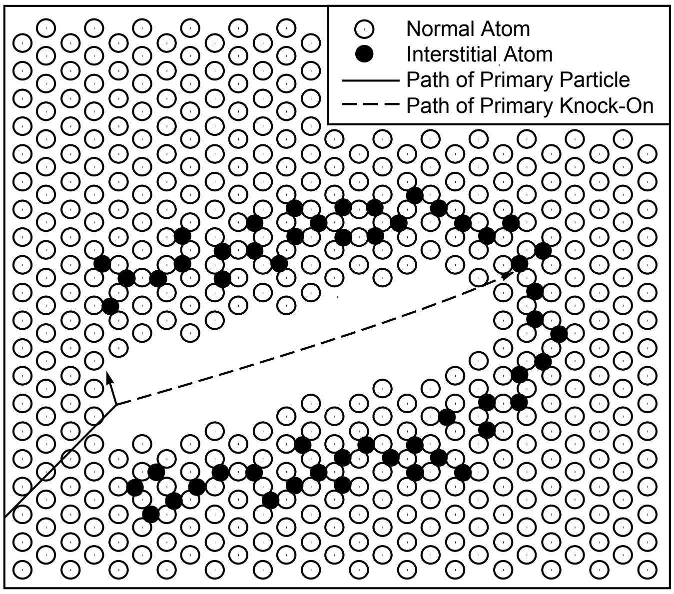

Fig. 7.5. Schematic of a highly damaged volume of material, formed when the mean free path between collisions, λ_d, approaches the atomic spacing of the target atoms. The dense cascade is referred to as a *displacement spike* (after Brinkman, 1956)

mean deposited energy density in the spike by

$$\bar{\theta}_D = \frac{3}{2} k_B T \quad (7.14)$$

where k_B is Boltzmann's constant.

The quench time, t_q, for a thermal spike of radius r is extremely small and can be estimated by

$$t_q = \frac{r^2}{4D_T} \quad (7.15)$$

(Davies 1983), where D_T is the thermal diffusivity of the target. Using Au as an example, with $D_T = 0.7\ cm^2\ s^{-1}$. and assuming $r = 8$ nm, results in a quench time $\approx 2 \times 10^{-13}$ s.

7.9 Damage Distribution from SRIM

Information about irradiation damage can also be obtained from the Monte Carlo simulations in SRIM. In these simulations the ion track of the implanted ion and all the resulting recoils and atomic displacements are displayed, as shown in Fig. 7.6, for a 40 keV Sb ion in Si. Figure 7.6 shows the path of the Sb ion and major Si recoils (dashed line) and Si displacements. As can be seen, the displacement population extends well beyond the Sb ion track. Each implanted Sb ion produces over 1,000 Si displacements.

With continued ion implantation, a dense structure of displaced atoms is formed. Figure 7.7 shows the atomic density of displaced Si atoms as a function of depth, normalized to the ion dose, which will be formed per incident Sb ion. This data represents the averaging of 5,000 ion histories. Note that the unit of length for the *Y* axis is angstroms, and the number of displaced Si atoms is give in units of number per unit volume per ion dose, (Si atoms cm^{-3})/(Sb ions cm^{-2}). This data can be used to determine the fraction of displaced atoms at a given depth for a given ion dose. For example, the peak value of the displacement curve, which occurs at approximately 180 Å, has a value of 40×10^8 displaced Si atoms ion^{-1} cm^{-1}. For an Sb ion dose of 1×10^{13} ions cm^{-2}, this corresponds to 4×10^{22} displaced Si atoms cm^{-3}. Dividing this value by the atomic density of Si (5×10^{22} cm^{-3}) gives the fraction of displaced Si atoms as 0.80.

For comparison, Fig. 7.8 shows the range distribution of implanted Sb ions in Si. This data also represents the averaging of 5,000 ion histories. The range profile shows a peak concentration at about 285 Å, approximately 100 Å deeper than the damage peak.

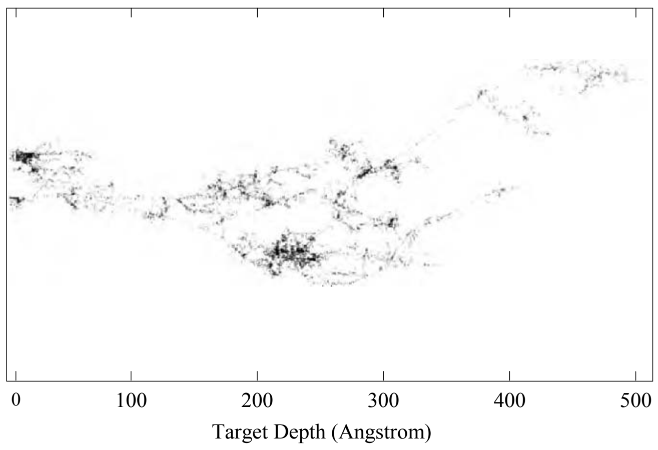

Fig. 7.6. Ion track for 40 keV Sb in Si showing Si recoils and Si displacements (Monte Carlo SRIM simulation)

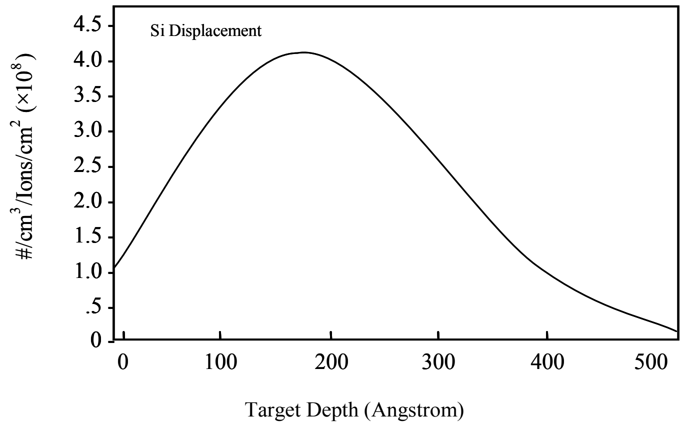

Fig. 7.7. Distribution of displaced Si atoms as a function of depth for 40 keV Sb in Si (Monte Carlo SRIM simulation)

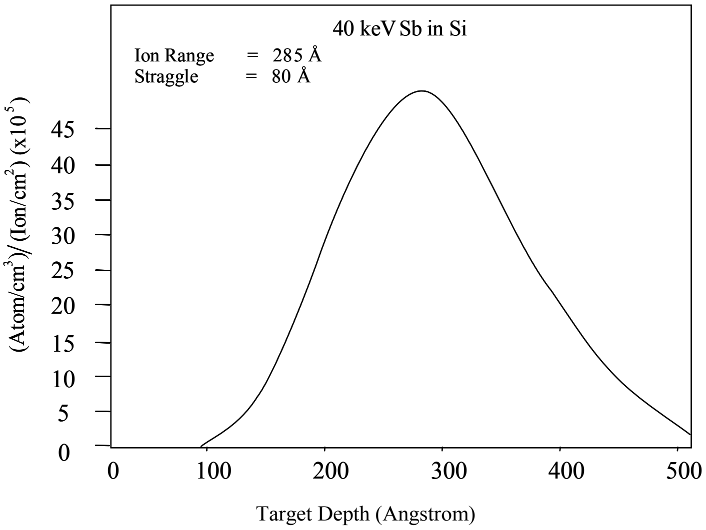

Fig. 7.8. The ion implantation range distribution for 40 keV Sb in Si (from Monte Carlo SRIM simulation)

References

Brinkman, J.A.: Production of atomic displacements by high-energy particles. Am. J. Phys. **24**, 246 (1956)
Davies, J.A.: Collision cascades and spike effects. In: Poate, J.M. Foti, G., Jacobson, D.C. (eds.) Surface Modification and Alloying by Laser, Ion, and Electron Beams, pp. 189–210. Plenum, New York (1983)
Haines, E.L., Whitehead, A.B.: Pulse height defect and energy dispersion in semiconductor detectors. Rev. Sci. Instrum. **37**, 190 (1966)
Kinchin, G.H., Pease, R.S.: The displacement of atoms in solids by radiation. Rept. Prog. Phys. **18**, 1 (1955)
Mayer, J.W., Erikson, L., Davies, J.A.: Ion Implantation in Semiconductors. Academic, New York (1970) (spelled Davies other places)
Robinson, M.T.: The influence of the scattering law on the radiation damage displace cascade. Phil. Mag. **12**, 741 (1965)
Sigmund, P.: Energy density and time constant of heavy-ion-induced elastic-collision spikes in solids. Appl. Phys. Lett. **25**, 169 (1974)
Thompson M.W.: Defects and Radiation Damage in Metals. Cambridge University Press, Cambridge (1969)

Suggested Reading

Averback, R.S., Kirk, M.A.: Atomic displacement processes in ion-irradiated materials. In: Rhen, L.E., Picraux, S.T., Wiedersich, H. (eds.) Surface Alloying by Ion, Electron, and Laser Beams, p. 91. American Society for Metals, Metals Park, (1987)
Nastasi, M., Mayer, J.W., Hirvonen, J.: Ion-solid interaction fundamentals and applications, Cambridge University Press (1996)
Thompson, M.W.: Defects and Radiation Damage in Metals, Cambridge University Press, (1969)

Problems

7.1 Using Fig. 7.3, determine the PKA energies where (7.4) is valid for C, Al, and Au?

7.2 Using the results from Problem 7.1, calculate $\langle N_d(E) \rangle$ assuming E_d = 24 eV, 27 eV, and 43 eV for C, Al, and Au, respectively.

7.3 Using (7.10)
(a) Calculate the damage energy for a 3 keV self-ion Si PKA.
(b) What is the damage energy predicted from Fig. 7.3?

7.4 For 50 keV B, P, As, and Sb ions incident Si, find the approximate value of dpa, (7.10), for doses of 5×10^{13} and 5×10^{15} ions cm^{-2}.

7.5 Using the power law energy-transfer cross-section, calculate the approximate mean free path, (7.11), between Si recoils for both Si and Sb ions with energy of 1, 10, and 50 keV.

7.6 Give a qualitative explanation for the differences in the depths of the damage peak relative to the implantation concentration peak (see Figs. 7.7 and 7.8).

8 Channeling

8.1 Introduction

All theories examined earlier concerning the ranges of ions and radiation damage of materials were based on the assumption that the stopping medium is disordered, i.e., amorphous. In practice, we are dealing with polycrystalline or monocrystalline substances. The main parameters determining the range of an ion are its energy, E, its atomic number, Z_1, and the atomic number of the substrate, Z_2. In the case of single crystals, the orientation of the substrate and the vibrational amplitude (i.e., temperature) of the lattice atoms are also important parameters.

With single-crystal substrates of Si or GaAs, for example, the orientation of the ion beam with respect to the crystallographic axes of the substrate can have a pronounced effect on the range distribution. Figure 8.1 shows the range distribution in Si for 100 keV As implanted with the beam aligned parallel to the $\langle 100\rangle$ crystal axis (solid line) and oriented away from any crystal axes or planes (dashed line). As is evident in the figure, implantation along crystal axes can lead to a fraction of the total number of ions that penetrate several times R_p.

The crystal orientation influence on ion penetration is called *channeling* or the channeling effect. When an ion trajectory is aligned along atomic rows, the positive atomic potentials of the line of atoms steers where the positively charged ion goes within the open space, or channels, between the atomic rows. These channeled ions do not make close-impact collisions with the lattice atoms and have a much lower rate of energy loss, dE/dx, and hence a greater range than those of nonchanneled ions. The depth distribution of channeled ions is difficult to characterize under routine implantation conditions. The channeling distribution depends on surface preparation, substrate temperature, beam alignment, and the disorder introduced during the implantation process itself. The channeled ions that penetrate beyond R_p often have a distribution that falls off exponentially with distance as $\exp(-x/\lambda_c)$, where $\lambda_c \gg R_p$.

Another consequence of channeling is that the energy spectrum of particles scattered back from a crystal aligned with the beam is dramatically different from that of a noncrystalline solid (Fig. 8.2). In the aligned spectrum the scattering yield from the bulk of the solid is reduced by almost two orders of magnitude, and a peak occurs at a position corresponding to scattering from the surface atoms. Both the surface peak and the reduction in yield are due to *shadowing* – the ability

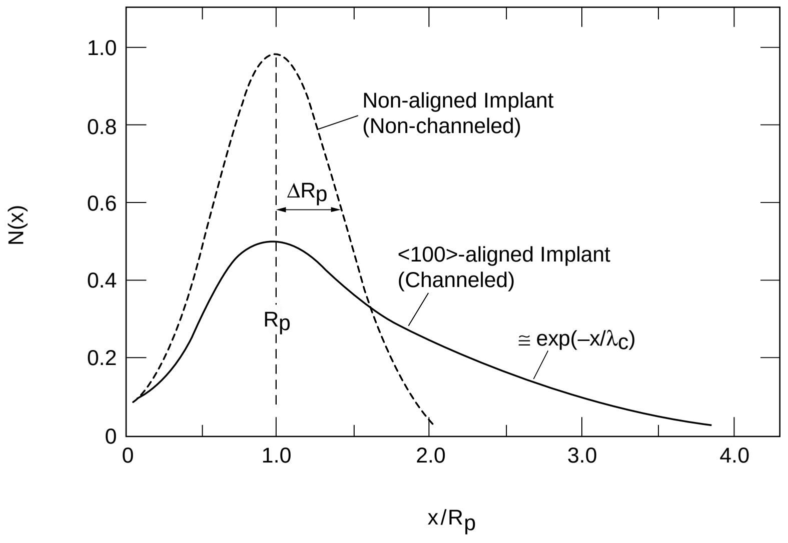

Fig. 8.1. Range distributions for channeled ion implanted along the ⟨100⟩ axis of Si. The *dashed line* shows the Gaussian distribution for incident ions aligned away from any channeling direction

of the outermost atoms to shadow the underlying atoms and hence shield these atoms from direct interactions with the beam.

As the ions penetrate deeper in the crystal they make only small angle collisions with the atomic rows. The initial motion is oscillatory, with the particles bouncing from row to row with a wavelength between bounces of some hundreds of Ångstroms. These channeled particles (~98% of the beam) cannot get close enough to the atoms of the solid to undergo close encounters such as large angle scattering. Hence the yield of backscattered particles decreases by almost two orders of magnitude.

The reduction in scattering yield associated with channeling can be applied to determine the lattice site position of impurity atoms and defects in the crystal (Fig. 8.3). An impurity on a lattice site has a reduction in scattering yield equal to that of the bulk crystal; interstitial impurities or atoms located more than 0.1 Å from a lattice site are exposed to the flux of channeled ions. Consequently, the backscattering yield from such nonsubstitutional atoms does not exhibit the same decrease as that of the host crystal.

The effects of lattice disorder defects and crystal imperfection on channeling are used to analyze ion-implanted samples. Host atoms displaced from their lattice sites can interact with the channeled beam, leading to an increase in the scattering yield.

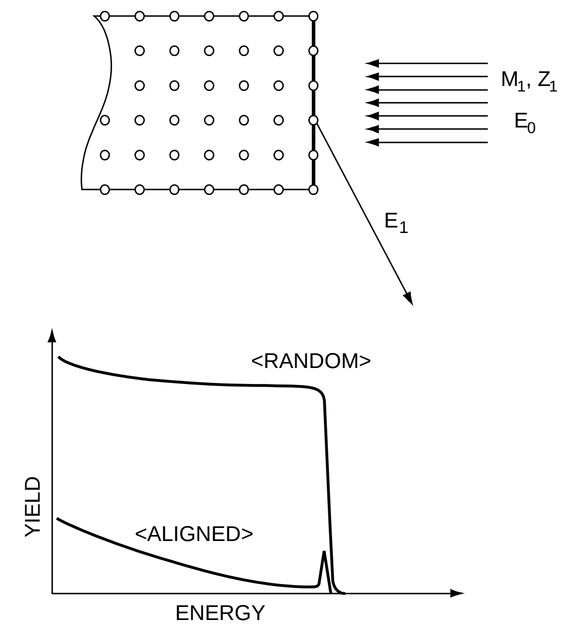

Fig. 8.2. Schematic of the energy spectra for the beam aligned with a symmetry direction of the crystal and in a "random" direction. A random direction denotes the beam misaligned with any major crystallographic direction and is a good representation of the spectrum from an amorphous solid

The channeling effect requires that the incident ions be aligned within a critical angle, ψ_c, of the crystal axes or planes. The critical angle depends on the ion energy, ion species, and substrate, but is typically less than 5°. Consequently, in ion implantation production the substrate holders are often aligned 7° away from a crystallographic axial direction to minimize channeling effects. However, some ions originally incident at angles greater than the critical angle can be scattered into a channeling direction. It is difficult to avoid channeling effects completely unless the implanted region has been made amorphous by a previous implantation.

In the following, we will briefly examine the underlying physics responsible for channeling effects during ion implantation. The application of channeling to the structural analysis of solids is based on nearly two decades of extensive theoretical and experimental investigations of particle–solid interactions in crystals. The early theoretical work of Lindhard and his associates in Aarhus University, and the computer simulation work at Oak Ridge, provide the framework on which these applications are built. The picture of channeling is based on investigations carried out in a wide range of laboratories concerned with atomic collisions in solids.

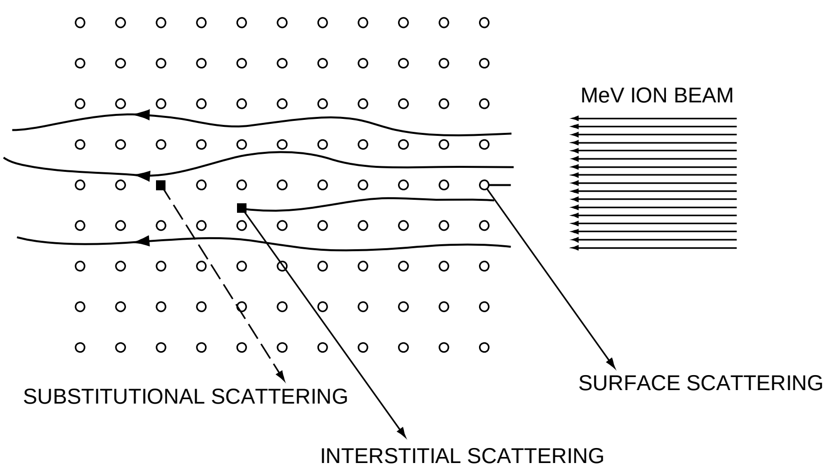

Fig. 8.3. Schematic of channeling trajectories and the interaction of the channeled particles with surface atoms and impurities. Scattering from the first monolayers of the solid, surface scattering, reveals details of the surface structure. The channeled ions, typically 98% of the incident beam, do not make close impact collisions with the host atoms or substitutional impurities. The *dashed line*, for substitutional scattering, indicates the small yield from substitutional impurities. The channeled particles can interact strongly with displaced host atoms or interstitial impurities

8.2 General Principles

If an energetic ion enters a crystal within a certain critical angle of a major axis, then each time it approaches one of the aligned rows of lattice atoms, the gradually increasing repulsion between the screened Coulomb fields of the projectile and the lattice row is sufficient to steer it away again, thereby preventing violent nuclear collisions from occurring. A reasonable estimate of this critical angle within which channeling occurs can be obtained from the theoretical work of Lindhard (1965); for heavy ions at kilo-electron-volt energies, the channeling criterion for a particle of energy E and angle of incidence ψ relative to a row is given by

$$\psi \le \psi_c \equiv [(a_{TF}/d)\psi_1]^{1/2} \tag{8.1}$$

where

$$\psi_1 = (2Z_1Z_2e^2/Ed)^{1/2} \tag{8.2}$$

and a_{TF}, the Thomas–Fermi screening distance, has a magnitude of 0.01–0.02 nm, and d is the atomic spacing along the aligned row. For energies less than a few hundred kilo-electron-volts, ψ_c is between 3° and 5° for standard dopants implanted in Si incident along either the ⟨110⟩ or ⟨111⟩ axes.

One obvious consequence of this steering mechanism is that the rate of energy loss is greatly reduced, and so the ion penetrates more deeply than in an amorphous target. Also, since nuclear stopping depends much more strongly on impact parameter than does electronic stopping, we find that, for a channeled beam, (1) the relative importance of nuclear to electronic stopping is much smaller than for a nonchanneled one, and (2) processes related to nuclear stopping, such as radiation damage or sputtering, are also much reduced. As a result, channeling offers at least two potential advantages for the implantation of semiconductors: deeper junctions and less lattice disorder.

On the other hand, it has at present one serious disadvantage, namely the difficulty of obtaining shallow junctions and reproducible range profiles. Ion trajectories of interest for axial channeling are shown schematically in Fig. 8.4, in which the crystal lattice is depicted as a set of atomic "strings." First, consider particles with oblique incidence (Fig. 8.4a). Particle B, incident at the midchannel with an angle ψ somewhat less than the critical angle ψ_c, will oscillate between strings without undergoing any large-energy-loss nuclear collisions. However, its path has wider-amplitude oscillations than particle C with smaller ψ. Particle A, with $\psi > \psi_c$, will not be steered by the lattice rows in Fig. 8.4a, and so has a trajectory similar to that of an amorphous solid – unless, of course, it happens to be aligned with some other low-index direction.

The impact position of a particle in the plane perpendicular to the channel axis also influences its trajectory. Consider ions incident parallel to the channel direction, as shown in Fig. 8.4b. Those entering the crystal close to an atomic row are scattered immediately through an angle large enough that they do not become channeled (trajectory A). Particles entering at a position slightly farther away are channeled (trajectory B), but with larger oscillations than particles entering near the center of the channel (trajectory C).

For convenience, therefore, the incident particles may be divided into three broad categories, corresponding to the trajectories shown in Fig. 8.4:

1. Group A, those particles that have a strong interaction with the lattice and so have a range distribution similar to those in amorphous material.

2. Group B, those particles that start out with large oscillations in the channel. Such particles are probably scattered out of the preferred direction – i.e., become *dechanneled* – long before they are stopped, and so do not penetrate as deeply as those in Group C.

3. Group C, those particles that start out *well channeled* and so have a better chance of remaining channeled throughout the slowing-down process.

The channeling effect can be seen most clearly in tungsten, which is characterized by small-amplitude thermal vibrations of atoms. Consequently, dechanneling of particles will be weak. In this case, the three sections corresponding to the three types of trajectory shown in Fig. 8.5 are quite pronounced on the concentration distribution curve, as shown in Fig. 8.5. Particles scattered by angles $\psi > \psi_c$ on entering the crystal belong to the first group, A. Their ranges roughly correspond to the case of an amorphous target. With constant increase in transverse energy, particles of the second group, B, having greater oscillation amplitudes in the channels, are dechanneled in the depth section between the two main peaks. Particles almost coming to a complete standstill in the channels correspond to the third group, C.

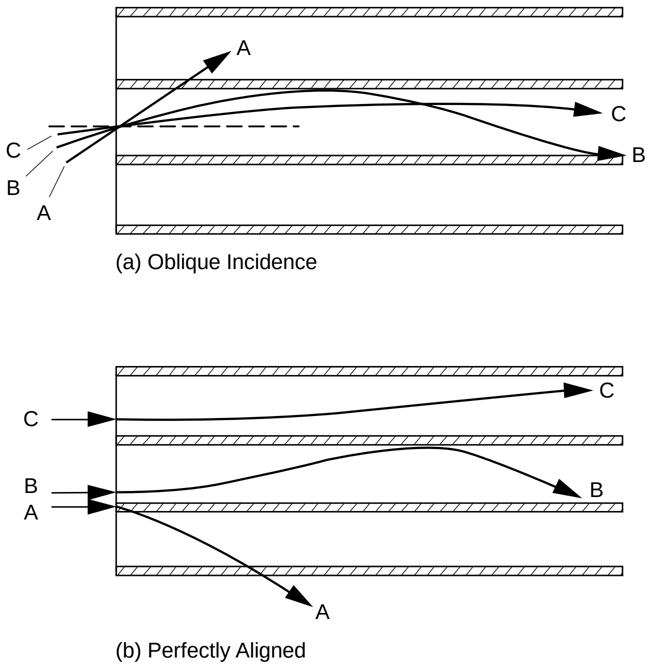

Fig. 8.4. Schematic representation of ion trajectories for axial channeling. The crystal lattice is depicted as a set of atomic "strings," i.e., the shaded rows. (**a**) Trajectories for various angles of incidence, ψ, relative to the lattice row: B and C represent trajectories for ψ values less than the critical angle, and A for values greater than the critical angle. (**b**) Trajectories for parallel incidence as a function of impact position (after Mayer et al. 1970)

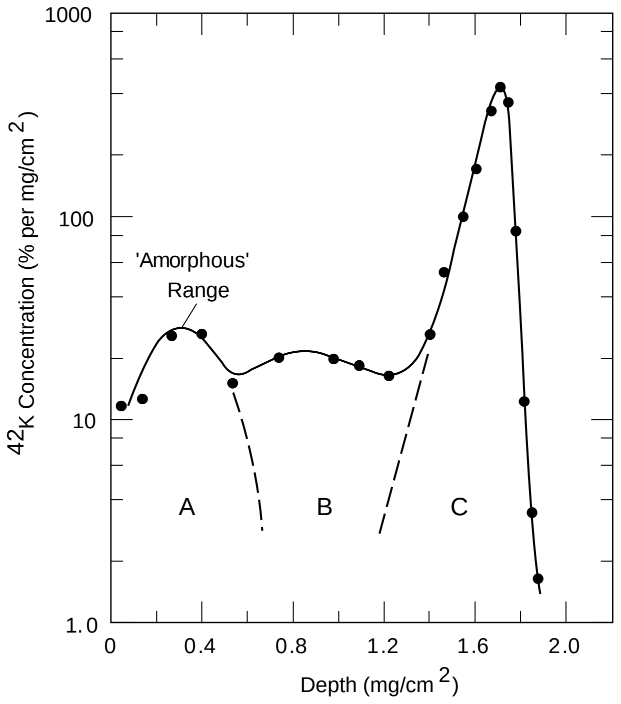

Fig. 8.5. The observed range distribution of 500 keV ^{42}K ions injected as 25°C along the ⟨111⟩ direction in *W*. Note that in *W*, 1 mg cm^{-2} is equivalent to 0.52 μm. (after Mayer et al. 1970)

8.3 The Maximum Range, R_{max}

The ranges of ions with $E = 50–150$ keV along the main crystallographic directions in the crystal can exceed their ranges in an amorphous target by factors of 2–50. If an ion enters the central part of a low-index axial or planner channel, then nuclear stopping will be reduced considerably. Considering that stopping of channeled ions is determined by reaction with electrons of the crystal, and that the stopping power $S_e(E)$ is proportional to $E^{1/2}$ in the velocity-proportional stopping regime (Nastasi et al. 1996), we have

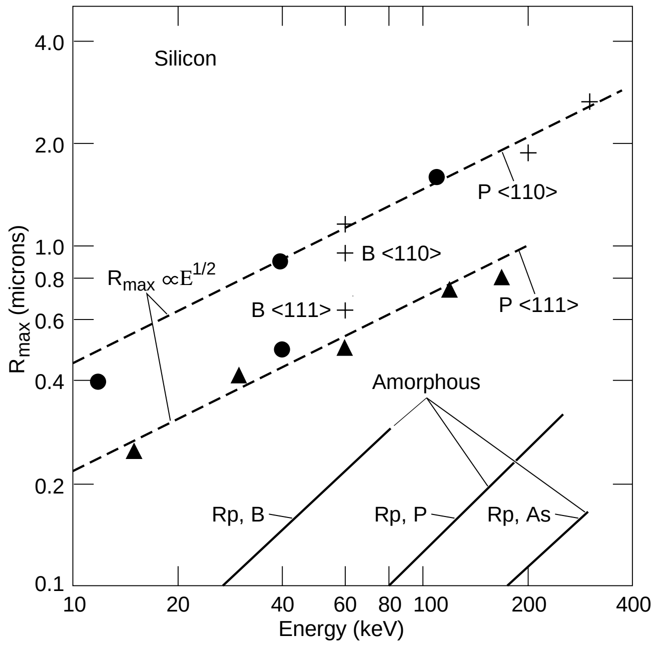

Fig. 8.6. Experimental measurements of R_{max} versus E for well-channeled ions in Si. The *dashed lines*, fitted to the P data, represent an $E^{1/2}$ dependence. Projected ranges, R_p, of B, P, and As in amorphous Si are shown by *solid lines* (after Mayer et al. 1970)

$$R_{max} = \frac{1}{N}\int_E^0 \frac{dE}{S_e(E)} = \frac{2E}{NS_e(E)} = AE^{1/2} \tag{8.3}$$

where A is a constant. The relation predicted by (8.3) between R_{max} and $E^{1/2}$ is confirmed experimentally for well-channeled ions of B, P, As, and Sb in ⟨110⟩ and ⟨111⟩ Si (see Fig. 8.6). The dashed lines are fitted representations of an $E^{1/2}$ dependence. The projected ranges for B, P, and As in amorphous Si are shown by solid lines.

8.4 Dechanneling by Defects

Ion channeling can also be used as a tool to examine radiation damage in ion implanted materials. This is accomplished using high energy ions where $M_1 = M_2$. Typical ions used are H and He with reduced energies $\varepsilon \geq 10$. Under these conditions the scattering is Coulombic and the power-law scattering cross-section exponent, m, has a value of 1 [see (4.19)–(4.21)].

Dechanneling is greatly enhanced by the presence of defects. First, displaced atoms in the center of the channel provide much stronger scattering than the electrons. The probability of dechanneling per unit depth dP_D/dz is then given by the product of the defect dechanneling factor, σ_D, and defect density, n_D,

$$\frac{dP_D}{dz} = \sigma_D n_D(z) \tag{8.4}$$

The probability of dechanneling per unit depth $\sigma_D n_D$ has units of cm^{-1}. For point-scattering centers, as for interstitial atoms, σ_D can be though of as a cross section for dechanneling, and n_D is given by the density of interstitial atoms per unit volume at a given depth.

The calculation is for a uniform beam incident on isolated atoms in a channel (Fig. 8.7). Since we are only interested in scattering angles greater than the critical angle ($\psi_c \sim 1°$), the impact parameter is relatively small ($r_1 \sim 10^{-2}$ Å); thus we use the unscreened Coulomb potential. In this calculation the dechanneling is a result of binary scattering by isolated displaced atoms in an otherwise perfect crystal.

The defect dechanneling factor under these conditions for isolated atoms in a channel is the cross section for the close-impact collision probability of scattering a particle through an angle θ greater than the critical angle ψ_c. The unscreened scattering cross section (Rutherford scattering cross section with $M_1 = M_2$) is given by

$$\frac{d\sigma}{d\Omega} = \left[\frac{Z_1 Z_2 e^2}{4E\sin^2(\theta_c/2)}\right]^2 \tag{8.5}$$

in center-of-mass coordinates. This expression does not include the small M_1/M_2 corrections found in exact calculation for laboratory coordinates (Chu et al. 1978). Equation 8.5 is integrated over angles greater than ψ_c for the cylindrically symmetrical case of axial channeling to yield

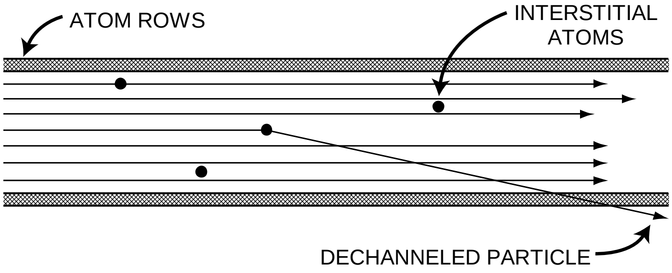

Fig. 8.7. Scattering of a beam of channeled particles by interstitial atoms

$$\sigma_D(\psi_c) = \int_{\psi_c}^{\infty} \frac{d\sigma}{d\Omega} d\Omega \tag{8.6}$$

$$\sim \frac{\pi Z_1^2 Z_2^2 e^4}{E^2 \psi_c^2} \tag{8.7}$$

where $d\Omega = 2\pi \sin\theta d\theta$, and the small angle expansion for $\sin\theta$ has been used. An estimate of σ_D for axial channeling can be obtained from (8.7) by approximating the critical angle by $\psi_c \sim \psi_1 = (2Z_1Z_2e^2/Ed)^{1/2}$ to give

$$\sigma_D \sim \frac{\pi}{2} \frac{Z_1 Z_2 e^2 d}{E} = 2.3 \times 10^{-21} \frac{Z_1 Z_2 d}{E} \text{cm}^2 \tag{8.8}$$

where the value of atomic spacing along an axial direction, d, is given in Ångstroms and the incident energy E is in megaelectron volts. For 2-MeV He ions incident along the ⟨100⟩ axis of Si, ($d = 5.43$), $\sigma_D = 1.7 \times 10^{-19}$ cm^2. This cross section is sufficiently small compared to the area of crystal channels (~10^{-15} cm^2), so that one isolated atom cannot close off channeling; the number of particles channeled remains essentially unchanged even for a collection of several isolated atoms in a channel.

Silicon is a material that can readily be converted to the amorphous state, for example, by implantation of sufficiently high doses so that the disordered regions around the ion tracks overlap and an amorphous layer is found. In backscattering measurements where the incident beam is aligned with the crystal substrate, the scattering yield from the amorphous layer coincides with the random spectrum, as shown in Fig. 8.8. There is a decrease in the aligned yield at the interface between the amorphous and single-crystal regions where the particles can be steered by the crystal rows and planes. The yield is greater than that from a perfect single crystal (dashed line in Fig. 8.7) because a fraction of the particles in the beam emerge from the amorphous layer after having been scattered through angles greater than the critical angle for channeling (Chu et al. 1978). It is the number of particles that are scattered outside the critical angle for a given thickness of amorphous material that determines the defect dechanneling factor.

In the more general case for channeling analysis of disorder profiles, both dechanneling and direct scattering contribute to the measured aligned yield, as shown in Fig. 8.9. The aligned yield $\chi_D(z)$ is related linearly to the defect concentration, $n_D(z)/n$, through a direct scattering contribution, and to the integral of $n_D(z)$ due to the dechanneling contribution.

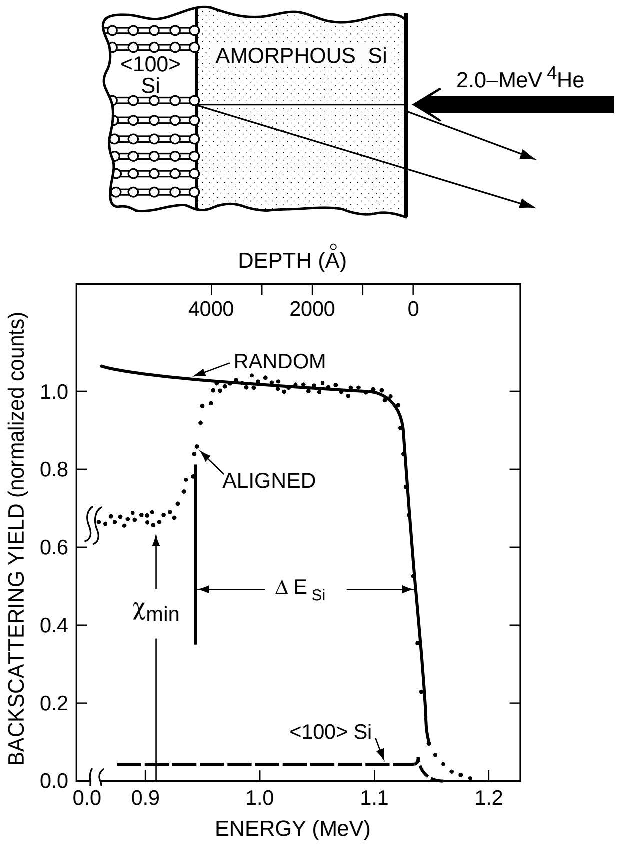

Fig. 8.8. Backscattering and channeling spectrum for amorphous Si layer on ⟨100⟩ Si crystal, showing dechanneled level χ below the amorphous layer

The number of dechanneled ions increases in direct proportion to the total number of defects traversed per unit area. The backscattering signal thus provides an integral measure of the depth profile of extended defects.

An example of the measurement of a disorder distribution is shown in Fig. 8.10 for a silicon implant at a substrate temperature of −150°C, with 5×10^{14} boron ions cm^{-2} at an energy of 200 keV, analyzed at room temperature with 1.8-MeV ions. The open circles in the upper part of the curve are the aligned yield. The dashed curve is the dechanneled fraction determined by use of the iterative procedure using multiple scattering theory to obtain the dechanneling factor σ_D. In this procedure, for example, the number of displaced atoms represented by the

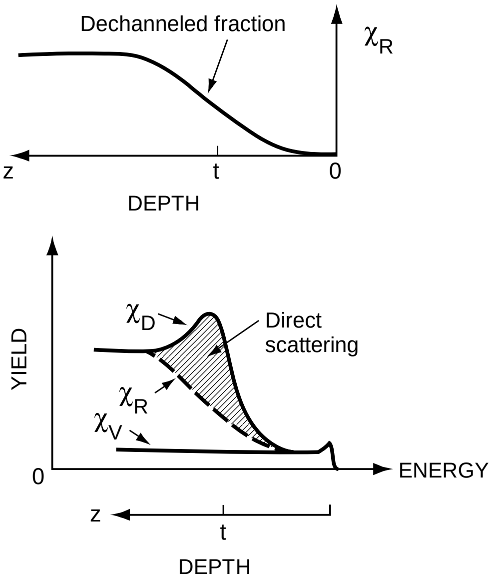

Fig. 8.9. Schematic of the change in backscattering yield as a function of depth through a region of disorder that gives rise to both dechanneling and direct scattering. The aligned fraction, χ_D, is greater than the random fraction, χ_R, in the depth region of the disorder

shaded area was used to determine the additional amount of dechanneling $\Delta\chi$ at a deeper depth. The procedure is followed through the implanted layer until $\chi_R = \chi_D$. The disorder distribution extracted by this procedure is shown by the open triangles in the lower portion of distribution. The amount of disordered produced by a 200 keV B implant into Si can also be simulated with the Monte Carlo portion of SRIM. A comparison of the SRIM simulation (see Problem 8.5) with the channeling data in Fig. 8.10 shows that there is reasonable agreement between experiment and simulation. In both cases damage is present at the surface and the damage extends to depth of between 7,500 Å (experiment) and 8,000 Å (simulation). The peak in the experimentally measure damage occurs at approximately 4,100 Å while the damage peak from the SRIM simulations occurs at approximately 5,500 Å. The differences in depth distributions are attributed to differences in the stopping power data used.

The analysis of defects by use of backscattering and channeling of MeV ^{4}He ions is a major tool in the study of formation and annealing of amorphous layers in silicon (see Chap. 10). In implanted semiconductors, the thickness of the amorphous layer is obvious, as shown in Fig. 8.8.

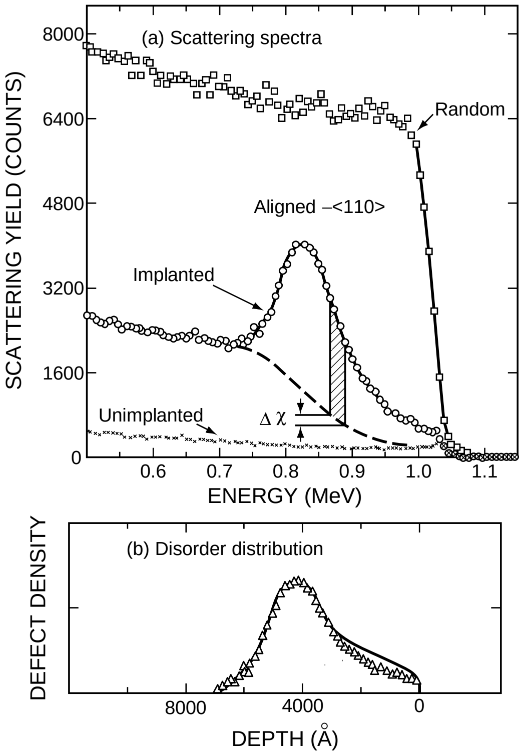

Fig. 8.10. (**a**) The 1.8-MeV He backscattering spectra for random and ⟨110⟩ aligned Si crystal before and after damage by a 5×10^{14} cm^{-2}, 200-keV B implant at –150°C. (**b**) The analyzed depth distribution of the disorder and the deposited energy into atomic collisions normalized to the disorder profile at a depth of 5,500 Å (after Feldman et al. 1982)

References

Chu, W.K., Mayer, J.W., Nicolet, M.-A.: Backscattering Spectrometry. Academic, New York (1978)

Feldman, L.C., Mayer, J.W., Picraux, S.T.: Materials Analysis by Ion Channeling: Submicron Crystallography. Academic, New York (1982)

Lindhard, J.: Channeling of energetic particles in crystals. Mat. Fys. Medd. Dan Vid. Selsk. **34**(14) (1965)

Mayer, J.W., Eriksson, L., Davies, J.A.: Ion Implantation in Semiconductors. Academic, New York (1970)

Nastasi, M., Mayer, J.W., Hirvoenen, J.K.: Ion-Solid Interactions: Fundamentals and Applications. Cambridge University Press, Great Britian (1996)

Problems

8.1 Calculate ψ_1 and ψ_2 for 2 MeV He ions incident on ⟨100⟩ Si where the lattice is $a = 0.543$ nm.

8.2 For 100 eV B along the ⟨100⟩ axis in Si, assume that the electronic stopping dominates in the channel with $\mathrm{d}E/\mathrm{d}x = kE^{1/2}$

(a) Calculate a value for k (see Chap. 6)

(b) Calculate the range and compare to the range where nuclear stopping dominates.

8.3 Channeling occurs not only along strings of atoms in axial directions but also between sheets of atoms that make atomic planes. Which would have a greater critical angle for MeV He?

8.4 Compare the angle ψ_2 for 1 Mev He and B in Si.

8.5 Use the SRIM program to simulate the disordered produced in Si by a 200 keV B implant. Compare the SRIM data with Fig. 8.10.

9 Doping, Diffusion and Defects in Ion-Implanted Si

9.1 Junctions and Transistors

The p–n junction, located at the juncture between p-type and n-type material, is the basic building block for semiconductor devices. At the transition between n- and p-type materials, a potential gradient is formed to separate the regions with high and low electron and hole concentrations.

A piece of Si with joined n-type and p-type regions, each with 10^{16} donors or acceptors, is shown in Fig. 9.1. In thermal equilibrium, the Fermi level, E_F, is constant across the transition from n- to p-type materials. The magnitude of the difference between conduction band edges (i.e., the barrier height eV_0) is given by

$$eV_0 = E_G - (E_C - E_F)_n - (E_F - E_V)_p \tag{9.1}$$

For semiconductors at room temperature ($kT \sim 0.025$ eV) with 10^{16} carriers cm^{-3} and densities of states N_c and N_v equal to $10^{19}\,cm^{-3}$, the values of $(E_c - E_f)_n$ and $(E_f - E_v)_p$ are 0.17 eV. Thus if the band gap, E_g, is 1.0 eV, the potential barrier is 0.66 eV, two-thirds of the band gap.

The electric field is established by the charge on the fixed donors and acceptors located within the potential barrier region, as shown in Fig. 9.2. The barrier region is in effect depleted of carriers, which gives rise to the term *depletion region*. Alternatively, it is called a *space-charge region* because of the charge on the fixed donors and acceptors.

The most important characteristic of the p–n junction is that it permits the passage of electric current in only one direction. When a negative voltage is applied to the n-region, a current begins to flow at a very small voltage (forward biased). In contrast, when a positive voltage is applied to the n-region, there is no current flow (reverse biased). This special current–voltage characteristic of p–n junctions is the basis for other important semiconductor devices such as bipolar transistors and field-effect transistors which consist of two p–n junctions in the vicinity of each other.

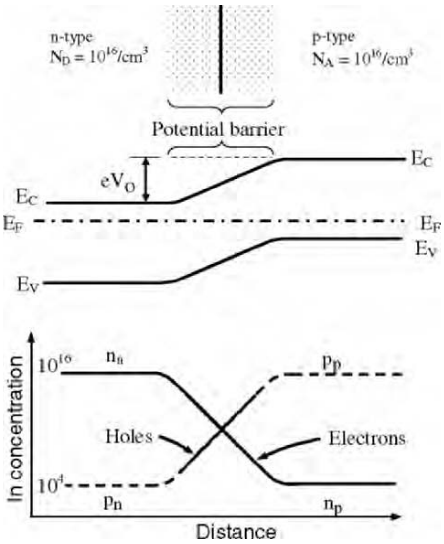

Fig. 9.1. Schematic of a p–n junction with an abrupt change in doping from $N_D = 10^{16}$ donors cm^{-3} to $N_A = 10^{16}$ acceptors cm^{-3} for the symmetrical step junction. The energy level and carrier concentration versus distance are shown for the transition from n- to p-type. The shaded area shows the extent of the depletion region for a junction potential of V_0 volts

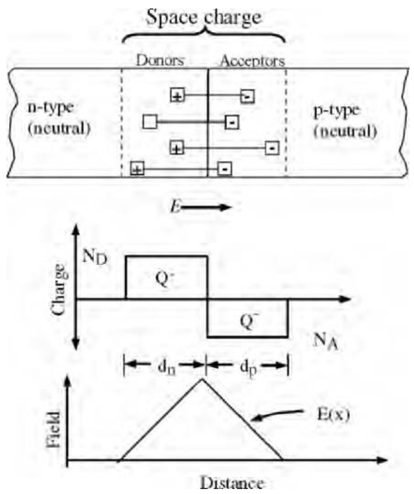

Fig. 9.2. Fixed charge (space charge) and electric field, E, in the depletion region of a symmetric step junction under the conditions that the free carriers are swept out of the depletion region

9.1.1 Bipolar Transistors

A bipolar transistor is a three terminal device which includes the components of emitter (E), base (B) and collector (C). There are two types of bipolar transistors, npn and pnp. The letters refer to the layers of semiconductor materials used to make the transistors. Fig. 9.3a, b shows the schematic illustrations of current flows and the circuit symbols of npn and pnp transistors. The shaded regions in the figure represent two depletion regions formed at the interfaces of emitter/base and base/collector.

In its "off " state, the emitter and base are at the same bias and no current flows through the device. In its "on" state, the emitter/base is forward biased and the base/collector is reverse biased. The reverse bias between base and collector creates a large electric field at the base/collector interface. Forward biasing injects minority carriers from emitter into the narrow base. The carriers entering into the base are immediately swept into the collector by the electric fields. A small current flow into the base controls a much larger current flow into the collector. Therefore, bipolar transistors amplify current. For example, they can be used to amplify the small output current from a logic chip so that it can operate other high-current devices. In many circuits a resistor is used to convert the changing current to a changing voltage so the transistor can be used to amplify voltage.

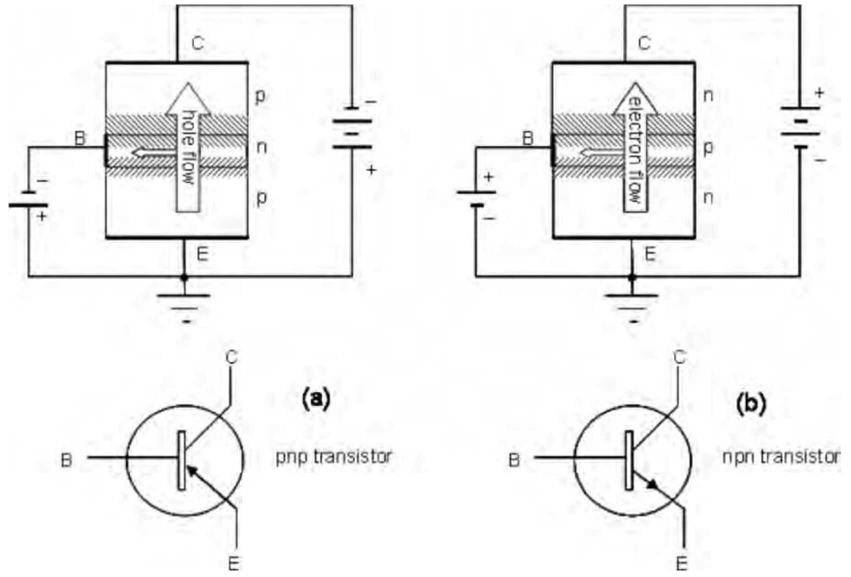

Fig. 9.3. Schematic illustration of current flow of pnp (**a**) and npn (**b**) transistors and their corresponding symbols

A bipolar transistor may be used as a switch (either fully on with maximum current, or fully off with no current) and as an amplifier (always partly on). Bipolar transistors are the quickest devices. However the current flow through the base creates heat. This disadvantage makes bipolar transistors less popular than other devices such as metal oxide semiconductor transistor.

A schematic diagram of the cross section and dopant distributions in a planar npn bipolar junction transistor in Si are shown in Fig. 9.4a, b. The transistor is made by implanting donors at high concentrations, N_D, into the n-type Si to form the emitter, and implanting a lower concentration, N_A, of acceptors deeper into the n-type Si to form the p-type base.

9.1.2 Metal-Oxide-Semiconductor Field-Effect Transistors

A metal-oxide-semiconductor field-effect transistor (MOSFET) is a four terminal device consisting of a gate, source, drain, and substrate. MOSFETs have an oxide layer (SiO_2) between the gate contact and the semiconductor. This insulating gate oxide layer prevents current flow from the semiconductor to the gate.

There are two types of MOSFETs, the n-channel MOSFET (NMOSFET) and the p-channel MOSFET (PMOSFET). Figure 9.5a, b shows a schematic illustration of NMOSFET and PMOSFET with their circuit symbols, respectively. An NMOSFET is fabricated by implanting donors into the source and drain region (forming n-regions) on p-type Si. The n-channel is formed by applying sufficient positive voltage to the gate so that there is an accumulation of electrons (and repulsion of holes) in the region under the oxide, thus defining the n-channel. A PMOSFET has p-type source and drain regions formed by implanting acceptors on n-type Si. The p-channel is formed by applying sufficient negative voltage to the gate to obtain an accumulation of holes (and repulsion of electrons) under the oxide layer, thus defining the p-channel.

The device functions of NMOSFET and PMOSFET are described as follows:

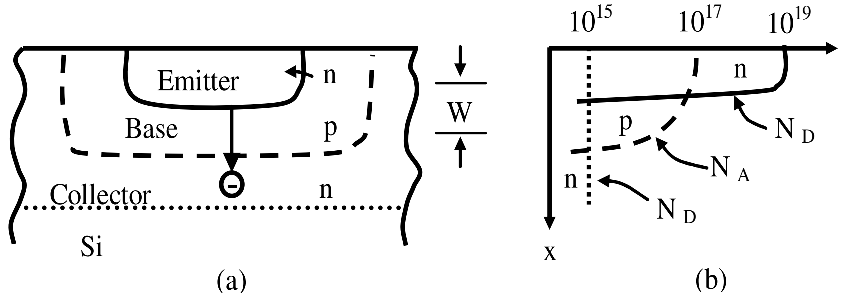

Fig. 9.4. A planar npn bipolar transistor with a base width *W* (**a**) cross section with electrons injected from emitter to base (**b**) dopant concentration profile

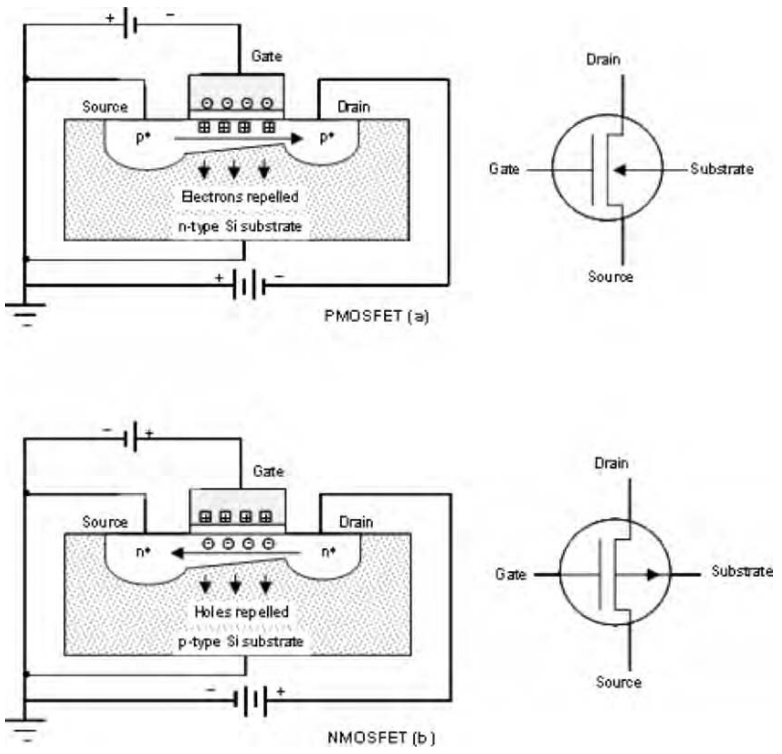

Fig. 9.5. Cross-sections of PMOSFET (**a**) and NMOSFET (**b**) and their corresponding symbols

The voltage applied on the gate induces the n- or p-channels with the accumulation of carriers (electrons for n-channel and holes for p-channel). The bias of source/gate injects the same type carriers into the channels. The bias of gate/drain creates a field that pulls the majority of these carriers into drain. Thus the device is turned "on" with current flowing through the source and drain regions.

We have only considered MOSFET in which a gate voltage, V_G, greater than the "turn on" voltage, V_T, is required for channel conduction. These structures are normally "off" unless a gate voltage is applied until the source-drain current increases. This model of operation is termed *enhancement*. By using ion implantation techniques to introduce dopants into the layer under the gate oxide, one can adjust the turn on or threshold voltage, V_T, and/or can form a channel layer with zero gate voltage. With a channel present at $V_G = 0$, the structures are normally "on" and, by proper voltage polarity on the gate, the source-drain current can be decreased – the *depletion* mode of operation.

The MOSFET is an extremely flexible circuit element because there can be n- and p-channel devices with current that increases or decreases with gate voltage. The capacitance of MOSFET structures can also be used for charge storage. The stored charge can be shifted from one capacitor to an adjacent element by control of the gate voltages.

9.1.3 Complementary Metal Oxide Semiconductor Devices

Complementary metal oxide semiconductor (CMOS) is one dominant type of semiconductor device for microprocessors, memories and specific integrated circuits. CMOS semiconductors use both NMOSFET and PMOSFET transistors to realize logic functions. Since only one of the circuit types is on at any given time, CMOS chips require less power than chips using just one type of transistor. The main advantage of the low power consumption of CMOS is that it allows the logic units to be integrated with a higher density than that of bipolar transistors.

The most important CMOS circuit is the CMOS inverter. It consists of only two transistors – a pair of one n-type and one p-type transistor. Both devices are enhancement-mode MOSFETs, with the threshold voltage of the PMOSFET less than zero and the threshold voltage of the NMOSFET greater than zero. Figure 9.6a–c shows the circuit diagram, the top view and the cross section of the CMOS inverter, respectively.

In a CMOS inverter, the gates of the two transistors are connected together as input terminal and the drains of the two transistors are connected together as output terminal. If the input voltage is positive and higher than the threshold voltage of NMOSFET (logic 1), the PMOSFET is nonconducting and the NMOSFET is conducting. It provides a path from V_{SS} (the ground) to the output. The output is therefore at ground potential (logic 0). Alternatively, a negative input voltage turns the PMOSFET *on* and the NMOSFET *off*. It provides a path from V_{DD} to the output, so that the output voltage is in the high voltage state of V_{DD} (logic 1). Thus the device operates an inverter with an output "1" for an input "0", or an output "0" for an input "1".

Ion implantations are the most critical tools for the fabrication of integrated circuits. We will further discuss the various ion implantation steps in CMOS device fabrication in Chap. 14. As we learned in the chapter on radiation damage (Chap. 7), the penetration of energetic ions into a semiconductor results in the production of damage to the crystal structure. The damage can be sufficiently great so that an amorphous layer is formed (see Chap. 10). High temperature processing (600–1,000°C) is required to anneal the lattice disorder, returning the implanted semiconductor to a single crystal state with a minimum number of lattice defects and ensuring that the implanted dopants are incorporated substitutionally in the semiconductor lattice. The remainder of this chapter will focus on the defects in semiconductor materials and on diffusion of implanted atoms.

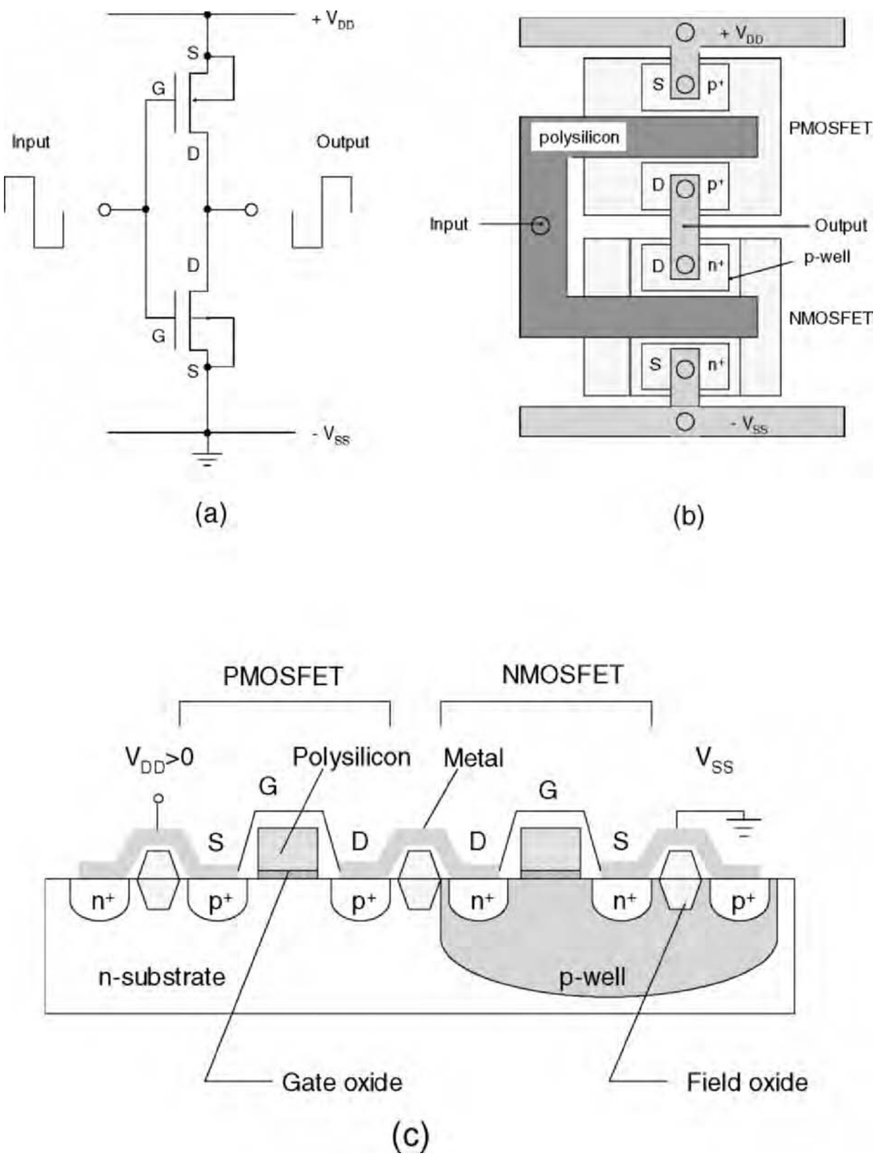

Fig. 9.6. A CMOS inverter (**a**) circuit diagram, (**b**) top view, and (**c**), cross section

9.2 Defects

Ion implantation and subsequent thermal processing will form defects. Defects may be categorized as (1) point defects, (2) line defects, (3) planar defects, and (4) volume defects. Table 9.1 lists examples of these four types of defects, and Fig. 9.7 shows schematically some of the point defects in a two-dimensional simple cubic lattice.

9.2.1 Point Defects

A point defect is a deviation in the periodicity of the lattice arising from a single point. Other defects, such as dislocations and stacking faults, extend over many lattice sites. Point defects may form due to nonequilibrium conditions such as those that occur during crystal growth or during thermal or mechanical processing of the material. Point defects may be categorized as (1) native defects, such as a vacancy, and (2) impurity-related defects due to the introduction of an impurity atom into the lattice. For semiconductors, point defects not only cause structural disturbances but also often introduce electronic states in the band gap. If an attractive potential exists between a native defect and an impurity atom, they may interact and form a defect complex, such as a vacancy-impurity pair.

9.2.2 Native Defects and Shallow Dopants

For Si, there are three types of native defects: the vacancy, the interstitial, and the interstitialcy. The vacancy, V, is an empty lattice site. Depending on the configuration of the unsatisfied bonds due to the missing atom, a vacancy in Si can be either neutral, negatively or positively charged. A vacancy is also referred to as a Schottky defect. A Si atom residing in the interstices of the Si lattice is defined as a self-interstitial. A Frenkel pair is a vacancy-interstitial pair formed when an atom is displaced from a lattice site to an interstitial site. An interstitialcy

Table 9.1. Defects in Semiconductors

Defect type	Examples
Point	vacancies, interstitials, impurity atoms, antisite defects
Line	dislocations
Planar	stacking faults, twins, and grain boundaries
Volume	precipitates and voids

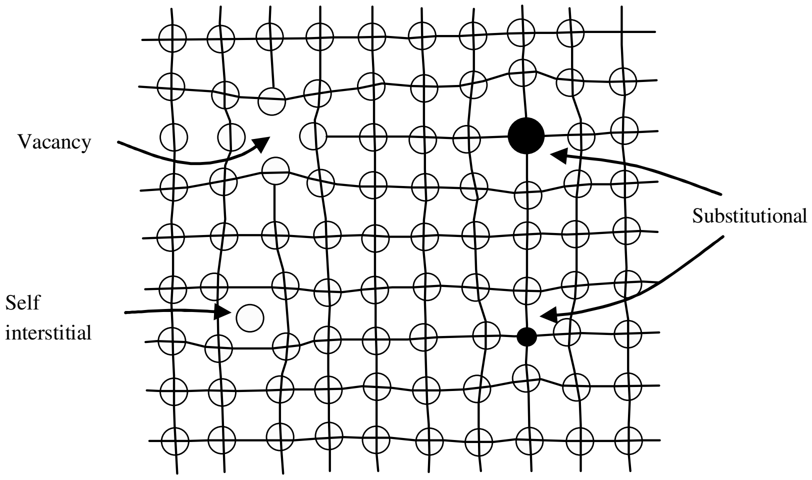

Fig. 9.7. Various points defects in a simple cubic lattice

consists of two atoms in nonsubstitutional positions configured about a single lattice site. Because of the similarity between an interstitial and an interstitialcy, a distinction is generally not made; both are abbreviated as "I" in the literature. When an impurity such as a shallow dopant (e.g., As in Si) occupies a lattice site, it is known as a substitutional defect. Such a defect, when surrounded only by Si atoms on their normal sites, is identified as "A". When a vacancy V forms next to A, it is known as an impurity-vacancy pair, usually referred to as an AV defect. If one of the atoms in the interstitialcy defect is a dopant atom, A, the defect is referred to as an AI defect. If the impurity atom occupies an interstitial site, it is designated as A_i; if the impurity atom occupies a substitutional site, it is designated as A_s.

9.2.3 Deep Level Centers

Shallow dopant impurities have small ionization energies (such as As and P in Si with ionization energies of ~0.04 eV). There are chemical impurities and charged point defects that form deep energy states in semiconductors. The energy levels of these centers in the band gap are usually far away from the band edges; thus they are called deep level centers. Typical deep level impurities are oxygen and metallic elements in Si. A deep level impurity may have several energy levels, with each energy level being either an acceptor state or a donor state. For example, Au in Si has an acceptor state at 0.54 eV between the conduction band edge, E_C, and a donor state 0.35 eV from the valence band edge, E_V (Fig. 9.8). Other than chemical impurities, charged point defects, such as a negatively charged vacancy, V^- in Si, also form deep level states.

A deep center may act either as a trap or as a recombination center, depending on the impurity, temperature, and other doping conditions. Consider a minority

carrier (holes in an n-type semiconductor, for example) captured at an impurity center. The minority carrier stays at the center for a period of time and is then ejected thermally into the band from which it came; this impurity center is known as a trap. Before ejection, if a majority carrier is captured, recombination of the carrier pair takes place and the center is therefore a recombination center.

9.2.4 Line Defects

Line defects in a crystalline material are known as dislocations. Dislocations are formed due to nonequilibrium conditions such as ion implantation and thermal processing. Under equilibrium conditions, there is no requirement for the presence of dislocations or any other defect (except native point defects) in the crystal. An edge dislocation may be viewed also as having an extra half-plane inserted into the crystal (see Fig. 9.9).

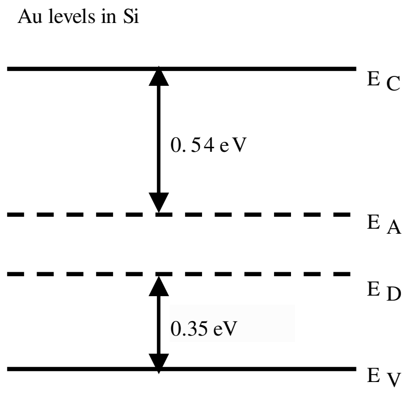

Fig. 9.8. Au in Si has an acceptor state, E_A (~ E_C – 0.54 eV) and a donor state, E_D (~ E_V + 0.35 eV). For strongly p-type Si, the Fermi level, E_F, is below E_D; the donor states are ionized (the electron in the state is given away) and become positively charged. The acceptor state at E_A is not ionized (the state has not received an electron because E_F is far below E_A). For strongly n-type Si, E_F is far above E_A; the acceptor states are ionized (the state has received an electron) and become negatively charged. The Au donor states are not ionized in strongly n-type Si

9.2.5 Planar Defects

Planar defects include grain boundaries, stacking faults, and twins. These defects are formed during ion implantation and thermal and processing. All three types of planar defects are enclosed by a single dislocation or by an array of dislocations separating the faulted area from the normal area or delineating the misorientation between various areas of the semiconductor.

Stacking faults are created during crystal growth processes, such as epitaxial growth and during the annealing of ion-implanted regions. Extrinsic stacking faults also are formed in Si due to oxidation. Silicon self-interstitials are created during oxidation; these interstitials then coalesce to form extrinsic stacking faults. Twins are related to stacking faults and also are formed during crystal growth. A twin fault is therefore formed by inserting a fault plan every other plane in the normal FCC stacking sequence.

9.2.6 Volume Defects

Volume defects include voids and local regions of different phases, such as a precipitate or an amorphous phase. In Si, oxygen precipitation is the most important volume defect. Silicon crystals are grown by either the Czochraski technique or by the float-zone technique. The typical concentration of oxygen in Czochraski Si crystals is about 10–20 ppm (parts per million) or 5×10^{17}–1×10^{18} cm^{-3}. The float-zone technique introduces less oxygen in Si than does the Czochraski technique. Most of the oxygen in the as-grown crystal is atomically

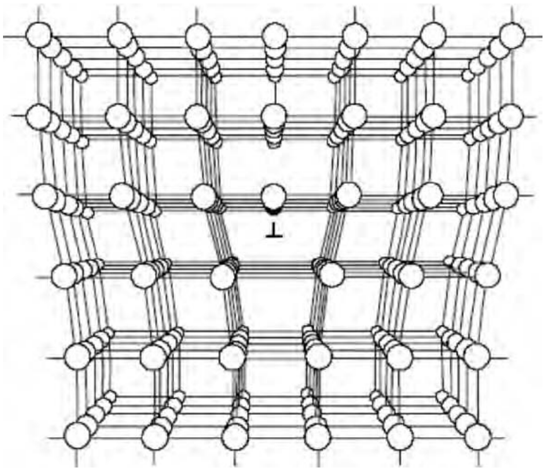

Fig. 9.9. Edge dislocation created by inserting an extra half-plane of atoms

dispersed and occupies interstitial sites. A low temperature annealing at 300 to 500°C causes the interstitial oxygen to move into substitutional sites and become donors.

Another type of volume defect is due to local amorphous regions encountered in ion-implanted semiconductors, especially in the case of low-dose irradiation where local amorphous regions around the ion tracks do not overlap to form a continuous layer. The amorphous phase can be considered to be a structure without long-range order. Figure 1.4 (Chap. 1) shows the schematic atomic arrangement for an amorphous solid and for a crystalline solid. A crystalline solid has long-range atomic order, an amorphous solid has a short-range order, and the nearest neighbor distance for both is nearly the same.

9.3 Fick's First and Second Law of Diffusion

After ion implantation, the defects are annealed at high temperatures, and diffusion of the implanted atoms occurs. Atoms will diffuse from regions of high concentration in a solid to regions of low concentration of atoms in units of atoms cm^{-3}.

The flux of atoms can be expressed in a one-dimensional system as

$$F = -D\frac{\partial C}{\partial x} \tag{9.2}$$

where D is the diffusion coefficient (D has units of $cm^2\,s^{-1}$) and $\partial C/\partial x$ is the concentration gradient. [(9.2) is called Fick's first law.] Note that there is a negative sign in (9.2) and that $\partial C/\partial x$ is negative for a decrease in the concentration with depth; consequently, the flux into the sample has a positive value. The flux equation indicates that atoms diffuse from high-concentration regions to low-concentration regions.

The parameter λ is commonly referred to as the characteristic diffusion length and it increases as $(Dt)^{1/2}$. It signifies the extent of the diffusion.

Consider a volume where the flux of atoms entering is different than the flux of atoms leaving. The change with time of the concentration of diffusing atoms in that volume is given by the gradient of the flux. This can be expressed as

$$\frac{\delta C}{\delta t} = \frac{\delta}{\delta x}\left(D\frac{\delta C}{\delta x}\right) \tag{9.3}$$

This is the so-called continuity equation or Fick's second law, where C, the concentration, is generally a function of position x and time t. For the case where D is constant,

$$\frac{\delta C(x,t)}{\delta t} = D\frac{\delta^2 C}{\delta x^2} \tag{9.4}$$

9.3.1 Diffusion Coefficient

The diffusion coefficient, D, is a strong function of temperature. The temperature dependence arises because some energy (typically a few electron volts, eV) is required for an atom to jump from one atomic position to another. This energy is often called the activation energy, E_A. The diffusion coefficient can be written

$$D = D_0 \exp\left(-\frac{E_A}{kT}\right) \tag{9.5}$$

where D_0 is a pre-exponential parameter with typical values between 10^{-1} and 10^2 cm^2 s^{-1} and values of E_A between 1 and 5 eV, depending on the diffusing species in Si.

9.3.2 Diffusion of Doping Atoms into Si

The diffusion of impurities into Si wafers typically is done in two steps. In the first step, dopants are implanted into the substrate to a relatively shallow depth of a few thousand angstroms. After the impurities have been introduced into the Si substrate, they are diffused deeper into the substrate to provide a suitable impurity distribution in the substrate. The solid solubility and diffusion of dopant atoms in Si are given in the top and bottom, respectively, of Fig. 9.10.

The dopants introduced by the ion implantation step can be redistributed deeper in the substrate to lower the concentrations by a drive-in step. In the drive-in step, the total amount of dopant atoms, Q, remains fixed. The concentration profile due to the drive-in diffusion is given by

$$C(x,t) = \frac{Q}{\sqrt{\pi D t}} \exp\left(-\frac{x^2}{4Dt}\right) \tag{9.6}$$

9.4 Diffusion Mechanisms

For diffusion in a crystalline solid, consider an impurity atom located between the host atoms, Fig. 9.11a. This impurity atom, called an interstitial, can jump from one interstitial site to the next vacant interstitial site. Occasionally, an impurity atom located in a lattice site that is normally occupied by a host atom will jump to

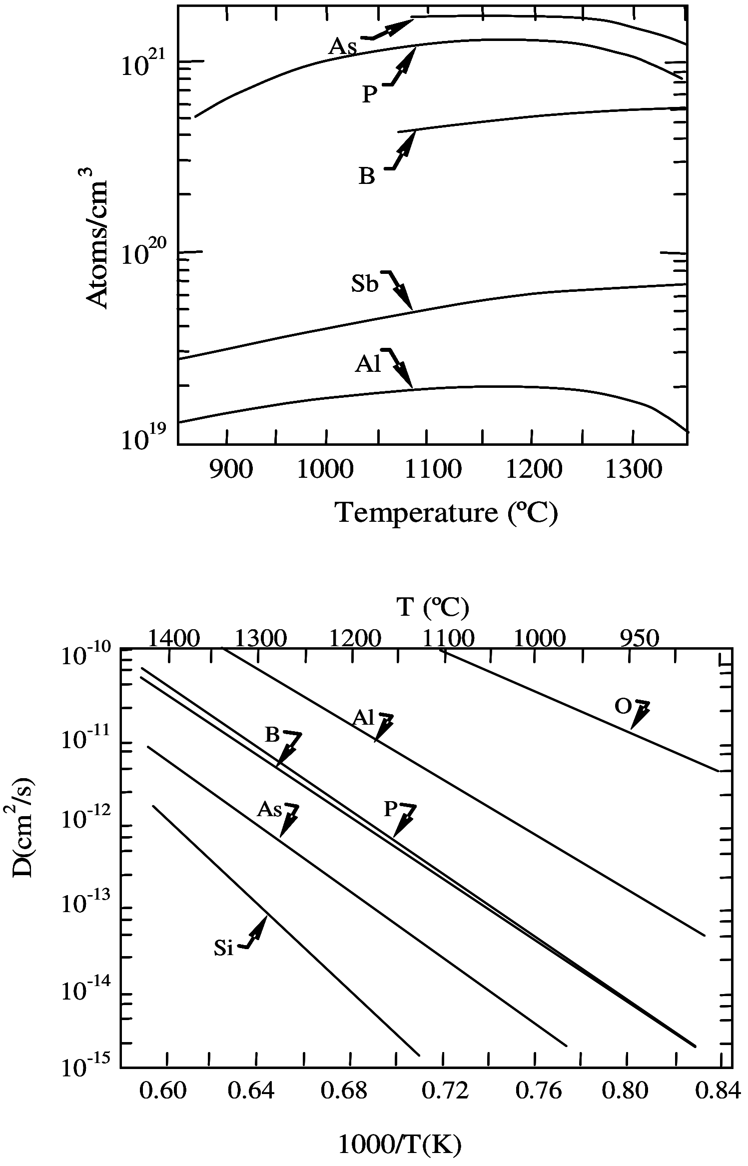

Fig. 9.10. Solid solubility of atoms in Si (*top*); diffusion coefficient of dopant atoms in Si (*bottom*) (after Beadle et al. 1985)

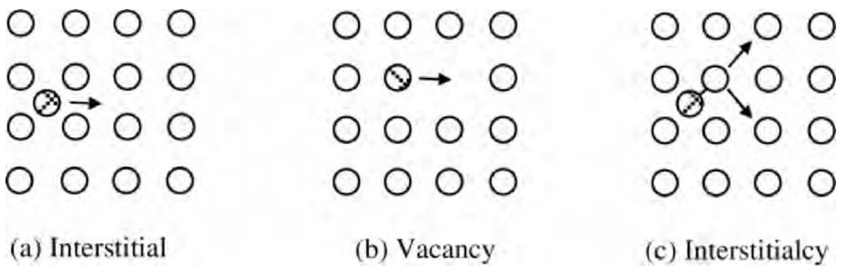

Fig. 9.11. Diffusion mechanisms

a neighboring vacant site, Fig. 9.11b. It is also possible for a substitutional impurity atom to push a neighboring host atom into an adjacent interstitial site and move into the vacant substitutional site thus created; this process is called the *interstitialcy mechanism.*

9.4.1 Interstitial Mechanism

The interstitial sites of a diamond or zinc blend lattice are usually vacant. The probability of an interstitial atom finding an available site to jump into is very high. As it jumps from one site to another, it faces a constriction due to the host atoms (see Fig. 9.11a); the jumping atom needs a little push to squeeze by. This situation is described as having an activation or energy barrier. In this case the barrier is also periodic in the lattice.

9.4.2 Substitutional or Vacancy Mechanism

The jumping of a substitutional atom to a neighboring substitutional site requires a vacancy to be created in the adjacent site, Fig. 9.11b. The probability of such an event is $\exp(-E_f/kT)$, where E_f is the formation energy of a vacancy in the lattice. The movement causes bonds to break and new bonds to be formed after the jump. The energy barrier for this jumping process is E_m (activation energy for migration). The value of $E_m + E_f$ is between 3 and 4 eV (Fair 1981).

9.4.3 Interstitial–Substitutional Mechanism

Many impurities have both an interstitial solubility, N_i, and a substitutional solubility, N_s. These interstitial impurity atoms and substitutional impurity atoms can diffuse independently or interdependently. Usually, N_s is larger than N_i, but substitutional diffusion is much slower than interstitial diffusion. In Si, these two components of diffusion appear to move interdependently. They are related by a

dissociative reaction of a substitutional impurity atom (S) into an interstitial impurity atom (I) and a vacancy (V):

$$S \Leftrightarrow I + V$$

The movement of impurities becomes primarily controlled by the rate of this dissociation.

9.4.4 Interstitialcy and the Kick-Out Mechanism

When the diffusing interstitial atoms have a size comparable to that of the lattice atoms, the interstitialcy mechanism for diffusion may take place. In this case the interstitial impurity atom moves into a host lattice site by pushing a neighboring normal atom into the adjacent interstitial site. This process repeats itself when a self-interstitial atom pushes the substitutionally located impurity atom into an interstitial site.

The kick-out mechanism is rather similar to the interstitialcy mechanism. In this case, a host self-interstitial atom diffuses around the lattice. When it reaches a substitutional impurity atom, the self-interstitial pushes the impurity atom into an adjacent interstitial site. The interstitial impurity then diffuses interstitially until it reverts back to a host lattice site by displacing a host atom. It is experimentally difficult to distinguish the kick-out mechanism from the interstitialcy mechanism. The generally accepted view is that the interstitial impurity atoms may tend to diffuse longer distances before returning to the normal lattice sites for the kick-out mechanism, whereas the impurity atoms tend to diffuse interstitially for a relatively short distance before going into the normal lattice sites for the interstitialcy mechanism.

9.5 Transient Enhanced Diffusion of Boron

Integrated circuit technology requires a reduction in device dimensions. The junction depth, where the donor and acceptor concentrations are equal, is set between 10 and 30 nm. These shallow junction requirements restrict ion implantation technology – not on the implantation procedures themselves, but on the subsequent diffusion of the implanted species during thermal annealing.

Figure 9.12 shows boron depth profiles for a B dose of 10^{15} cm^{-2} at an implantation energy of 0.5 keV and thermal heat treatment at 1,050°C for 10 s. The boron depth profile for 0.5 keV implants is consistent with shallow junction requirements of junction depths of ~20 nm. After thermal annealing, the boron profile has spread to depths of 100 nm or more – well beyond the shallow junction

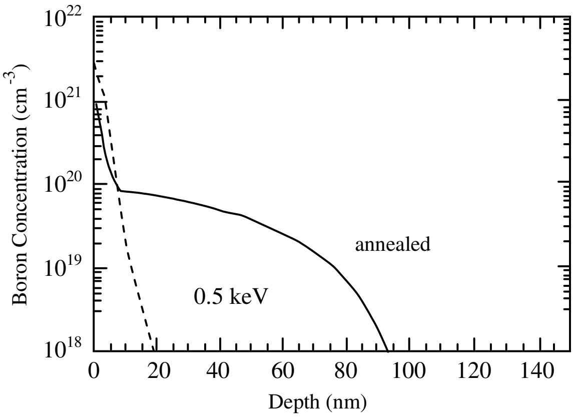

Fig. 9.12. Profiles of boron concentrations for a dose of 10^{15} B cm^{-2} (**a**) as-implanted and (**b**) as-annealed at 1,050°C for 10 s (Ziegler 2000)

limits. The diffusion length, $(Dt)^{1/2}$, is orders of magnitude greater than that predicted from $D \sim 10^{-13}$ cm^{-2} s^{-1} at 1,050°C.

Silicon self-interstitials emitted from the ion implantation damages interact with the boron atoms to form B–Si pairs that diffuse very fast until they are trapped or dissociated. Enhancement of boron diffusion can be up to 10^7 times the normal diffusion value during postimplant annealing. Observation of transient enhanced diffusion (TED) of boron, the mechanisms of TED, and experimental results have been reviewed recently by Jain et al. (2002) and Shao et al. (2003). For light ions and low doses, ion implantation produces Frenkel pairs of vacancies and interstitials. The diffusing interstitials may encounter and kick out substitutional boron atoms during the first moment of annealing, leading to ultra-fast boron-enhanced diffusion. When ion implantation doses are high enough, rod-like extended defects appear. These defects, called {311} defects, precipitate on the {311} planes along ⟨100⟩ directions (Eaglesham et al.). With low implantation doses and hence low damage, the intrinsic TED is driven by the annealing of small clusters, while {311} defects contribute to TED with higher dose implantation.

Most of the implantation damage is removed during the early stage of annealing via point defect recombination, leaving excess interstitials approximately equal in number to the implanted dose. These interstitials then coalesce into extended defects. After a short annealing, these extended defects are primarily {311} defects. Transmission electron measurements of the total interstitial density in {311} defects as a function of annealing time show that the emission of interstitials from {311} defects is the main source of interstitials responsible for TED after annealing of small clusters (Eaglesham et al.).

Nearby vacancies and interstitials recombine either dynamically during irradiation or subsequently during postimplant annealing. Extra atoms corresponding to the implant dose at end-of-range defect positions are responsible for TED. However, since the momentum transfer from an incident ion to a target atom is in the forward

direction, the depth profile of interstitials would naturally be slightly deeper than that of the vacancies. SRIM simulations of 50 keV or 500 keV Si implanted into Si reveals the formation of a net vacancy-rich region with a depth of about half of the Si projected range. The average separation between vacancy locations and interstitial locations increases when the implantation energy increases.

The implantation of MeV Si ions into a Si substrate can also suppress boron-enhanced diffusion normally associated with a high boron concentration layer (Shao et al. 2003). Junction depths of 20 nm were achieved in samples implanted with 0.5 keV B ion at a dose of 10^{15} cm^{-2} following a 1,000°C thermal anneal.

9.6 Irradiation-Enhanced Diffusion

Ion irradiation is quite efficient in forming vacancy-interstitial pairs, as shown in Chap. 7 and in the simulation in the previous sections. The atomic displacements resulting from energetic recoiling atoms can be highly concentrated into small, localized regions containing large concentrations of defects well in excess of the equilibrium value. If the defects are produced at temperatures where they are mobile and can, in part, anneal out, the balance between the rate formation and the rate of annihilation leads to a steady state of excess concentration of defects. Since the atomic diffusivity is proportional to the defect concentration, an excess concentration of defects leads to an enhancement in the diffusion process.

Enhanced diffusion has been found in Si. It is featured in alloys. Atomic motion in most metals and solid-solution alloys usually occurs by the interchange between atoms and neighboring vacant sites. For such a diffusion process, the atomic diffusion coefficient is given by

$$D = \Gamma d^2/6 \tag{9.7}$$

(Shewmon 1963), where Γ is the atomic jump frequency for uncorrelated jumps, and d is the atomic jump distance. For diffusion driven by the vacancy mechanism, Γ is given by

$$\Gamma = f_{\mathrm{v}} C_{\mathrm{v}} \Gamma_{\mathrm{v}} \tag{9.8}$$

where C_{v} is the vacancy concentration, Γ_{v} is the vacancy jump frequency, which is proportional to $\exp -E_{\mathrm{m}}^{\mathrm{v}}/k_{\mathrm{B}}T$, where $E_{\mathrm{m}}^{\mathrm{v}}$ is the vacancy migration energy, and f_{v} is a correlation factor (which is nearly unity).

The vacancy diffusion coefficient can be described by an expression similar to the atomic diffusion coefficient,

$$D_v = \Gamma_v d^2/6 \tag{9.9}$$

Substituting (9.9) and (9.8) in (9.7) allows us to express the vacancy-driven atomic diffusion coefficient as

$$D = f_v C_v D_v \tag{9.10}$$

From (9.10) we see that an enhancement in the vacancy concentration level leads directly to an enhancement in the atomic diffusivity.

In addition to a vacancy-driven process, diffusion under irradiation may also be enhanced by the formation and diffusion of other point defects, such as self-interstitials, divacancies, and other defect aggregates, which are not present under equilibrium conditions. A general statement for the atomic diffusion coefficient can be written in terms of the various point defects as

$$D = f_v D_v C_v + f_i D_i C_i + f_{2v} D_{2v} C_{2v} + \cdots \tag{9.11}$$

where C_i and C_{2v} are the concentrations of interstitials and divacancies, respectively, and D_i and D_{2v} are the corresponding diffusion coefficients. From (9.11) we see that an irradiation-induced enhancement in the vacancy, interstitial, or divacancy concentration will result in a corresponding increase in *D*.

References

Beadle, W.E., Tsai, J.C.C., Plummer, R.D. (eds.): Quick Reference Manual for Silicon Integrated Circuit Technology. Wiley, New York (1985)

Eaglesham, D.J., Stolk, P.A., Gossman, H.-J., Poate, J.M.: Ion implantation and transient b diffusion in Si: the source of the interstitials. Appl. Phys. Lett. **65**, 2304–2307 (1994)

Fair, R.B.: Concentration profiles of diffused dopants in silicon. In: Wang, F.F.Y. (ed.) Impurity Doping. North-Holland, Amsterdam (1981)

Jain, S.C., Schenmaker, W., Lindsay, R., Stak, P.A., Decoutere, S., Willander, M., Maes, H.E.: Transient enhanced diffusion of boron in Si, Applied Physics Reviews. J. Appl. Phys. **91**, 8919–8949 (2002)

Shewmon, P.G.: Diffusion in Solids. McGraw-Hill, New York (1963)

Shao, L., Liu, J., Chen, Q.Y., Chu, W.K.: Boron diffusion in silicon: the anomalies and control by point defect engineering. Mater. Sci. Eng. R, **42**, 65–114 (2003)

Ziegler, J.F. (ed.): Ion Implantation – Science and Technology. Ion Implantation Technology Co., Edgewater, MD (2000)

Problems

9.1 What is the value of the diffusion length $\lambda = (4Dt)^{1/2}$ for Boron in Si annealed at 1,000°C for 10 s? Compare with the B profile shown in Fig. 9.12.

9.2 What is the value in eV for the activation energy, E_A, when the diffusion values change by a factor of 10 for a value of 1,000/T of 0.65 and 0.70.

9.3 Consider a drive in diffusion step for implanted As into Si. The As dose is 1×10^{14} As cm^{-2} and the drive temperature is 1,000°C
(a) How much time is required to reduce the surface concentration to ½ of its initial value?
(b) What will the value of the diffusion length be?

9.4 What is the atomic jump frequency for Si self-diffusion at 1,000°C assuming that the atomic jump distance is 0.235 nm?

9.5 Calculate the activation energy for Si self-diffusion assuming $D_0 = 1.5 \times 10^3$ cm^{-2} s^{-1}.

9.6 During ion implantation in Si, the vacancy concentration can be very high. Using SRIM, calculate the vacancy concentration at the damage peak for 40 keV B implanted to a dose of 1×10^{14} B cm^{-2}. The sample will be heated to 1,000°C for 10 s to activate the B. What enhancement is expected in the diffusivity due to radiation-enhanced diffusion?

10 Crystallization and Regrowth of Amorphous Si

10.1 Introduction

During ion implantation, each ion produces a region of disorder around the ion track. As the implantation dose increases, the disorder increases until all the atoms have been displaced and an amorphous layer is produced over a depth R_p. The buildup and saturation of disorder are shown in Fig. 10.1 for 40 keV phosphorus ions incident on Si. In this example, about 4×10^{14} phosphorus ions cm^{-2} are required to form an amorphous layer. Except for low doses or implantation with light ions, we can anticipate that an amorphous layer is formed during the implantation process. This assumes that no recovery of lattice order occurs around the ion track.

Amorphous regions also can be formed by light ion implantation at suitable target temperatures and doses. For light ion implantation the defect density in the single collision cascade is quite low, and amorphization occurs when the material accumulates enough damage that it reaches a critical threshold in the defect density (Rimini 1995). In general, for light ion amorphization, cascade overlap is required and the layer becomes amorphous when the free energy of the cascade-induced defect-rich region equals the free energy of the amorphous phase.

In terms of energy deposition, it has been found that amorphous formation requires an energy deposition of 6×10^{23} keV cm^{-3} at low temperature and low energy. The deposited energy for a given implant is given by $\phi\nu/R_p$, where ϕ is the dose and ν is the damage energy (see Chap. 7, Sects. 4 and 5). In the case of a B implant at low energy with $dE/dx|_n \sim 0.6$ eV nm^{-1}, a fluence of 1.6×10^{15} cm^{-2} is required for amorphization. These estimates are valid at sufficiently low temperatures where defect mobility is low and therefore defect recombination is limited. For any ion, the threshold dose for amorphization increases with increasing target temperature up to a critical value, above which amorphization does not occur. The critical temperature depends on the ion mass and energy, i.e., on the energy density deposited into nuclear collisions. Experimental results are shown in Fig. 10.2.

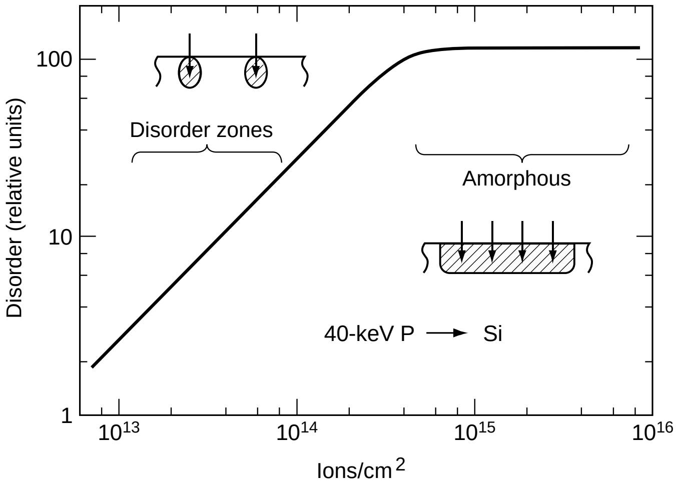

Fig. 10.1. Schematic of disorder build up as a function of ion dose for 40 keV phosphorous ions incident on Si (from Mayer et al. 1970)

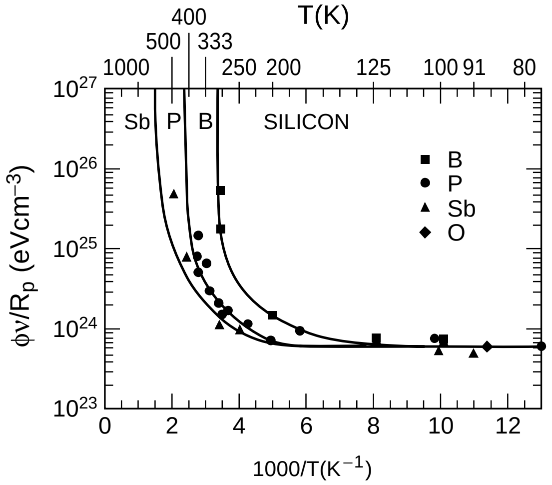

Fig. 10.2. Amorphization dose as a function of $1/T$ for several species implanted in Si at low energy (Rimini 1995)

This figure shows, for ions of various mass implanted at different temperatures, the energy density that must be deposited per unit volume through nuclear collision processes to produce a continuous amorphous layer. At low temperatures

the energy density for amorphization is nearly independent of ion mass and temperature. For a light ion, such as B implanted at room temperature or higher, a continuous amorphous layer never is formed. Qualitatively, for heavy ions, the temperature dependence of the threshold dose can be visualized by assuming that a cylindrical amorphous track is instantaneously formed by the passage of a single ion, and that the radius of the track is reduced through annealing in proportion to the sample temperature. Therefore, as the sample temperature is increased, larger doses are needed to ensure track overlap and complete amorphization. In the case of implantation with light ions, a track of lattice-damaged material is formed and, as the temperature of the samples is increased, less and less of the lattice damage is retained. At sufficiently high temperatures the defect density never builds to a value high enough to produce a transformation to the amorphous phase. The real picture probably is much more complex than this simple description, due to the variety of mobile species that can interact among themselves or with pre-existing damage.

10.2 Epitaxial Growth of Implanted Amorphous Si

By use of self-ion implantation (i.e., Si ions implanted into ⟨100⟩ oriented Si) an amorphous layer several 100 nm thick can be formed on a single-crystal substrate. When the sample is annealed in a furnace at a fixed temperature of approximately half the melting temperature of Si (about 550°C), the amorphous layer reorders on the underlying single-crystal substrate. As shown in Fig. 10.3, the thickness of the reordered layer increases linearly in time, thus indicating a constant growth velocity. The velocity is about 10^{-8} cm s^{-1}. at half the melting-point temperature, and it increases rapidly with increasing temperature. In the reordering process, the amorphous material takes on the crystal structure of the underlying crystalline Si and the reordering grows from the amorphous/crystal interface, growing towards the surface, a process know as *epitaxial growth*. The epitaxial reordering process that takes place at 550°C is called *solid-phase epitaxy* because it occurs at temperatures well below the melt temperature; this is in contrast to *liquid-phase epitaxy*, where growth occurs from the melt.

The simplest description of epitaxial growth is represented by *homoepitaxy*, in which one grows a crystal layer on a substrate of the same composition. A common example is the growth of Si epitaxial layers of controlled thickness and impurity doping on silicon wafers cut from bulk-doped ingots. It is not necessary to deposit a Si over-layer in order to study epitaxial growth. One may also start with a single crystal, make an amorphous layer several thousand angstroms thick by implanting ions into the substrate, and then study the epitaxial regrowth of the amorphous film on the underlying crystal matrix. Implantation produces an internal interface, which resides between the amorphous layer and the underlying crystal substrate. This internal interface is not subject to the same contamination that is commonly encountered in deposition processes, thus it provides an ideal system for regrowth studies (Lau et al. 1980).

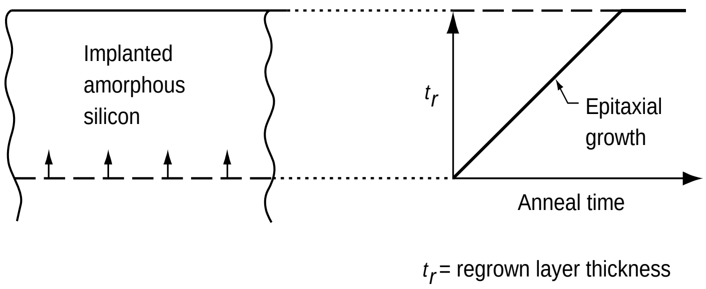

Fig. 10.3. Solid-phase epitaxial regrowth versus anneal time for an amorphous-implanted layer on (100) oriented single crystalline Si

The driving force for the epitaxial growth is the lower free energy of the single crystal relative to the amorphous layer. Crystallization of Si by way of solid-phase epitaxy readily occurs at temperatures equal to or greater than 550°C. The combination of Rutherford backscattering and channeling measurements, which have a depth resolution of 20 nm or better, allows measurements of growth kinetics at submicron depths. The decrease in the yield of backscattered particles at the transition from the amorphous region to the crystal substrate allows a clear identification of the growth interface, as shown in Fig. 10.4.

The scattering yield from the amorphous region is equal to the nonaligned yield from an undamaged crystal substrate. At the transition from the amorphous layer to the crystal substrate there is a decrease in the scattering yield as the beam undergoes channeling in the underlying crystalline substrate (Feldman et al. 1982). The scattering yield does not drop to the minimum yield values (~4%), because some fraction of the beam will be scattered in the amorphous layer to angles greater than the channeling critical angle. The amount of multiple scattering depends on the thickness of the amorphous layer, and hence the aligned yield in the crystal substrate increases as the layer's thickness increases.

The series of spectra presented in Fig. 10.4 shows the reduction in thickness of the amorphous layer as a function of anneal time for a ⟨100⟩ Si sample held at 550°C. This data demonstrates that the regrowth originates at the interface between the amorphous layer and the underlying single crystalline Si and proceeds to the surface. The interface on ⟨100⟩ Si shifts to the surface linearly with time, indicating a uniform regrowth velocity.

Channeling measurements have been used to study the epitaxial regrowth of Ge and Si crystals amorphized by ion implantation for a variety of crystal orientations (Csepregi et al. 1977). These studies have shown that, with the exception of ⟨111⟩ orientated Si crystals and samples cut within 16° of the ⟨111⟩ direction, the amorphous/crystal interface moves with a constant velocity toward the surface (at a fixed annealing temperature) and maintains a laterally uniform front.

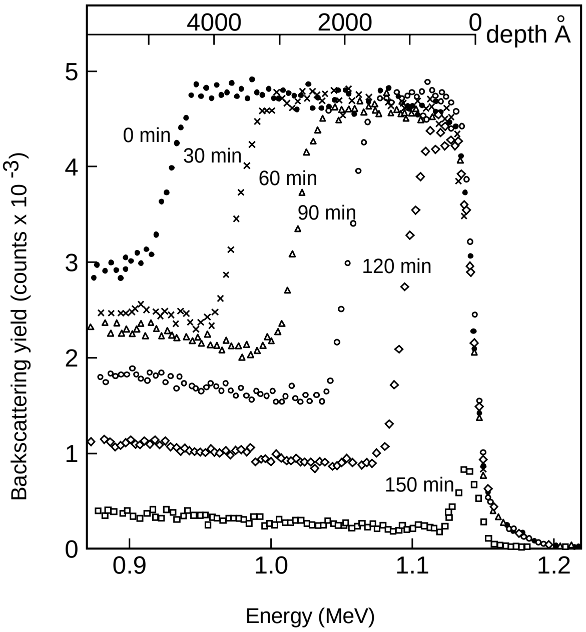

Fig. 10.4. Aligned spectra for 2 MeV He ions incident on Si samples implanted at liquid nitrogen temperature, preannealed at 400°C for 60 min and annealed at 550°C. The depth scale is calculated assuming the bulk density of Si (after Csepregi et al. 1976)

Measurements of the growth velocity as a function of temperature indicate that the growth process is thermally activated, with an activation energy of about 2.7 eV for Si and 2.0 eV for Ge. The Arrhenius plot of regrowth rate versus $1/T$ (Fig. 10.5) shows that the rate is strongly dependent on the orientation of the underlying crystal substrate, and that the same activation energy (solid lines) describes the growth for the different orientations. For ⟨111⟩ oriented Si crystals, the initial growth rate over the first 1,000 Å of regrowth is plotted.

Measurements of the growth velocity, v_g of the crystal-amorphous interface are shown in Fig. 10.6. The measured velocities extend over nearly ten orders of magnitude and can be characterized by a single-activation energy, E_A = 2.76 eV, (Olson and Roth 1988) so that

$$v_g = v_0 \exp\left(-\frac{E_A}{kT}\right) \tag{10.1}$$

where the pre-exponential factor $v_0 = 3.68 \times 10^8$ cm s^{-1}. The activation energy measured for the epitaxial regrowth process is about half the value that is observed

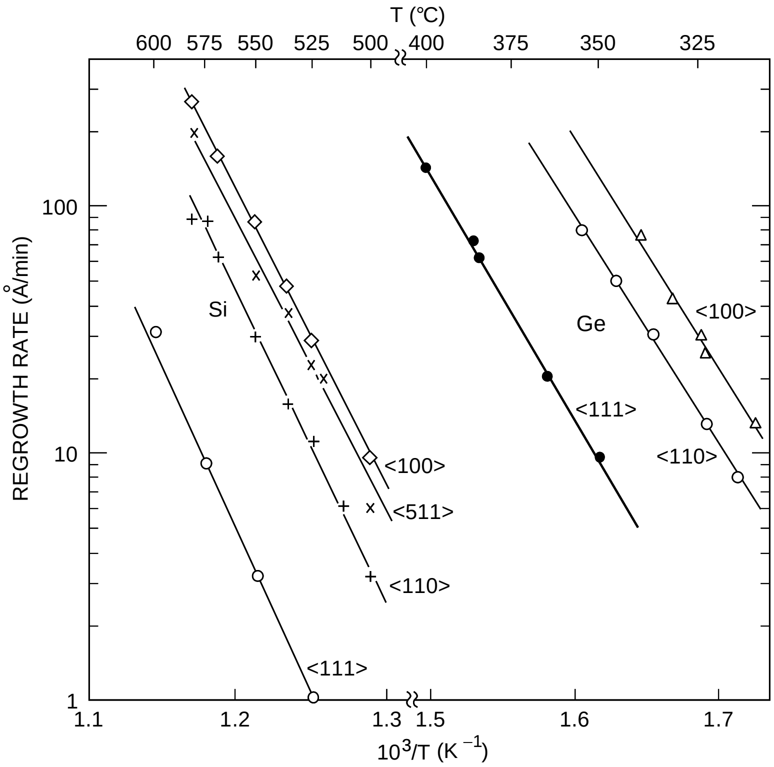

Fig. 10.5. Regrowth rate versus $10^3/T$ (K) for different substrate orientations of amorphous-implanted Si and Ge (from Lau et al. 1980)

in diffusion of dopants in Si. Consequently, regrowth of implanted amorphous layers can be accomplished on time scales that are relatively short compared to those required for appreciable dopant diffusion.

During the epitaxial growth process, implanted dopants move onto substitutional lattice sites as the interface between the amorphous and crystalline region sweeps by their locations. Since the time for regrowth is much shorter that the time for significant dopant diffusion, the dopants are effectively frozen in the lattice at low regrowth temperatures, and substitutional concentrations of group III and V dopants can be increased to exceed the equilibrium solubility limit. A second annealing treatment at high temperatures of 900 or 1,000°C (carried out to remove residual defects in the regrown layer) will allow the dopants to diffuse. After this high-temperature process, the substitutional concentration of dopants is reduced to the equilibrium solubility concentration value. The excess concentration of implanted ions form nonsubstitutional precipitates or clusters.

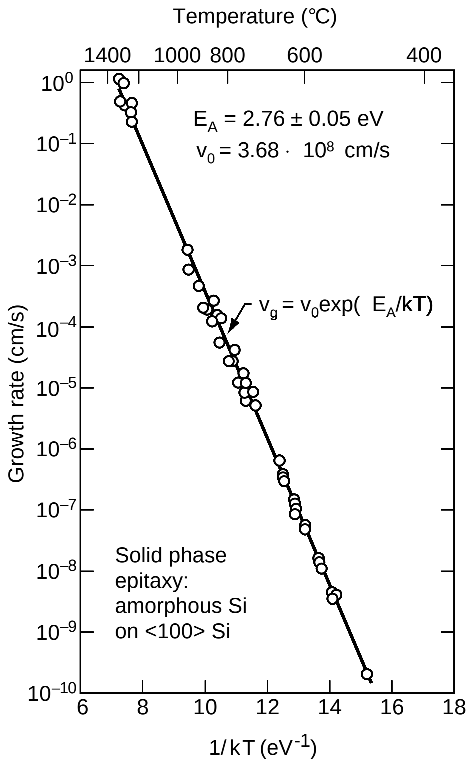

Fig. 10.6. Growth rate versus $1/kT$ for solid-phase epitaxial regrowth of implanted amorphous Si on ⟨100⟩ Si (from Olson and Roth 1988)

The presence of high concentrations of implanted dopants influences the epitaxial growth rate. As shown in Fig. 10.7, concentrations of phosphorus at levels greater than 0.1 atomic percent (5×10^{19} cm^3) cause an increase in the growth rate. This increase is similar to the increase in the diffusion coefficient of dopants, which is attributed to an increase in the vacancy concentration in heavily doped Si, where the Fermi level is near the conduction or valence-band edges. The concentration of vacancies in Si depends on the charge state of the vacancy. The neutral vacancy concentration $[V^x]$ (Mayer and Lau 1990) is given by

$$[V^x] = N \exp\left(\frac{S_v^f}{k}\right) \exp\left(\frac{-H_v^f}{kT}\right) \tag{10.2}$$

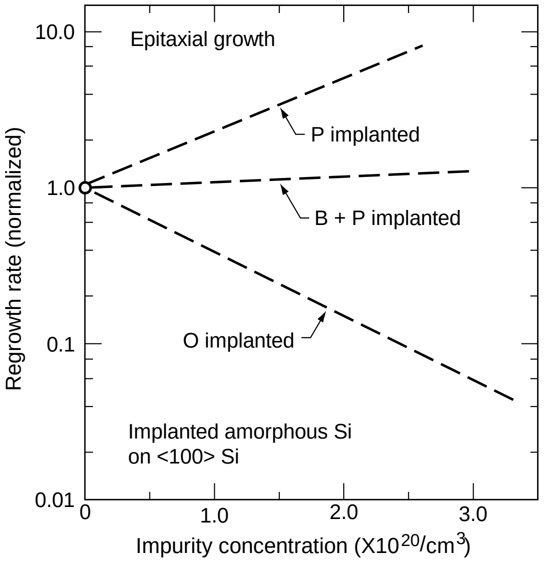

Fig. 10.7. Growth Rate versus impurity concentration for epitaxial regrowth of implanted amorphous Si on ⟨100⟩ Si (Csepregi et al. 1977; Kennedy et al. 1977)

A square bracket notation indicates concentrations. The equilibrium concentration of neutral vacancies in Si is independent of the position of the Fermi level, and so there is no reference to the Fermi energy in (10.2). For Si, $H_v^f \cong 3.6\,\text{eV}$ for a neutral vacancy and the term $S_v^f \cong 1.1K$, which gives the first expeditional term a value of 3, and $N = 5.0 \times 10^{22}\ \text{cm}^{-3}$ (the concentration of Si lattice sites),

$$\begin{aligned}[V^x] &= 5.0 \times 10^{22} \times 3 \times e^{-3.6/kT} = 1.5 \times 10^{23} e^{-3.6/kT} \\ &= 14\,\text{cm}^{-3} \quad \text{at } 823K(550°\text{C})\end{aligned} \tag{10.3}$$

There is a significant difference between the defects (vacancies and interstitials) in semiconductors and those in metals; that is, defects in a semiconductor can be charged electrically, whereas defects in a metal are considered neutral. Since they can be charged (or ionized), the concentration of these defects becomes a function of the Fermi level position in the semiconductor. Consider the charged states of vacancies in Si as an example. It is generally accepted that the single vacancy in Si can have four charge states (Van Vechten 1980): V^+, V^x, V^-, and $V^=$, where + refers to a donor state, x a neutral species, and – an acceptor state (= refers to a doubly charged acceptor state). Figure 10.8 shows the energy levels of the charged vacancies in the Si band gap as a function

of temperature. These energy levels are estimated values but are sufficient for demonstration purposes.

The concentration of charged vacancies is governed by Fermi–Dirac statistics and is given (using V^- as an example) by

$$[V^-] = \frac{[V_T]}{1 + e^{(E^- - E_F)/kT}} \tag{10.4}$$

where E_F is the Fermi level, E^- is the energy level of the acceptor state vacancy, and $[V_T]$ is the total vacancy concentration:

$$[V_T] = [V^x] + [V^-] + [V^=] + [V^+] \tag{10.5}$$

After some algebraic manipulation of (10.4) and (10.5) we find that

$$[V^-] = [V^x]\exp[(E_F - E^-)/kT] \tag{10.6}$$

and similarly,

$$[V^+] = [V^x]\exp[(E^+ - E_F)/kT] \tag{10.7}$$

Upon examining (10.6), we find that the concentration $[V^-]$ is large compared to $[V^x]$ only when $(E_F - E^-) >> kT$ and positive. This means that $[V^-]$ is significant when the Si sample is strongly n-type (i.e., E_F is located far above E^-). As the Si sample becomes less n-type and E_F is far below E^-, $[V^-]$ decreases accordingly. For p-type samples where E_F is far below E^-, $[V^-]$ is negligibly small compared to $[V^x]$.

As an example of (10.6), consider Fig. 10.7 where the amorphous Si regrowth rate is enhanced by implanted P. Taking the P concentration as 2.5×10^{20} cm^{-3} and 550°C (823 K) as the regrowth temperature, we find that the donor density is equal to the density of states in the conduction band (Mayer and Lau), which locates E_F at E_C.

Referring to Fig 10.8, at 823 K, the band gap (see the energy of the conduction band, E_c) of Si is reduced from 1.15 eV at 300 K to 0.91 (Van Vechten 1980). The energy level of E^- tracks the band gap and is located at 0.37 eV + E_v at 823 K. Therefore, the concentration $[V^-]$ is given by (10.6).

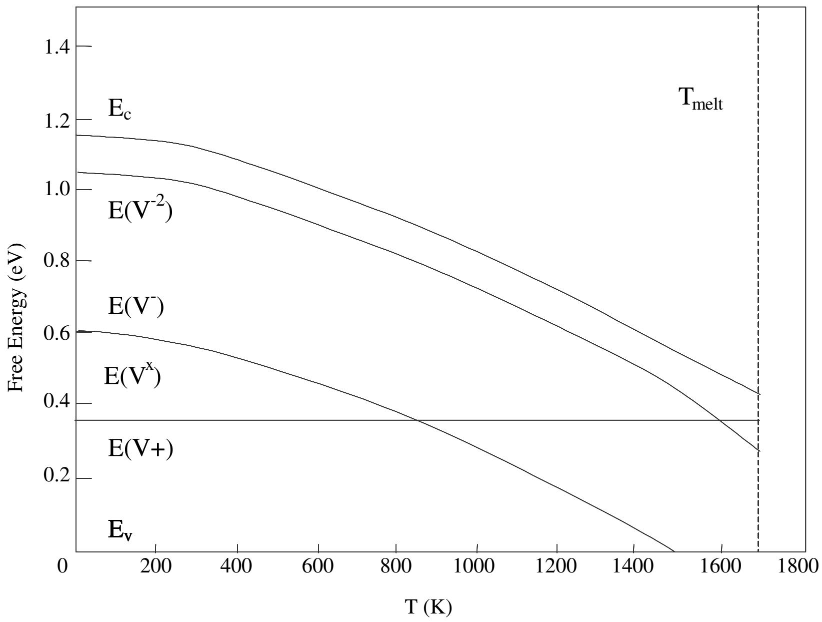

Fig. 10.8. Variations of the donor and acceptor ionization levels of the single vacancy in Si as a function of temperature (from Van Vechten 1980)

$$
\begin{aligned}
[V^-] &= [V^x]\exp\left(\frac{E_F - E^-}{kT}\right) = [V^x]\exp\left(\frac{E_C - 0.37 - E_V}{kT}\right) \\
&= [V^x]\exp\left(\frac{E_G - 0.37}{kT}\right) = [V^x]\exp\left(\frac{0.54}{0.07}\right) \\
&= 2022[V^x]
\end{aligned}
$$

From the above example, $[V^-]$ is about 2,000 times larger than $[V^x]$ at 823 K, which explains in part the enhanced regrowth that amorphous Si experiences when it is doped with P. As one would anticipate, the growth rate is not increased by implantation of both B and P at equal concentrations. In this case, the implanted layer has equal concentrations of donors and acceptors, and the Fermi level is near the center of the energy gap.

Implantation of oxygen ions tends to decrease the growth rate. If a sufficiently high concentration of oxygen is implanted, the growth rate will be slowed enough so that the remaining amorphous material recrystallizes in the form of a polycrystalline layer. The electrical characteristics of this polycrystalline layer are markedly inferior to those of the epitaxial regrown layer.

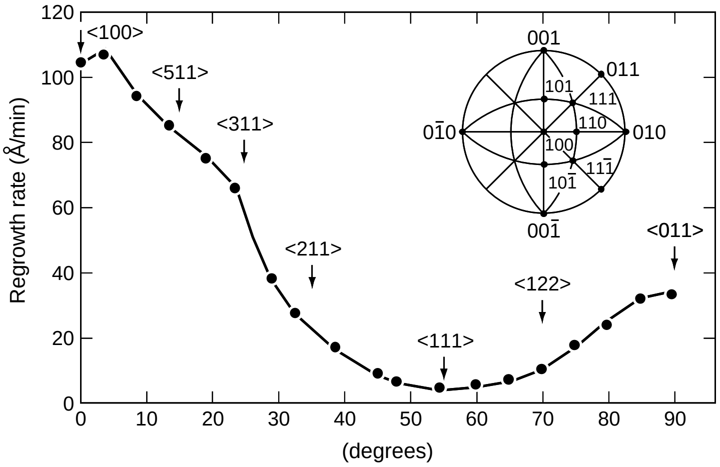

Fig. 10.9. Regrowth rate versus orientation of the Si substrate for implanted amorphous Si annealed at 550°C (Csepregi et al. 1978)

The regrowth rate is also strongly dependent on the orientation of the Si substrate (Csepregi et al. 1978). Figure 10.9 shows regrowth velocities on single-crystal substrates at different orientations. Samples with the ⟨111⟩ direction perpendicular to the surface have the slowest growth rate, while ⟨100⟩ samples have the fastest. This orientation dependence has been explained (Spaepen and Turnbull 1982) by crystallization proceeding along ledges on the densely packed {111} interfacial planes. The growth velocity is maximized when the crystallographic planes containing the ledges are perpendicular to the surface. It decreases when the ledges are inclined to the surface.

10.3 Ion Beam-Induced Enhanced Crystallization

Studies on ion beam-induced epitaxial crystallization are performed by heating a pre-existing amorphous layer (α-layer) that is interfaced to a single-crystal substrate at a fixed temperature and by irradiating it with ion beams at low current densities in order to avoid further heating. Here we follow the description given by Rimini (1995). The ion energies are chosen such that the projected range of the irradiating ions is well beyond the original c–α interface. This allows one to discriminate between damage clustering, which is typically produced at the end of the ion's range, and effects due to the interaction of point defects created by the ion with an α-layer. Under such conditions a large enhancement in the crystallization kinetics is observed. It is possible to regrow the crystalline phase at

temperatures as low as 250°C at a rate of 0.007 nm s^{-1}. with an irradiation of 600 keV Kr at a dose rate of 1×10^{12} Kr cm^{-2} s^{-1}. At this temperature the pure thermal regrowth rate is negligible (~10^{-11} nm s^{-1}).

As shown in Fig. 10.10, the ion beam-induced regrowth of amorphous Si depends on the energy density deposited into nuclear collisions, as demonstrated by the correlation between the growth rate and the number of vacancies generated by the 600 keV Kr beam irradiation. (Vacancies were calculated by the SRIM code.) This trend suggests that the ion-induced growth rate is coupled with the production of point defects, or in a more general way, with the energy lost through elastic collisions at the α–c interface by the impinging ions.

The role of the α–c interface in Ion Beam Induced Epitaxial Crystallization (IBIEC) is demonstrated in Fig. 10.11, which shows that the regrowth rate is orientation dependent. The data shows that the rate is much lower (almost by a factor of 4) for ⟨111⟩ substrates relative to ⟨100⟩ substrates. These results suggest that the same interfacial defects that are responsible for thermal regrowth also are important in IBIEC, with the role of the ion beam being that of changing the average defect concentration.

The dependence of the growth rate on temperature is illustrated in Fig. 10.12, for both IBIEC and thermal annealing. The growth rate is reported both in Å s^{-1}.

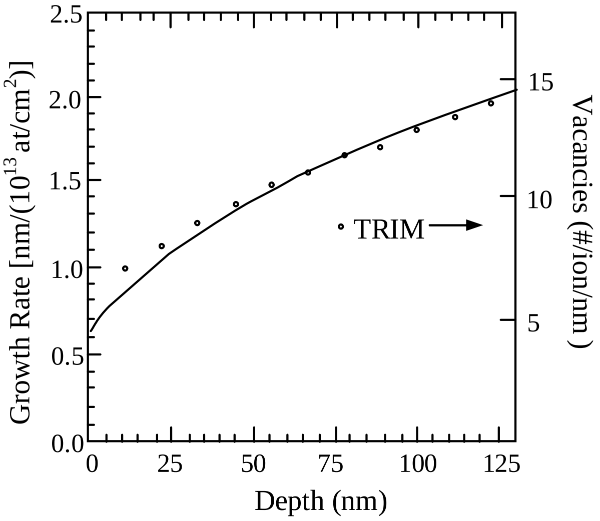

Fig. 10.10. Growth rate versus depth for an α–Si layer recrystallized at 350°C by 600 Kr ions (after Priolo et al. 1989)

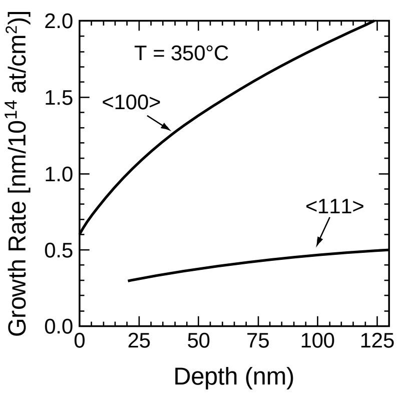

Fig. 10.11. Growth rate versus depth for α–Si layers onto ⟨100⟩ and ⟨111⟩ oriented substrates and recrystallized at 350°C by Kr ions (after Priolo et al. 1989)

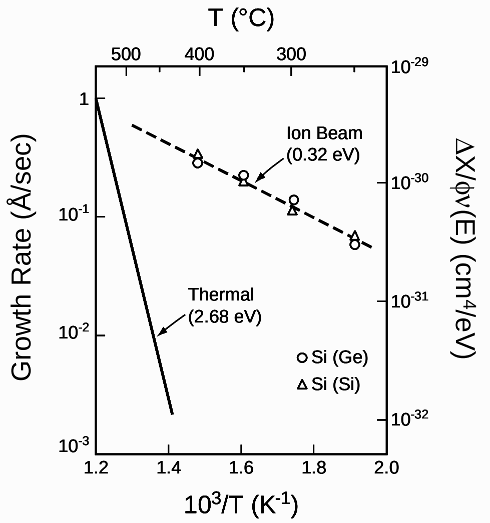

Fig. 10.12. Ion-induced growth rate versus reciprocal temperature for α–Si layers recrystallized by irradiation with a 600 keV Kr beam (Olson and Roth 1988)

(left-hand side) and in $cm^4\ eV^{-1}$ (right-hand side), which takes into account that the ion flux was 1×10^{12} Kr $cm^{-2}\ s^{-1}$. This latter scale represents the growth rate in the form $\Delta X/\phi\nu(E)$, where ΔX is the extent of the regrowth, ϕ is the ion fluence,

and $\nu(E)$ is the energy deposited into displacement production at the α–c interface. The data indicates an activation energy of 0.32 eV for IBIEC, which is approximately an order of magnitude smaller that the activation energy of 2.7 eV for the pure thermal process.

10.4 Laser Annealing of Si

Directed laser beams provide another method of supplying the thermal energy required for the annealing of defects in Si and the regrowth of amorphous layers. (Poate and Mayer 1982). Laser annealing not only presents a new annealing technique but also has the additional advantage of selective area energy deposition. That is, one deposits the energy (heat) not only in a small area but also in a near surface layer that contains the region damaged by the ion beam.

The laser annealing concept is demonstrated by the channeling spectra of the arsenic-implanted and pulsed ruby laser annealed Si sample in Fig. 10.13. On the basis of channeling, the reduction in Si disorder is as complete for the laser as for thermal annealing. The interesting differences lie in the impurity behavior, the broadening of the depth distribution of the impurity, and the very high substitutional concentration. From an analysis of Fig. 10.13, with a peak concentration near 10^{21} As cm^{-3}, the ratio of random and aligned spectra indicates ~98% substitutional arsenic.

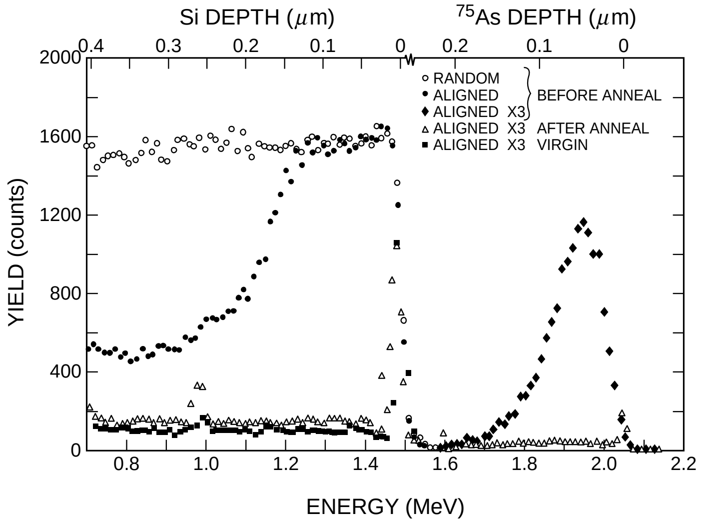

Fig. 10.13. Random and channeling backscattering spectra of as-implanted Si (100) showing the annealing results from pulsed laser irradiation (Q-switched ruby laser 1.6 J cm^{-2}, ^{75}As 100 keV, 1.4×10^{16} in ⟨100⟩ Si, [110] aligned spectrum) (after White et al. 1979)

As a result of the laser anneal, the depth distribution of the implanted arsenic changes from the original Gaussian implantation profile to a broad distribution extending some 300 nm into the crystal. To explain this requires a diffusion coefficient near 10^{-4} cm^2 s^{-1}, since the near surface region is hot for only a few hundred nanoseconds. The magnitude of this diffusion coefficient is some eight orders of magnitude higher than the diffusion coefficient in the solid state, indicating that the near surface region of the silicon reaches a liquid state. In this picture, the annealing process is viewed as the formation of a molten layer for the duration of a laser pulse, and a fast diffusion ($D \sim 10^{-4}$ cm^2 s^{-1}) of impurities occurs within the molten layer. On termination of the pulse, the liquid–solid interface cools and resolidification occurs. Further evidence that the crystal growth is from the liquid phase is found in the high crystal quality of laser annealed (111) oriented Si – an orientation that does not regrow well thermally. Calculation of heat flows indicates that the solid–liquid interface sweeps to the surface at rates of a few meters per second. This rate is orders of magnitude faster than the maximum rate (~0.1 cm s^{-1}) for solid-phase epitaxy extrapolated to near the melting point. This growth velocity is also orders of magnitude faster than that used in growing large Si ingots.

References

Csepregi, L., Mayer, J.W., Sigmon, T.W.: Regrowth behavior of ion-implanted amorphous layers on (111) silicon. App. Phys. Lett. **29**, 92 (1976)

Csepregi, L., Kennedy, E.F., Gallagher, T.J., Mayer, J.W., Sigmon, T.W.: Reordering of amorphous layers of Si implanted with ^{31}P, ^{75}As, and ^{11}B. J. Appl. Phys. **48**, 4234 (1977)

Csepregi, L., Kennedy, E.F., Mayer, J.W., Sigmon, T.W.: Substrate-orientation dependence of the epitaxial regrowth rate from Si-implanted amorphous Si. J. Appl. Phys. **49**, 3906 (1978)

Feldman, L.C., Mayer, J.W., Picraux, S.T.: Materials Analysis by Ion Channeling: Submicron Crystallography. Academic, New York (1982)

Kennedy, E.F., Csepregi, L., Mayer, J.W., Sigmon, T.W. Influence of ^{16}O, ^{12}C, ^{14}N, and nobel gases on the crystallization of amorphous Si layers. J. Appl. Phys. **48**, 4241 (1977)

Lau, S.S., Mayer, J.W., Tseng, W. Handbook on Semiconductors. North-Holland Publishers, Amsterdam (1980)

Mayer, J.W., Eriksson, L., Davies, J.A. Ion Implantation in Semiconductors. Academic, New York (1970)

Mayer, J.W., Lau, S.S.: Electronic Materials Science: For Integrated Circuits in Si and GaAs. Macmillan Publishing Company, New York (1990)

Nastasi, M., Mayer, J.W., Hirvoenen, J.K.: Ion-Solid Interactions: Fundamentals and Applications. Cambridge University Press, Great Britain (1996)

Olson, G.L., Roth, J.A.: Kinetics of solid phase crystallization in amorphous silicon. Mater. Sci. Rep. **3**, 1 (1988)

Poate, J.M., Mayer, J.: Laser and Electron Beam Processing of Semiconductor Structures. Academic, New York (1982)
Priolo, F., Spinella, C., La Ferla, A., Rimini, E., Ferla, G.: Appl. Surf. Sci. **43**, 178 (1989)
Rimini, E.: Ion Implantation: Basics to Device Fabrication. Kluwer, Boston (1995)
Spaepen, F., Turnbull, D.: Laser annealing of semiconductors. In: Poate, J.M., Mayer, J.W. (eds.), p. 15. Academic, New York (1982)
Van Vechten, J.A.: A simple man's view of the thermochemistry of semiconductors, Moss, T.S. (ed.) vol. 3. In: Keller, S.P. (ed.) Materials, Properties and Preparation. North Holland, Amsterdam (1980)
White, C.W., Pronko, P.P., Wilson, S.R., Appleton, B.R., Narayan, J., Young, R.T.: Effects of pulsed ruby-laser annealing on As and Sb implanted silicon. J. Appl. Phys. **50**, 3261 (1979)

Problems

10.1 Arsenic is implanted in silicon at 100 keV at a high enough dose to form an amorphous layer of thickness equivalent to $R_p + \Delta R_p$
(a) What is the thickness of the amorphous layer?
(b) How long would it take to recrystallize the layer at 550°C?

10.2 A 200 μA beam of singly ionized As ions, swept across a 200 cm^2 area for 100 s., gives a dose of how many As cm^{-2}. Is this dose high enough to form an amorphous layer?

10.3 Silicon is implanted with B ions at 30 keV with R_p = 106 nm and ΔR_p = 39 nm
(a) What is the peak concentration?
(b) After anneal at 950°C for 30 min, $D = 8 \times 10^{-15}$ cm^2 s^{-1}, what is the peak concentration?

10.4 If an amorphous layer 5×10^{-5} cm thick were formed on ⟨100⟩ Si and annealed at 550°C,
(a) How long would it take to regrow the layer?
(b) What would the time be if 2×10^{20} P atoms cm^{-3} were present?
(c) If the sample was (110) Si, what would the time be?

10.5 Calculate the concentration of $[V^-]$ in Si at 1,400 K in n-type Si with a donor concentration of 2.8×10^{20} donors cm^{-3}. Verify that the Fermi level is at the conduction band edge E_c. Then from (10.6), show that $[V^-]$ is about 100 times greater than that of the neutral vacancy $[V^x]$ peak concentration.

11 Si Slicing and Layer Transfer: Ion-Cut

Contributed by Tobias Höchbauer

11.1 Introduction

A new technology for the integration of dissimilar materials will be needed to meet many of the advanced technological needs of the future. Existing technology does not allow for the integration of dissimilar materials. Current technologies are limited in their ability to integrate materials systems together on a single platform (e.g., a Si wafer that combines applications in microelectronic, optoelectronic, and microelectromechanical systems, or MEMS). If materials processes could overcome this barrier, then new microelectronics, three-dimensional electronics, and the integration of small mechanical systems made from dissimilar materials would become standard.

In 1977, Chu et al. discovered that, when hydrogen ions are implanted into silicon and the sample undergoes a subsequent heat treatment, exfoliation of the silicon layer above the implantation zone occurs (Chu et al. 1977). This effect initially was used to experimentally determine the ion ranges in ion implantation experiments. Almost 20 years later, researchers realized the potential significance of this phenomenon in terms of a promising application: a new layer splitting and layer transfer process, the "Smart Cut" (Bruel et al. 1995) or, as it is more commonly called, the *Ion-Cut* process (Höchbauer et al. 1999, 2000, 2001). The essence of the Ion-Cut process is to preimplant the device wafer with high-dose gas atoms, such as hydrogen, at a well-defined depth before joining it to a handle wafer. Then, on subsequent annealing of the joined pair, complete shearing or *exfoliation* of the device wafer occurs at the depth of the implanted gas ions.

The Ion-Cut process is an innovative approach for engineering materials. It provides an effective, versatile, and economical method of transferring thin surface layers from bulk substrates onto a host of other substrates and thus offers a novel method to achieve multimaterial integration.

11.2 Formation of SOI by the Ion-Cut Process

The formation of silicon on insulator (SOI) by the Ion-Cut process consists of four steps (a) hydrogen ion implantation into a Si wafer; (b) cleaning of the bond surfaces; (c) bonding of the implanted wafer to another substrate, e.g., a SiO_2 capped Si wafer; and (c) annealing of the bonded wafers. During the heat treatment, the implanted hydrogen evolves into highly pressurized H_2 gas bubbles, which grow in size and ultimately lead to a crack propagation throughout the whole hydrogen-implanted silicon wafer. The process is illustrated in Fig. 11.1.

Hydrogen is introduced into a single crystal silicon wafer by H-ion implantation to a well-defined depth. After the ion implantation, the surfaces of the implanted silicon wafer and another silicon wafer capped with a silicon dioxide layer (the so-called stiffener or handle wafer) undergo a modified Radio Corporation of America (RCA) clean – a surface cleaning process developed by the RCA). The cleaning step is necessary to remove surface contaminants introduced by the H ion implantation process. The cleaning of the wafer surfaces prior to the bonding must be carried out very carefully to leave both surfaces free of particles and organic contaminations. The cleaning procedure results in hydrophilic clean oxide surfaces on both substrates. The substrate surfaces are then bonded together. When the two substrates are pressed together, interactions between water adsorbed

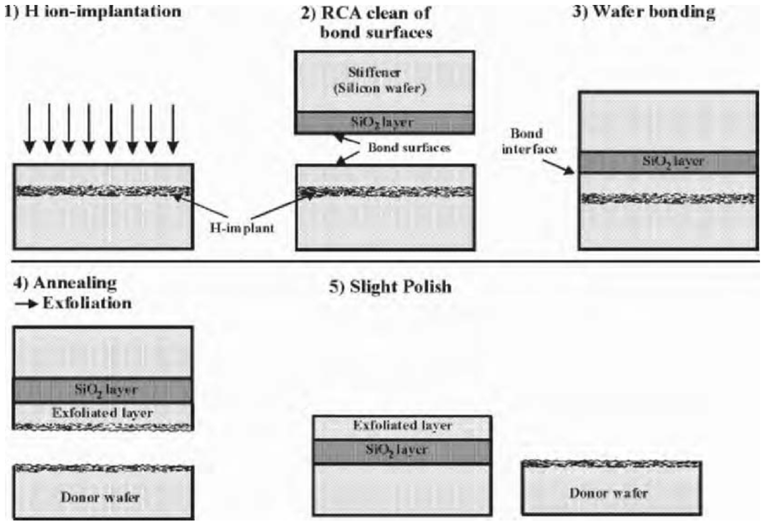

Fig. 11.1. Schematic illustration of the Ion-Cut process for the production of SOI

on both surfaces lead to a weak bond the wafers. Next, the joined pair is heated to about 200°C for a few hours to establish a strong chemical bond between the two wafers.

After a strong bond strength between the wafers is achieved, the joined pair undergoes an anneal at elevated temperatures of typically 400°C. During this heat treatment, the implanted hydrogen atoms rearrange within the implantation zone, forming H_2 gas bubbles of high internal pressure. Raman spectroscopy experiments have measured H_2 gas pressures of up to 50 kbar. The larger and energetically more favorable gas bubbles grow in size at the expense of smaller gas bubbles via Ostwald ripening. Finally, at a critical anneal duration or anneal temperature, the H_2 gas bubbles coalesce and lead to the propagation of a crack through the whole silicon crystal. In the final step, the Ion-Cut surface is polished slightly to remove the damaged layer that resulted from the H ion-irradiation process.

The development of Ion-Cut provides for the first time a methodology for producing ultra thin silicon layers that are required for state-of-the-art devices. Over the last two decades, SOI technology has relied on two methods known as *wafer-bonding and etch-back SOI*, or BESOI, and *separation by implantation of oxygen*, or SIMOX. The Ion-Cut process offers many benefits over BESOI and SIMOX. Because in Ion-Cut the electrically insulating oxide layer is thermally produced, the buried oxide layer is of high quality and uniform thickness. The SOI structure is produced in one step without the need for costly grinding or etchback. Furthermore, the hydrogen-induced fracturing of the silicon wafer leaves an extremely uniform, nearly defect-free silicon layer bonded to the handle wafer, requiring only a moderate polish to achieve the 0.1–0.2 nm rms (root mean square) roughness necessary for further processing. The thickness of the exfoliated silicon layer is highly uniform. In addition, the silicon wafer, from which the hydrogen implanted layer is exfoliated, can be reused.

11.3 The Silicon–Hydrogen System

The physics and chemistry of hydrogen in silicon has been the subject of considerable scientific and technological interest for more than three decades. This interest has been driven by the omnipresent appearance of hydrogen in silicon processing, which always leads to either intentional or unintentional hydrogen incorporation into the substrate. Importantly, this hydrogen may strongly alter the electrical characteristics of the resultant device by diffusion into active regions and passivation of the dopant. Attention has been focused primarily – although not exclusively – on the diffusion of atomic hydrogen, its molecule formation, and its complex formation with and passivation of dopant impurities.

The diffusion of H in Si is complex due to the presence of several charge states and the fact that hydrogen is often present in different forms; it can be atomic, molecular (or larger clusters), or bound to a defect or impurity. The probability of the formation of these different forms depends on the defect and impurity concentration in the material and the hydrogen concentration itself. Thus, the

apparent diffusivity is dependent on the method of hydrogen insertion. Hydrogen can be introduced into silicon through various processes – such as reactive ion-etching, glow discharge, plasma hydrogenation, or H-ion implantation – and consequently each method, with its distinct influence on defect or impurity generation in the silicon crystal, leads to a different behavior of hydrogen in the material. For example, hydrogen appears to diffuse more rapidly under conditions of low hydrogen concentration than it does under conditions of high hydrogen concentration. Furthermore, H diffusion is a function of the silicon conductivity and type.

The earliest work on the behavior of hydrogen in crystalline silicon (c-Si) found that hydrogen is very mobile in c-Si and that, in the temperature regime between 900 and 1,200°C, the diffusion coefficient could be expressed as

$$D_{\mathrm{H}} = 9.4 \times 10^{-3} \exp\left(\frac{-0.48\,\mathrm{eV}}{kT}\right) \mathrm{cm}^2\,\mathrm{s}^{-1}, \tag{11.1}$$

where k is the Boltzmann constant (Van Wieringen and Warmoltz 1956). At these high temperatures the interaction of H atoms with defects and impurities is low. Studies performed with tritium diffusion in c-Si at lower temperatures, in the range of 400–550°C, found that the diffusion in c-Si could be described as (Ichimiya and Furuichi 1968)

$$D_{\mathrm{T}} = 4.2 \times 10^{-5} \exp\left(\frac{-0.56\,\mathrm{eV}}{kT}\right) \mathrm{cm}^2\,\mathrm{s}^{-1}. \tag{11.2}$$

Experimental and theoretical studies on H diffusion in silicon at lower temperatures, where trapping of hydrogen at defects and impurities and H_2-molecule formation are significant, discovered much lower effective diffusivities. Values for the H-diffusion coefficient in silicon expected from an extrapolation of the diffusion coefficient of (11.1) to lower temperatures are several orders of magnitude higher than experimentally obtained diffusivities. This is illustrated in Fig. 11.2, which shows (11.1) and (11.2) extrapolated to low temperatures with experimentally determined values from Johnson et al. (1986).

Several processes have been invoked to explain the details of hydrogen profiles in silicon. These processes include reactions of hydrogen at dopant sites and with lattice defects, reactions between hydrogen atoms, and the dissociation of trapped hydrogen. Pseudopotential density functional calculations showed that atomic hydrogen in silicon can appear in all three charge states: H^+, H0, and H^- (Van de Walle et al. 1989). The charge state depends on the position of the Fermi level. The positive charge state is more stable in p-type silicon and the negative charge state more stable in highly n-type doped silicon. Therefore, charge state-dependent diffusion coefficients have been incorporated into many kinetic studies.

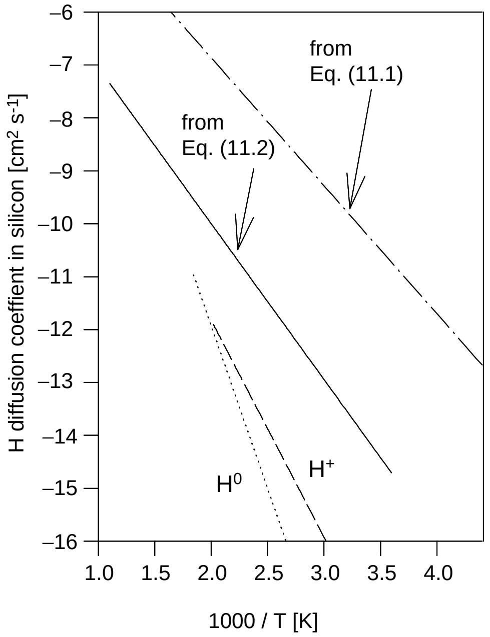

Fig. 11.2. Arrhenius plot of expected H-diffusivity. The predictive diffusivities of neutral and positively charged H-atoms are from Capizzi and Mittiga (1987). Equation (11.1) is from Van Wiering and Warmhotz (1956). Equation (11.2) is from Ichimiya and Furuichi (1968)

Ion implantation into c-Si breaks chemical bonds and creates point defects in the implantation zone (Chap. 7). This effect is crucial in the Ion-Cut process: since the diffusivity of H in c-Si is very high, one would expect out-diffusion of the H implant during the heat treatment of the silicon sample. However, the hydrogen gets trapped at the implantation damage by passivating the dangling bonds in the implantation zone, where the number of lattice defects is very high. As an example, Fig. 11.3 illustrates possible local Si-H defects, formed at a silicon monovacancy. A vacancy in the silicon lattice leaves four dangling bonds behind, which can be passivated with H atoms.

Detailed information about the evolution of Si–H complexes in H ion-implanted silicon were gained by the infrared vibrational studies of Weldon et al. (1997) and Chabal et al. (1999). Implanted H atoms form complexes of the form V_xH_y or I_xH_y, where V denotes a silicon vacancy and I denotes silicon interstitial. Also observed was the so-called H_2^* complex, a hydrogen molecule formation in which one H atom is located at the bond-centered site and the other at the antibond site, with a silicon lattice atom residing between the H_2 bonds. Upon annealing of the H ion-implanted samples, the IR studies uncover a net loss of bound hydrogen

and an agglomeration of hydrogen at existing vacancies. A comparison of the infrared vibrational studies with elastic recoil detection (ERD) analysis – an analysis method which monitors not only atomic hydrogen but also molecular hydrogen – reveals that a net conversion from Si–H complexes into H_2 takes place at elevated temperatures

Earlier investigations showed that H can insert itself between Si–Si bonds at the bond-centered sites to form extended structural defects, described as hydrogen-stabilized platelets (Johnson et al. 1987). The H platelets are the nuclei of the H_2 gas bubbles that lead to ion-cutting in H-implanted material. It has been hypothesized that the H_2 molecules that form within these bubbles do so with a bond length almost equal to the H_2 bond length in vacuum. This leads to an energy gain that counterbalances the energy required for the strain build up around the bubble in the silicon crystal (Cerofolini et al. 1992). Recent Raman spectroscopy measurements verify this assumption (Leitch et al. 1999). The vibrational frequency of H_2 molecules is practically the same as the well-known value for gaseous hydrogen.

The interaction of hydrogen in silicon with acceptor or donor dopants has a considerable influence on the kinetics in the formation of H platelets and H_2 gas bubbles. Shallow acceptors in silicon, such as B, represent the presence of negatively charged ions, B^-, residing in the silicon lattice. Therefore, passivation should eliminate a hole and result in increased resistivity. The first studies of the interaction of hydrogen with acceptors in silicon showed hydrogen could neutralize boron, with neutralization being maximized near 100°C. Neutralization is limited by hydrogen diffusion at lower temperatures and by the dissociation of Si–H–B complexes at higher temperatures.

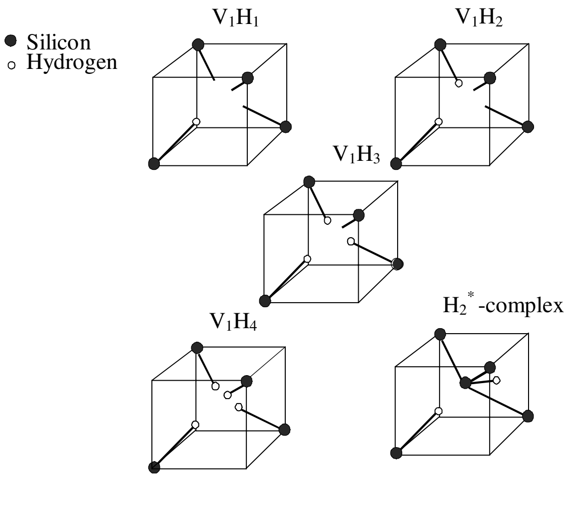

Fig. 11.3. Illustration of Si–H defects observed in H ion-implanted silicon. V denotes a vacancy, and H denotes a H atom

The ways hydrogen interacts with acceptors was further demonstrated by hydrogen in-diffusion experiments into c-Si with a buried layer of high boron concentration. The experiments showed significant trapping of hydrogen within the boron-doped layer. The amount of H atoms trapped was found to far exceed the amount of boron atoms present in the layer. Hydrogen in p-type material is in a H^+ charge state and will be attracted to the negatively charged acceptor, B^-. Under these conditions, the hydrogen–boron capture radius is large (Coulomb interaction), and the boron trap site can pull multiple H^+ ions that can react to form molecular H, thereby enabling the trapping of 8–12 hydrogen atoms by one boron atom in the silicon crystal (Borenstein et al. 1993).

11.4 The Mechanisms Behind the Ion-Cut Process

The process of hydrogen-induced silicon surface layer exfoliation has been investigated by a variety of spectroscopic methods to determine how hydrogen interacts with silicon at the atomic level. The general belief has been that the silicon cleavage takes place at the peak in the H implantation concentration profile. However, as was shown in Chap. 7, the implantation of ions always produces some level of lattice damage, which influences the interaction between the H implant and the Si host atoms. The resulting distribution of ions and lattice damage that occurs from a 175 keV H implant of 5×10^{16} H cm^{-2} in Si is shown in Fig. 11.4.

The nominal H ion implantation dose in the Ion-Cut application for the production of SOI is 5×10^{16} cm^{-2}. At this implantation dose, cleavage of the H-implanted silicon wafer can be accomplished easily by annealing at around 400°C for several minutes, depending on the conductivity type of the silicon and the dopant concentration.

11.4.1 The Ion-Cut Depth

Figure 11.5 shows the ion implantation damage distribution in Si following the 175 keV H implantation at a dose of 5×10^{16} H cm^{-2}. The data is obtained from ion channeling experiments. The implantation damage peak is located at a depth of 1.41 μm.

Figure 11.6 shows the hydrogen concentration in the sample as a function of sample depth as determined by ERD (Tesmer and Nastasi 1995). The H concentration peaks at a depth of 1.51 μm, somewhat deeper than the implantation damage peak. The ratio of the depth of the H concentration peak to the ion implantation damage peak is 1.06, consistent with the SRIM Monte Carlo simulations presented in Fig. 11.4.

After bonding and annealing to produce the complete delamination of the hydrogen-implanted wafer, the thickness of the transferred layer is measured by

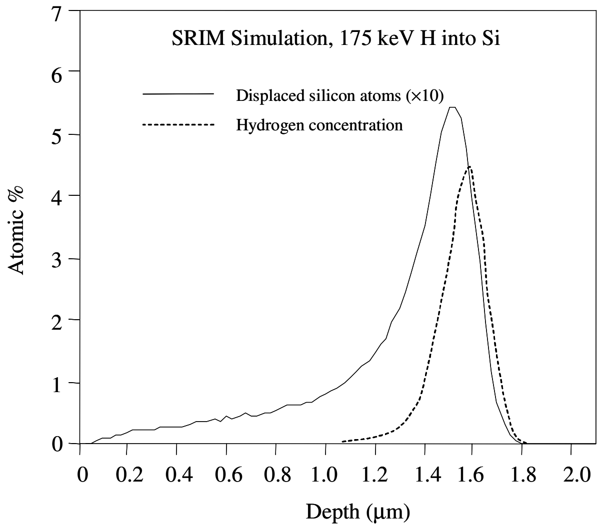

Fig. 11.4. SRIM Monte Carlo calculation of the H concentration distribution and the implantation-induced damage distribution in silicon after a 175 keV H ion implantation to a dose of 5×10^{16} cm^{-2}

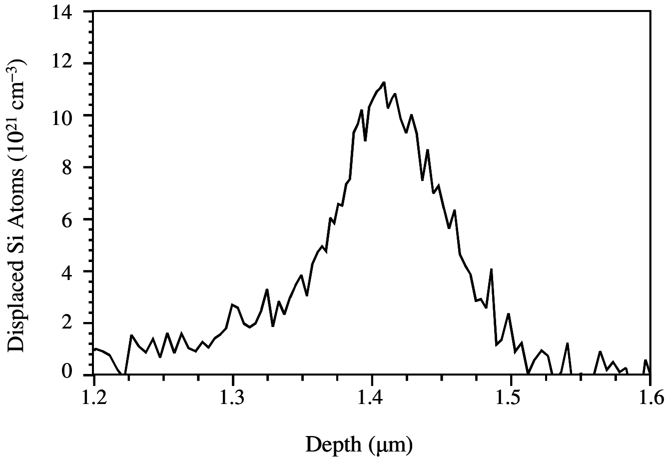

Fig. 11.5. The damage depth distribution obtained from an analysis of ion channeling data

a number of techniques. Figure 11.7 shows a high resolution scanning electron microscopy (SEM) cross-section image of the exfoliated layer. The image shows the roughness of the surface, where the Ion-Cut occurred, to be quite small. Also visible is the 75 nm thick silicon oxide layer beneath the bond interface. The large area analysis possible with SEM reveals a uniform thickness of the exfoliated layer and consequently a smooth cut of the H-implanted silicon crystal. The SEM-determined thickness of the exfoliated layer is measured to be 1.42 μm. A surface height analysis using atomic force microscopy (AFM) shows the transferred layer to be 1.40 μm thick. Examination of the exfoliated layer by means of cross-section transmission electron microscopy (XTEM) measures the thickness of the transferred layer as 1.42 μm.

Figure 11.8 combines all the data mentioned above. The H concentration and Si lattice damage distributions are superimposed. The dashed vertical lines in the figure represent the range in the Ion-Cut location determined by XSEM, AFM and XTEM. This data clearly shows that the Ion-Cut occurs at the region of highest implantation damage rather than at the H concentration peak. To understand why the Ion-Cut depth is correlated with the ion implantation damage requires a closer examination of the nature of the damage.

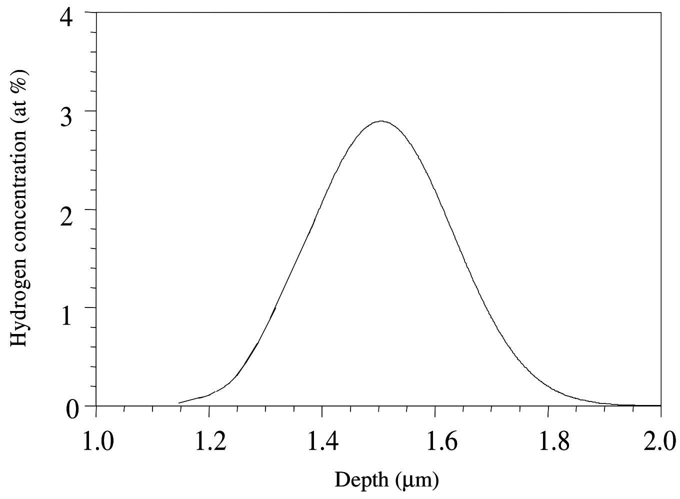

Fig. 11.6. The H concentration depth distribution obtained from an ERD analysis on the silicon sample implanted with 175 keV protons to a dose of 5×10^{16} H cm^2

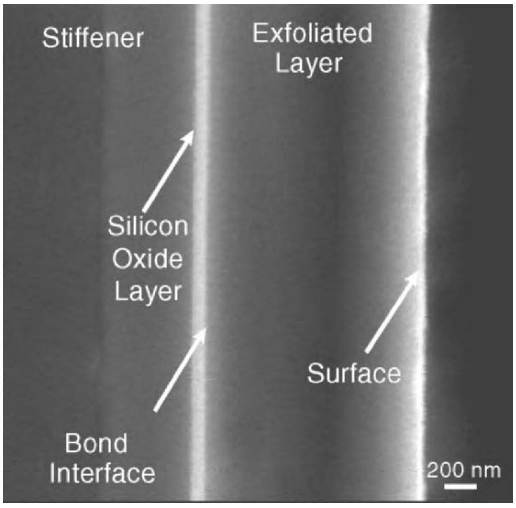

Fig. 11.7. Cross-section SEM image of the exfoliated silicon surface layer after bonding and ion-cutting

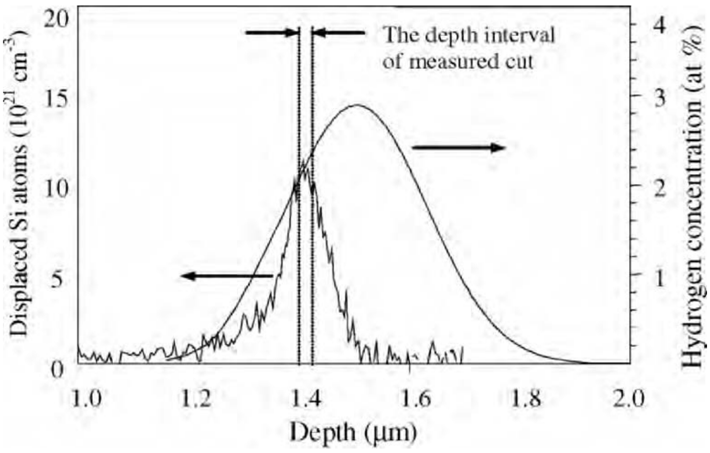

Fig. 11.8. The ion implantation damage distribution co-plotted with the H depth distribution. The *dashed vertical lines* represent the range in the measured Ion-Cut cleavage depth as determined by XSEM, AFM and XTEM

11.4.2 Microstructure of the Implantation Zone

Figure 11.9 shows an image of the H-implanted region in Si that was obtained using transmission electron microscopy in a cross-sectional view (XTEM). The image shows clearly the broad, densely damaged region starting at a depth of 1.32 µm.

A higher magnification view of the implanted region is presented in Fig. 11.10. Figure 11.10a shows an in-focus image of platelet-like defects in the as-implanted sample, whereas Fig. 11.10b presents the platelet defects after the Ion-Cut in the exfoliated layer. The image in Fig. 11.10b was obtained in an under-focused condition, which makes the platelets appear as bright stripes. An analysis of the XTEM image shows that the platelets all are about 1 nm thick and are filled with a very low atomic number element (i.e., hydrogen).

An analysis of the hydrogen platelet distribution is shown in Fig. 11.11. The density of the platelets in the as-implanted sample (upper part of the figure) increases gradually from the depth of the platelets' first occurrence, reaching a maximum at the damage peak (1.42 µm). Towards larger depths, platelet density decreases to the depth of 1.62 µm, at which point it vanishes. The lower part of the figure plots the depth distribution of the platelet density in the exfoliated layer and the donor wafer after ion cutting. In comparison to the as-implanted sample, the bell shape of the platelet density depth distribution is intensified after annealing.

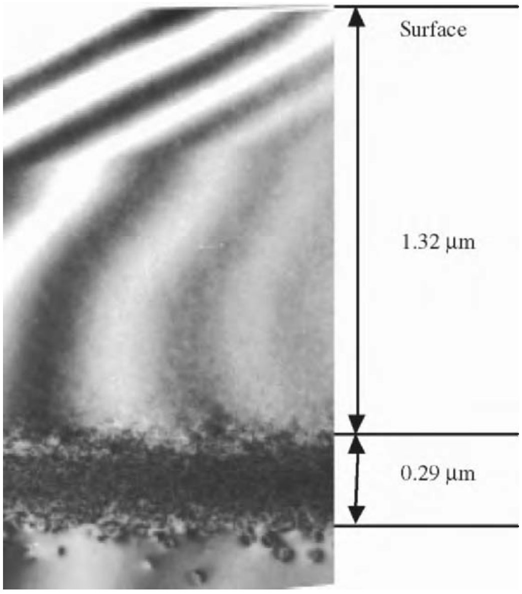

Fig. 11.9. Low magnification cross-section TEM bright field image of the hydrogen-implanted silicon wafer in the as-implanted state

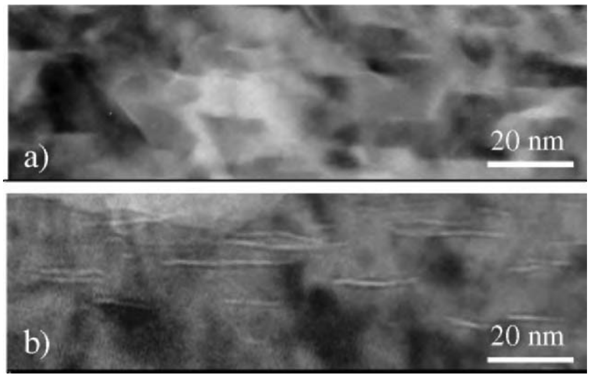

Fig. 11.10. High magnification bright field XTEM images of the implantation damage zone in the (**a**) as-implanted sample and (**b**) in the near surface region in the exfoliated layer after ion cutting. The microcavities are viewed in focus in the as-implanted sample and in under focus in the exfoliated layer

The peaks near the newly-formed surfaces are much more pronounced than in the as-implanted sample.

The data presented here shows that the H implanted into Si evolves into H platelets, and that the H-platelet distribution follows the damage profile. It is obvious that the H platelets play an important role in the Ion-Cut process. However, to produce cleavage of the silicon crystal, the H atoms must ultimately agglomerate to produce highly pressurized H_2 gas bubbles, which provide the force for crack propagation. Hydrogen platelets are apparently the nuclei for H_2 gas bubbles. Figure 11.12 shows schematically the development of implanted hydrogen into hydrogen platelets and ultimately into H_2 gas bubbles. In silicon, implanted hydrogen is known to be trapped at various implantation-induced lattice defects, such as vacancies or silicon interstitials, passivating the dangling silicon bonds. A common location for hydrogen atoms in p-type Si is the bond-centered site between two Si atoms at their lattice site. The occupation of hydrogen in the bond centers of the silicon crystal results in the formation of {100} H planes.

Studies have shown that ion irradiation damage in Si creates defects that in turn produce in-plane compressive stresses (Volkert 1991) and an elastic out-of-plane tensile strain; the peak in the strain distribution is collocated with the damage peak (Paine et al. 1987; Tkachev et al. 1984). The out-of-plane tensile strain facilitates the incorporation of hydrogen atoms into the bond-centered sites between two neighboring silicon atoms by reducing the strain energy needed in replacing the Si–H–Si bond with the Si–Si bond. Prestraining the lattice with radiation damage results in a smaller length change upon H incorporation, thereby reducing the strain energy barrier to this process. This explains why the H-platelet density peaks at the depth of maximum implantation damage.

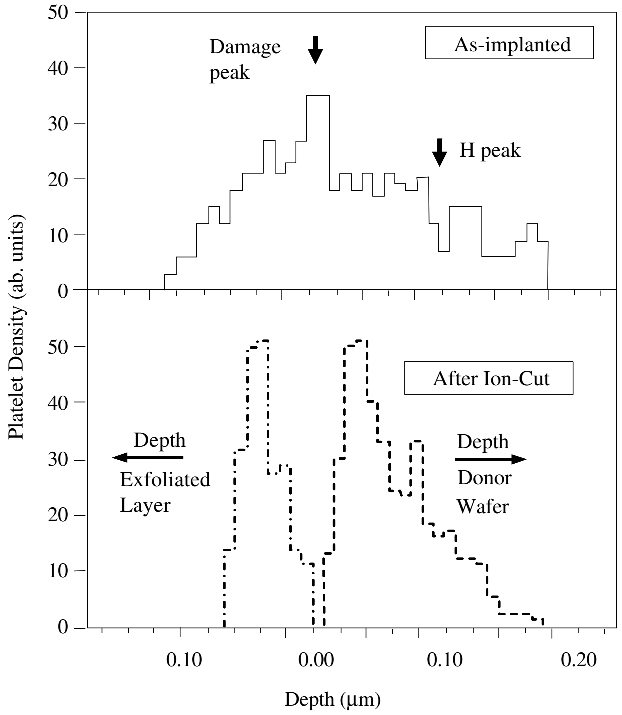

Fig. 11.11. Depth distribution of the platelet density in the as-implanted sample (*solid line*) (*upper part*) and also after ion-cutting in the exfoliated layer (*dashed line)* and the donor wafer (*dash-dotted line*) (*lower part*). The data was deduced from XTEM images

During annealing, the single-hydrogen atoms at the bond-centered sites are replaced with two-hydrogen atoms. In this state the atomic arrangement changes from Si–H–Si to Si–H–H–Si, forming two H atom layers, bonded only by the weak Van der Waals interaction between them. In-diffusing, H atoms split the two H layers and agglomerate into a H_2 gas. Further in time or temperature, hydrogen atoms from other Si–H defects in the system are released from the traps, diffuse to the H–H platelets and agglomerate, forming regions of highly pressurized H_2 gas bubbles. The high pressure in the H_2 gas bubbles provide the force needed to generate a crack opening displacement, with cleavage occurring between the weakly bonded H–H atoms. As mentioned earlier, it has been shown that the H_2 molecules that form within these bubbles do so with a bond length almost equal to the H_2 bond length in vacuum (Leitch et al. 1999). The H_2 molecule formation in the gas bubbles releases the energy necessary for the strain build up around the bubble in the silicon crystal (Cerofolini et al. 1992).

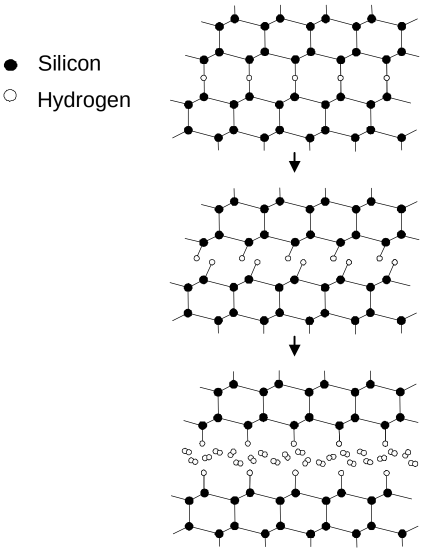

Fig. 11.12. Schematic illustration of the H-platelet formation and development into H_2 gas bubbles

It appears that, due to their low surface energy, the H–H planes that form in hydrogen-implanted Si provide a favorable site for the formation and growth of H_2 gas bubbles. During further heat treatment the H_2 gas bubbles grow in size via Ostwald ripening. Finally, at a critical anneal duration or anneal temperature, the H bubbles coalesce and lead to the propagation of a crack through the whole silicon crystal.

It is apparent that the depth region with highest H platelet concentration becomes the location of highest H_2 gas bubble concentration and ultimate cleavage. Thus the Ion-Cut takes place at the peak of the implantation damage profile and not at the region of highest H concentration.

Repeatedly applying the Ion-Cut process enables the production of advanced circuits, which utilize multiple layers of SOI-type device silicon. These circuits could allow the combination of electrical and optical signal processing into a single chip, resulting in applications such as in the entertainment and communication technology. To date, the Ion-Cut process has been applied to a variety of materials, including germanium, silicon-carbide, diamond thin films, and GaSb, proving the versatility of this layer transfer process.

References

Borenstein, J.T., Corbett, J.W., Pearton, S.J.: Kinetic model for hydrogen reactions in boron-doped silicon. J. Appl. Phys. **73**, 2751 (1993)

Bruel, M., Aspar, B., Charlet, B., Maleville, C., Poumeyrol, T., Soubie, A., Auberton-Herve, A.J., Lamure, J.M., Barge, T., Metral, F., Trucchi, S.: 'Smart cut': a promising new SOI material technology, p.178. Proc. IEEE Tucson, Arizona. Piscataway, NJ (1995)

Capizzi, M., Mittiga, A.: Hydrogen in crystalline silicon: a deep donor? Appl. Phys. Lett. **50**, 918 (1987)

Cerofolini, G.F., Meda, L., Balboni, R., Corni, F., Frabboni, S., Ottaviani, G., Tonini, R., Anderle, M., Canteri, R.: Hydrogen-related complexes as the stressing species in high-fluence, hydrogen-implanted, single-crystal silicon. Phys. Rev. B **46**, 2061 (1992)

Chabal, Y.L., Weldon, M.K., Caudano, Y., Stefanov, B.B., Raghavachari, K.: Spectroscopic studies of H-decorated interstitials and vacancies in thin-film silicon exfoliation. Physica B **273-274**, 152 1999

Chu, W.K., Kastl, R.H., Lever, R.F., Mader, S., Masters, B.J.: Distribution of irradiation damage in silicon bombarded with hydrogen. Phys. Rev B, **16**, 3851 (1977)

Höchbauer, T., Nastasi, M., Mayer, J.W.: Hydrogen blister depth in boron and hydrogen coimplanted n-type silicon. Appl. Phys. Lett. **75**, 3938 (1999)

Höchbauer, T., Misra, A., Verda, R., Nastasi, M., Mayer, J.W., Zheng, Y., Lau, S.S.: Hydrogen-implantation induced silicon surface layer exfoliation. Phil Mag. B **80**, 1921 (2000)

Höchbauer, T., Misra, A., Nastasi, M., Mayer, J.W.: Investigation of the cut location in hydrogen implantation induced silicon surface layer exfoliation. J. Appl. Phys. **89**, 5980 (2001)

Ichimiya, T., Furuichi, A.: On solubility and diffusion coefficient of tritium in single crystals of silicon. Int. J. Appl. Rad. Isot. **19**, 573 (1968)

Johnson, N.M, Burnham, R.D., Street, R.A., Thornton, R.L.: Hydrogen passivation of shallow-acceptor impurities in para-type GaAs. Phys. Rev. B **33**, 1102 (1986)

Johnson, N.M, Ponce, F.A., Street, R.A., Nemanich, R.J.: Defects in single-crystal silicon induced by hydrogenation. Phys. Rev. B **35**, 4166 (1987)

Leitch, A.W.R., Weber, J., Alex, V.: Formation of hydrogen molecules in crystalline silicon. Mat. Sci. and Eng. B **58**, 6 (1999)

Paine, B.M., Hurvitz, N.N., Sperious, V.S.: Strain in GaAs by low-dose ion implantation. J. Appl. Phys. **61**, 1335 (1987)

Tesmer, J.R., Nastasi, M. (eds.): Handbook of Modern Ion Beam Analysis. Materials Research Society, Pittsburgh, PA (1995)

Tkachev, V.D., Holzer, G., Chelyadinskii, A.R.: Damage profiles in ion implanted silicon. Phys. Stat. Sol. (a) 85, k43 (1984)

Van de Walle, C.G., Denteneer, P.J.H., Bar-Yam, Y., Pantelides, S.T.: Theory of hydrogen diffusion and reactions in crystalline silicon. Phys. Rev. B **39**, 10791 (1989)

Van Wieringen, A., Warmoltz, N.: On the permeation of hydrogen and helium in single crystal silicon and germanium at elevated temperatures. Physica **22**, 849 (1956)

Volkert, C.A.: Stress and plastic flow in silicon during amorphization by ion bombardment. J. Appl. Phys. **70**, 3521 (1991)

Weldon, M.K., Marsico, V.E., Chabal, Y.J., Agarwal, A., Eaglesham, D.J., Sapjeta, J., Brown, W.L., Jacobson, D.C., Caudano, Y., Christman, S.B., Chaban, E.E. On the mechanism of the hydrogen-induced exfoliation of silicon. J. Vac. Sci. Technol. B **15,** 1065 (1997)

12 Surface Erosion During Implantation: Sputtering

12.1 Introduction

This chapter deals with the erosion of the sample by energetic particle bombardment. In this process, called *sputtering*, surface atoms are removed by collisions between the incoming particles and the atoms in the near surface layers of a solid. Sputtering limits the maximum concentration of atoms that can be implanted and retained in a target material. The yield of sputtered atoms – the number of sputtered atoms per incident ion – typically falls in the range of 0.5–20, depending on ion species, ion energy, and target material. For direct ion implantation into a target material, the maximum concentration of implanted species is inversely proportional to the sputter yield. Consequently, for ion-target combinations with high sputter yields, the maximum concentration may be only a few atom percent.

12.2 Sputtering of Single-Element Targets

Sputtering is the erosion of a sample by energetic particle bombardment and is characterized primarily by the sputtering yield, Y, which is defined as

$$Y = \text{Sputtering Yield} = \frac{\text{Mean Number of Emitted Atoms}}{\text{Incident Particle}} \tag{12.1}$$

The sputtering yield depends on the structure and composition of the target material, the parameters of the incident ion beam, and the experimental geometry. Sputtering yield experiments have measured values of Y that span more than seven decades; however, for the medium mass ion species and keV energies of general interest in ion–solid interactions, the typical values of Y are between one and ten. An extensive list of sputtering yields is given by Matsunami et al. (1984). Yields can also be calculated using SRIM Monte Carlo simulations.

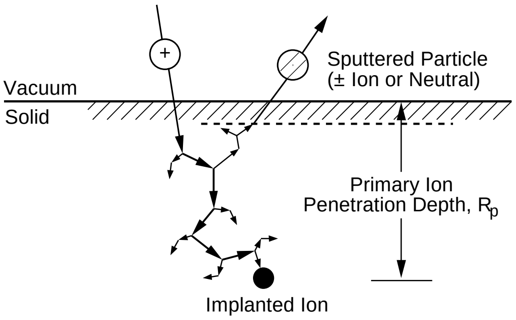

Fig. 12.1. Schematic of ion–solid interactions and the sputtering process

In the sputtering process, atoms are ejected from the outer surface layers. Each bombarding ion transfers energy in collisions to target atoms, which recoil with sufficient energy to generate other recoils (Fig. 12.1). Some of these backward recoils (about one to two atoms for a 20 keV Ar ion incident on Si) will approach the surface with enough energy to escape from the solid. It is these secondary recoils which make up most of the sputtering yield.

Sputtering yields can be predicted by theory for single-element materials. Figure 12.2 shows the energy and incident particle dependence of the sputtering yield of Si. The experimental values (solid circles) are in agreement with calculations (solid line) by Sigmund (1981) and SRIM Monte Carlo simulation (plus sign, +).

The sputtering process involves a complex series of collisions (the collision cascade) involving a series of angular deflections and energy transfers between many atoms in the solid. The most important parameter in the process is the energy deposited at the surface.

The sputtering yield is proportional to the number of displaced or recoil atoms. In the linear cascade regime, which is a reasonable approximation for medium mass ions (such as Ar), the number of recoils is proportional to the energy deposited per unit depth in nuclear energy loss. The sputtering yield, Y, for particles incident normal to the surface is then expressed as (Sigmund 1981)

$$Y = \Lambda F_D(E_0) \tag{12.2}$$

where Λ is called the *materials factor* since it contains all the material properties, such as surface binding energies, and $F_D(E_0)$ is the energy deposited per unit length into nuclear processes at the surface, which can be expressed as

$$F_D(E_0) = \alpha N S_n(E_0) \tag{12.3}$$

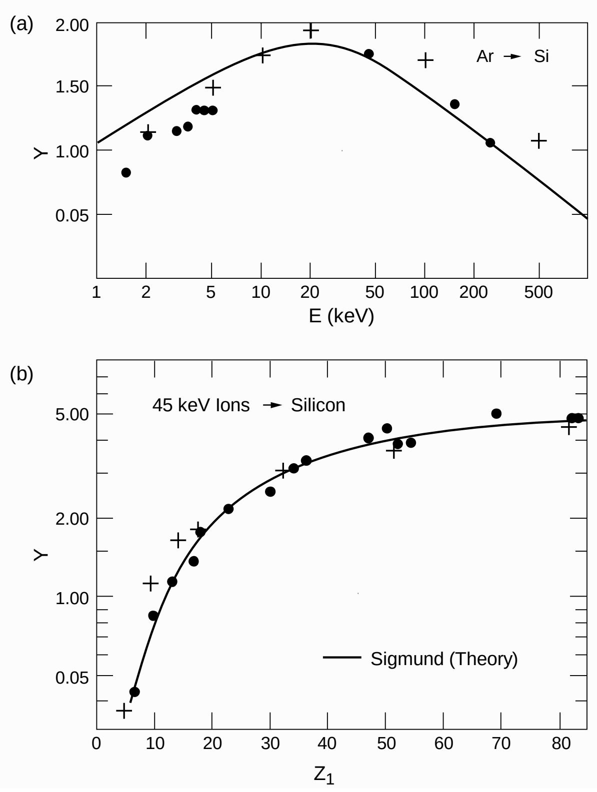

Fig. 12.2. (**a**) Energy dependence of the Ar sputtering yield of Si and (**b**) incident ion dependence of the Si sputtering yield. The *solid line* represents the calculations of Sigmund. The data in *solid circles* is from Andersen and Bay (1981), and the *plus* signs (+) represent SRIM Monte Carlo simulations (Ziegler et al. 1985)

where N is the atomic density of target atoms, $S_n(E_0)$ is the nuclear stopping cross-section at energy E_0, and $NS_n(E_0) = dE_0/dx|_n$ is the nuclear energy loss rate at energy E_0. The energy-dependent nuclear stopping cross section can be most accurately calculated using the ZBL nuclear stopping cross section given by (5.13). In (12.3), α is a correction factor, which is a function of M_2/M_1 and ranges between 0.2 and 1.4, as shown in Fig. 12.3a. The value of α also increases with the angle of incidence because of increased energy deposition near the surface, Fig. 12.3b.

The material factor Λ in (12.2) contains the material parameters and is a description of the number of recoil atoms that can escape from the solid. In Sigmund's description (1981)

$$\Lambda \cong 4.2 / NU_0 \,(\text{nmeV}^{-1}) \tag{12.4}$$

where N is the atomic density in $(\mathrm{nm})^{-3}$, and U_0 is the surface binding energy in eV. U_0 can be estimated from the cohesive energy and has typical values between 2 and 4 eV. Values of the cohesive energy are given in Kittel (1987, 6th edn., Chap. 3) and for Si has a value of 4.6 eV.

Equation (12.2) can be reduced to a final form of

$$\begin{aligned} Y &\cong 4.2\,\alpha S_{\mathrm{n}}(E_0)/U_0 \\ &= 4.2\,\alpha(\mathrm{d}E_0/\mathrm{d}x)_{\mathrm{n}}(NU_0)^{-1} \end{aligned} \tag{12.5}$$

For calculation purposes, use values of α from Fig. 12.3, U_0 in eV, dE/dx in eV nm^{-1}, and N in atoms nm^{-3}. Examples of this calculation for the sputtering of Si are shown in Fig. 12.2 along with experimental data and sputtering coefficients determined using Monte Carlo simulations.

12.3 Ion Implantation and the Steady State Concentration

During ion implantation, the sputtering process removes both target and implanted atoms. Eventually an equilibrium condition (steady state) is reached wherein as many implanted atoms are removed by sputtering as are replenished by implantation. The depth concentration distribution of implanted atoms under this condition typically has a maximum at the surface and falls off over a distance comparable to the initial ion range. Figure 12.4 schematically demonstrates the development of the atomic concentration profile during a high-dose implantation.

The steady-state surface concentrations are relatively easy to obtain. Consider the implantation of ion species A into the host material B, where N_A and N_B are the concentrations (per unit volume) of A atoms and B atoms, respectively, at the surface of the sample. Therefore N_A/N_B represents the surface composition. Let J_A and J_B be the flux of sputtered atomic species A and B, respectively. Then

$$J_B/J_A = r(N_B/N_A) \tag{12.6}$$

where r is the ratio of the probability for a B atom near the surface to be sputtered to that of an A atom to be sputtered. Defining the flux of incident ions of species A as J_i, the total sputtering yield Y can be expressed as

$$(J_A + J_B) = YJ_i \tag{12.7}$$

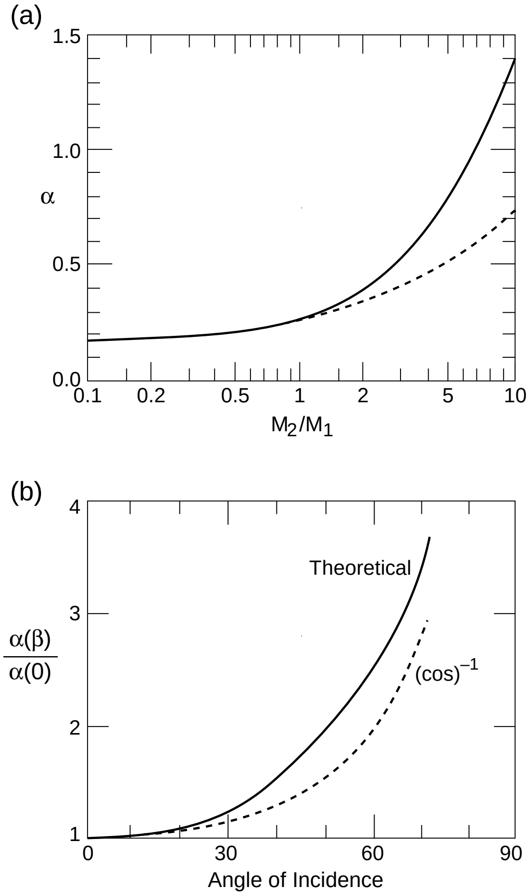

Fig. 12.3. Factor α occurring in (12.5). (**a**) Dependence on mass ratio M_2/M_1: (*solid line*) theoretical, evaluated for elastic scattering only, no surface correction applied; (*dash-dotted line*) interpolated from experimental sputtering yields for 45 keV ions on Si, Cu, Ag, and Au. (The difference is mainly due to the neglect of a surface correction at large mass ratios.) (**b**) Dependence on angle of incidence β, where β is measured from the surface normal: (*solid line*) theoretical for Ar ions on Cu: (*dashed line*) $(\cos)^{-1}$ dependence, valid mainly in the high-velocity limit (from Sigmund 1981)

At steady state, there is no change in the total number of A atoms in the material. Therefore

$$J_A = J_i. \tag{12.8}$$

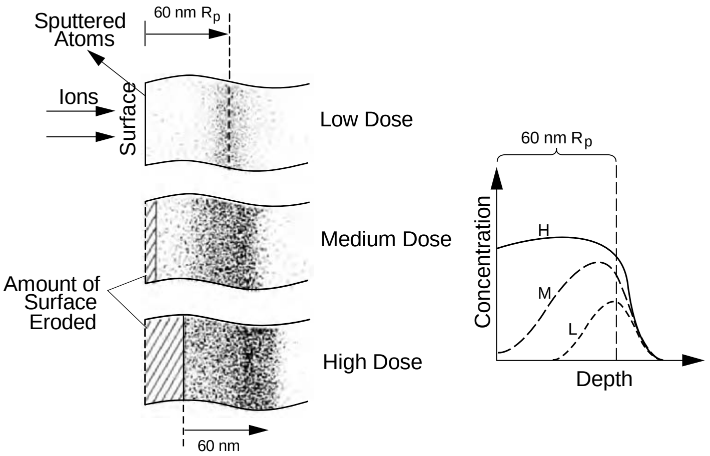

Fig. 12.4. Schematic view of the development of the concentration profile of ions implanted from low (L) to high (H) doses. The projected range, R_P, in this example is 100 nm (from Hubler, NRL Memorandum Report 5928, 1987)

Combining (12.7) and (12.8) yields

$$J_B = (Y - 1)J_i. \tag{12.9}$$

Substituting J_A and J_B, as given by (12.8) and (12.9), into (12.6) yields

$$N_A/N_B = r(Y - 1)^{-1}. \tag{12.10}$$

This is the steady-state surface composition, which is roughly inversely proportional to the total sputtering yield Y, but multiplied by the preferential sputtering factor r. For $r = 1$, (12.10) reduces to $N_A/(N_B + N_A) = 1/Y$.

12.4 Sputtering of Alloys and Compounds

The general theory discussed in Sect. 12.2 explains that most sputtering phenomena in elemental materials are based on a collision cascade picture: The incident ion initiates collisions in a volume (the collision cascade) surrounding the ion track. The energy of the incident ion is shared among those atoms within that volume and then dissipated. Only collisions that occur near the surface of the material can knock atoms out of the material. Most sputtered atoms emerge only from the first few atomic layers. The more collisions that occur near the surface,

the higher the sputtering yield. Therefore the sputtering yield is proportional to the nuclear stopping power of the incident ion in the near surface region.

The main features remain the same for composite materials such as binary alloys. There are additional complications, however, because there are two kinds of atoms in the material. The two species may not be sputtered at an equal rate because of differences in energy sharing (in the collision cascade), ejection probabilities, or binding energies. Indeed, preferential sputtering of one species over the other has been observed in many alloys and compounds.

Since ion implantation is also a bombardment of energetic ions, there is always some sputtering, especially when heavy ions and high doses are used. Sputtering makes the sample surface recede; therefore it affects the implantation profile and also removes atoms that have been implanted. This eventually leads to a steady-state condition in which there is no further increase in the amount of implanted species retained in the material.

12.4.1 Preferential Sputtering

In a description of sputtering from a multicomponent system, the influence of preferential sputtering and surface segregation must be included. For a homogeneous sample with atomic components A and B, and in the absence of surface segregation, the surface concentration, N^s, is equal to that in the bulk, N^b. Therefore, at the start of sputtering

$$N_A^s / N_B^s = N_A^b / N_B^b. \tag{12.11}$$

The partial yield of atomic species A and B is defined by

$$Y_{A,B} = \frac{\text{Number of Ejected Atoms A, B}}{\text{Incident Particle}} \tag{12.12}$$

The partial sputtering yield, Y_A, of species A is proportional to the surface concentration, N_A^s, and similarly Y_B is proportional to N_B^s. The ratio of partial yields is given by

$$\frac{Y_A}{Y_B} = r\frac{N_A^s}{N_B^s} \tag{12.13}$$

where the sputtering factor, r, takes into account differences in surface binding energies, sputter escape depths, and energy transfers within the cascade. Measured values of r generally are in the range between 0.5 and 2.

In the case when r is unity, $Y_A/Y_B = N_A^s/N_B^s$. In the case when $r \neq 1$, the surface concentrations and yields change from their initial values, $N_A^s(0)$ and

$Y_A(0)$, to values of $N_A^s(\infty)$ and $Y_A^s(\infty)$, which occurs at times sufficient to achieve steady state.

At the start of sputtering, $t = 0$, (12.13) takes the form

$$\frac{Y_A(0)}{Y_B(0)} = r\frac{N_A^b(0)}{N_B^s(0)} = r\frac{N_A^b}{N_B^b} \tag{12.14}$$

When steady state conditions have been achieved, conservation of mass requires that the ratio of partial yields equals the bulk concentration ratio

$$\frac{Y_A(\infty)}{Y_B(\infty)} = \frac{N_A^b}{N_B^b} \tag{12.15}$$

For example, if there is preferential sputtering where $r > 1$, the sputtering yield of A is greater than that of B, and the surface will be enriched in B. This enrichment produces an increase in the sputtering yield of B (more B atoms) and a decrease in the sputtering yield of A (fewer A atoms). As the process continues with macroscopic amounts (greater than 10 nm) of material removed, the increased concentration of B balances out the preferential sputtering of A. Therefore, at steady state the surface concentration ratio will differ from that of the bulk ratio when $r \neq 1$.

$$\frac{N_A^s(\infty)}{N_B^s(\infty)} = \frac{1}{r}\frac{N_A^b}{N_B^b} \tag{12.16}$$

That is, the surface composition will be rearranged so that the total sputtering yield gives the bulk composition despite differences in yields of the individual atom species.

12.4.2 Composition Changes

An example of the change in composition of a silicide layer is shown in Fig. 12.5 for PtSi that was sputtered with 20 keV argon ions and then analyzed with 2 MeV ^{4}He ions. The Rutherford backscattering spectrum shows an enrichment of the Pt concentration in the surface region. The ratio of Pt/Si increased from the value of unity associated with that of the bulk to a value near two in the surface region. The increased concentration of Pt at the surface occurs because the partial

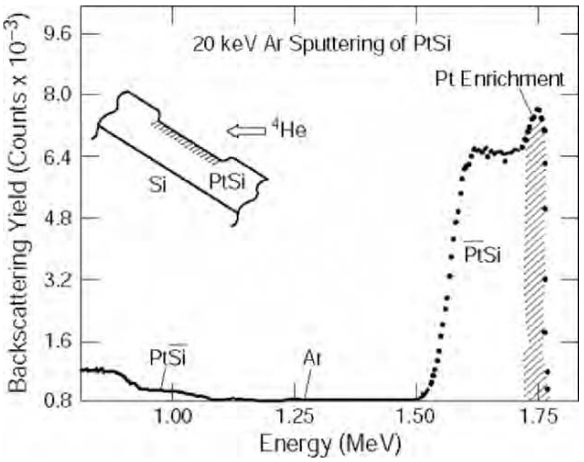

Fig. 12.5. RBS spectrum of a PtSi film after sputtering with 20 keV Ar ions. The *shaded* portion in this Pt signal indicates an increase in the concentration of Pt in the near surface region as a result of the enhanced Si sputtering (from Liau and Mayer 1978)

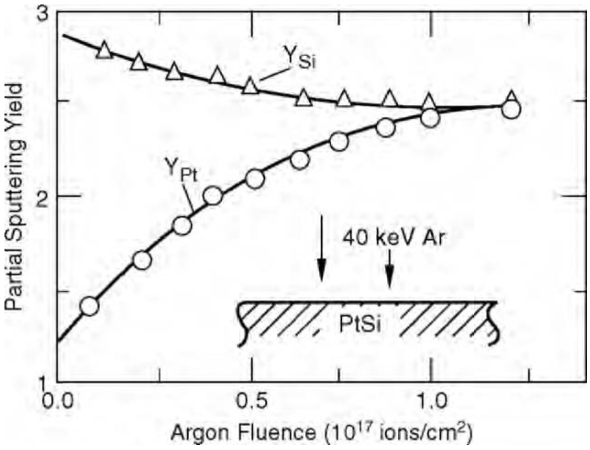

Fig. 12.6. Dose dependence of the partial sputtering yields of Si and Pt emitted from PtSi for 40 keV AR bombardment (from Liau and Mayer 1980)

sputtering yield of Si is greater than that of Pt, $Y_{Si} > Y_{Pt}$. Figure 12.6 shows the partial yields as a function of argon ion dose. At low bombardment doses the sputtering yield of Si is significantly greater than that of Pt and at the onset of sputtering the yield ratio is $Y_{Si}(0)/Y_{Pt}(0) = 2.4$. As the bombardment proceeds, the

partial sputtering yields merge into the same value. The equality of the Si and Pt yields merely reflects that the yield ratio, after steady state has been reached, is equal to the bulk concentration ratio, which for PtSi is unity.

12.4.3 Composition Depth Profiles

In many systems, composition changes extend to a depth comparable to the range of the ion used for sputtering. The composition reaches a steady state after an amount of material comparable to the thickness of the altered surface layer has been sputter-removed. The steady-state surface composition is independent of the mass and energy of the sputtering ion. Composition depth profiles have been

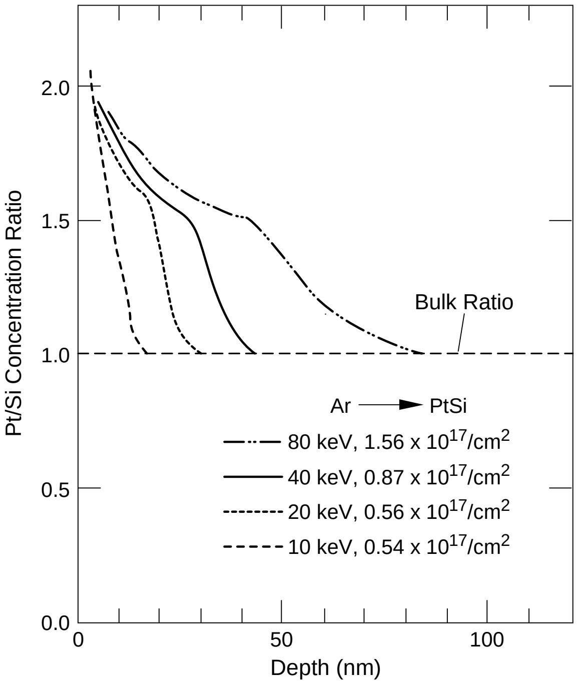

Fig. 12.7. Steady-state Pt/Si profiles of 10, 20, 40, and 80 keV Ar^+ sputtered PtSi samples from RBS measurements. The thickness of the altered layer increases with bombarding ion energy, while the surface composition within the depth resolution limits of RBS is independent of ion energy (Liau and Mayer 1980)

measured for PtSi sputtered with Ar at energies of 10, 20, 40, and 80 keV, as shown in Fig. 12.7. A sufficiently high Ar dose was used at each energy to ensure that the Pt enrichment reached steady state. The depth of Pt enrichment was found

to be related to the Ar energy. However, the steady-state surface composition was quite independent of the Ar energy.

The majority of sputtered atoms emerge only from the outermost few atomic layers. Therefore, with preferential sputtering, a compositional change is only expected in the outermost few atomic layers versus a compositional change in a depth comparable to the ion range. The observed thickness of the altered layer requires some atomic mixing or interdiffusion that can propagate the compositional change from the surface to the deeper region. Either the atoms move inward to dilute the surface enrichment, or they move outward to replenish the depletion of preferentially sputtered atoms at the surface, eventually changing the composition over the whole layer.

12.5 High-Dose Ion Implantation

In high-dose implantation, the atomic mixing, sputtering, and chemical effects determine the state of the material after implantation. In general, the maximum concentration attainable by ion implantation is given by the reciprocal of the sputtering yield. This occurs because of the receding of the sample surface (due to sputter erosion) or, equivalently, because of the sputter removal of the implanted species. This maximum concentration is obtained after the sputter removal of a layer of thickness comparable to the ion range, R_P (more exactly, $R_P + \Delta R_P$).

However, more careful consideration should be given if there is preferential sputtering between atoms of the host material and those of the implanted species. There is also an interesting variation when ion species A is implanted into a compound, AB. In this analysis it will be assumed that atomic mixing is very efficient, so that the implanted species spreads out rather uniformly over an effective width R_P, after an initial amount of implantation, say 10^{16} atoms cm^{-2}. The shape of the profile is assumed to remain approximately unchanged, with its amplitude increasing with further implantation. This model is illustrated in Fig. 12.8.

The conservation of atoms requires

$$R_P \frac{dN_A}{dt} = J_i - J_A \tag{12.17}$$

where N_A is the atomic concentration of the implanted species, J_i is the flux of incident ions (of species A), and J_A is the flux of the sputtered A atoms. The relationship between J_A, J_B, and J_i is the same as given by (12.6) and (12.7), namely $J_B/J_A = r(N_B/N_A)$ and $(J_A + J_B) = YJ_i$. The sputtering yield Y is approximated as a constant throughout the implantation process, and the variable x is defined as $x = N_A/N_B$. Then, (12.6) and (12.7) give

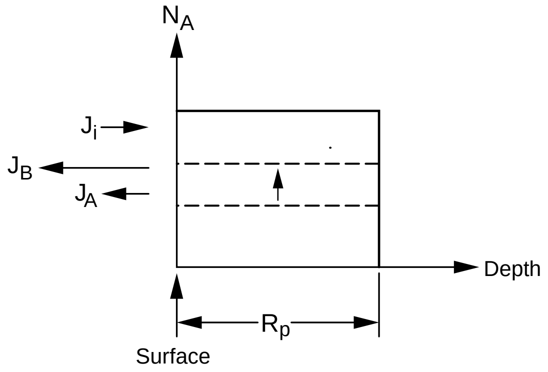

Fig. 12.8. A model for the buildup of implanted concentration as a function of implantation dose. Assuming a very efficient atomic mixing, this model approximates the implanted profile with a constant shape, but with an increasing amplitude. The rate of increase of the implanted concentration is due to the difference between the flux of incident ions of species A, J_i, and that of the sputtered particles of species A, J_A

$$J_A = \frac{x}{r + x} Y_i \tag{12.18}$$

$$J_B = \frac{r}{r + x} Y J_i \tag{12.19}$$

Substituting (12.7) and (12.8) into (12.6), yields

$$R_p \frac{d}{dt}\left(\frac{x}{1 + x}\right) N_0 = J_i - \frac{x}{r + x} Y J_i \{ \}. \tag{12.20}$$

Where $N_0 \equiv N_A + N_B$. After some rearrangement, (12.20) becomes

$$\frac{r + x}{(1 + x)^2[r + (1 - Y)x]} dx = \frac{1}{N_0 R_P} (d\phi_A), \tag{12.21}$$

where $d\phi_A \equiv J_i dt$ is the incremental ion dose. Equation (12.21) is a differential equation for $x(\phi_A)$, which can be solved by taking the partial fractions for the left-hand side and integrating. The result is

$$Y\left[\frac{Ax}{1 + x} + B\ln\left(\frac{1 + x}{1 - x/x(\infty)}\right)\right] = \frac{Y\phi_A}{N_0 R_P} \tag{12.22}$$

where $A \equiv (r-1)/[r-(1-Y)]$, $B = Yr/[(1-Y)-r]^2$, and $x(\infty) = r/(Y-1)$. Note that $Y\phi_A/N_0R_P$ can be interpreted as the amount of material sputtered in units of thickness, normalized by the ion range. An example of the calculated $x(\phi_A)$ is given in Fig. 12.9.

The steady-state compositions are the same as those predicted by (12.10), i.e. $N_A/N_B = r(Y-1)^{-1}$. Note that for $r = 2$, it takes about twice as much sputtering to reach the steady-state composition.

12.6 Concentrations of Implanted Species

This section will examine the influence of sputtering yield, Y, and the sputtering parameter r, on the buildup of the concentration of implanted species. Specific examples will include implanting Pt and Si into Si, Pt and PtSi.

12.6.1 Si Implanted with 45 keV Pt Ions

As (12.6) illustrates, the parameter r, for the case of Pt implanted into Si, is defined by the expression $J_{Si}/J_{Pt} = r(N_{Si}/N_{Pt})$. A value of $r = 2$ is assumed based

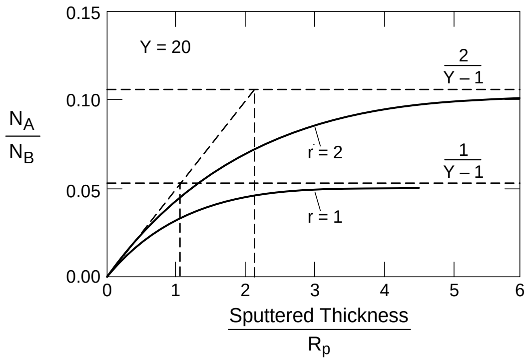

Fig. 12.9. Buildup of the implanted concentration calculated from the simple model of Fig. 12.8. Examples with $Y = 20$ and $r = 1$ or 2 are shown. With a preferential sputtering of the target material ($r = 2$), a correspondingly higher implanted concentration can be achieved. The curves are calculated from (12.11) (Liau and Mayer 1980)

on experimental data of PtSi sputtering with Ar ions. Setting $Y = 4.5$ and $r = 2.0$, (12.10) predicts the steady-state surface Pt concentration ratio to be $N_{Pt}/N_{Si} = 2(4.5 - 1)^{-1} = 0.57$, or a Pt concentration of $N_{Pt}/(N_{Si} + N_{Pt}) = 36\%$.

To calculate the Pt dose required to reach this maximum concentration, the parameter R_P is estimated to be 29 nm for 45 keV Pt in Si. To reach ~90% of the steady-state concentration, a thickness of ~$4R_P$ or 116 nm, has to be sputtered. This thickness corresponds to 5.8×10^{17} atoms cm^{-2} (based on an atomic density of 5.0×10^{22} cm^{-3} for Si), which requires a Pt dose of 1.3×10^{17} cm^{-2} for a sputtering yield of 4.5.

12.6.2 Pt Implanted with 45 keV Si Ions

For Si implanted in Pt, the parameter r is now defined by $J_{Pt}/J_{Si} = r\, N_{Pt}/N_{Si}$ and is approximately 1/2. With $Y = 3.0$ and $r = 1/2$, (12.10) predicts the maximum surface Si concentration to be $N_{Si}/N_{Pt} = 0.25$, or a Si concentration of $N_{Si}/(N_{Pt} + N_{Si}) = 20\%$.

To achieve ~90% of the maximum Si concentration, a sputter removal of a thickness of 32 nm is required. This thickness corresponds to 2.1×10^{17} atoms cm^{-2} (based on an atomic density of 6.6×10^{22} cm^{-3} for Pt), which requires a Si dose of 0.7×10^{17} cm^{-2} for a sputtering yield of 3.

The discussions about the two implantations (1) Pt implanted into Si and (2) (Si implanted into Pt), are summarized in Table 12.1. The sputtering yield of Case (1) is higher than that of Case (2). However, because of the difference in r values, Case (1) can achieve a higher implanted concentration than Case (2). For the same reason, it also takes much more sputtering for Case (1) to reach its maximum concentration.

12.6.3 PtSi Implanted with Si

Implantation of Si into PtSi would be expected to result in a Si-rich Pt–Si mixture. However, instead of increasing the Si concentration, the Si implantation may *decrease*

Table 12.1. Comparison of two ion implantations (45 keV)

	Pt into Si	Si into Pi
sputtering yield Y	4.5	3.0
preferential sputtering parameter r	2	1/2
maximum implanted concentration	36 at. %	20 at. %
implanted layer thickness W	29 nm	32 nm
material sputtered to reach ~90%	116 nm	32 nm
of dose required for max. conc.	1.3×10^{17} Ions cm^{-2}	0.7×10^{17} Ions cm^{-2}

the Si content in the PtSi sample because of Si preferential sputtering. The composition in the implanted sample is determined by a competition between implantation and sputtering.

Consider the implantation of atomic species A into the alloy AB. Having an AB alloy to begin with sets a different boundary condition at the steady state. Instead of $J_A = J_i$ as given in (12.8), the new condition is

$$J_A - J_B = J_i \tag{12.23}$$

at steady state. The total sputtering yield is still $(J_A + J_B) = Y J_i$, (12.7). The relation expressed in (12.6) still holds. Thus, combining (12.23) and (12.7) yields

$$J_A = (Y+1)J_i / 2 \tag{12.24}$$

$$J_B = (Y-1)J_i / 2 \tag{12.25}$$

Substituting J_A and J_B into (12.6) $[J_B/J_A = r(N_B/N_A)]$ yields

$$N_A / N_B = r(Y+1)/(Y-1) \tag{12.26}$$

This gives the steady-state surface composition.

When $Y \gg 1$, (12.26) reduces to $N_A/N_B = r$, which is the same result as inert-gas ion sputtering of alloy AB. On a physical basis, this is because, with high sputtering yield Y, very few of the implanted atoms are retained in the material.

For the example of implantation into PtSi, the steady-state surface composition is given by (12.26), i.e., $N_{Si}/N_{Pt} = r(Y+1)/(Y-1)$, with $r = 1/2$. The surface composition is therefore dependent upon the total sputtering yield, Y. This dependence is plotted in Fig. 12.10. For $Y > 3$, the implanted PtSi sample becomes depleted of Si, because Y is sufficiently large that not enough implanted Si atoms stay in the sample to overcome the preferential sputtering of Si. For $Y = 3$, the Si-implanted PtSi sample remains PtSi. For $Y < 3$, more implanted Si atoms stay in, and the sample becomes Si enriched.

12.7 Concentrations in High-Dose Ion Implantation

Since the majority of sputtered atoms have relatively low energies and emerge from the first few atomic layers near the surface, the probability of sputtering is very sensitive to surface conditions. A thin layer of surface contaminants or oxide

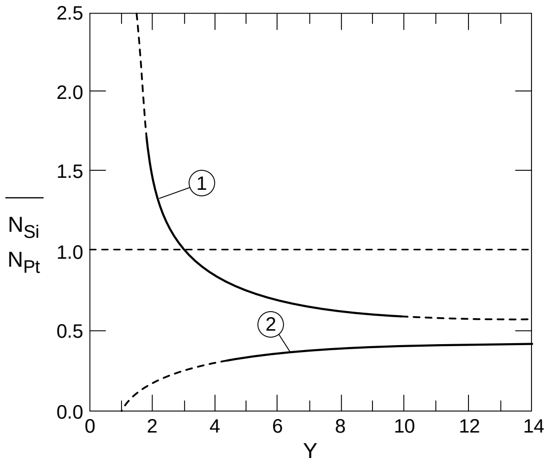

Fig. 12.10. Steady-state surface composition predictions of high-dose implantation of Si (1) and Pt (2) into PtSi. Note that the implantation of Si into the PtSi sample will result in a depletion of Si if the total sputtering yield, *S*, is higher than three. This is because of preferential sputtering of Si. The composition is determined by a competition between implantation and sputtering, as seen in (12.26) (from Liau and Mayer 1980)

can protect the material from being sputtered, and therefore can strongly affect the parameters *Y* and *r*, which in turn determine the state of the implanted materials.

The surface conditions are influenced by several factors, such as residual gas in the vacuum, the target material, and the current density of the incident ion beam. For example, it is well known that ion implantation in a bad vacuum can cause the formation of a carbon layer on the sample surface. Formation of thin oxide layers are often encountered in the sputtering of easily oxidized materials. A good vacuum and high ion-beam current (high sputtering rate) are often desirable to minimize surface oxidation. Both carbon and oxide layers can greatly reduce the sputtering yield of the material, which can significantly increase the maximum implanted concentration. The surface oxide layer can also affect the preferential sputtering parameter, *r*, because of the segregation effects of oxides.

It might appear desirable to have surface oxide and carbon layers intentionally to enhance the implant concentration. However, because of atomic mixing, the surface oxygen and carbon can become mixed into the implanted layer after prolonged implantation. These impurities can cause significant side effects.

Sputtering can also give rise to surface roughness, which can affect the high-dose implantation. Surface roughness has been found to be related to crystallographic

orientation, impurities in the material, ion species, and angles used for sputtering. An extremely rough surface can reduce the sputtering yield.

Gas bubble formation and blistering effects have been widely observed in high-dose implantations of inert-gas ions. Backscattering measurements of depth distributions often show very low concentrations of implanted species in the near-surface region. This indicates that the inert-gas atoms can escape from the material even without sputtering. In these cases, the simple model described in the previous sections does not apply.

12.8 Computer Simulation

Sputtering has been modeled using both Monte Carlo and molecular dynamic computer simulations. A review of the simulation literature is given in Eckstein (1991).

The SRIM program, a binary collision Monte Carlo approach, has been used to predict sputtering yields (Fig. 12.2). The incident ions and the recoil atoms are

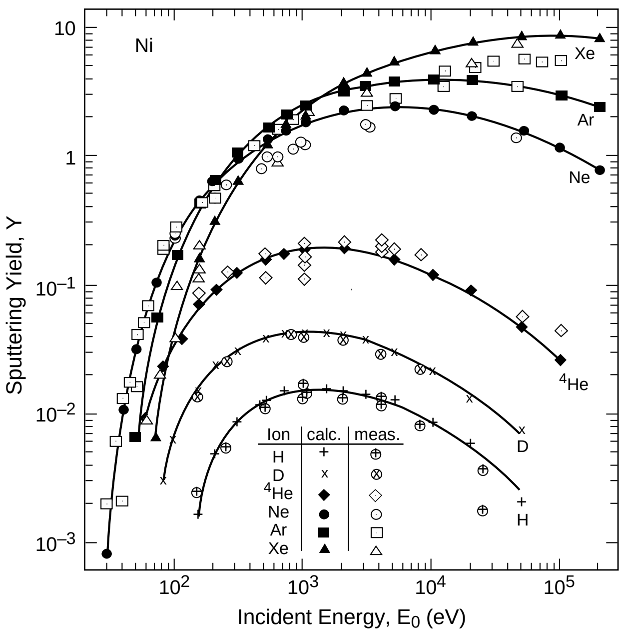

Fig. 12.11. Comparison of SRIM calculations with experimental measurement of the sputtering yield, *Y*, versus incident energy for gas ions incident on a Ni target (from Ziegler et al. 1985)

followed throughout their slowing-down process until their energy falls below a predetermined energy. Usually, the incident ion is followed to a cutoff energy of 5 eV, and the surface binding energy is used for the cutoff of the knock-on atoms. Fig. 12.11 compares the SRIM calculated and experimentally determined sputtering yield, *Y*, versus incident energy for ions incident normal to the surface. There is good agreement between SRIM and experimental data in Figs. 12.2 and 12.11.

References

Andersen, H.H., Bay, H.L.: Sputtering yield measurements. In: Behrisch, R. (ed.) Sputtering by Particle Bombardment. I. Physical Sputtering of Single Element Solids, Topics in Applied Physics, vol. 47, pp. 145–218. Springer, Berlin (1981)

Eckstein, W. Computer Simulations of Ion–Solid Interactions, chap. 12. Springer, Berlin, (1991)

Hubler, G.K.: Ion Beam Processing, NRL Memorandum Report 5928. Naval Research Laboratory, Washington, DC (1987)

Kittel, C.: Introduction to Solid State Physics, 6th edn. Wiley, New York (1987)

Liau, Z.L., Mayer, J.W.: Limits of composition achievable by ion implantation. J. Vac. Sci. Technol. **15**, 1629–1635 (1978)

Liau, Z.L., Mayer, J.W.: Ion bombardment effects on material composition. In: Hirvonen, J.K. (ed.) Treatise on Materials Science and Technology. Academic Press, New York (1980)

Matsunami, N., Yamamura, Y., Itikawa, Y., Itoh, N., Kazumata, Y., Miyagawa, S., Morita, K., Shimizu, R., Tawara, H.: Energy dependence of the ion-induced sputtering yields of monatomic solids. At. Data Nucl. Data Tables **31**, 1–84 (1984)

Sigmund, P.: Sputtering by ion bombardment: theoretical concepts. In: Behrisch, R. (ed.) Sputtering by Particle Bombardment. I. Topics in Applied Physics, vol. 47, pp. 9–71. Springer, Berlin Heidelberg New York (1981)

Ziegler, J.F., Biersack, J.P., Littmark, U.: The Stopping and Range of Ions in Solids. Pergamon, New York (1985)

Suggested Reading

Andersen, H.H.: Ion-bombardment-induced composition changes in alloys and compounds. In: Williams, J.S., Poate, J.M. (eds.) Ion Implantation and Beam Processing, chap. 6. Academic Press, New York (1984)

Behrisch, R. (ed.): Sputtering by Particle Bombardment. I. Physical Sputtering of Single Element Solids, Topics in Applied Physics, vol. 47. Springer, Berlin Heidelberg New York (1981)

Behrisch, R. (ed.): Sputtering by Particle Bombardment. II. Sputtering of Alloys and Compound, Electron and Neutron Sputtering, Surface Topography, Topics in Applied Physics, vol. 52. Springer, Berlin Heidelberg New York (1983)

Behrisch, R., Wittmaack, K. (eds.): Sputtering by Particle Bombardment. III. Characteristics of Sputtered Particles, Technical Applications, Topics in Applied Physics, vol. 64. Springer, Berlin Heidelberg New York (1991)
Matsunami, N., Yamamura, Y., Itikawa, Y., Itoh, N., Kazumata, Y., Miyagawa, S., Morita, K., Shimizu, R., Tawara, H.: Energy dependence of the ion-induced sputtering yields of monatomic solids. At. Data Nucl. Data Tables **31**, 1–84 (1984)
Nastasi, M., Mayer, J.W., Hirvonen, J.K.: Ion–Solid Interactions: Fundamentals and Applications, chap. 9. Cambridge University Press, Cambridge (1996)
Sputtering, Y., Yamamura, Y., Itoh, N.: In: Itoh, T. (ed.) Ion Beam assisted Film Growth, chap. 4. Elsevier, Amsterdam (1989)

Problems

12.1 Consider the case of (1) Si ions incident on Au; and (2) Au ions incident on Si; both cases for 100 keV incident energies at normal to the sample. Which would have the largest value
(a) The dimensionless energy, ε;
(b) The electronic energy-loss-rate, $dE/dx|_e$;
(c) Nuclear energy-loss-rate, $dE/dx|_n$;
(d) The projected range, R_P
(e) Sputtering yield, Y:, (assume binding energy $U = 5$ eV);
(f) Maximum concentration of implanted species.

12.2 Calculate the sputtering yield values of Ne, Ar, and Xe incident on Si at 45 keV using the expressions for ZBL nuclear stopping given in Chap. 5 and a binding energy of 4.6 eV:
(a) Compare your values with the data given in Fig. 12.1
(b) Calculate values of the dimensionless energy ε for the three cases. Are these ε values in a region where nuclear stopping rates would dominate? (See Chap. 5.)
(c) For a current of 10 μA cm^{-2} of Ar, now many monolayers (10^{15} atoms cm^{-2}) would be removed per second.

12.3 (a) Calculate the sputtering yields for 45 keV Ge incident on Si ($U = 4.5$ eV), and compare with the data in Fig. 12.2a for 45 keV Ar ions incident on Si compare your values with the data given in Fig. 12.1
(b) Estimate the maximum concentration of implanted Ge for preferential sputtering factor values of 2 and 1/2

12.4 Assume you have a target of $Si_{50}Ge_{50}$ sputtered by 50 keV Ar ions with a preferential sputtering yield of Si twice that of Ge. Assume $R_P(Ar) = 50$ nm
(a) What is the initial sputter yield ratio Y_{Si}/Y_{Ge}?
(b) What is the steady state yield ratio Y_{Si}/Y_{Ge}?
(c) What is the surface concentration ratio of Si to Ge at steady state?
(d) How thick a layer of SiGe must be removed to achieve steady state?

12.5 If the sputtering yield of species A is twice that of species B in a matrix AB
(a) What is the ratio A to B of the flux of sputtered species at (i) the initial time and (ii) the steady state time?
(b) What is the ratio A to B of surface composition at (i) the initial time; and (ii) the steady time?
(c) If the projected range of the sputtering ion species is 100 nm, how much material must be sputtered away to achieve steady state?
(d) If A is the sputtering species, the sputtering yield Y must be below what value if the ratio of A/B is to exceed unity at steady state?

13 Ion-Induced Atomic Intermixing at the Interface: Ion Beam Mixing

13.1 Introduction

Materials under ion irradiation undergo significant atomic rearrangement. The most obvious example of this phenomenon is the atomic intermixing and alloying that can occur at the interface separating two different materials during ion irradiation. This process is known as *ion beam mixing*. An early observation of the ion mixing phenomenon was made following the irradiation of a Si substrate coated with a thin Pd film. A reaction between Pd and Si was observed when the irradiating Ar ions had sufficient energy to penetrate through the Pd/Si interface (van der Weg et al. 1974). This process is schematically displayed in Fig. 13.1 for a layer M on a substrate S for successively higher irradiation doses.

Early in the irradiation, when ion tracks are well isolated, each incident ion initiates a collision cascade surrounding the ion track. Atoms within the cascade volume will be mobile and undergo rearrangement for a short period of time, resulting in an intermixed region near the interface. At this stage of the ion mixing process, the interfacial reaction is considered to be composed of many localized volumes of reaction (Fig. 13.1a). As the irradiation dose is increased, overlap of localized regions occurs (Fig. 13.1b), and for higher doses, a continuous reacted layer is formed at the interface (Fig. 13.1c).

A major driving force in the development of the ion beam mixing process is the process's ability to produce ion-modified materials with higher solute concentrations at lower irradiation doses than can be achieved with conventional high-dose implantation techniques. A case-in-point is the formation of Au–Cu alloys on Cu substrates (Fig. 13.2).

Figure 13.2 shows Au concentration as a function of ion dose for both Xe ion mixing of an Au layer on Cu and the direct implantation of Au into Cu. The ion mixing experiment was carried out by depositing a 20 nm Au film on Cu, then irradiating the sample with Xe ions at energy sufficient to penetrate the Au layer. As the data shows, the amount of Au that can be introduced into the Cu by ion mixing greatly exceeds the maximum concentration that can be achieved by direct implantation, where sputtering effects generally set the concentration limits.

Several processes are responsible for the ion mixing effect, all of which are initiated by the interaction of an energetic ion with a solid. The ballistics or

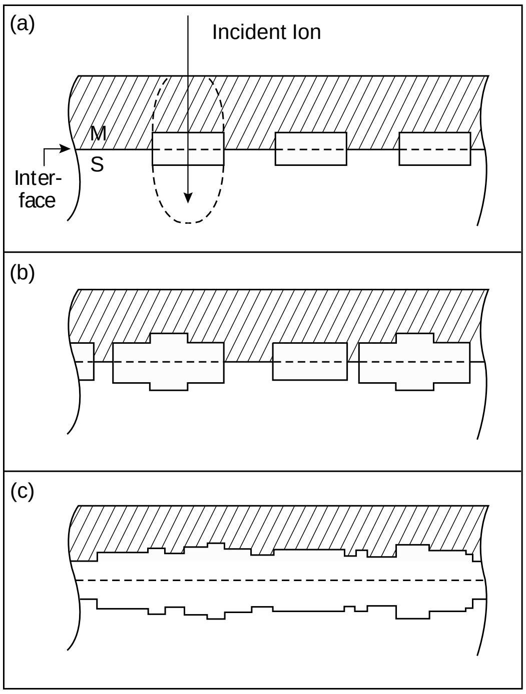

Fig. 13.1. Schematic of the ion mixing process for a layer M on a substrate S for successively higher irradiation doses

kinematics of the ion/target interaction play a role, as does the formation of collision cascades and the total number of ions that have passed through the interface, i.e., the ion dose, ϕ. Both ballistic and cascade effects can be altered by changing the mass of the irradiating ion; increasing the mass of the ion increases the amount of energy deposited in nuclear collisions per unit length traveled by the ion. An example of mass and dose effects in ion mixing is clearly evident in Fig. 13.3. This shows that the average thickness of reaction at the Pt/Si interface, in units of Si atoms cm^{-2}, increases with both increasing mass of the incident ion and the increasing dose, ϕ, and that the mixing rate for all irradiating ions is proportional to $(\phi)^{1/2}$. For a given dose, the ratio of the number of atoms reacted, Q, scales with the ion mass and with the nuclear energy loss $(\mathrm{d}E/\mathrm{d}x)_\mathrm{n}$ in the Pt layer to the 1/2 power. These trends lead to a general condition for the amount of mixing, Q, at the interface between two different materials, which can be expressed as

$$Q \propto \sqrt{\phi\left(\frac{\mathrm{d}E}{\mathrm{d}x}\right)_\mathrm{n}} \tag{13.1}$$

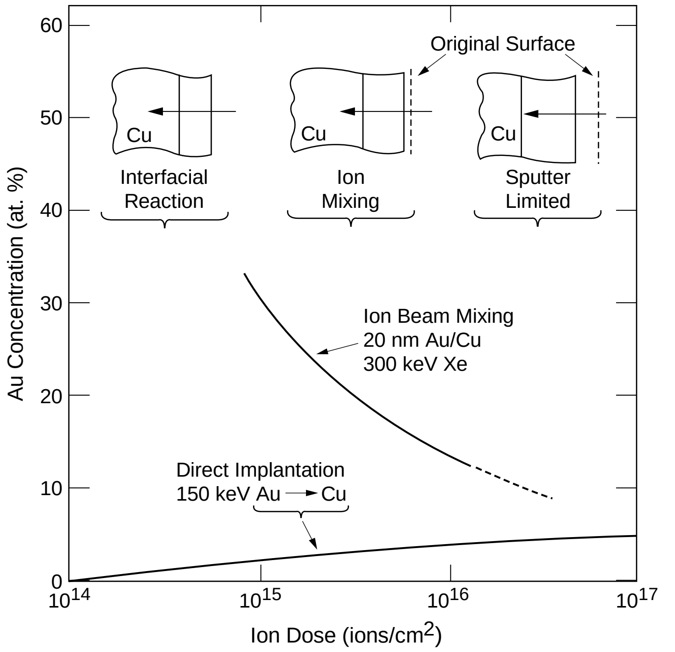

Fig. 13.2. Concentration as a function of ion dose for the ion mixing of a 20 nm Au layer on Cu with 300 keV Xe and the direct implantation of 150 keV Au into Cu (from Mayer and Lau 1983)

Since the dose rate, ions cm^{-2} s^{-1}, is nominally held constant during each ion mixing experiment and, hence, ion dose is proportional to time, the observation that mixing is proportional to $(\text{dose})^{1/2}$ implies that ion mixing is also proportional to $(\text{ion mixing time})^{1/2}$. This latter proportionality is very similar to that observed for a reaction layer formed between two materials by thermally activated interatomic diffusion. The width of the reacted layer, W, in a thermal diffusion experiment has been observed to have the following trend:

$$W \propto \sqrt{\tilde{D}t} \tag{13.2}$$

where $\tilde{D}$ is the interdiffusion coefficient. This observation has led to a general formulation that ion mixing has characteristics similar to a diffusion-like process.

In addition to the primary effects of ion/target atom collisions, external variables, such as the sample temperature during irradiation, also can influence mixing behavior. At low temperatures, the amount of mixing observed for a given ion dose typically is found to be insensitive to temperature variations, while above a

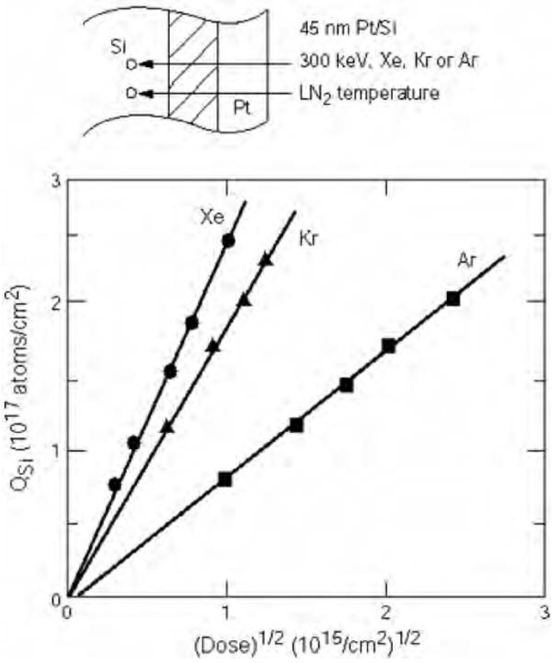

Fig. 13.3. An example of mass and dose effects in the ion mixing of Pt/Si. Mixing increases with both increasing mass of the incident ion and increasing dose ϕ. The mixing rate for all irradiating ions is proportional to $\phi^{1/2}$ (from Tsaur et al. 1979)

critical temperature the mixing is very temperature-dependent. This behavior can be seen in Fig. 13.4 for the case of Cr/Si irradiated with 300 keV Xe ions to a dose of 1×10^{16} cm^{-2}. For temperatures below 0°C, the amount of mixing that occurs is relatively insensitive to the sample temperature during irradiation; this temperature interval is known as the temperature-independent ion mixing regime.

However, as the sample temperature is increased to above ~100°C, the mixing rate changes rapidly with temperature and is observed to increase with increasing temperature; this temperature interval is known as the temperature-dependent ion mixing regime.

13.2 Ballistic Mixing

The interaction of an energetic ion with a solid involves several processes. As an ion penetrates a solid, it slows down by depositing energy both to the atoms and to the electrons of the solid. During the nuclear collision portion of this process, target

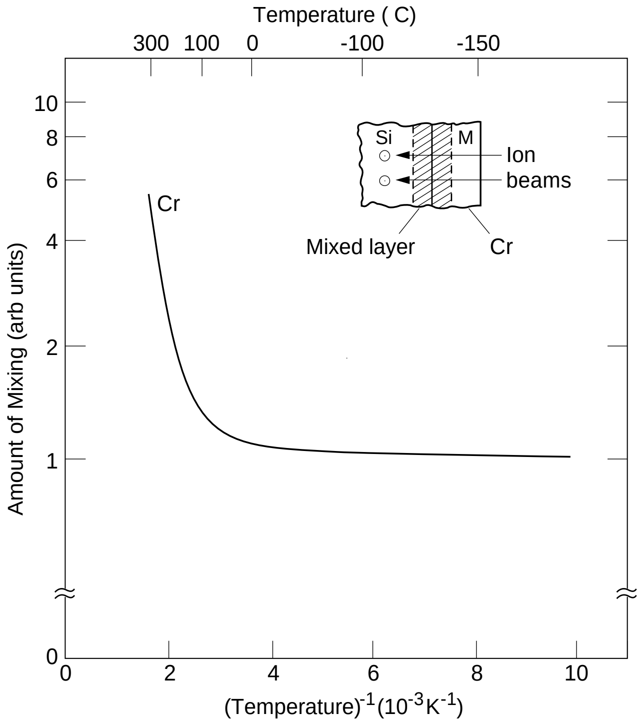

Fig. 13.4. The amount of Si atoms contained in the Cr/Si mixed layer versus reciprocal irradiation temperature (from Mayer et al. 1980)

atoms can be permanently displaced from their lattice sites and relocated several lattice sites away. When this occurs at the boundary separating two different materials, interface mixing results. The displacement mechanism of atomic rearrangement is the fundamental principle governing ballistic mixing.

13.2.1 Recoil Mixing

When an incident ion strikes a metal target atom, M, near a metal/substrate interface, some of the incident ion's kinetic energy is transferred to the target atom. For high-energy collisions, the target atoms recoil far from their initial location. This process, which results in the transport of atoms through repeated single collision events between the incident ions and target atoms, is the simplest form of ballistic mixing. It is known as *recoil implantation* or *recoil mixing*. For mixing to be effective by this process, the recoil should travel the maximum range

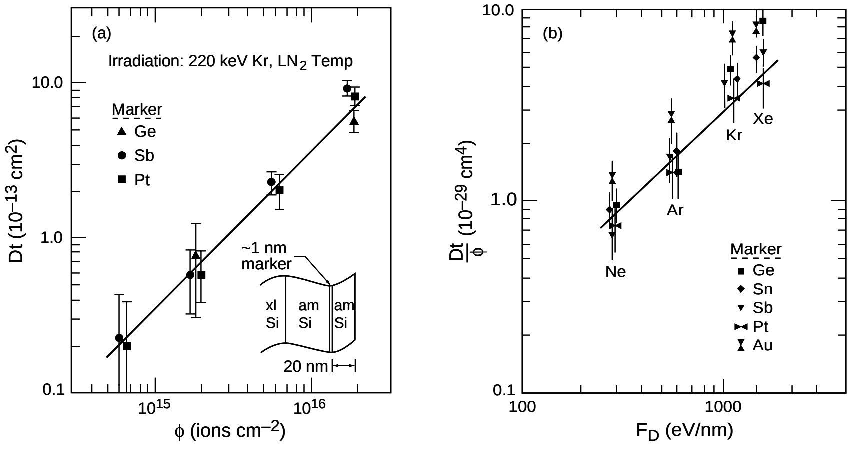

Fig. 13.5. Marker mixing data of several different markers in amorphous Si. This data shows (**a**) the relationship between the effective ion mixing diffusion coefficient, Dt, and ion mixing dose, ϕ, and (**b**) the effective mixing parameter, Dt/ϕ, and the damage energy deposited per unit length, F_D (from Matteson et al. 1981)

possible; a maximum range will result when the collision between the incident ion and the target atom is head-on ($\theta = 0°$). The probability of a head-on collision is very small, with most collisions being *soft* (i.e., $\theta > 0°$). The recoils produced in such soft collisions will possess significantly less energy, and head-on collisions and their trajectories will not be in the forward direction. As a result, the number of target atoms contributing to mixing by the mechanism of recoil implantation will be small.

Insight into the collisional mixing factors operating in ion beam mixing can be gained by the use of embedded marker studies. In these studies, a thin layer of a marker material, such as Ge, is placed between two layers of a matrix element, such as Si. The effective diffusion coefficient observed during marker ion mixing is proportional to the ion mixing dose, ϕ, and the damage energy deposited per unit length, F_D. These two relationships are shown in Fig. 13.5 for several different markers in amorphous Si. These and other similar results have led to the definition of an effective mixing parameter, Dt/ϕ, as indicated in Fig. 13.5b. The deposited energy, F_D, should be considered when defining the effective mixing parameter, casting it as $Dt/\phi F_D$ Strictly speaking, F_D is the total kinetic energy of the incident ion deposited into nuclear collisions per unit length, and it is obtained from the recoil energy by factoring in electronic losses. However, the damage energy at a given location in the sample is occasionally approximated by the nuclear stopping at that location, which provides an overestimate of F_D.

13.2.2 Cascade Mixing

In addition to recoil mixing, other ballistic phenomena are possible during ion irradiation and implantation. For example, enhanced atomic mixing can occur when multiple displacements of target atoms result from a single incident ion. In the multiple displacement process, an initially displaced target atom (primary recoil) continues the knock-on-atom processes, producing secondary recoil atom displacements which in turn displace additional atoms. The multiple displacement sequence of collision events is commonly referred to as a *collision cascade.*

Unlike the highly directed recoil implantation process, in which one atom receives a large amount of kinetic energy in a single displacement, atoms in a collision cascade undergo many multiple uncorrelated low-energy displacement and relocation events. Atomic mixing resulting from a series of uncorrelated low-energy atomic displacements is referred to as *cascade mixing.*

The ballistic interactions of an energetic ion with a solid are shown schematically in Fig. 13.6. The figure shows sputtering events at the surface, single-ion/single-atom recoil events, and the development of a collision cascade that involves many low-energy displaced atoms. The cascade is shown in the early displacement stage of development, where the displaced atoms occupy interstitial positions surrounding a core of vacant lattice sites.

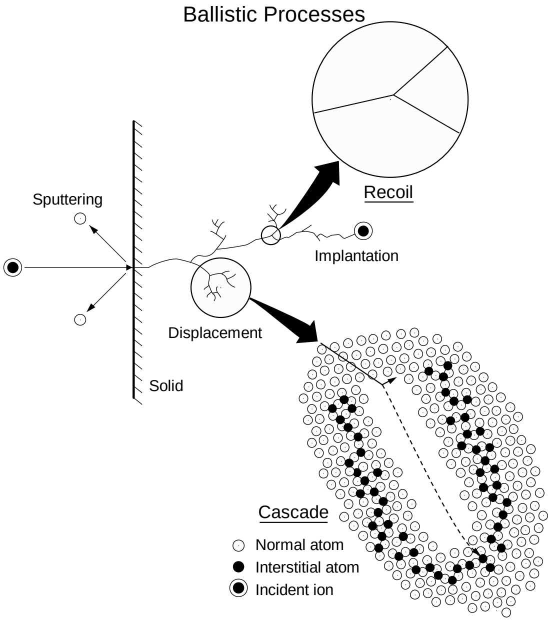

Fig. 13.6. The ballistic interactions of an energetic ion with a solid. Graphically displayed are sputtering events at the surface, single-ion/single-atom recoil events, the development of a collision cascade that involves a large number of low-energy displaced atoms, and the ion implantation of the incident ion

Calculations of the mean energy of atoms in a cascade show that most recoils are produced near the minimum energy necessary to displace atoms, E_d. Due to the low-energy stochastic nature of these displacement events, the initial momentum of the incident particle is soon lost, and the overall movement of the atoms in a collision cascade becomes isotropic. This isotropic motion gives rise to an atomic redistribution that can be modeled as a random-walk of step size defined by the mean range of an atom with energy near E_d. The effective diffusivity, D_{cas}, for a collision cascade-induced random-walk process is expressed in the diffusion equation as (Andersen 1979)

$$D_{cas}t = \frac{\mathrm{dpa}(x)\langle r^2 \rangle}{6} \tag{13.3}$$

where dpa(x) is the number of cascade-induced displacements per atom at distance x, and $\langle r^2 \rangle$ is the mean squared range of the displaced target atoms. The dpa, resulting from a given dose of ions, can be expressed as

$$\mathrm{dpa}(x) = \frac{0.4 F_D(x)\phi}{E_d N} \tag{13.4}$$

where $F_D(x)$ is the damage energy per unit length at distance x, ϕ is the ion dose, and N is the atomic density. Combining (13.3) and (13.4) gives the effective diffusion coefficient due to ballistic cascade mixing as

$$D_{cas}t = 0.067 \frac{F_D(x)\langle r^2 \rangle}{NE_d}\phi \tag{13.5}$$

Sigmund and Gras-Marti (1981) made a more detailed theoretical formulation of collisional mixing based on linear transport theory. This formulation also accounts for mass difference between the ion, M_1, and the target atom, M_2. The effective diffusion coefficient obtained from calculations examining the ion irradiation-induced spreading of an impurity profile in a homogeneous matrix is given by

$$D_{cas}t = \frac{\Gamma}{6}\xi \frac{F_D\langle r^2 \rangle}{N\,E_d}\phi \tag{13.6}$$

where Γ is a dimensionless parameter with a value of 0.608, and ξ is a mass-sensitive kinematic factor given by $[4M_1M_2/(M_1 + M_2)^2]^{1/2}$. In the case of $M_1 = M_2$, $\xi = 1$, and (13.5) and (13.6) become very similar.

The primary features of (13.5) and (13.6) are that the effective diffusion coefficient should scale with the dose, ϕ, and the damage energy, F_D, in good

agreement with the trends observed in Fig. 13.5. An additional characteristic of this expression is that it does not contain any temperature-dependent terms. The effective diffusion coefficient described by (13.5) is independent of temperature and can be compared only with experiments in which mixing also is observed to be independent of temperature. The data in Fig. 13.3 shows the influence of temperature on the mixing between Cr and Si. This data shows that ion mixing remains independent of temperature up to about 0°C.

Equation (13.5) and the marker data presented in Fig. 13.5 can be used to estimate the average atomic displacement distance of a marker atom in a collision cascade formed in a matrix of amorphous Si. For example, from the temperature-independent data in Fig. 13.5a, a typical value of $D_{irr}t/\phi$, for both Sn and Sb markers, is $4(10^{-29}$ cm$^4)$, or 0.4 nm^4. From Fig. 13.5b, the corresponding damage energy is 1,500 eV nm^{-1}. Using the atomic density of crystalline Si, 50 atoms nm^{-3}, for the amorphous Si value of N, the ratio of F_D/N will be 30 eV nm^{-4}. This indicates that $\langle r^2\rangle^{1/2}$ should be approximately 1.6 nm for a Si displacement energy of $E_d \cong 13$ eV.

13.3 Thermodynamic Effects in Ion Mixing

Chemical driving forces, which are not considered in ballistic models, play an important role in ion mixing when concentrated alloys are formed. For example, Au on Cu and W on Cu both should have the same ballistic response to ion mixing because of their nearly identical parameters (atomic density, atomic number, and atomic mass) for ion–solid interactions. The Au/Cu data shows that Au is well intermixed, while the W/Cu data shows W is relatively unchanged after irradiation, showing only signs of material loss due to sputtering. An evaluation of this data reveals that ion mixing in the Au/Cu system is ten times that observed in W/Cu (Westendorp et al. 1982). These results were attributed to the miscibility differences in the two systems: Au and Cu are completely miscible in liquid and the solid states, while W and Cu are immiscible in liquid and the solid states.

Similar observations were also made in the different ion mixing responses of Hf/Ni and Hf/Ti bilayers (van Rossum et al. 1984). Again, from a ballistic view, ion mixing for these two systems should be nearly identical. However, it was observed that the mixing rate of Hf/Ni was significantly higher than that of Hf/Ti. This difference was attributed to differences in the heat of mixing, ΔH_{mix}, for the two systems. In Table 13.1, the four bilayer systems – Au/Cu, W/Cu, Hf/Ni, and Hf/Ti – are listed, along with their values of ΔH_{mix} at the equiatomic alloy concentration, and the nuclear energy loss at the initial bilayer interface.

Table 13.1 shows that the bilayer systems that undergo extensive ion mixing (Au/Cu and Hf/Ni) possess a negative heat of mixing, while the systems that experienced little or no mixing (W/Cu and Hf/Ti) possess a zero or positive heat of mixing.

The heat of mixing, similar to the heat of alloy formation, gives a measure of how attractive different elements are to each other relative to their attractiveness to

Table 13.1. Heat of mixing and stopping in bilayer systems

bilayer system	ΔH_{mix} (kJ (gram-atom)$^{-1}$	dE/dx (eV nm^{-1})
Au/Cu	−9	31.0
W/Cu	+36	32.2
Hf/Ni	−62	32.9
Hf/Ti	0	23.5

dE/dx from SRIM. ΔH_{mix} after de Boer et al. (1989)

themselves. The enthalpy difference, ΔH_{mix}, results from the chemical joining of A and B atoms and the formation of A–B bonds during alloying. The more negative the heat of mixing, the greater the tendency to form A–B alloys.

In bilayer systems with negative heats of mixing, there is a driving force to form interface alloys during ion irradiation. Although it would seem that ion beam irradiation would intermix layered structures, thermodynamic effects can overwhelm ballistic processes. If heats of mixing are positive and the sample temperature is sufficiently low, ion irradiation can cause intermixing. However, when the sample temperature is increased, the mixed layer back-segregates into its components, a process known as *demixing.*

The mixing rate in bilayer systems is expressed as the derivative expression $\mathrm{d}(4\tilde{D}t)/\mathrm{d}\phi$, where the variable $\tilde{D}$ is the chemical interdiffusion coefficient. In Fig. 13.7, $\mathrm{d}(4\tilde{D}t)/\mathrm{d}\phi$ is plotted for several metal bilayer systems as a function of the systems' heat of mixing (heat of mixing data is taken at the 50 atomic % composition). Figure 13.7 shows that the mixing rate is thermodynamically biased. When thermodynamic driving forces are important, the mixing rate equation for bilayer mixing can be expressed as

$$\frac{4\tilde{D}t}{\phi} = \frac{4\tilde{D}_o t}{\phi}\left(1 - \frac{2\,\Delta H_{mix}}{k_B T}\right) \tag{13.7}$$

where $4\tilde{D}_o t/\phi$ is the ballistic-induced mixing term, defined as

$$\frac{4\tilde{D}_o t}{\phi} = 0.268\frac{F_D\langle r^2\rangle}{NE_d} \tag{13.8}$$

Equation (13.7) is a linear expression with ΔH_{mix}, with a slope defined by

$$\frac{4\tilde{D}_o t}{\phi}\frac{2}{k_B T} = 0.536\frac{F_D\langle r^2\rangle}{NE_d k_B T} \tag{13.9}$$

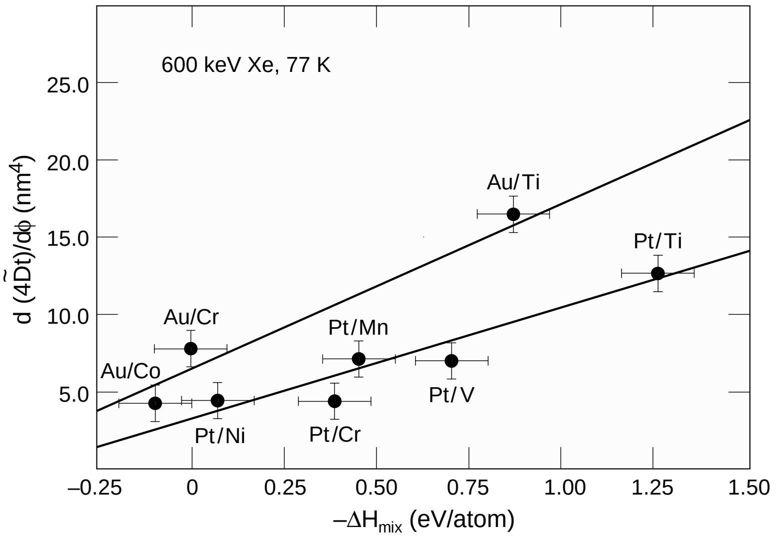

Fig. 13.7. The experimentally observed mixing rates and ΔH_{mix} for several metallic alloy systems following ion irradiation with 600 keV Xe ions and a sample temperature of 77 K. (From Cheng et al. 1984)

Reasonable average values for the ballistic terms in (13.9) are: $F_D = 5{,}500$ eV nm^{-1}, $\langle r^2 \rangle = 2.25$ nm^2, $N_0 = 74$ atoms nm^{-3}, and $E_d = 30$ eV. These values give a calculated slope of $3.0/k_B T$ nm^4 eV^{-1}. The experimental slopes (Fig. 13.10) for the Au and Pt bilayer mixing data are approximately 5 and 7.0 nm^4 eV^{-1}, respectively. Setting the experimental and calculated values equal to each other and taking $k_B = 8.63 \times 10^{-5}$ eV K^{-1} gives an effective cascade temperature of 3,310 and 4,966 K in the Au and Pt samples, respectively. The average kinetic energy of the atoms in the cascade can be estimated using the law of equipartition of energy, $E = 3/2 k_B T_{eff}$, which gives 0.43 eV atom^{-1} and 0.64 eV atom^{-1} in the Au and Pt bilayers, respectively.

A more detailed analysis of the thermodynamic influence on ion mixing by Johnson et al. (1985) resulted in the following phenomenological expression

$$\frac{\mathrm{d}4\tilde{D}t}{\mathrm{d}\phi} = \frac{K_1 F_D^2}{\bar{N}^{5/3} (\Delta H_{coh})^2} \left(1 + K_2 \frac{\Delta H_{mix}}{\Delta H_{coh}} \right) \tag{13.10}$$

where ΔH_{coh} is the cohesive energy of the alloy system; F_D is the damage energy per unit length; $\bar{N}$ is the average atomic density; and K_1 and K_2 are fitting parameters. Based upon experimentally determined mixing rates for 600 keV Xe irradiation at 77 K, the values of the fitting parameters were found to be

$K_1 = 0.0034$ nm and $K_2 = 27.4$. The cohesive energy of the alloy system composed of elements A and B are approximated by

$$\Delta H_{\text{coh}} \cong (X_A \Delta H_A^o + X_B \Delta H_B^o) + \Delta H_{\text{mix}} \tag{13.11}$$

where ΔH^0 are the cohesive energies of individual elements (see Kittel 1976), X is the atomic fraction of the elements and ΔH_{mix} alloy's heat of mixing.

Equation (13.10) is demonstrated in Fig. 13.8, which shows the experimental mixing rate $\text{d}(4\tilde{D}t)/\text{d}\phi$ (scaled by $N^{-5/3} H_{\text{coh}} F_D^{-2}$) versus the ratio $\Delta H_{\text{mix}}/\Delta H_{\text{coh}}$. The linear relationship indicates that the amount of mixing scales with $\Delta H_{\text{mix}}/\Delta H_{\text{coh}}$ and that (13.10) provides a reasonable prediction of the ion beam mixing rate in metal/metal bilayer systems irradiated with heavy ions at low temperatures.

Ballistic effects resulting from the early stages of cascade evolution are important factors in the ion mixing process, but materials properties, such as heat of mixing and cohesive energy, also influence the process. Such material properties

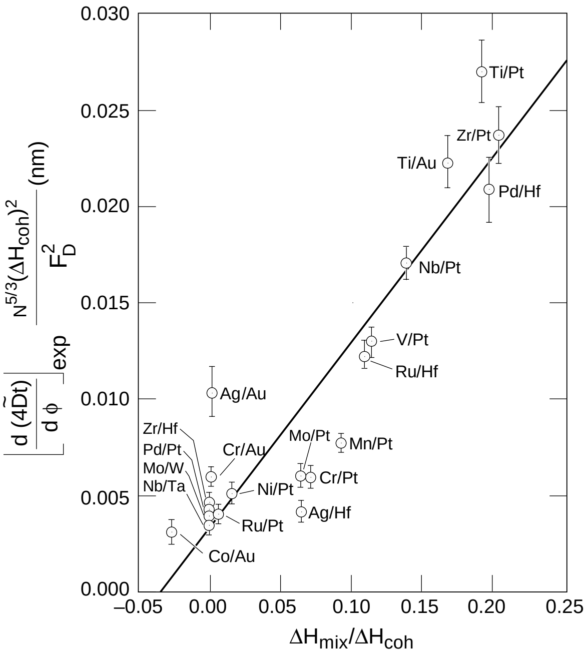

Fig. 13.8. Experimental mixing data showing a linear relationship between the mixing rate versus the ratio $\Delta H_{\text{mix}}/\Delta H_{\text{coh}}$ (after Cheng 1990)

dominate the rate of mixing and the phase formation possibilities in the ion-reacted layers, influencing the final structures that form.

References

Andersen, H.H.: The depth resolution of sputter profiling. Appl. Phys. **18**, 131 (1979)

Cheng, Y.-T.: Thermodynamic and fractal geometric aspects of ion–solid interactions. Mater. Sci. Rep. **5**, 45 (1990)

Cheng, Y.-T., van Rossum, M. Nicolet, M-A., Johnson, W.L.: Influence of chemical driving forces in ion mixing of metallic bilayers. Appl. Phys. Lett. **45**, 185 (1984)

de Boer, F.R., Boom, R., Mattens, W.C.M., Miedema, A.R., Niessen, A.K.: Cohesion in Metals. North-Holland, Amsterdam (1989)

Johnson, W.L., Cheng, Y.-T., Van Rossum, M., Nicolet, M-A.: When is thermodynamics relevant to ion-induced atomic rearrangements in metals? Nucl. Insrut. Meths. **B7/8**, 657 (1985)

Kittel, C.: Introduction to Solid State Physics, 5th edn. Wiley, New York (1976)

Matteson, S., Paine, B.M., Grimaldi, M.G., Mezey, G., Nicolet, M.-A.: Ion beam mixing in amorphous silicon. I. Experimental investigation. Nucl. Instrum. Meths. **182/183**, 43 (1981)

Mayer, J.W., Lau, S.S.: In: Poate, J.M., Foti, G., Jacobson, D.C. (eds.) 'Ion Beam Mixing', Surface Modification and Alloying by Laser, Ion, and Electron Beams, p. 241. Plenum, New York (1983)

Mayer, J.W., Lau, S.S., Tsaur, B.Y., Poate, J.M., Hirvonen, J.K.: In: Preece, C.M. Hirvonen, J.K. (eds.) High-Dose Implantation and Ion-Beam Mixing, Ion Implantation Metallurgy, p. 37. The Metallurgical Society of AIME, New York (1980)

Sigmund, P., Gras-Marti, A.: Theoretical aspects of atomic mixing by ion beams. Nucl. Instrum. Meths. **182/183**, 25 (1981)

Tsaur, B.Y., Lau, S.S., Liau, Z.L., Mayer, J.W.: Ion-beam induced intermixing of surface layers. Thin Solid Films **63**, 31 (1979)

van der Weg, W.F., Sigurd, D., Mayer, J.W.: In: Picraux, S.T., EerNisse, E.P., Vook, F.L. (eds.) Ion Beam Induced Intermixing in the Pd/Si System, Applications of Ion Beams to Metals, p. 209. Plenum Press, New York (1974)

van Rossum, M., Shreter, U., Johnson, W.L., Nicolet, M-A.: Amorphization of thin multilayer films by ion mixing and solid state amorphization. Mat. Res. Soc. Symp. Proc. **27**, 127 (1984)

Westendorp, H., Wang, Z.-L., Saris, F.W.: Ion-beam mixing of Cu–Au and Cu–W systems. Nucl. Instrum. Meths. **194**, 543 (1982)

Suggested Reading

Averback, R.S.: Fundamental aspects of ion beam mixing. Nucl. Instrum. Meths. **B15**, 675 (1986)

Besenbacher, F., Bottiger, J., Nielsen, S.K., Whitlow, H.J.: Short- and long-range ion-beam mixing in Cu:Al. Appl. Phys. **A29**, 141 (1982)

Johnson, W.L., Cheng, Y.-T., Van Rossum, M., Nicolet, M.-A.: When is thermodynamics relevant to ion-induced atomic rearrangements in metals? Nucl. Instrum. Meths. **B7/8**, 657 (1985)

Mayer, J.W., Lau, S.S.: Ion beam mixing. In: Poate, J.M., Foti, G., Jacobson, D.C. (eds.) Surface Modification and Alloying by Laser, Ion, and Electron Beams, p. 241. Plenum, New York (1983)

Nastasi, M., Mayer, J.W.: Ion beam mixing in metallic and semiconductor materials. Mater. Sci. Rep. **R12**, 1 (1994)

Problems

13.1 The mean square diffusion distance $\overline{x}^2$ for a random-walk diffusion process is $\overline{x}^2 = nr^2 = 6Dt$, where n is the number of jumps and r is the jump distance. Assume that the cascade volume can be modeled by a gas, then $n = \overline{v}t/r$ where $\overline{v}$ is the mean speed of the ions in the cascade. Assume that the energy deposited in the cascade is 1 eV atom^{-1} and that the cascade lifetime is 10^{-11} s

(a) What is D in the cascade?

(b) What is $\overline{x}$?

13.2 Using the thermodynamic equations for mixing [(13.7) and (13.8)] and assuming a deposited energy $F_D(E) = 4 \times 10^3$ eV nm; atomic density $N = 6 \times 10^{22}$ atoms cm^{-3}; displacement energy $E_d = 25$ eV; and $\Delta H_{mix} = 90$ kJ g-atoms^{-1},

(a) What is the cascade temperature for $4Dt/\phi = 15$ nm^4 and $\langle r^2\rangle^{1/2} = 1$ and 5 nm?

(b) What is the cascade temperature for $4Dt/\phi = 30$ nm^4 and $\langle r^2\rangle^{1/2} = 1$ and 5 nm?

13.3 Using (13.11), calculate the average alloy cohesive energy in eV atom^{-1} assuming $X_A = X_B = 0.5$ for

(a) Ni/Al ($\Delta H_{mix} = 12.2$ kcal mol^{-1})

(b) Au/Ag ($\Delta H_{mix} = 0$)

(c) C Pt/Ti ($\Delta H_{mix} = 30$ kcal mol^{-1})

13.4 Calculate the mixing rate [(13.10)] using the thermodynamic model for Ni/Al, Au/Ag, and Pt/Ti assuming a deposited energy of $F_D = 500$ eV nm^{-1}.

13.5 Calculate $\langle r^2\rangle^{1/2}$ for a system with $N = 6 \times 10^{22}$ atoms cm^{-3} under irradiation conditions where $D_{irr}t/\phi$ is 0.5 nm^4 and F_D is 2,000 eV nm.

(a) If A is the sputtering species, the sputtering yield Y must be below what value if the ratio of A/B is to exceed unity at steady state?

14 Application of Ion Implantation Techniques in CMOS Fabrication

Contributed by Lin Shao, Los Alamos National Laboratory

14.1 Introduction

This chapter deals with ion implantation in complementary metal oxide semiconductor (CMOS) fabrications. CMOS has become the dominant MOS technology since its invention in the 1960s. The number of transistors integrated on a die tends to double every 14–18 months. This is known as Moore's Law. This requires a continuous reduction in the size of CMOS devices. Given that there is greater complexity in fabricating n- and p-channel CMOS devices relative to other devices, reducing the size of CMOS devices faces fundamental physical limitations, such as short-channel effects and hot-electron effects. These issues will be discussed later in this chapter. Some of these complexity-derived limitations have been alleviated by the use of ion implantation, which is well suited for current integration processes.

14.2 Issues During Device Scaling

To maintain a proper device function during device size scaling, the threshold voltage, V_T, must not change significantly. The threshold voltage is defined as the value of the gate voltage needed to induce a conducting channel under the gate oxide. The threshold voltage is given by

$$V_T = V_{ms} + V_{ox} + V_d + V_i \tag{14.1}$$

where V_{ms} is the *work function* difference between the gate and the Si substrate. The work function of a material is the minimum amount of work required to move an electron from its Fermi level to the vacuum level. V_{ox} denotes the fixed charge at the oxide–silicon interface. V_d is due to the charge in the depletion region, and V_i is the voltage needed to invert the surface. A major component that contributes to the threshold voltage is V_d, which can be expressed as

$$V_d = Q_B / C_{ox} \tag{14.2}$$

where C_{ox} is the oxide capacitance per unit area, and Q_B is bulk charge, which is controlled by the gate. One basic model to estimate the effect of device scaling on the change in V_T was given by Yau (1974). Figure 14.1a–c shows a three-dimensional sketch of a NMOSFET with its cross-section views. The key in Yau's model is the introduction of a trapezoidal region representing the gate-controlled charge. The charge beyond that region (shaded area) is controlled by the source and drain. By subtracting the shaded triangular region from the rectangular region, the charge controlled by the gate is given by

$$\begin{aligned} Q_B &= \text{area(EFHG)} - 2 \times \text{area(AGH)} \\ &= qN_B\left(\text{WLW}_c - 2W\frac{\Delta L W_c}{2}\right) \end{aligned} \tag{14.3}$$

where q is the electric charge, N_B is the channel doping concentration, W is the width of the device, and L is the gate length. The model has assumed that source, drain, and gate have the same depletion width, W_c. The value of ΔL in (14.3) can be obtained by using a triangle encompassed by ABC, as shown in Fig. 14.2c. Hence

$$(\Delta L + r)^2 + W_c^2 = (W_c + r)^2 \tag{14.4}$$

where r is a radius of curvature, which describes the lateral and vertical depth of source and drain junctions. Combining the above equations allows Q_B to be expressed as

$$Q_B = qN_B\text{WLW}_c\left\{1 - \left[\left(1 + \frac{2W_c}{r}\right)^{1/2} - 1\right]\frac{r}{L}\right\} \tag{14.5}$$

Equation (14.5) describes the total depletion charge in the channel that is terminated on the gate. It should be noted that the gate length, L, in (14.3) and (14.5) is the effective gate length, which has taken into the account the lateral dopant diffusion of source and drain junctions under the gate. L is less than the physical gate length, as shown in Fig. 14.1b.

One important conclusion resulting from (14.5) is that the threshold voltage depends not so much on the actual value of r, but on the ratio of r to the gate length, L. The requirement that the depth of the source and drain junctions should be scaled linearly with the gate length is one important rule guiding device scaling. The physical gate length of MOSFET has been reduced from 10 μm in the 1970s to a present day size of sub-100 nm. Correspondingly, the depths of source and drain junctions have been reduced from a few microns to sub-100 nm.

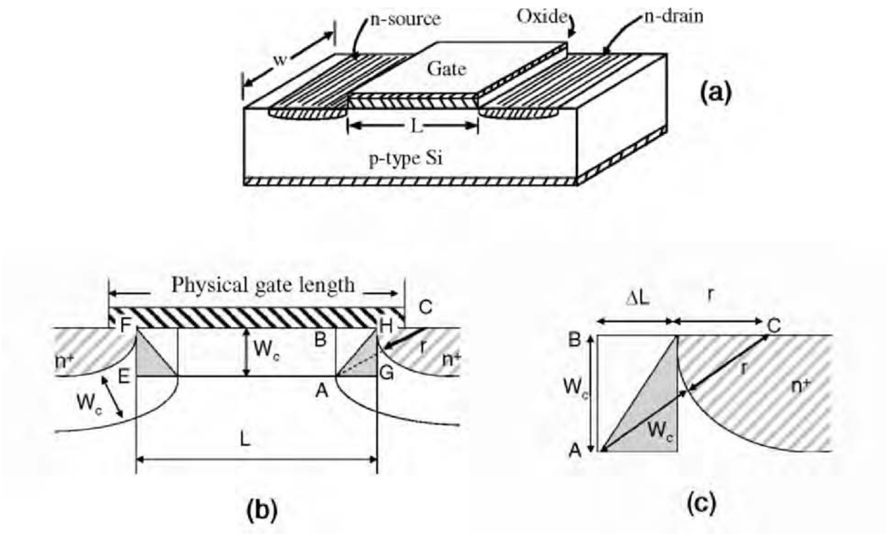

Fig. 14.1. Three-dimensional sketch (**a**) and cross-section view (**b**) of an NMOSFET, with an enlarged cross section to show the triangle encompassed by ABC (**c**) for Yau's model

However, the anomalous dopant diffusion that occurs during activation annealing imposes a critical challenge in obtaining a small value of *r*. Advances are needed to economically produce shallower implants with greater control of dopant diffusion. Such requirements have greatly affected the development of high-current (> 1 mA) ultra low energy (< 0.5 keV) implanters.

14.2.1 Short-channel Effects

As device dimensions are reduced from the long-channel case to the short-channel cases, source and drain will be in closer proximity. Under such conditions the source and drain depletion regions can extend into the channel. When the bias is increased, the increased drain depletion region can lower the barrier potential, as illustrated in Fig. 14.2a, b. This phenomenon is called drain-induced barrier lowering. Reducing the barrier height results in the loss of gate control. For the extreme conditions of the intrusion of the source and drain depletion regions into the channel region, the punch-through effect happens, in which a continuous depleted region is formed from source to drain. For this condition, the current between source and drain becomes independent of the drain voltage, and easy diffusion of electrons from source and drain prevents the gate control of the current.

The short-channel effect is closely related to the lateral spreading of dopants from the source and drain areas to the gate region, which is contributed by two effects:

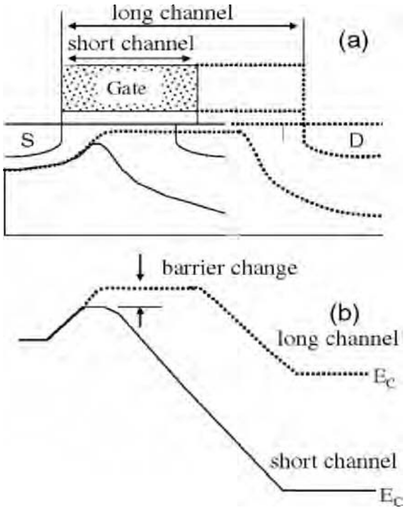

Fig. 14.2. Schematic illustration of (**a**) the intrusion of the source and drain depletion regions and (**b**) conduction band energy along the surface. The *dotted line* represents the long-channel condition, and the *solid line* represents the short-channel condition (after Muller and Kamins 1986)

ion straggling during dopant implantation and the anomalous dopant diffusion during thermal annealing (see Chap. 9, Sect. 5). A physical picture of these two effects can be obtained with the help of the modeling program Stanford University Process Engineering Modeling (SUPREM, Law et al. 1986), which accounts for ion straggling and dopant diffusion during the activation annealing process.

Figure 14.3a, b shows the calculated two-dimensional boron atom distributions, obtained by using SUPREM for 5 keV boron implantation through a 100 nm wide aperture, before and after subsequent annealing at 1000°C for 10 s. The maximum lateral penetration depth (measured at the boron concentration of 1×10^{18} cm^{-3}) is around 100 nm for the as-implanted profile and around 200 nm for annealed profiles. This anomalous lateral spreading of dopants shows the severe challenge to the device scaling. The vertical and lateral spreading of dopants can be alleviated, but not eliminated, by using ultra low energy ion implantations. All group IV and group V dopants show defect-enhanced diffusion phenomena called *transient enhanced diffusion* (TED) (see Chap. 9, Sect. 5). For n-type dopants such as As and Sb, their diffusion is mediated by interaction with vacancies. The diffusion of the p-type dopant B, on the other hand, is mediated by the interaction with Si self interstitials. As and Sb have larger masses compared with B. The heavier mass more easily creates an amorphous substrate layer during ion implantations. Diffusivities of As and Sb are also slower than that of B. Therefore, the formation of B-doped p^+ ultra shallow junctions is more challenging than that of n^+ shallow junctions.

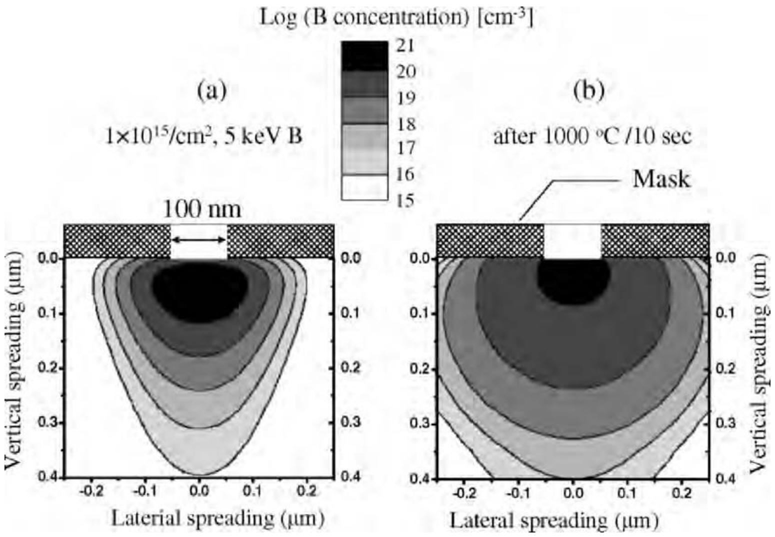

Fig. 14.3. Two-dimensional boron atomic distributions before and after annealing (calculated by Hong-Jyh Li at International SEMATECH)

14.2.2 Hot-Electron Effect

In p-channel transistors, holes are accelerated from the source to the drain. The velocity of the hole during this acceleration process can sometimes be high enough to create electron-hole pairs in the channel by collision. The penetration of holes into the oxide is difficult due to the high potential barrier at the silicon and gate oxide interface; such a barrier for electrons, however, is low. The electrons created from electron-hole pair generation can be scattered into the gate oxide. Therefore, negative charge is built up in the oxide. This charge accumulation in the oxide can cause holes to accumulate below the gate, as illustrated in Fig. 14.4. The hot-electron effect causes a reduction in channel length and makes the device more susceptible to short-channel effects. One effective way to reduce the hot-electron effect is to reduce the high electric field in the channel region. The maximum electric field usually takes place at the boundary between the channel and the highly doped source/drain region. The electric field can be reduced by forming lightly doped-drain (LDD) structures. The details of the LDD doping method will be further discussed in Sect. 14.3.

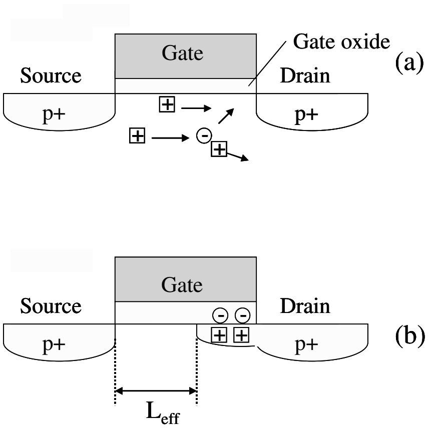

Fig. 14.4. Schematic illustration of hot-electron effects (**a**) avalanche multiplication in the channel and (**b**) hot-electron-induced channel shortening

14.2.3 Latchup

CMOS devices can develop a serious problem called *latchup*, in which junctions in different devices connect and form a forward-biased diode structure, leading to a catastrophic current which destroys the circuit. As illustrated in Fig. 14.5a, the latchup is caused by the formation of a pnpn device between the terminal of VSS and VDD (see Chap. 9, Sect. 1.3). In a latchup condition, the pnpn device is biased such that the collector current of the pnp bipolar transistor supplies a base current to the npn bipolar transistor in a positive feedback situation. The latchup can cause device function failure or even self-burnout. Figure 14.5b shows the bipolar components and resistive components of a latchup configuration. The conduction state of a pnp device requires $V_E < V_B << V_C$, and the conduction state of a npn device requires $V_E > V_B >> V_C$, where V_E, V_B, and V_C are electric potentials of the emitter (E), the base (B), and the collector (C) (see Chap. 9, Sect. 1.1). In both cases, the devices will be turned “off” if $V_B \sim V_E$ or $V_B \sim V_C$. Therefore, the latchup can be minimized by making the resistances of R_S and R_W in Fig. 14.5b as small as possible, or by physically separating the base from the collector of the two transistors. In Sect. 14.3, we will discuss how ion implantation is used in CMOS fabrication to form retrograde wells for the purpose of reducing latchup.

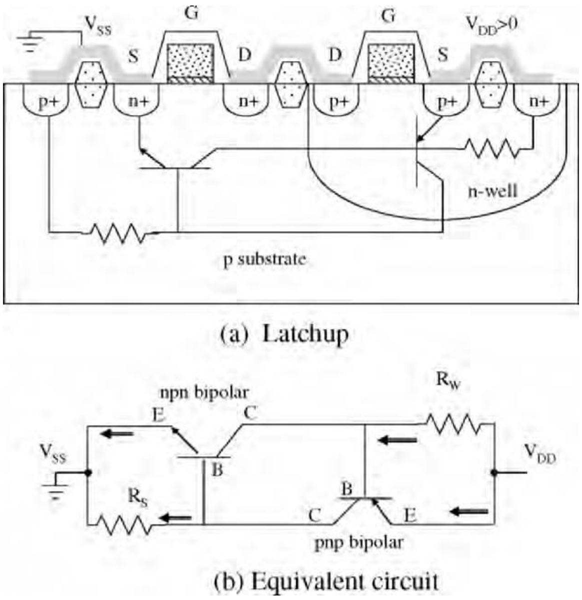

Fig. 14.5. Schematic illustration of a pnpn device made up by (**a**) a CMOS device and (**b**) its equivalent circuit

14.3 Ion Implantation in Advanced CMOS Device Fabrication

In the mid 1950s, the process of ion implantation of Group III or Group V ions with sufficient energy to penetrate the surface and to change the internal conductivity was disclosed. The importance of the thermal annealing process to anneal out the irradiation-induced damages and to activate dopants was gradually recognized in the middle 1960s. In the late 1960s and early 1970s, ion implantation supplanted predeposition by diffusion as the primary method of junction formation and doping in semiconductor industry. Today, ion implantations have been used for almost all doping processes in device fabrication.

With decreasing CMOS device size, short-channel effects become severe (see Sect. 14.2). To improve device performance, multiple ion implantations have been used to fabricate advanced CMOS devices. The standard fabrication process, as illustrated in Fig. 14.6a–e, starts from a high energy dopant implantation to form a retrograde well, then a medium energy dopant implantation for a punch-through-stop, and a low energy dopant implantation for threshold voltage adjustment. After gate patterning, source (S) and drain (D) extension ion implantation, and high

angle tilted implants, called *halo implants,* are performed. Finally, the deep S/D ion implantations are performed after the formation of gate spacers. To achieve different implantation purposes, the dose and the energy requirement of the above implantations can vary by several orders of magnitudes. Figure 14.7 shows the desired dose and energy for the above implantations. The aim of each implantation step will be further discussed in the following sections.

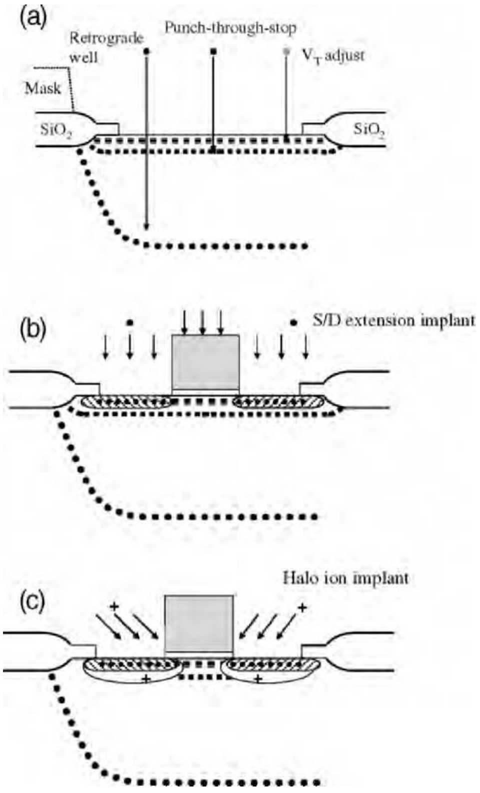

Fig. 14.6. Application of ion implantations in advanced CMOS structure at several stages of the process. (**a**) Ion implants for retrograde well formation, punch-through-stop, and threshold voltage adjust; (**b**) shallow source/drain (S/D) implant and (**c**) halo implant

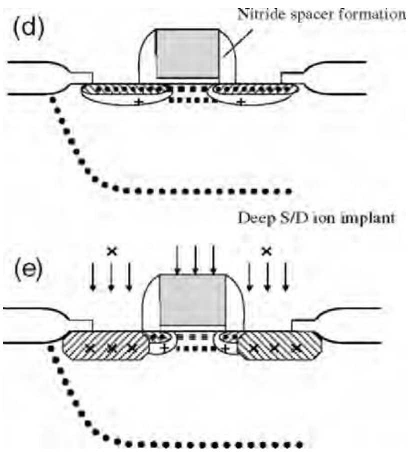

Fig. 14.6. Application of ion implantations in advanced CMOS structure at several stages of the process. (**d**) Nitride spacer formation; and (**e**) deep source/drain (S/D) implant

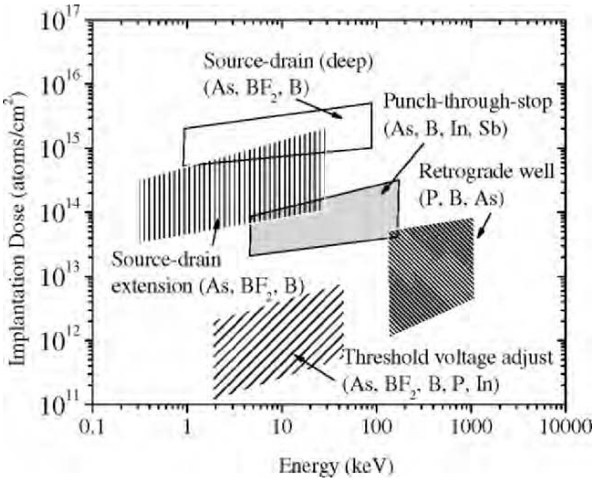

Fig. 14.7. Dose and energy requirement for major implantations steps in CMOS device fabrications (modified from Rubin and Poate 2003)

14.3.1 Retrograde Well Implant

Retrograde wells are formed by high energy dopant implantations, usually in the energy region of 0.1–2 MeV. Such wells are characterized by a peak concentration at a depth about 1 μm below the surface. Previously, well structures were formed using *conventional well formation*, in which low energy dopant implantation is performed and followed by a long time thermal process for dopant drive-in diffusion. Conventional wells are characterized by a peak concentration at the surface. Figure 14.8 shows the typical doping profiles in retrograde wells and conventional wells. Compared with conventional wells, the retrograde wells provide some advantages (1) only a very small thermal budget is needed for deep well formation and (2) the peak of the dopant concentration is buried at a deep depth instead of at the surface. Therefore carrier scattering by dopants is reduced and the carrier mobility at the channel region (surface) is increased.

The use of high-energy ion implantation makes alternative well formation schemes possible. In the so-called twin well process, two separate wells for n- and p-channel transistors are formed in a lightly doped substrate. The twin well structure, as illustrated in Fig. 14.9, has the advantages of independent adjustment and optimization of n-channel or p-channel devices. Devices fabricated using a twin well processes are independent of the original substrate type. More important, twin well structures reduce the resistance across the base and the emitter of both npn and pnp bipolar transistors (RS and RW in Fig. 14.2.3). Therefore, the latchup is greatly reduced.

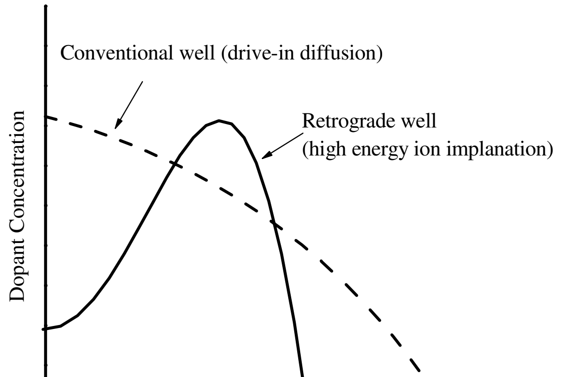

Fig. 14.8. Schematic dopant distributions in a conventional well formed by the drive-in diffusion and in a retrograde well formed by high energy implantation

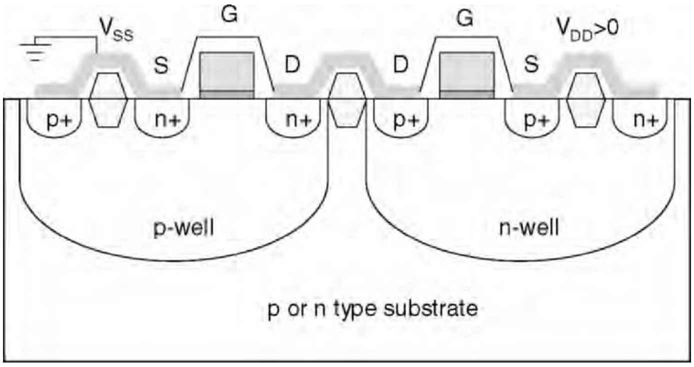

Fig. 14.9. Schematic illustration of a twin well CMOS device

14.3.2 Punch-Through-Stop Implant

The second implant in substrate engineering is the punch-through-stop implant. It is an implant of extra dopants to keep the gate and drain confined and to prevent the expansion of the drain depletion region into the source and gate field. Therefore, short-channel effects such as punch-through and drain-induced-barrier-lowering can be alleviated. To keep an abrupt doping profile, typically a slow diffusing dopant species is used for punch-through stop implants; arsenic or antimony is used for PMOS and indium is used for NMOS transistors.

14.3.3 Threshold Adjust Implant

The substrate doping below the gate determines the threshold voltage of the transistors. The device doping level can be adjusted by the *threshold adjust implant*; the voltage properties of the device are ideal when the threshold voltage of the NMOS and PMOS transistors are of equal magnitude, and as low as possible. For example, the threshold voltage of a n^+ polycrystalline silicon gate can be easily adjusted from 0 to +1 V with a substrate doping range of 10^{15}–10^{17} cm^{-3}.

Equation (14.1) in Sect. 14.2 discusses the various contributions to the threshold voltage, V_T. It shows that

$$V_T = V_{ms} + V_{ox} + V_d + V_i$$

For a given choice of gate materials, the gate oxide thickness, t_{ox}, and the doping concentration, N_B, are two parameters which can be used to adjust the threshold voltage. t_{ox} determines the value of V_{ox} by

$$V_{ox} = -\frac{Q_{ox}}{C_{ox}} = -\frac{Q_{ox}}{(\varepsilon_{ox}/t_{ox})} \tag{14.6}$$

where Q_{ox} is the fixed charge at the oxide–silicon interface, C_{ox} is the oxide capacitance per unit area and ε_{ox} is the permittivity of SiO_2.

The substrate doping, N_B, affects the threshold voltage through both V_d and V_i by

$$V_d = -qN_B x_d / C_{ox} \tag{14.7}$$

where x_d is the depletion-layer width beneath the gate, and by

$$V_i = \frac{2kT}{q} \ln \frac{N_B}{n_i} \tag{14.8}$$

where n_i is the intrinsic carrier concentration.

It is obvious from (14.7) and (14.8) that the threshold voltage can be adjusted to the desired level by increasing the doping level through a low energy ion implantation into the channel region. For simplicity, assuming that a shallow ion implantation creates a boxlike shape profile of dopants with an uniform concentration of N_i over a depth of x_i, the dopant concentration for a depth $< x_i$ is given by $N_B + N_i$, where N_B is the substrate doping concentration before adding a threshold adjust implant. For a depth $> x_i$, the dopant concentration is given by N_B. The implantation causes a shift in the threshold voltage, ΔV_T, given approximately by (Jaeger 1988)

$$\Delta V_T = (1/C_{ox})(qQ_i)(1 - x_i/2x_d), \quad x_i \ll x_d \tag{14.9}$$

where $Q_i = x_i N_i$ represents the implanted dose, and x_d represents the depletion-layer width beneath the gate. The threshold-voltage shift is negative for donor impurities and positive for acceptor impurities. An example of this technique is shown in Fig. 14.10, where the threshold voltages of both n-type (V_{Tn}) and p-type (V_{Tp}) transistors are adjusted and have positive shifts that increase with increasing boron implant doses.

14.3.4. Source and Drain Implant

As described in (14.5), when the gate length of a device is scaled down, the junction depth of the source and drain must be made very shallow. In addition to that, the maximum channel electric field, which occurs at the drain end of the channel, must be reduced or carriers may acquire sufficient energy from the electric field to give rise to electron-hole pair production. This hot-electron effect poses a limit to device scaling, since the electric field tends to increase with reduced device geometries. The hot-electron effects can be reduced by adding a lightly doped buffer region between the heavily doped drain and the channel; this significantly reduces the maximum electric field. Such a structure, called the LDD, can be fabricated by the process illustrated in Fig. 14.6a–e, in which source and drain extensions are formed first by using low dose and low energy dopant implantations. After the formation of the nitride spacers, the higher dose and higher energy dopant implantations are then followed to form the source/drain region by using the spacers as masks. Fig. 14.11 compares the electric-field distribution for a conventional device and a LDD device, where the electric filed is reduced in the LDD structures.

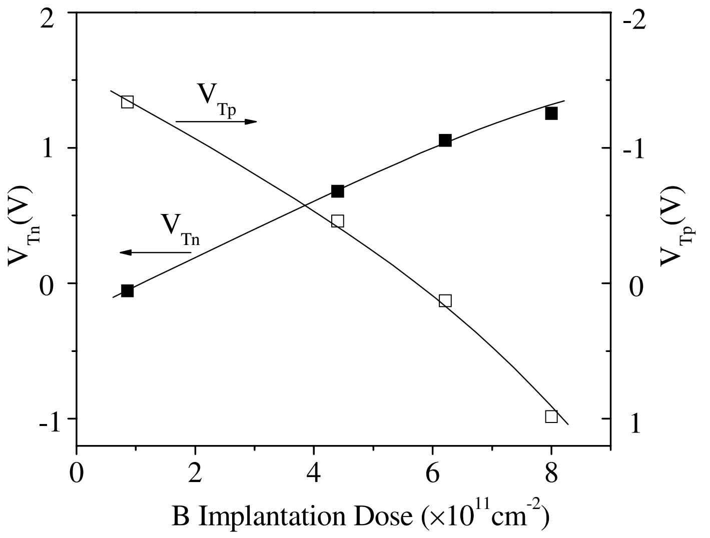

Fig. 14.10. Threshold voltages of n-channel (V_{Tn}) transistors and p-channel (V_{Tp}) as a function of boron implantation doses (Ohzone et al. 1980)

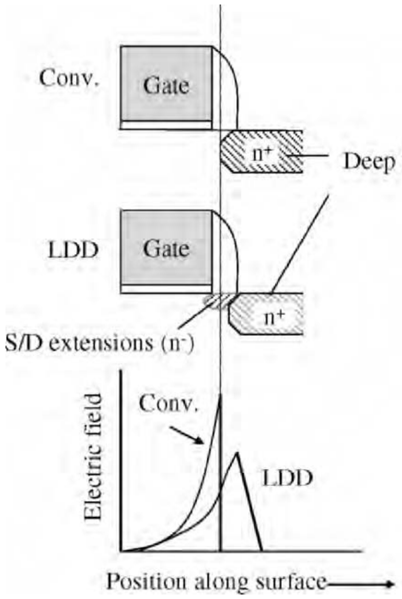

Fig. 14.11. Schematic diagrams comparing the channel electric-field distribution of conventional device and LDD device

14.3.5 Halo implant

The halo implant is a high-angle implant usually introduced in the same lithography step used to dope the source/drain extension regions, which is after polysilicon gate patterning but before nitride spacer formation. Halo implants need to be performed with four 90° rotations of the wafers to ensure both sides of the differently orientated transistors are doped. The halo implant uses the same types of dopants used in the punch-through-stop implants. It creates a nonuniform channel doping profile around the source and drain extensions. The halo implant, together with the punch-through-stop implant, helps to reduce short-channel effects. By introducing halo implants, the dose needed for punch-through-stop implants can be reduced. This helps to enhance carrier mobility in the channel region since the density of carrier scattering centers (dopants) is reduced.

14.3.6 Gate Implant

At the same time as source/drain implantation, the polycrystalline silicon gates are simultaneously doped by ion implantation. After the source/drain/gate doping, a rapid thermal anneal is required to activate the dopants and repair lattice damages created by the implantation. Different from diffusion in monocrystalline bulk silicon, dopant diffusion in the polycrystalline silicon gate material is very fast. This is due to the grain boundaries in polycrystalline silicon, which provide dopants with quick diffusion pathways (Wolf and Tauber 1986). This rapid diffusion of dopants results in a more uniform doping distribution at short annealing times. Phosphorus, boron, and arsenic are usually used for gate doping. It is critical that the dopants do not diffuse into the channel region. The presence of a thin oxide layer between the polycrystalline silicon gate and the substrate is sufficient to block most of the diffusion. However, if some of gate dopants penetrate through the oxide layer, an undesired threshold voltage variation will occur (Schaber 1985).

Dopant penetration can be a serious issue for alternative high-permittivity (high-*k*) gate dielectric materials. One typical example is HfO_2. It has been reported that the dopant penetration through HfO_2 is accelerated by the presence of grain boundaries that form when an amorphous HfO_2 layer is transformed into a polycrystalline layer after high temperature annealing (Quevedo-Lopez et al. 2002). To reduce dopant penetration, several different approaches have been proposed, which include either incorporating other impurities into the dielectric layer or by depositing a thin intermediate buffer layer between the polycrystalline silicon gate and the gate dielectric layer (Park et al. 2000).

14.4 Issues of Ion Implantations During Device Scaling

Shrinking devices demand a higher level of control of the ion implantation dose and ion energy purity. Extreme low energy ion beams with high beam currents are of crucial importance to achieve the production needs of CMOS devices with physical gate lengths less than 100 nm. Both conditions require the production of new implant tools that can minimize space charge effects, energy contamination, and beam shadowing effects.

14.4.1 Space Charge Effects

During ion beam transport along the beam line, the beam will experience a blow-up as a consequence of the mutual repulsion of the charged particles. The magnitude of this space-charge phenomenon is related to the charge-state, Z, the beam energy, E, and the mass of particles, m. The space charge effect can be approximated by Kanaya et al. (1972)

$$I \propto \left(\frac{Z}{m}\right)^{1/2} E^{3/2} \qquad (14.10)$$

where I is the beam current extracted from the source. Since the beam current scales as beam energy to the power of 3/2, the device fabrication throughput will be significantly reduced for low energy implantations. Due to the space charge effect, the drift mode, in which the extraction voltage of ions from the source equals the final beam energy, is being replaced by the *deceleration mode*, in which a reverse bias is applied to decelerate the high energy ions down to the final desired energy.

14.4.2 Energy Contamination

One issue associated with the deceleration mode approach is charge exchange and beam neutralization, which occur when the ion beam interacts with residual gases in the beam lines. If ion neutralization happens during the deceleration process, neutralized ions will not undergo any further deceleration. As a consequence, a portion of the beam will have higher energies due to incomplete deceleration. The extra radiation damage that comes from high energy ions increases the TED of dopant implants (Shao et al. 2004). Reducing the beam line pressure can minimize the charge exchange process and ion energy contamination. Lowering injection (initial acceleration) beam energies can further reduce energy contamination because the charge exchange cross section between energetic ions and residual gases decreases with ion energy.

14.4.3 Beam Shadowing Effect

Coulomb repulsion between charged ions in the ion implanter can cause the beam to blow up. Furthermore, when the beam is not perfectly vertical to the mask, asymmetrical source and drain doping will occur. Figure 14.12 shows a schematic of beam blow-up and also of the doping effect from beam shadowing effect. Beam blow-up by the Coulomb explosion process can be reduced by adding an electron flood gun to the implanter. The electron shower results in a charge neutralization by forming a mixture of positively charged dopant ions and negatively charged electrons, thereby reducing beam divergence. The beam shadowing effect can be further reduced by decreasing the mask thickness.

14.5 The Role of Ion Implantations in Device Fabrications

As this chapter has shown, ion implantation is an essential technology in the production of semiconductor devices. In addition, it plays a key role in sustaining the rapid pace of development required by the ever evolving semiconductor industry.

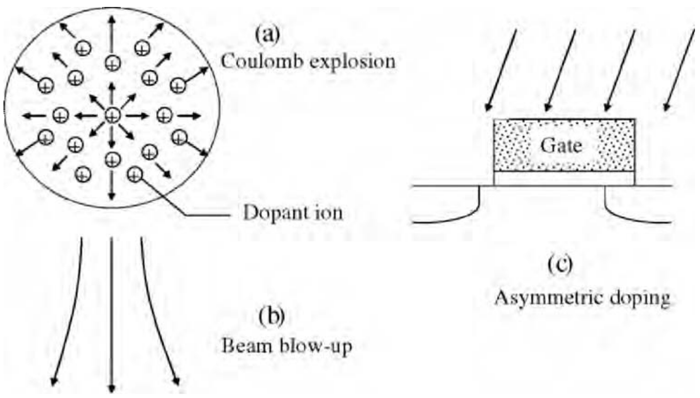

Fig. 14.12. Schematic illustration of (**a**) Coulomb explosion of the beam, (**b**) beam blow-up and (**c**) the asymmetric doping caused by tilted beam

Before the implementation of ion implantation in semiconductor device fabrications, semiconductors could not be properly termed "doped" because of severe contamination issues that arose during the then state-of-the-art drive-in diffusion doping process. These contamination issues were completely eliminated by the advent of semiconductor doping by ion implantation. The unique features of ion implantation relevant to device fabrication are its accurate control of the dose, depth, and purity of the implanted ions; high processing throughput; and high reproducibility of the doping process.

As we discussed in this chapter, ion implantation also plays a crucial role in device scaling. In fact, today's integrated circuits would not be possible without implantations. Furthermore, the design evolution of transistor electronics has been critically linked to the progress in the development of high current ion implanters at ever lower and higher energies. Continuing trends towards smaller device sizes are pushing ion implantation into previously unexplored territory. While these trends present significant challenges in device development, it is clear that doping by ion implantation is the tool of choice to meet these and future challenges in the evolution of the semiconductor industry.

References

Jaeger, R.C.: Modular series on solid state devices. In: Neudeck, G.W., Pierret, R.F. (eds.) Introduction to Microelectronic Fabrication, vol. V. Addison-Welsley, Massachusetts (1988)

Kanaya, K., Koga, K., Toki, J.: Phys E: Sci. Instrum. **5**, 641–648 (1972)

Law, M.E., Rafferty, C.S., Chin, G., Lin, C.C., Hansen, S.E.: User's Reference Manual (SUPREM), Stanford University (1986)

Muller, R.S., Kamins, T.I.: Device Electronics for Integrated Circuits, 2nd edn. Wiley, New York (1986)

Ohzone, T., Shimura, H., Tsuji, K., Hirao, T.: Silicon-gate n-well CMOS process by full ion-implantation technology. IEEE Trans. Electron Devices, **27**, 1789 (1980)

Park, D-G., Cho, H-J., Yeo, I-S., Roh, J-S., Hwang, J-M.: Boron penetration in p^+ polycrystalline-Si/Al_2O_3/Si metal-oxide-semiconductor system. Appl. Phys. Lett. **77**, 2207–2209 (2000)

Quevedo-Lopez, M.A., El-Bouanani, M., Kim, M.J., Gnade, B.E., Wallace, R.M., Visokay, M.R., Li-Fatou, A., Bevan, M.J., Colombo, L.: Phosphorus and arsenic penetration studies through HfSi xOy and HfSi xOyNz films. Appl. Phys. Lett. **81**, 1609–1611 (2002)

Rubin, L., Poate, J.: Ion Implantation in silicon technology. Indus. Physicist **9**(3), 12 (2003)

Schaber, H., Criegern, R.V., Weitzel, I.: Analysis of polycrystalline Si diffusion sources by secondary ion mass spectrometry. J. Appl. Phys. **58**, 4036–4042 (1985)

Shao, L., Chen, J., Zhang, J., Tang, D., Patel, S., Liu, J., Wang, X., Chu, W-K.: Using point defect engineering to reduce the effects of energy nonmonochromaticity of B ion beams on shallow junction formation. J. Appl. Phys. **96**, 919–921 (2004)

Wolf, S., Tauber, R.N.: Silicon Processing for the VLSI Era Voluml-Process Technology, pp. 261. Lattice, California (1986)

Yau, L.D.: A simple theory to predict the threshold voltage of short-channel IGFET's. Solid State Electron **17**, 1059–1063 (1974)

Suggested Readings

Einspruch, N.G., Gildenblat, G.S.: VLSI Electronics Microstructure Science, Advanced MOS Device Physics, vol. 18. Academic, California (1989)

Ghandi, S.K.: VLSI Fabrication Principles: Silicon and Gallium Arsenide. Wiley, New York (1994)

Grove, A.S.: Physics and Technology of Semiconductor Devices. Wiley, New York (1967)

Mayer, J.W., Lau, S.S.: Electronic Materials Science: For Integrated Circuits in Si and GaAs. Macmillan, New York (1990)

Rimini, E.: Ion Implantation: Basics to Device Fabrication. Kluwer, Boston (1995)

Sze, S.M.: VLSI Technology. McGraw-Hill, New York (1988)

Problems

14.1 In the drift mode (defined in Sect. 14.1.1), an ion implanter is used to extract 10 keV B^+ ions and the measured B^+ beam current is 2 mA. If the same implanter is used to extract 1 keV B^+ ions, what is the estimated B^+ beam current?

14.2 The same implanter in 14.1 is modified into deceleration mode (defined in Sect. 14.1.1), in which a reverse bias of E_1 (10 keV) is applied to the

ions after beam extraction. The final energy of B ions is determined by E_0–E_1, where E_0 is the extraction voltage. Assuming space charge effect only happens during beam extraction, what is the B^+ beam current for 1 keV B^+ ion implantation?

14.3 The same implanter in 14.1 (drift mode) is modified to extract BF_2^+ ions, instead of B^+ ions, in order to get same doping effect as that of 1 keV B^+ ion implantation
(a) What is the extracting energy for BF_2^+ ion implantation?
(b) What is the beam current of BF_2^+ ions?

14.4 In order to increase throughput of ion implantation, large beam current is required. Compare the beam currents of 1 keV B implantation obtained from the case of 14.1–14.3. Which one is the best to obtain a large beam current?

This page intentionally blank

15 Ion Implantation in CMOS Technology: Machine Challenges

Contributed by Aditya Agarwal[1], Hans-Joachim Gossmann[1], Michael Graf, Thomas Parrill[2], Leonard Rubin, and John Poate[3] (Axcelis Technologies, Inc.)

15.1 Introduction

The history of ion implantation in semiconductors stretches back some 50 years. The first published report of the bombardment of semiconductor surfaces to change electrical properties appears to be that of Ohl at Bell Laboratories in 1952 (Ohl 1952). Shockley, at the same institution in 1954, filed a remarkably prophetic patent in which he detailed the doping possibilities of implanting donor or acceptor impurities to control the electrical properties (Shockley 1954). This patent basically describes the art as it is practiced today, including the annealing to remove damage and diffuse the dopant. There was much worldwide research in the 1960s investigating the implantation phenomenon, but the technique was not widely accepted into production until the 1970s. It was then that the value of implantation for threshold voltage adjustment and highly doped, self-aligned structures contributed significantly to the integrated circuit (IC) revolution.

The sophistication of implant machines and the devices they produce have evolved continuously over the past 50 years, and this chapter will give a flavor of the state-of-the-art of the technology and current challenges. At the same time, the economic challenges or drivers cannot be overemphasized. Economics have been an important factor in ion implantation from its inception in chip manufacturing because the implanter cost was incremental to the diffusion systems with which implant competed (McKenna 2000; Rose 1985).

Silicon technology drives the modern world. A manifestation of its importance is Moore's Law, which describes the continuous shrinking of devices to improve performance and cost. Tremendous investment is required to meet the demands of

---

[1] Advanced Micro Devices, Inc.
[2] Varian Semiconductor Equipment Associates
[3] Colorado School of Mines

Moore's Law. Some of those demands, such as reducing implant energies, are described in this chapter.

While device dimensions have been shrinking, Si substrate dimensions have been increasing. In the 1970s, Si wafers increased from 50 to 125 mm, and IC manufacturers sometimes developed and built their own implanters to achieve new capability. Today we are in the midst of transitioning from 200 to 300 mm wafers with a relatively small number of implantation equipment suppliers. There are now 30 of these 300 mm IC factories being built around the world, and each will require, on the average, 25 implant machines to produce 20,000–50,000 wafers per month. The capital and operation costs of IC factories ($2–3 billion) are so enormous that processing tools such as implant machines must run very reliably with high throughput to produce defect-free devices.

Although the scope of this chapter is limited to Complementary Metal Oxide Semiconductor (CMOS) technology in silicon substrates, ion implantation is widely used in advanced bipolar and BiCMOS processes as well as in other materials systems, including GaAs and InP. Besides being used for doping semiconductors or for introducing crystalline damage in selected regions, ion implantation plays a major role in the manufacture of semiconductor on insulator (SOI) substrates.

15.2 Implanters Used in CMOS Processing

The various implants are typically serviced by distinct types of tools, each engineered to provide a solution for a specific segment of the implant application space. Traditionally, these segments have been called *high current*, *medium current*, and *high energy*, and can be characterized mainly by the dose and the energy of implanted ions.

High current implantation typically refers to doses in the 10^{13}–10^{16} cm^{-2} range at energies no higher than about 180 keV but as low as 0.2 keV. The most common applications for which high current implanters are used include: source/drain contact and extension junction formation (both preamorphization and doping); gate electrode doping (currently polysilicon but metal in the future); and SOI substrate manufacturing.

Medium current implantation typically refers to doses in the 10^{11}–10^{14} cm^{-2} range at maximum energies of several hundred keV and as low as 3 keV. The most common applications for which medium current implanters are used include: threshold voltage adjustment; halo or pocket implants; field isolation and channel engineering.

High energy implantation typically refers to doses in the 10^{11}–10^{13} cm^{-2} at energies up to several MeV. The most common applications for which high energy implanters are used include retrograde and triple well formation, buried layer formation, and field isolation.

It should be noted that there is substantial applications overlap among the implantation segments. For example, medium current systems can run high dose source drain implants for pilot lines, albeit at low throughput. High energy

implanters are often used to dope channels and adjust threshold voltage. Likewise, some processes employ retrograde wells with energies in the range of medium current systems. Finally, the dosimetry systems of HC implanters are perfectly capable of controlling implants in the 10^{12}–10^{13} cm^{-2} range and are therefore used to perform channel implants normally defined as medium current. With the transition to 300 mm wafer size, sub-65 nm technology nodes, and ultra-thin body device architectures, it is quite possible that a further blurring of the traditional segments will follow. Whatever implantation segment is required for device fabrication, the processing constraints (such as across-wafer dose uniformity or contamination) are exacting. These are shown in Table 15.1.

All segments use the same basic set of primary dopant species. The dominant p-type dopant in use today is boron, usually delivered by the implanter in the form of B^+ or BF_2^+ ions. These ions are typically generated from BF_3 (boron trifluoride) ion source feed gas. The dominant n-type dopants in use are phosphorous and arsenic, usually delivered in the form of P^+ and As^+ ions from PH_3 (phosphine) and AsH_3 (arsine) feed gases, respectively. Formerly, these species were delivered from solid P and As heated in vaporizers built into the implantation sources. For some higher energy applications in both the medium current and high energy segments, multiply charged ions – including doubly and triply charged n-type dopants (P^{++}, P^{+++}, As^{++}) and doubly charged p-type dopants (B^{++}) – are not uncommon. Other species that are important but typically used less frequently include indium and antimony from solid source materials $InCl_3$ (indium trichloride) and Sb_2O_3 (antimony oxide), respectively. Nondopant species germanium and silicon from GeF_4 (germanium tetrafluoride) and SiF_4 (silicon tetrafluoride) are often used for preamorphization of the crystal lattice. In addition, nitrogen, oxygen, and fluorine are used for materials modification.

15.2.1 Beamline Architectures

There are elements of beamlines that are generally common among the three major types of implanters. All beamlines begin with an ion source and extraction optics, responsible for injecting an appropriately shaped beam of ions into the subsequent

Table 15.1. Control and contamination requirements for production-grade ion implanters

Specification	Target
dose uniformity	< 0.5%
dose repeatability	0.5 – 1.0%
energy integrity	< 1.0%
angular integrity	< 1°
metallic contamination	$< 1 \times 10^{10}$ cm^{-2}
particle contamination	< 0.1 cm^{-2} for particles < 0.12 μm

elements of the beamline. Today, the majority of new implant systems use an indirectly heated cathode (IHC) (Horsky 1998). The IHC is able to realize source-operating lifetimes two to five times longer than could be achieved with the earlier Freeman- or Bernas-type sources, which consisted of a hot filament immersed in a plasma discharge. Virtually all implanter beamlines also require a mass analysis device – almost universally a dipole electromagnet – which provides momentum dispersion and transverse focusing of the ion beam.

High Current Beamlines

The primary objective of high current implanters is to deliver multi-mA beams in the range from as low as sub-keV to as high as 180 keV. Recently, the maximum energy requirement often has been relaxed to 60 keV. The increasingly lower low-energy requirements have driven the design of high current beamlines to be relatively short and to have large cross-sections. Each of these attributes is favorable for delivering the highest possible usable beam current to the wafer.

The primary challenges to delivering high beam currents at lower energies center around the effects of space charge forces on these beams. Ions in an ion beam experience a repulsive force exerted by neighboring ions, causing the beam to expand in size as it propagates through the beamline. This beam size expansion typically becomes worse as the beam current or ion mass is increased, or as the energy of the beam is decreased (as a result of a lower energy beam moving more slowly, thereby allowing more time for the expansion forces to act on the beam). Beam size expansion due to space charge is a problem primarily due to the loss of ion current (and hence productivity) whenever the beam passes through an aperture in the beamline which is smaller than the beam. Beam size expansion can also affect angle control, depending on the design of the endstation and/or the beam scanning mechanism, as discussed in Sect. 15.5.2.

Most common high current beamlines are optically simple, consisting of only an ion source, an analyzer magnet with focusing elements, and a resolving aperture. This allows the beam to travel through the entire beamline without any externally imposed electrostatic fields present (see Fig. 15.1). This mode of operation is called *drift mode* since the ions are given their final energy via the ion source and extraction optics alone and are left to drift through the remainder of the beamline at that energy.

The analyzer magnet in high current tools typically bends the beam through ~90° with a radius of ~300 mm. The total beamline length is in the 1.0–1.5 m range, consisting of 200–300 mm from the ion source to the entrance of the analyzer magnet, 200–300 mm from the exit of the analyzer magnet to the resolving aperture, and 400–700 mm from the resolving aperture to the wafer. Emerging from the ion source and extraction optics, the beam is approximately 50 mm tall and converging slightly in the nondispersive plane and it is approximately 5 mm wide and diverging in the dispersive plane. In the dispersive plane, the beam is focused by the analyzer magnet to a waist at the resolving aperture. The beam size passing through the resolving aperture is approximately 5–25 mm, depending

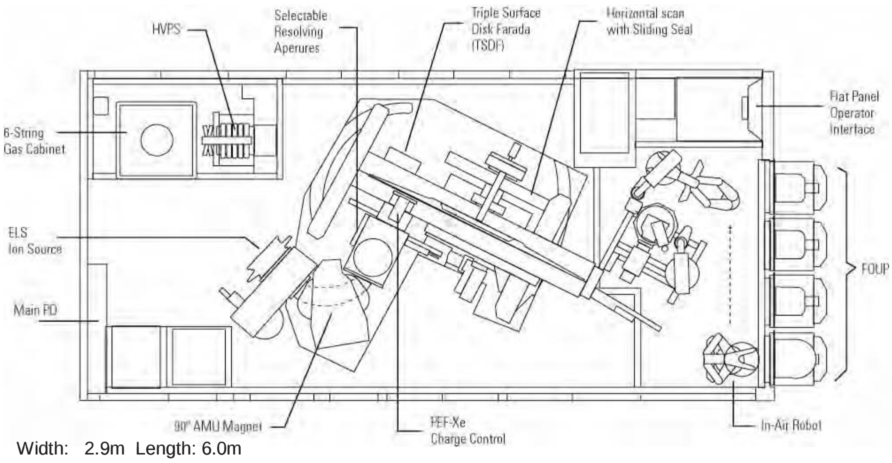

Fig. 15.1. Plan view (dispersive plane) schematic of a batch mode high current implanter, the Axcelis HC3

largely on energy. The beam arrives at the wafer with a dispersive plane size in the range of 30–100 mm. In the nondispersive plane, there is typically much less focusing applied to the beam, and the size of the beam is similar (approximately 50 mm) from source to wafer.

The requirement for dose uniformity across the entire wafer to be of order 1% or better places demands on how the wafers are scanned through the fixed spot beams. Given that these spot beams are typically somewhat Gaussian in shape, a near absolute requirement for achieving dose uniformity of this order is that the wafers are scanned so that all points on the wafer are eventually exposed to the entire area of the beam. The larger the beam size at the wafer, the greater the mechanical scan length through which the wafer must travel in order to achieve this dose uniformity requirement. Failure to do so inevitably leads to a shortfall in the dose delivered to the edges of the wafer.

In multiwafer configurations, which are common for high current tools, the wafers typically are mounted onto a rotating disk, which is then linearly translated across the ion beam. The rotation of the disk ensures that each wafer passes completely out of the beam in the direction of rotation. The linear translation must be at least as long as the wafer diameter plus the nominal beam diameter in that direction. Some high current configurations have the linear translation direction across the dispersive plane of the beam, while others have it across the nondispersive plane. Beam utilization efficiency (see Sect. 15.4) is directly coupled to the demands placed on this translation length.

In single-wafer configurations, a fixed spot beam and two orthogonal linear translations of the wafer typically are used. Flexibility is generally provided to tailor the relative speed of scanning in each direction in order to achieve optimum

beam utilization efficiency. This takes into account the size and shape of the beam, the number of passes of the beam across the wafer required to provide adequate dose uniformity, and the speed with which the mechanical system can accelerate at the end of each scan. In general, due to the finite acceleration times at the end of each scan (which become proportionately larger compared to the time spent with the beam on the wafer as the scan speed increases), the single-wafer architectures typically suffer from lower beam utilization efficiencies than the multiwafer architectures.

Most ion implanters with the simple fixed-spot beamline described above also make use of a multiwafer, mechanically scanned type endstation to provide adequate wafer cooling and improve overall tool productivity (discussed in more detail in Sect. 15.4). A rendered drawing of a typical high current tool with a multiwafer batch endstation is shown in Fig. 15.2.

High current beamlines can alternatively be designed using a fixed ribbon beam with a single-wafer process chamber. The challenge here is in producing a fixed ribbon beam with a uniform spatial extent that covers at least the entire diameter of the wafer, thus enabling a single direction of mechanical wafer scanning only. A significantly more complicated beamline is required to produce such a fixed ribbon beam with sufficiently uniform ion flux and beam angle uniformity across the wafer. In addition to the usual ion source, analyzer magnet, and resolving aperture, an additional parallelizing magnet, as well as multiple independent tuning elements along the width of the ribbon, are required. The chief motivation for a ribbon-beam-based architecture is to achieve the advantages associated with single-wafer processing.

Medium Current Beamlines

The primary objective of medium current implanters is to deliver a wide range of beam currents, from a few μA to several mA at energies in the range of a few keV to a few hundred keV. This broad set of expectations for medium current tools make them among the most versatile, with the capability to perform almost any implant required in typical processing, albeit sometimes at the expense of optimum productivity. There has been significant variety in the architecture of medium current beamlines, but with the onset of 200 mm processing in the early 1990s, all commercially successful implementations involve the use of scanned ion beams.

Formation of the ion beam takes place in a manner similar to high current tools, at energies typically in the range of 40–80 keV. Following the analyzer magnet and resolving aperture, the beam is typically scanned in the dispersive plane via either an electric or a magnetic scanning element. The scanning takes place at frequencies ranging from 100 to 1,000 Hz (slower for magnetic scanning, where the inductance of the electromagnet poses a limitation) and over an angular extent of 10–20°. Following scanning, the beam must then be made parallel. This is typically achieved with either an electrostatic or a magnetic optical element.

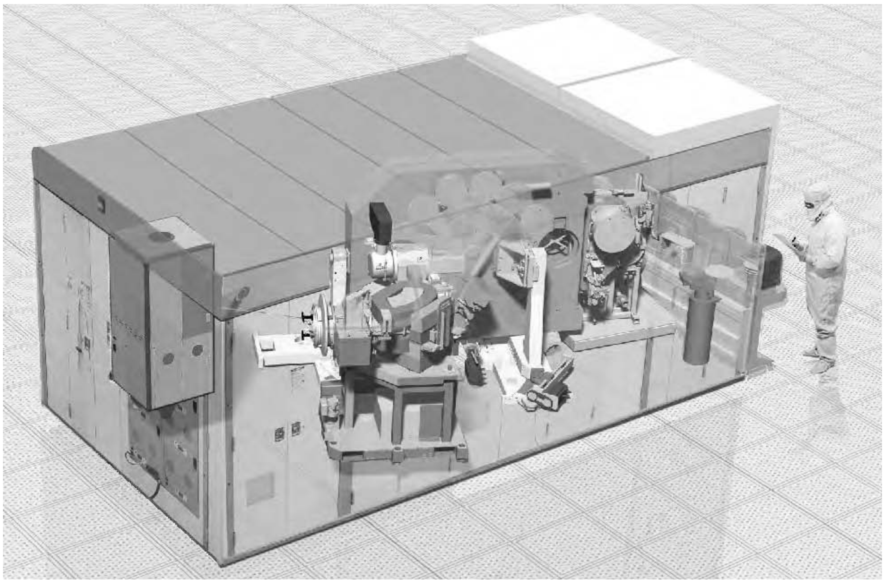

Fig. 15.2. A 300 mm high current implanter showing (*left* to *right*) gas delivery system, ion source, analyzer magnet, process chamber, and wafer handling system

Following this parallelizing element, the beam may also be electrostatically deflected once more to provide energy filtering. This filtering removes ions of unwanted energy that may have had coincidental paths through the beamline.

Acceleration of the beam to its final energy (which may be as high as several hundred keV for multiply charged ions) may occur before or after the scanning and parallelizing stages. Schematically, a typical medium current beamline with electric scanning and electrostatic parallelizing is shown in Fig. 15.3. Given that the beam is scanned in one dimension, there is only a need for one dimension of mechanical wafer scanning. For this reason, medium current beamline architectures are almost exclusively coupled with single-wafer processing chambers.

High Energy Beamlines

High energy implanters are designed to deliver up to hundreds of μA beams at energies up to several MeV. There are two fundamental beamline approaches to achieving this. Most commercial high energy systems today use an RF linear accelerator (referred to as a linac) to deliver the MeV range of energies. The commercial RF linac beamline relies on a conventional ion source and analyzer magnet similar to those found in a high current beamline, to produce a DC beam of up to several mA at ~80 keV. This DC beam is then injected into a series of 8–12

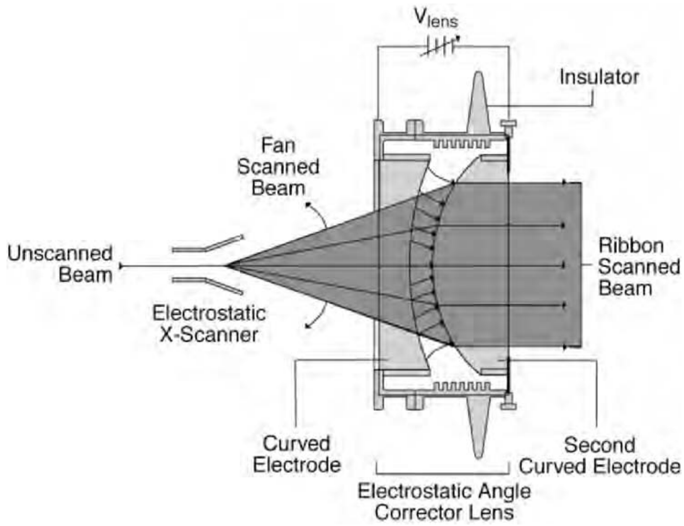

Fig. 15.3. Medium current beamline showing an electric scanner and electrostatic parallelizing lens. The ion source, analyzer magnet, and resolving aperture serve to inject the unscanned beam from the left. The parallel scanned beam on the right is passed through a postacceleration column and an electrostatic deflector before reaching the wafer

electrodes separated by quadrupole lenses. The electrodes, each connected to an RF resonator, bunch the beams into packets and accelerate the packets by modulating the phase of the RF signal on each subsequent electrode. The resonators serve to provide accelerating voltages of up to ~80 keV on each electrode.

Following acceleration to the final energy in the linac stage of the beamline, the beam passes through an electromagnet (typically referred to as the final energy magnet, or FEM), which deflects, disperses, and focuses the beam, ensuring that only ions of the desired momentum pass through to the wafer. Emerging from the ion source and extraction optics, the DC beam is typically smaller than in high current tools, both in the dispersive and nondispersive planes, by approximately a factor of two. The typical beam diameter passing through the linac and exiting the FEM is ~20 mm, and this beam arrives at the wafer ~30 mm in diameter. The overall beamline length in the linac-based high energy implanter is approximately 2.5 m. Figure 15.4 features a rendered drawing of the beamline.

As an alternative to the linac-based implanter, a DC-tandem accelerator is used in some commercial high energy implanters. The basic concept of a tandem accelerator relies on charge exchange to effectively double the accelerating capability of any given potential placed on the high voltage terminal of the beamline. In operation, positive ions are extracted from the source, converted to negative ions in a gas charge exchange cell, and then stripped of electrons to single,

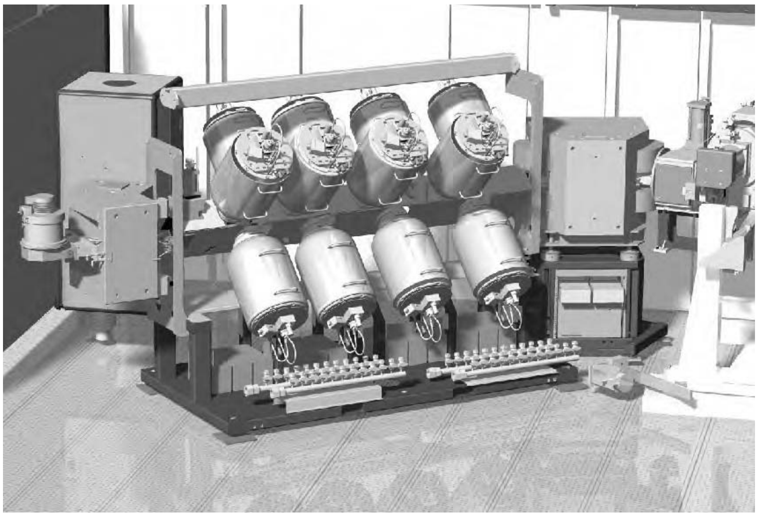

Fig. 15.4. High energy beamline featuring an RF linac with 12 resonators. The ion source and analyzer magnets are on the left. The final energy magnet is on the right

double or triple charge states in a second charge exchange cell. Typical beam sizes and overall beamline length are comparable to the linac-based beamline.

15.2.2 Other Subsystems

The effective generation and transport of ion beams is the raison d'etre of ion implanters, but working machines in wafer factories require a variety of other technologies.

Wafer Handling

Because ion implanters are high-throughput, high-vacuum systems, wafer handling is rather unique and has been an area of proprietary technology development. Mechanical throughput has been on the order of 200 wafers per hour (wph) for many years, and recently throughput has increased to more than 300 wph on new machines. Complex robotics are needed to automatically remove wafers from cassettes or pods (in the case of 300 mm), orient them to ensure correct twist angle, transfer them to high vacuum (usually through a load-lock mechanism) and then to a spinning disk or electrostatic platen for implantation. Parallel operations minimize wafer-handling overhead in order to increase the fraction of time spent implanting.

High Voltage Power Supplies

Since commercial ion implanters for semiconductor applications were derived and adapted from machines designed in the 1940s–1960s for nuclear research programs (including both the study of nuclear interactions over a wide energy range and collection of isotopically enriched material), the development and capability of power supplies cannot be underestimated. Today's DC supplies that drive beamline electrodes and other components must resist arcing while providing voltages up to 80 keV with an accuracy of 0.5% or better. Linac power supplies drive resonators up to 80 keV at 13.56 MHz with accurate phase control. In tandem accelerators, power supplies must maintain voltages up to 750 keV.

High Vacuum Systems

Since ions propagate effectively only in high vacuum (pressures of 10^{-4} Torr or lower), vacuum technology is a critical part of all ion implanters. Turbomolecular pumps are typically used on the source side of the machine to continuously remove residual material from the source plasma. On the endstation side, cryogenic pumps are often used since they are effective at removing hydrogen and other species that are evolved from photoresist during ion bombardment. If endstation pressure becomes too high, dose control can be affected as increasing fractions of ions are neutralized by residual gas. On the other hand, residual gas species in the appropriate amount are often helpful for space charge neutralization. In some high current systems, for instance, beamline water bleed has been effective at improving low-energy transport. In high vacuum, OH-species from the water are attracted to the positive charge of the beam – the heavier OH-molecules can be more effective neutralizers than electrons since they possess a higher residence time in the beam.

Control Systems

Because ion implanters are incredibly versatile, high-speed machines running in highly automated manufacturing facilities, the control systems are very complex. At a basic level, control systems must automatically sense component positions (everything from door interlocks to source electrode tilt), vacuum levels, wafer locations, ion current, ion beam scanning parameters, etc. Rapid beam tuning is a must to lower nonproductive time, so source plasma pressure and power, extraction settings, mass-analysis magnetic field, and uniformity compensation must occur automatically. Implanters must also manage user recipes; accept information downloaded from the wafer fab manufacturing execution system (MES), and upload information collected during process to the MES so that the wafers can be logged to the next operation.

15.3 Low Energy Productivity: Beam Transport

The need for ultra shallow junction formation in advanced devices makes the development of high productivity ion implantation solutions at very low energies increasingly more important. There are fundamental challenges associated with delivering these high productivity solutions. Nonetheless, progress in this area has been steady and significant.

The delivery of low energy p-type dopants (usually B^+ ions) has long been regarded as the most challenging task for an ion implanter to perform. Typical beam current specifications for B^+ implants, sampled across the entire industry over a 25-year period and spanning at least four generations of high current implant tools, are shown in Fig. 15.5. Each new generation of ion implanters exhibits basically the same characteristic dependence of usable beam current on implant energy. It is only the threshold, where a significant loss of usable beam current begins to occur, that has shifted to significantly lower energies over the years. The energies that are considered useful in high-volume manufacturing today are approximately two orders of magnitude lower than they were when ion implantation was in its infancy, decreasing from ~30 keV in the early 1980s to <0.5 keV today.

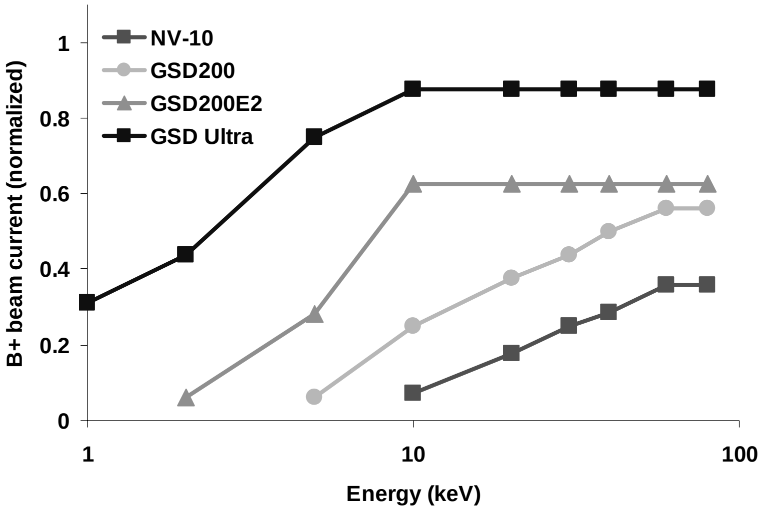

Fig. 15.5. Boron beam current specifications versus energy over numerous implanter generations from Eaton Semiconductor Equipment/Axcelis Technologies, spanning 25 years: NV-10 (1978); GSD-200 (1993); GSD-200/E2 (1997); and GSD Ultra (2004)

The challenges of overcoming space charge neutralization to increase low-energy beam transport are described in the following section. Novel approaches, such as molecular ion implantation, are also discussed.

15.3.1 Space Charge Neutralization

A major component of beam degradation at low energies is Coulombic repulsion between the charged ions. These repulsive effects, known as space charge, can be minimized by neutralizing the beam with an electron plasma. Figure 15.6 shows the effects of space charge neutralization on a low energy beam. We modeled a zero emittance, zero divergence B^+ beam of 10 mA at 2 keV in a beamline drift region 500 mm long. Each individual curve in the figure represents a different percentage of the total beam current (in the range 0–4%) that is not neutralized. The effects of space charge forces in producing beam divergence are clearly seen. With 4% non-neutralized current, the beam has expanded in size in one dimension by a factor of almost six after traveling 500 mm. Even if only 1% of the beam current is non-neutralized, the beam still expands more than a factor of two in this distance. The challenge over the past 5–10 years has been to reduce the beam blow up effects. This has been achieved by effective production and trapping of low-energy electrons in the beam liner and by reducing all transit lengths.

15.3.2 Decel Implantation

One way to contend with the physics limitations on extraction and transport of low-energy beams is to extract the ions from the ion source at a multiple of the desired beam energy (the decel-ratio) and decelerate them immediately before they reach the wafer. This way, most of the beam transport is accomplished at relatively high energies, yielding a higher beam current. Unfortunately, a certain fraction of ions always neutralize due to collisions with residual gas atoms; those neutrals will not be slowed by the deceleration optics and will therefore be implanted at the extraction voltage, far higher than the intended implant energy. This phenomenon is referred to as *energy contamination*, and it degrades the energy purity of the beam.

Energy contamination is inherently difficult to control since it depends on the residual gas pressure in the beam line. Typical values for the amount of energy contamination (defined here as fraction of ions implanted at a higher energy than the desired final energy) are 1–2%. However, energy contamination of as little as 1% can pose a problem. Figure 15.7 shows that the as-implanted junction depth for a 0.5 keV implant increases from 13 to 20 nm when decel from extraction at 2 keV is used. Such increases in the implanted dose and the depth of the extension junction can shift the transistor's threshold voltage (Gossmann and Agarwal 2004). Figure 15.7 also illustrates that the impact of a finite percent of energy contamination on the junction profile diminishes with the extraction energy at the source. This brings us back to requiring larger beam currents at low energy.

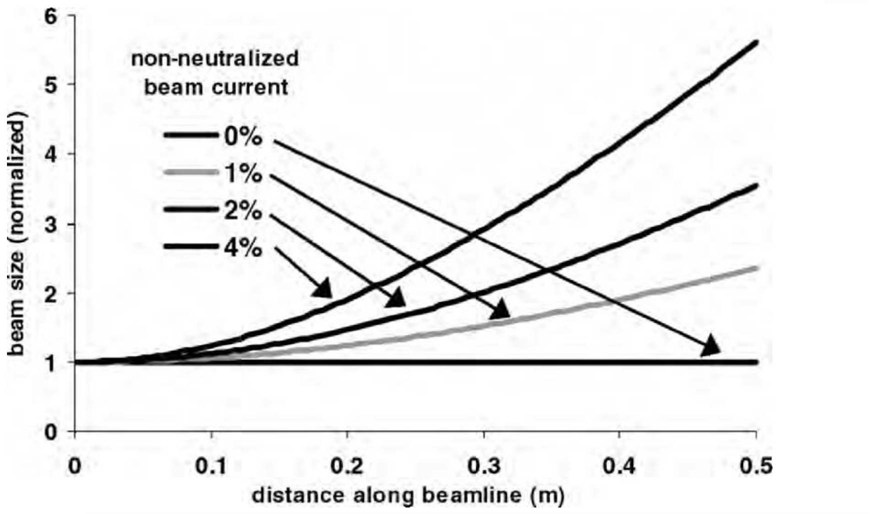

Fig. 15.6. Beam size expansion due to space charge at low energies for various amounts of non-neutralized beam current

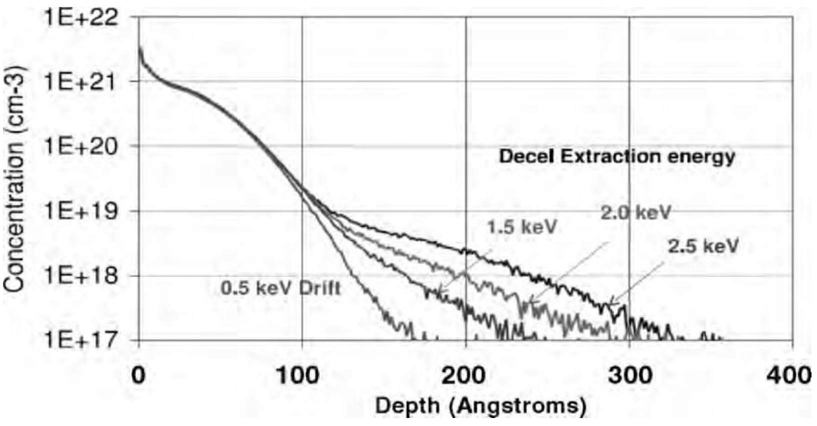

Fig. 15.7. Dependence of as-implanted dopant profiles for 0.5 keV boron "decel" implants on the source extraction energy

15.3.3 Molecular Implantation

Another way to take advantage of improved transport at higher beam energies is to implant a molecule containing the desired dopant atom, e.g., BF_2 (boron difluoride). With a molecular mass of 49, compared with 11 for atomic B, the BF_2^+ ion can be implanted at 4.5× the energy while still achieving the same projected range for the boron atom. Of course, one also gets an implant of the other atom in the molecule, in this case F at twice the boron dose. The extra species might offer some process advantage, but at the least it must not lead to a process disadvantage.

The list of molecular species in common use at this time includes boron difluoride, BF_2^+, the phosphorus and arsenic dimer ions P_2^+ and As_2^+, and tetramers P_4^+ and As_4^+. Additional molecular ion species currently under consideration include decaborane, $B_{10}H_{14}^+$, icosaborane (a decaborane dimer), $B_{20}H_{28}^+$, and octadecaborane $B_{18}H_{22}^+$. The molecular ions containing more than one dopant atom per ion offer an additional advantage in that there is effectively more atoms implanted per unit of ion current. A figure of merit for the use of molecular implants is the relative atomic mass ratio which gives directly the higher energies needed for molecular implants (Fig. 15.8). These higher energies result in more efficient beam transport because of lower space charge effects.

15.4 Low Energy Productivity: Beam Utilization

Increasing beam currents through improvements in beam transport is only part of the solution for improving productivity. The other part is to minimize the time the beam spends off the water, characterized as *beam utilization*. We present here a treatment of utilization, developed by Brown et al. (2004). We then include a categorization of implanters commercialized over the last 35 years, in terms of beam type and scanning mechanism and the implication of each implanter's architecture on beam utilization.

atom or molecule	**B**	**BF_2**	**$B_{10}H_{14}$**	**$B_{18}H_{22}$**	**P**	**P_2**	**As**	**As_2**
relative perveance	**1**	**0.22**	**0.09**	**0.05**	**1**	**0.5**	**1**	**0.5**

Fig. 15.8. Relative mass ratios of atomic and molecular dopant ions

15.4.1 Beam Utilization

A general working definition of beam utilization is the ratio of beam time on the wafer to total beam time:

$$\Upsilon = \frac{\text{beam time on the wafer}}{\text{total beam delivery time}} \tag{15.1}$$

where Υ represents the beam utilization. Often, however, it is more convenient to express the beam utilization as a ratio of areas, or:

$$\Upsilon = \frac{\text{effective area of the product wafer}}{\text{effective area scanned by the beam}} \tag{15.2}$$

The effective areas must of course accurately represent the times in (15.1). The beam utilization is critically dependent on the particulars of the implanter, such as beam type (spot or ribbon), endstation type (single or multiwafer) and scan mechanism (mechanical, electric, magnetic, or hybrid). Expressions are developed below for three different types of endstations and scanning mechanisms in use today.

Multiwafer Endstation: Dual Mechanism Scan (Rotary Disk), with Unscanned Spot Beam

This type of multiwafer endstation (13–17 wafers per disk, for 150–300 mm wafer sizes), is typically implemented on high current and high energy implanters. A spinning disk provides two-dimensional mechanical scanning (one rotation and one linear translation) of the wafers across the fixed spot beam, as shown in Fig. 15.9. Disk rotation typically occurs at speeds on the order of 1,000 RPM at a nominal radius of about 650 mm. This is sufficient to maintain wafer temperatures below about 80°C for beam powers up to 2–3 kW. Linear disk translation speeds can be up to approximately 100 mm s^{-1}. over a travel of up to 400 mm (enough to allow a beam of order 100 mm in size to be scanned completely off a 300 mm diameter wafer). Multiwafer batch disks typically allow implantation at incident angles that can be varied over ~10° about two orthogonal axes. At maximum throughput, this architecture can process up to approximately 230 wafers h^{-1}.

For the multiwafer endstation, (15.2) can be rewritten as

$$\Upsilon = \frac{n\pi R_w^2}{\pi(R_2^2 - R_1^2)} \tag{15.3}$$

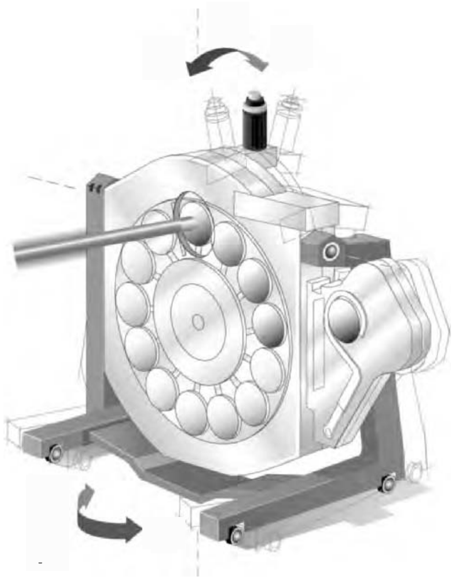

Fig. 15.9. Multiwafer batch processing chamber, showing 13-wafer process disk and multiaxis tilt capability

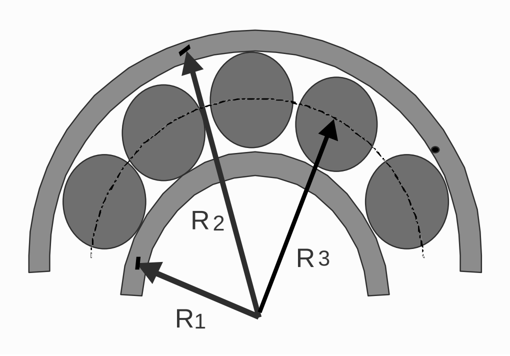

Fig. 15.10. The total scan area on a typical multiwafer system is characterized by three radii. R_1 and R_2 define an annulus sufficiently large to include the required overscan, and R_3 locates the centerline of the wafer ring

where n is the number of wafers of radius R_w, and R_1 and R_2 are the inner and outer radii of the annulus over which the beam scans (see Fig. 15.10).

Single-Wafer Endstation: Linear Mechanical Scan with Scanned Spot Beam

A processing chamber in which only one wafer is implanted at a time is typically employed for medium current implanters. The endstation consists of a single scanning arm capable of linear motion of up to 140–200 mm s^{-1}. over a range of up to 400 mm. The wafer is typically held on an electrostatic chuck which may be gas-cooled to maintain adequate wafer temperature.

The wafer can usually be tilted at angles of up to 60° and rotated through a full 360° either while on the chuck or prior to being placed there. When operating at maximum throughput, a typical single-wafer architecture can process up to 350 wph.

For the single-wafer endstation described above, (15.2) can be rewritten as:

$$\Upsilon = \frac{\pi R_{\mathrm{w}}^2}{(2R_{\mathrm{w}} + d_{\mathrm{beam}} + 2d_{\mathrm{ta}-x})(2R_{\mathrm{w}} + d_{\mathrm{beam}} + 2d_{\mathrm{ta}-y})} \tag{15.4}$$

where d_{beam} refers to the beam diameter, and $d_{\mathrm{ta}-x,y}$ refers to the effective distance for the beam to decelerate and reaccelerate for the x and y directions, see Fig. 15.11. It should be apparent from (15.5) and Fig. 15.11 that a relatively simple way to improve beam utilization (and hence throughput) for the single-wafer platform is to "paint" not a rectangular region but a circular region only, the radius of which would be $R = R_{\mathrm{w}} + 1/2d_{\mathrm{beam}} + d_{\mathrm{ta-effective}}$. This eliminates wasting beam on the "corners" of the rectangular region.

Equation (15.2) now becomes

$$\Upsilon = \frac{R_{\mathrm{w}}^2}{\left(R_{\mathrm{w}} + \frac{1}{2}d_{\mathrm{beam}} + 2d_{\mathrm{ta-effective}}\right)^2} \tag{15.6}$$

Single-Wafer Endstation: Linear Mechanical Scan with Unscanned Ribbon Beam

Achieving uniformity with this type of a system necessarily requires a beam broader than the wafer. Assuming a beam 10% wider than the wafer, (15.2) now becomes

$$\Upsilon = \frac{\pi R_{\mathrm{w}}^2}{2(1.1R_{\mathrm{w}})(h_{\mathrm{beam}} + d_{\mathrm{ta}})} \tag{15.7}$$

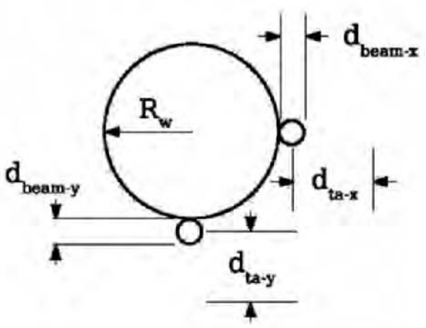

Fig. 15.11. The effective total scan area for a serial wafer endstation can be described by a rectangle with sides equal to the sum of twice the wafer radius $2R_w$, the beam diameter d_{beam}, and twice the effective turn around distance d_t a required for the beam to decelerate and reaccelerate

Single-Wafer Endstation: Dual Mechanical Scan (Linear) with Unscanned Spot Beam

The utilization equation for this design is identical to (15.4) except that the turnaround distances correspond to those of the mechanically moving endstations.

Using the formulations above, it is possible to compare the relative productivity of the multi- and single-wafer endstations (see Fig. 15.12).

15.4.2 Implanters Commercialized in the Past 35 Years

It is useful to arrange various types of implanter platforms according to the methods by which the ions are distributed uniformly across the wafer(s), i.e., the scanning methods. Over 100 variants of the basic implanter design have been introduced in the past 35 years.

The first commercial implanters, available in the early 1970s, were either electrostatically scanned, uncollimated single-wafer systems or mechanically scanned multiwafer machines. The electrostatically scanned “spot” beam systems were viable for single-wafer low current and medium current machines into the early 1980s but were phased out due to unacceptable beam angle variations across newer and larger 150 and 200 mm substrates. Ulvac attempted to extend the concept with electrostatic collimation beamline elements for parallelism in the early 1990s, but this was not widely adopted. Eaton addressed angle control by “wobbling” the wafer in synchronization with the scanned beam, but this was not adopted either. Instead, hybrid systems with electric or magnetic scanning plus collimation in only one direction were adopted and dominate the market today. Since modern implanters no longer use two-dimensional beam scanning, this design was not included in the previous section on beam utilization.

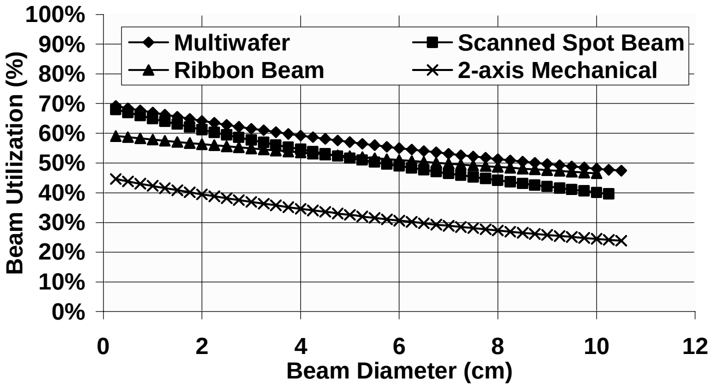

Fig. 15.12. Beam utilization versus beam diameter for different implanter architectures

Hybrid systems typically feature a slow (~0.1 Hz) mechanical scan in one direction and a fast (~1,000 Hz) beam scan in the orthogonal direction. As discussed above, the scanned beam approaches use electrostatic or magnetic scanning elements in the beamline coupled with another electrostatic or magnetic collimating element for parallelism. These systems, known for their superior process control (mass resolution, dose energy, and angle), are typically used for channel applications in the 10^{12}–10^{13} cm^{-2} dose range. Since throughput is limited for these processes by wafer handling speed and uniformity requirements rather than beam current, beam utilization is not an important consideration in these cases.

Most two-dimensional mechanically scanned systems consist of rotary disk multiwafer systems. These have been continuously developed over the past 30 years and are widely used for both high current and high energy processes. The adoption of multiwafer platforms, driven largely by the need to cool substrates under high beam-power conditions, also yields utilization advantages. Interestingly, before spinning disk technology was developed, early versions of multiwafer high current systems used translating plates mounted in stage, carousel, or ferris wheel configurations that moved wafers in x/y (relative to the unscanned spot beam) rather than R/θ as with a spinning disk. Recently, the x/y scanning method has been resurrected in the form of a single-wafer high current machine, with significant implications for beam utilization.

Two other categories of ion implanter deserve mention. First, the hybrid ribbon beam system is unique since the broad, unscanned ion beam does not scan off the wafer in the x-direction. Overscan does occur in the slow mechanically scanned y-direction, however. While offering an advantage for beam utilization, the ribbon beam must sacrifice uniformity and angle control to some degree. Second, Varian's broad beam approach utilizing nonmass-analyzed plasma doping,

although of significant technological interest for niche applications, has not yet achieved market adoption.

15.5 Angle Control

One of the enabling advantages ion implantation offers is precise spatial placement of the dopant within the device. There are however a number of situations that might lead to an error in placement, either in depth or in the lateral direction. Energy contamination, discussed in an earlier section, can result in an error in depth. Similarly, an error in the angular alignment of the beam can result in an error in ion placement in the lateral direction. Control over the angular alignment of the beam is critical in modern implanters. Angular alignment of the beam can be influenced by a number of factors including beam steering, beam divergence, as well as the method of beam scan or endstation design. In the subsections below we describe a number of endstation and scan configurations which can impact angle control. It is worthwhile to note that the need for improved angle control for smaller devices on larger wafers has been a significant driving force behind implanter development, particularly during the transition from 125/150 to 200 and 300 mm wafers.

15.5.1 Impact of Beam Steering Errors on Device Performance

The most general case of angular misalignment is the tilting of an otherwise perfect (collimated and nondivergent) ion beam relative to the wafer normal. If the tilt of an extension implant is in the plane of the length dimension of a transistor, it will result in an undercut of the gate stack on one side and shadowing of the extension by the gate stack on the other. It is apparent that any deleterious effects due to the shadowing and undercut would only worsen as the transistor dimensions and thermal budgets shrink further. Device simulations show that at the 65 nm node angle tilt errors on the order of 1° can lead to large deviations in the transistor on current (I_{on}) from the nominal value, see Fig. 15.13.

One technique for reducing the impact of beam steering errors is to employ a *quad-mode* implant, i.e., an implant whereby a quarter of the dose is implanted at azimuthal rotations of 0°, 90°, 180°, and 270°. For a beam steering angle of −1°, a quad implant restores I_{on} to nearly the maximum value, provided that the tilt-angle is sufficiently large (see Fig. 15.14). A quad-mode implant can be executed efficiently on any endstation with in situ wafer repositioning. In this case very little time is wasted between the segments.

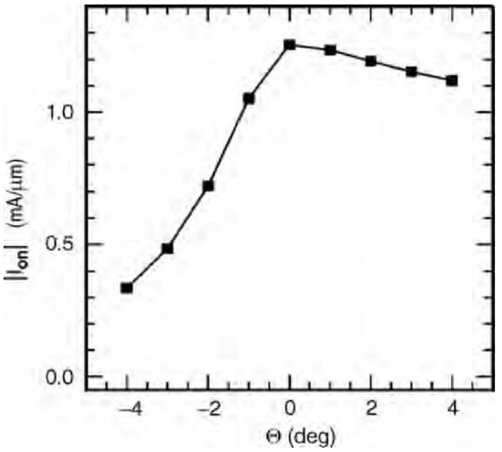

Fig. 15.13. On current of a 65 nm node NMOS transistor versus beam steering angle. A positive angle corresponds to shadowing of the extension region on the drain side, while a negative angle corresponds to shadowing on the source side. The *curve* is not symmetric since the resistivity of the source side is far more important than the resistivity of the drain side (Ghani et al. 2001)

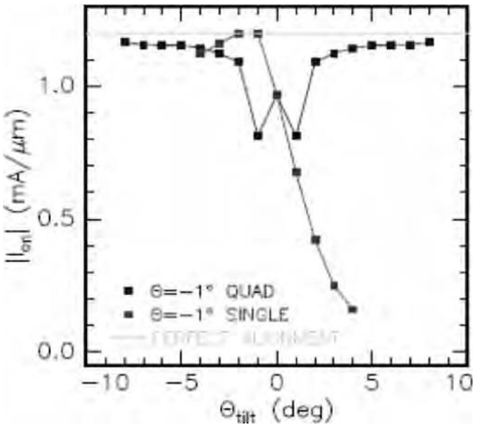

Fig. 15.14. On current of the same NMOS transistor as in Fig. 15.13 as a function of tilt angle for a beam steering angle of −1°, for a single implant (*triangles*) and for a quad implant (*squares*). The *line* indicates I_{on} for perfect alignment

15.5.2 Impact of Endstation Design and Beam Scan Mechanism

The choice of endstation design and the mechanism of beam scan can also compromise angle control. We consider several examples below.

Wafer Rotation Effect on Multiwafer Endstation

All multiwafer implanters with adjustable disk tilt angle induce a systematic error in ion beam angle due to geometric effects. When the disk is tilted to achieve the desired tilt and/or twist, the resulting misalignment between the ion beam and the axis of disk rotation results (under most circumstances) in a rotation of the wafer as it is passed under the stationary ion beam. Additionally, the wafers are mounted on pedestals angled up a few degrees from the disk face in the direction of the incoming ion beam (to ensure adequate thermal contact for wafer cooling). The net result is that the wafer tilt and twist become functions of positions on the wafer surface. It is the disk rotation about an axis not parallel to the ion beam that causes the tilt and twist angles to vary; the slow scan motion has no effect because it is linear. Since the tilt and twist angles are functions of positions only in the fast scan direction, the set of points on any disk radius will all have the same tilt and twist angles.

Travel Path Length Effect for a Ribbon Beam on a Single-Wafer Endstation

If a beamline utilizes symmetrical scanning, the distance traveled by the ion beam from the source to the wafer will be nearly independent of scan position. However, some modern implanters have highly asymmetric parallelizing magnets (see Fig. 15.15). As suggested by the figure, this architecture makes the distance traveled by the beam vary considerably across the wafer. Were it not for the beam divergence (see Sect. 15.3.1), this might not matter. We have seen that divergence causes not only the beam diameter but also the angle of the ions at the edge of the beam envelope to be functions of beam travel distance. Consequently, this type of architecture causes beam density and potentially beam angle to vary horizontally across the wafer. This may result in across-wafer variations in device performance, especially for implants near the amorphization threshold. The effect will be most severe for the most divergent (i.e., lowest energy) ion beams.

Implanters utilizing a fast-scanned beam with a one-dimensional mechanical scan can be further divided into a vertical scan and a plane-of-wafer scan, see Fig. 15.16. In the former, the mechanical scan direction is always perpendicular to the ion beam vector. In the latter, the mechanical scan direction is adjusted with the wafer tilt, so that it is always in the plane of the wafer. It is clear that, for the case of a zero-degree implant, the two methods are identical. However, for tilted implants, the vertical scan method results in the beam travel distance (and hence the beam size in the case of highly divergent beams) becoming a function of vertical position on the wafer. The degree of across-wafer variation increases with the

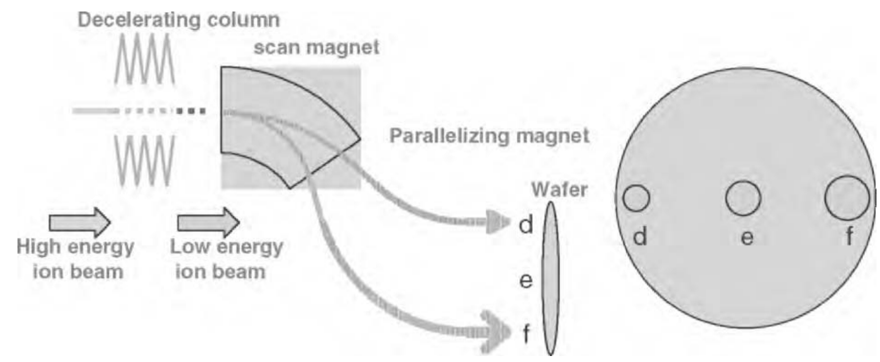

Fig. 15.15. Illustration of how unequal travel paths through the scan magnet and parallelizing lens can lead to a large variation in beam size and beam divergence

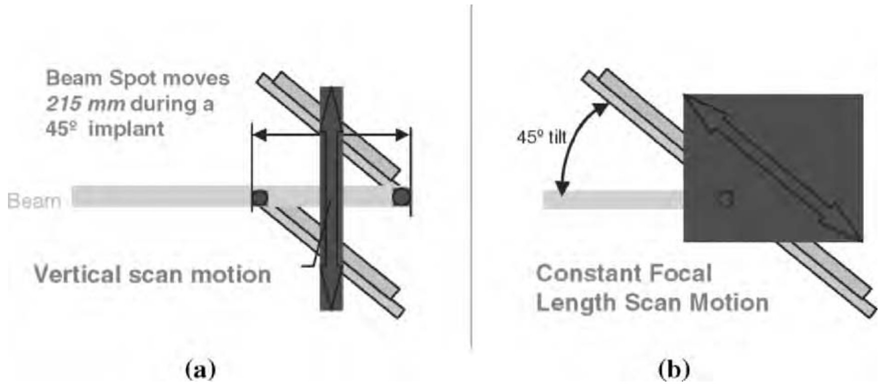

Fig. 15.16. A comparison of two different types of endstation motion. (**a**) A vertical scan (perpendicular to the beam) can result in different beam spot sizes on opposite edges of the wafer (the numbers here are for a 300 mm wafer) and (**b**) a plane-of-wafer (constant focal length) scan which exposes all points to the same size beam

sine of the tilt angle. This type of variation does not occur for the plane-of-wafer method; hence this method is referred to as the *constant focal length* method of scanning. It improves the across-wafer reproducibility of the implant at the expense of additional endstation complexity. The complexity occurs because the scan mechanism must be designed so that the scan direction can change with wafer tilt angle.

15.6 Conclusions and the Future of Ion Implantation in Semiconductors

We have discussed some of the device and economic imperatives driving ion implantation technology today. Ion implant remains one of the most productive equipment sectors in a fab, despite arguably being one of the most complex. The implantation machine landscape looks very different than it did ca. 1974 when low current implanters used for threshold voltage adjustment comprised more than 60% of a small ($14 M) market (Rose 1998). The number of implanter types has increased with the number and type of implants. Medium current implanters supplanted low current implanters in the mid-1970s. This was followed by the widespread manufacturing use of high current and high energy implanters in the early 1980s and the mid 1990s, respectively. Figure 15.17 shows the number of implant steps for an individual process flow as a function of node and year. What will the next 20 years bring in terms of implantation technology? This question will be answered by some combination of the laws of physics and the vagaries of economics.

The shrinking of devices over the past 30 years has been fairly accurately described by Moore's Law, with no fundamental physical constraints encountered in this evolution. However, in the next 5–10 years, new classes of materials and devices will be required as physical limits are reached. The most obvious example of this limit is the transition from SiO_2 (SiO_xN_y) gate dielectrics, which have reached their physical thickness limit, to new higher permittivity dielectrics. This transition and others require unparalleled investment to prevent Moore's Law from faltering. Similarly, continuous increases in wafer size have been driven by the economic advantage of being able to produce more devices per wafer at a relatively constant manufacturing cost. However, the next projected wafer size of 450 mm requires not only a *tour-de-force* in crystal growth technology but enormous investment in both wafer processing and wafer transport hardware.

The biggest impact on implant technology will come from the widespread adoption of SOI technologies. Devices built on SOI substrates are now in production. The use of oxide instead of p–n junctions to provide much of the circuit isolation significantly reduces the number of implants required. This is especially true for higher energy (well) implants, since the buried oxide layer is in the region formerly occupied by the well structures. How widely SOI technologies are eventually adopted will depend mainly on how much the substrate cost can be reduced. In the unlikely event that 450 mm substrates are ever used, only single-wafer endstations will be practical in terms of footprint. It will be interesting to see how all these forces play out, but one thing is certain: ion implantation will continue to play a central role in Si technology. The unequalled precision and versatility of doping achievable by ion implantation ensures this.

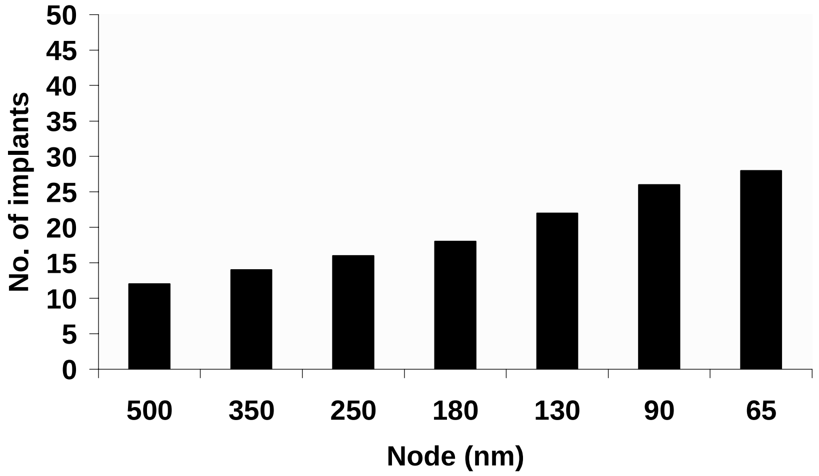

Fig. 15.17. The number of implant steps per wafer as a function of technology node (as defined by the International Technology Roadmap for Semiconductors)

Acknowledgements

All figures are from Axcelis unless specified elsewhere. We gratefully acknowledge our engineering colleagues: Pat Splinter, Andy Ray, Doug Brown, and Brian Freer at Axcelis Technologies, USA, and Michiro Sugitani, Genshu Fuse and Mitsukuni Tsukihara at Sumitomo Eaton Nova, Japan.

References

Brown, D., Tsukihara, M., Ray, A., Splinter, P.: Productivity Comparisons of Various Wafer Scanning Schemes in Ion Implanters, Using Beam Utilization as the Figure of Merit, Proceedings of the Fourteenth International Conference on Ion Implantation Technology (2004)

Ghani, T., Mistry, K., Packan, P., Armstrong, M., Thompson, S., Tyagi, S., Bohr, M.: Asymmetric Source/Drain Extension Transistor Structure for High Performance Sub-50 nm Gate Length CMOS Devices," VLSI Technology Digest of Technical Papers, 17 (2001)

Gossmann, H.-J., Agarwal, A.: Junction Formation in Advanced Planar and Vertical Devices, Proceedings of the Seventh International Conference Solid-State Integrated Circuit Technol (2004)

Horsky, T.: Indirectly heated cathode arc discharge source for ion implantation of semiconductors. Rev. of Sci. Instrum. **69**(2), 840 (1998)

McKenna, C.M.: A Personal Historical Perspective of Ion Implantation Equipment For Semiconductor Applications, Proceedings of the Thirteenth International Conference on Ion Implantation Technology, vol. 1 (2000)

Mihara, Y., Niikura, K., Tsukakoshi, O., Sakurada, Y.: Parallel Beam Ion Implanter: IPX-7000. Nucl. Instrum. Methods **B55**, 417 (1991)

Mihara, Y., Niikura, K., Araki, M., Tsukakoshi, O., Sakurada, Y.: 8-Inch Parallel Ion Implanter: IPZ-9000. Nucl. Instrum. Methods **B74**, 405 (1993)

Ohl, R.S.: Bell Syst. Tech. J. (1952)

Rose, P.: A history of commercial implantation. Nucl. Instrum. Meths. Phys. Res. B **6**, 1 (1985)

Rose, P.: A History Mainly About Ion Implantation Equipment Since 1984, Proceedings of the Twelfth International Conference on Ion Implantation Technology, vol. 1 (1998)

Ryding, G.: Target chambers for ion implantation using mechanical scanning. Nucl Instrum Methods **189**, 239 (1981)

Shockley, W.: US patent #2,787,564 (1954)

The International Technology Roadmap for Semiconductors. Semiconductor Industry Association (2004), http://public.itrs.net

Tsukakoshi, O., Niikura, K., Nishihashi, T., Mihara, Y., Sakurada, Y.: Ion Optics of Parallel Scan Implanter Using Two Octupole Deflectors, Proceedings of the 11th International Conference on Ion Implantation Technology, 342 (1996)

Proceedings of the Seventh International Conference on Ion Implantation Technology, 1988, 601

Appendix A

Table of the Elements

element	atomic number (Z)	isotopic mass (amu)	relative abundance	atomic weight (amu)	atomic density (atoms cm^{-3})	mass density (g cm^{-3})
H	1	1.0078	99.985	1.00794		
		2.0141	0.015			
He	2	3.0160	0.0001	4.002602		
		4.0026	99.9999			
Li	3	6.0151	7.5	6.941	4.60×10^{22}	0.53
		7.0160	92.5			
Be	4	9.0122	100	9.01282	1.24×10^{23}	1.85
B	5	10.0129	19.9	10.811	1.30×10^{23}	2.34
		11.0093	80.1			
C	6	12.0000	98.9	12.011	1.31×10^{23}	2.62
		13.0034	1.1			
N	7	14.0031	99.63	14.00674	5.38×10^{22}	1.251
		15.0001	0.37			
O	8	15.9949	99.762	15.9994	5.38×10^{22}	1.429

element	atomic number (Z)	isotopic mass (amu)	relative abundance	atomic weight (amu)	atomic density (atoms cm^{-3})	mass density (g cm^{-3})
		16.9991	0.038			
		17.9992	0.2			
F	9	18.9984	100	18.9984032	5.38×10^{22}	1.696
Ne	10	19.9924	90.51	20.1797	2.69×10^{22}	0.901
		20.9938	0.27			
		21.9914	9.22			
Na	11	22.9898	100	22.989768	2.54×10^{22}	0.97
Mg	12	23.9850	78.99	24.305	4.31×10^{22}	1.74
		24.9858	10.			
		25.9826	11.01			
Al	13	26.9815	100	26.981539	6.03×10^{22}	2.70
Si	14	27.9769	92.23	28.0855	5.00×10^{22}	2.33
		28.9765	4.67			
		29.9738	3.1			
P	15	30.9738	100	30.973762	3.54×10^{22}	1.82
S	16	31.9721	95.02	32.066	3.89×10^{22}	2.07
		32.9715	0.75			
		33.9679	4.21			
		35.9671	0.02			
		36.9659	24.23			

element	atomic number (Z)	isotopic mass (amu)	relative abundance	atomic weight (amu)	atomic density (atoms cm^{-3})	mass density (g cm^{-3})
Ar	18	35.9675	0.337	39.948	2.69×10^{22}	1.784
		37.9627	0.063			
		39.9624	99.6			
K	19	38.9637	93.2581	39.0983	1.32×10^{22}	0.86
		40	0.0117			
		40.9618	6.7302			
Ca	20	39.9626	96.941	40.078	2.33×10^{22}	1.55
		41.9586	0.647			
		42.9588	0.135			
		43.9555	2.086			
		45.9537	0.004			
		47.9525	0.187			
Sc	21	44.9559	100	44.95591	4.02×10^{22}	3.0
Ti	22	45.9526	8.0	47.88	5.66×10^{22}	4.50
		46.9518	7.3			
		47.9479	73.8			
		48.9479	5.5			
		49.9448	5.4			
V	23	49.9472	0.25	50.9415	6.86×10^{22}	5.8
		50.9440	99.75			

element	atomic number (Z)	isotopic mass (amu)	relative abundance	atomic weight (amu)	atomic density (atoms cm^{-3})	mass density (g cm^{-3})
Cr	24	49.9461	4.35	51.9961	8.33×10^{22}	7.19
		51.9405	83.79			
		52.9407	9.5			
		53.9389	2.36			
Mn	25	54.9380	100	54.93805	8.14×10^{22}	7.43
Fe	26	53.9396	4.35	55.847	8.44×10^{22}	7.83
		55.9349	83.79			
		56.9354	9.5			
		57.9333	2.36			
Co	27	58.9332	100	58.9332	9.09×10^{22}	8.90
Ni	28	57.9353	68.27	58.69	9.13×10^{22}	8.90
		59.9308	26.1			
		60.9311	1.13			
		61.9283	3.59			
		63.9280	0.91			
Cu	29	62.9296	69.17	63.546	8.49×10^{22}	8.96
		64.9278	30.83			
Zn	30	63.9291	48.6	65.39	6.58×10^{22}	7.14
		65.9260	27.9			
		66.9271	4.1			

element	atomic number (Z)	isotopic mass (amu)	relative abundance	atomic weight (amu)	atomic density (atoms cm^{-3})	mass density (g cm^{-3})
		67.9248	18.8			
		69.9253	0.6			
Ga	31	68.9256	60.1	69.723	5.10×10^{22}	5.91
		70.9247	39.9			
Ge	32	69.9243	20.5	72.61	4.41×10^{22}	5.32
		71.9221	27.4			
		72.9235	7.8			
		73.9212	36.5			
		75.9214	7.8			
As	33	74.9216	100	74.92159	4.60×10^{22}	5.72
Se	34	73.9225	0.9	78.96	3.66×10^{22}	4.80
		75.9192	9.0			
		76.9199	7.6			
		77.9173	23.5			
		79.9165	49.6			
		81.9167	9.4			
Br	35	78.9183	50.69	79.904	2.35×10^{22}	3.12
		80.9163	49.31			
Kr	36	77.9204	0.35	83.8	2.69×10^{22}	3.74
		79.9164	2.25			

element	atomic number (Z)	isotopic mass (amu)	relative abundance	atomic weight (amu)	atomic density (atoms cm^{-3})	mass density (g cm^{-3})
		81.9135	11.6			
		82.9141	11.5			
		83.9115	57.			
		85.9106	17.3			
Rb	37	84.9118	72.17	85.4678	1.08×10^{22}	1.53
		86.9092	27.83			
Sr	38	83.9134	0.56	87.62	1.79×10^{22}	2.6
		85.9093	9.86			
		86.9089	7.00			
		87.9056	82.58			
Y	39	88.9059	1000	88.90585	3.05×10^{22}	4.5
Zr	40	89.9047	51.45	91.224	4.28×10^{22}	6.49
		90.9056	11.27			
		91.9050	17.17			
		93.9063	17.33			
		95.9083	2.78			
Nb	41	92.9064	100	92.90635	5.54×10^{22}	8.55
Mo	42	91.9068	14.84	95.94	6.40×10^{22}	10.2
		93.9051	9.25			
		94.9058	15.92			

element	atomic number (Z)	isotopic mass (amu)	relative abundance	atomic weight (amu)	atomic density (atoms cm^{-3})	mass density (g cm^{-3})
		95.9047	16.68			
		96.9060	9.55			
		97.9054	24.13			
		99.9075	9.63			
Tc	43	98	100			11.5
Ru	44	95.9076	5.52	101.07	7.27×10^{22}	12.2
		97.9053	1.88			
		98.5059	12.7			
		99.9042	12.6			
		100.9056	17.0			
		101.9043	31.6			
		103.9054	18.7			
Rh	45	102.9055	100	102.9055	7.26×10^{22}	12.4
Pd	46	101.9056	1.02	106.42	6.79×10^{22}	12.0
		103.9040	11.14			
		104.9051	22.33			
		105.9035	27.33			
		107.9039	26.46			
		109.9052	11.72			
Ag	47	106.9051	51.84	107.8682	5.86×10^{22}	10.5

element	atomic number (Z)	isotopic mass (amu)	relative abundance	atomic weight (amu)	atomic density (atoms cm^{-3})	mass density (g cm^{-3})
		108.9048	48.16			
Cd	48	105.9065	1.25	112.411	4.63×10^{22}	8.65
		107.9042	0.89			
		109.9030	12.49			
		110.9042	12.80			
		111.9028	24.13			
		112.9044	12.22			
		113.9034	28.73			
		115.9048	7.49			
In	49	112.9041	4.3	114.82	3.83×10^{22}	7.31
		114.9039	95.7			
Sn	50	111.9048	1.			
		113.9028	0.7	118.71	3.70×10^{22}	7.30
		114.9033	0.4			
		115.9017	14.7			
		116.9030	7.7			
		117.6016	24.3			
		118.9033	8.6			
		119.9022	32.4			
		121.9034	4.6			

element	atomic number (Z)	isotopic mass (amu)	relative abundance	atomic weight (amu)	atomic density (atoms cm^{-3})	mass density (g cm^{-3})
		123.9053	5.6			
Sb	51	120.9038	57.3	121.75	3.30×10^{22}	6.68
		122.9042	42.7			
Te	52	119.9041	0.096	127.6	2.94×10^{22}	6.24
		121.9031	2.6			
		122.9043	0.908			
		123.9028	4.816			
		124.9044	7.14			
		125.9033	18.95			
		127.9045	31.69			
		129.9062	33.8			
I	53	126.9045	100	126.90447	2.33×10^{22}	4.92
Xe	54	123.9061	0.10	131.29	2.70×10^{22}	5.89
		125.9043	0.09			
		127.9035	1.91			
		128.9048	26.40			
		129.9035	4.10			
		130.9051	21.20			
		131.9041	26.90			
		133.9054	10.40			

element	atomic number (Z)	isotopic mass (amu)	relative abundance	atomic weight (amu)	atomic density (atoms cm^{-3})	mass density (g cm^{-3})
		135.9072	8.90			
Cs	55	132.9054	100	132.90543	8.47×10^{21}	1.87
Ba	56	129.9063	0.106	137.327	1.53×10^{22}	3.5
		131.9050	0.101			
		133.9045	2.417			
		134.9057	6.592			
		135.9046	7.854			
		136.9058	11.230			
		137.9052	71.700			
La	57	137.9071	0.09	138.9055	2.90×10^{22}	6.7
		138.9063	99.91			
Ce	58	135.9071	0.19	140.115	2.91×10^{22}	6.78
		137.9060	0.25			
		139.9054	88.48			
		141.9092	11.08			
Pr	59	140.9077	100	140.90765	2.89×10^{22}	6.77
Nd	60	141.9077	27.13	144.24	2.92×10^{22}	7.00
		142.9098	12.18			
		143.9101	23.80			
		144.9126	8.30			

element	atomic number (Z)	isotopic mass (amu)	relative abundance	atomic weight (amu)	atomic density (atoms cm^{-3})	mass density (g cm^{-3})
		145.9131	17.19			
		147.9169	5.76			
		149.9209	5.64			
Pm	61	145	100	(145)	2.69×10^{22}	6.475
Sm	62	143.9120	3.1	150.36	3.02×10^{22}	7.54
		146.9149	15.0			
		147.9148	11.3			
		148.9172	13.8			
		149.9173	7.4			
		151.9197	26.7			
		153.9222	22.7			
Eu	63	150.9198	47.8	151.965	2.08×10^{22}	5.26
		152.9212	52.2			
Gd	64	151.9198	0.2	157.25	3.02×10^{22}	7.89
		153.9209	2.18			
		154.9226	14.8			
		155.9221	20.47			
		156.9240	15.65			
		157.9241	24.84			
		159.9271	21.86			

element	atomic number (Z)	isotopic mass (amu)	relative abundance	atomic weight (amu)	atomic density (atoms cm^{-3})	mass density (g cm^{-3})
Tb	65	158.9253	100	158.92534	3.13×10^{22}	8.27
Dy	66	155.9243	0.06	162.5	3.16×10^{22}	8.53
		157.9244	0.1			
		159.9252	2.34			
		160.9269	18.9			
		161.9268	25.5			
		162.9287	24.9			
		163.9292	28.2			
Ho	67	164.9303	100	164.93032	3.21×10^{22}	8.80
Er	68	161.9288	0.14	167.26	3.26×10^{22}	9.05
		163.9292	1.61			
		165.9303	33.6			
		166.9320	22.95			
		167.9324	26.8			
		169.9355	14.9			
Tm	69	168.9342	100	168.93421	3.33×10^{22}	9.33
Yb	70	167.9339	0.13	173.04	2.43×10^{22}	6.98
		169.9348	3.05			
		170.9363	14.30			
		171.9364	21.90			

element	atomic number (Z)	isotopic mass (amu)	relative abundance	atomic weight (amu)	atomic density (atoms cm^{-3})	mass density ($g\ cm^{-3}$)
		172.9382	16.12			
		173.9389	31.80			
		175.9426	12.70			
Lu	71	174.9408	97.4	174.967	3.39×10^{22}	9.84
		175.9427	2.6			
Hf	72	173.9400	0.16	178.49	4.42×10^{22}	13.1
		175.9414	5.20			
		176.9432	18.60			
		177.9437	27.10			
		178.9458	13.74			
		179.9465	35.20			
Ta	73	179.9475	0.012	180.9479	5.52×10^{22}	16.6
		180.9480	99.988			
W	74	179.9467	0.13	183.85	6.32×10^{22}	19.3
		181.9482	26.30			
		182.9502	14.30			
		183.9509	30.67			
		185.9544	28.60			
Re	75	184.9530	37.4	186.207	6.79×10^{22}	21.0
		186.9557	62.6			

element	atomic number (Z)	isotopic mass (amu)	relative abundance	atomic weight (amu)	atomic density (atoms cm^{-3})	mass density (g cm^{-3})
Os	76	183.9525	0.02	190.2	7.09×10^{22}	22.4
		185.9538	1.58			
		186.9557	1.6			
		187.9558	13.3			
		188.9581	16.1			
		189.9584	26.4			
		191.9615	41.0			
Ir	77	190.9606	37.3	192.22	7.05×10^{22}	22.5
		192.9629	62.7			
Pt	78	189.9599	0.01	195.08	6.61×10^{22}	21.4
		191.9610	0.79			
		193.9627	32.9			
		194.9650	33.8			
		195.9650	25.3			
		197.9679	7.2			
Au	79	196.9666	100	196.96654	5.90×10^{22}	19.3
Hg	80	195.9658	0.15	200.59	4.06×10^{22}	13.53
		197.9668	10.1			
		198.9683	17.			
		199.9683	23.1			

element	atomic number (*Z*)	isotopic mass (amu)	relative abundance	atomic weight (amu)	atomic density (atoms cm^{-3})	mass density (g cm^{-3})
		200.9703	13.2			
		201.9706	29.65			
		203.9735	6.8			
Tl	81	202.9723	29.524	204.3833	3.49×10^{22}	11.85
		204.9744	70.476			
Pb	82	203.9730	1.4	207.2	3.31×10^{22}	11.4
		205.9745	24.1			
		206.9759	22.1			
		207.9767	52.4			
Bi	83	208.9804	100	208.98037	2.82×10^{22}	9.8
Po	84	208.9824	100	(209)	2.71×10^{22}	9.4
At	85	210	100	(210)		
Rn	86	222.0176	100	(222)	2.69×10^{22}	9.91
Fr	87	223	100	(223)		
Ra	88	226.0254	100	226.0254	1.33×10^{22}	5.
Ac	89	227	100	227.0278	2.67×10^{22}	10.07
Th	90	232.0381	100	232.0381	3.04×10^{22}	11.7
Pa	91	231.0359	100	231.0359	4.01×10^{22}	15.4
U	92	234.0410	0.0055	238.0289	4.78×10^{22}	18.9
		235.0439	0.7200			

element	atomic number (Z)	isotopic mass (amu)	relative abundance	atomic weight (amu)	atomic density (atoms cm^{-3})	mass density (g cm^{-3})
		238.0400	99.2745			
Np	93	237.0482	100	237.0482	5.18×10^{22}	20.4
Pu	94	244.0642	100	(244)	4.89×10^{22}	19.8
Am	95	243.0614	100	(243)	3.37×10^{22}	13.6

Parentheses indicate estimated values of atomic weights
Data taken from *Nuclides and Isotopes*, 14th edn., revised 1989 (General Electric Co., San Jose, California)

Appendix B

Physical constants, conversions, and useful combinations

physical constants	
acceleration due to gravity	$g = 98$ dyne $g^{-1} = 9.81$ m s^{-2}
atomic mass unit	$u = 1.6606 \times 10^{-27}$ kg
Avogadro's constant	$N_A = 6.022 \times 10^{23}$ particles mol^{-1}
Boltzmann's constant	$k = 8.617 \times 10^{-5}$ eV K^{-1}
	$= 1.38 \times 10^{-23}$ J K^{-1}
Coulomb's constant	$k_c = 8.988 \times 10^{9}$ N m^2 C^{-2}
electron mass	$m_e = 9.1095 \times 10^{-31}$ kg
elementary charge	$E = 1.602 \times 10^{-19}$ C
permittivity (free space)	$\varepsilon_0 = 8.85 \times 10^{-14}$ F cm^{-1}
Planck's constant	$h = 4.136 \times 10^{-15}$ eV s
	$= 6.626 \times 10^{-34}$ J s
speed of light	$c = 2.998 \times 10^{10}$cm s^{-1}
useful combinations	
Coulomb's constant	$k_c e^2 = 1.44$ eV nm
permittivity (free space)	$\varepsilon_0 = 55.3$ e/V μm
permittivity (Si)	$\varepsilon = \varepsilon_r \varepsilon_0 = 1.05 \times 10^{-12}$ F cm^{-1}
photon energy	$E = 1.24$ eV at $\lambda = 1$ μm
thermal energy (300 K)	$kT = 0.0258$ eV $\cong$ 1 eV/40

Prefixes

k = kilo = 10^3; M = mega = 10^6; G = giga = 10^9; T = tera = 10^{12}; m = milli = 10^{-3}; μ = micro = 10^{-6}; n = nano = 10^{-9}; p = pica = 10^{-12}

symbols for units

ampère (A) coulomb (C); farad (F); gram (g); joule (J); kelvin (K); meter (m); newton (N); ohm (Ω); pascal (Pa); second (s); siemen (S); tesla (T); volt (V); watt (W); weber (Wb)

conversions

$1 \text{ nm} = 10^{-9} \text{ m} = 1 \text{ Å} = 10^{-7} \text{ cm}$

$1 \text{ eV} = 1.602 \times 10^{-19} \text{ J} = 1.602 \times 10^{-12} \text{ erg}$

$1 \text{ eV per particle} = 23.06 \text{ kcal mol}^{-1} = 96.5 \text{ kJ mol}^{-1}$

1 N = 0.102 kgf (kilogram force)

$10^6 \text{ N m}^{-2} = 146 \text{ psi} = 10^7 \text{ dyne cm}^{-2}$

$1 \text{ µm} = 10^{-4} \text{ cm}$

0.001 in. = 1 mil = 25.4 µm

$1 \text{ bar} = 10^6 \text{ dyne cm}^{-2} = 10^5 \text{ N m}^{-2}$

$1 \text{ Wb m}^{-2} = 10^4 \text{ gauss} = 1 \text{ T}$

$1 \text{ Pa} = 1 \text{ N m}^{-2} = 7.5 \times 10^{-3} \text{ torr}$

$1 \text{ erg} = 10^{-7} \text{ J} = 1 \text{ dyne cm}$

1 calorie = 4.184 J

1 J = 1 N m = 1 W s

Index

Alpha particle 8
amorphization 128
amorphous
  crystallization kinetics 138
  phase 117
  Si 127
  solid 3
analyzer magnet 216
angular differential scattering
    cross-section 37
  momentum 31
anomalous dopant diffusion 195
areal density 6
atomic
  densities 5, 7
  jump frequency 124
  mass unit 8
  number 2
  volume 6
Avogadro's number 6

Backscattered particles 94
base 109
beamline architectures 215
beam
  angular alignment 232
  blow-up 208
  ribbon 234
  scan mechanism 234
  shadowing effect 208
  size expansion 216
  steering 232
  transport 223
  travel path length effect 234
  utilization 226
binary collisions 23
binding energy 12
bipolar transistor 109
  amplifier 110
  switch 110

Bohr
  atom 8
  radius 9, 15
  screening length 19
  velocity 9

Calculations
  projected range 69
  range 67
  straggling 70
cascade 86
  energy 127
  ion beam mixing 184
  temperature 87
center-of-mass
  coordinates 27
  total energy 29
  velocity 28
central force
  energy conservation 31
  force field 12
  motion 30
centrifugal energy 32
channel area 102
channeling 93
  critical angle 95, 97
  damage 105
  dechanneling 98, 100
  defects 94
  distribution 93
  energy loss 97
  implantation 93, 102
  impurity atoms 94
  ion trajectories 97
  maximum range 99
  measurements 130
  range 93
  scattering yield 94
charge neutralization 208
classical theory, scattering 24

closest approach
  distance of 34
CMOS 112, 193, 199, 213
cohesive energy 162, 189
  ion beam mixing 189
collector 109
collision
  binary elastic 23
  diameter 34
  elastic 25, 51
  electronic 50
  head-on 30
  inelastic 25
  kinematics 25
  nuclear 50
  probability 44
  replacement 80
  small-angle 94
  soft 24
  two-body 23, 79
  violent 24
collision cascade 78
  high density 176
  ion beam mixing 184
  random-walk 186
conservation
  angular momentum 32
  energy 24
  momentum 25
coordinates
  center-of-mass 27
  laboratory 25
Coulomb
  explosion 208
  force 6–7, 11
  interatomic potential 11–13, 15
  unscreened potential 101
critical angle channeling 97
cross section 37
  angular-differential scattering 40
  differential 40, 42
  electronic 58
  energy-transfer 42, 46
  nuclear 52
  Rutherford scattering 101
  stopping 51
  total 49
crystallization
  ion beam induced 137
Damage 77
  depth 90
  efficiency 82
  energy 81
  radiation 77
  depth distribution 93, 150
  displacements per atom 85
  Kinchin-Pease 80
  primary knock-on 77
  spatial distribution 90
  SRIM 89
  strain 154
  stress 154
DC-tandem accelerators 220
deceleration mode 208, 224
dechanneling 98, 101
  cross section 101
  defect factor 101
  fraction 104
  probability 101
deep level centers 115
defect
  charge state 134
  density 101, 127
  dislocation 114
  Frenkel 78, 114
  hydrogen platelet 153
  interstitial 114
  interstitialcy 114
  line 114, 116
  mobility 127
  planar 114, 117
  point 114
  recombination 127
  Si-H, complexes 147
  substitutional 115
  vacancy-interstitial 77, 114
  volume 114
density
  areal 6
  atomic 5
density of states 107
depletion-layer width 204
depletion region 107, 193
detector
  solid angle 38
deuteron 8
device scaling 193
diamond cubic lattice 5

differential cross-section 40, 42
diffusion
  activation energy 119
  boron 123
  coefficient 118, 119
  dopants 119
  drive-in 119, 202
  Fick's law 118
  hydrogen in silicon
  interstitial 122
  interstitialcy 122
  irradiation enhanced 124
  interdiffusion coefficient 181
  kick-out 122
  mechanisms 121
  radiation enhanced 126
  random-walk 186
  substitutional 122
  transient enhanced 122
  vacancy formation energy 121
direct scattering 104
dislocation defects 116
disorder
  lattice 3
  Si 127
displacement
  energy 77
  per atom 85
  spike 87
displacement energy 78
distance
  of closest approach 34
  screening 34
distribution of range 2, 65
  Gaussian 66
  Polyatomic targets 70
  standard deviation 65, 70
  straggling 2, 65
dose 1
dose rate 1
dose uniformity 215
drain implant 205
drift mode 216

Electron 8
electron flood gun 208
electron-volt 6
electronic stopping
  Bethe formula 58
  Bohr 57
  channeling 97
  Fermi-Teller 58
  Firsov 59
  high energy 57
  Lindhard-Scharff 59
  low energy 58
emitter 109
endststion
  design 234
  multi-wafer 227
  single-wafer 229
energy
  activation 119
  central force 31
  cohesive 13, 162, 189
  conservation 25
  contamination 208, 224
  damage 81, 127
  deposited 127
  dimensionless unit 34
  displacement 77,
  excitation 57
  loss 49
  maximum transferred 30
  reduced 34
  transferred 29
  transferred cross-section 42
  vacancy formation 12
enthalpy of mixing 187
epitaxial growth
  amorphous Si 129
  velocity 131
epitaxy
  homo 129
  liquid-phase 129
  solid-phase 129
exfoliation 143

Face-centered-cubic 5
Fermi level 107
Fermi-Teller electronic stopping 58
Firsov electronic stopping 58
fluence 1
flux 1
focused replacement sequence 86
force
  attractive 14
  Coulomb 7, 11
  interatomic 12
  long-range interatomic 12

repulsive 14
restoring 13
forward bias 107
Frenkel-defect 78
function
displacement damage 79
Kinchin-Pease damage 81
function screening 16
Bohr 17
Lenz-Jensen 17
Lindhard 17
Moliere 17
Sommerfeld asymptotic 17

Gate implant 207
gate dielectric material 207
gate length 194
Gaussian range distribution 66
grain boundaries 117

Halo implant 200, 206, 214
high current beamlines 216
high current implantation 214
high dose ion implantation 169
high energy electronic stopping 57
high energy beamlines 219
high energy implantation 214
Hook's law 14
hot electron effects 193, 198, 205
hydrogen ion implantation 144

Impact parameter 32, 39, 101
ion dose 1
interatomic
Coulomb interaction 11
forces 11, 13
separation equilibrium 13
interatomic potential 11, 13
Lennard-Jones 13, 15
interface
crystal-amorphous 131
interdiffusion coefficient 181
intermixing 179
ion beam mixing 179
ballistic 180, 182
cascade 180, 185
cohesive energy 189
de-mixing 188
effective mixing parameter 184
heat of mixing 187
recoil 183
thermodynamic effect 187
temperature-dependent 182
temperature-independent 182
ion-cut 143
depth 149
mechanisms 149
microstructure 153
ion implanters 215
CMOS processing 214
commercialization 230
contamination 215
control systems 222
high vacuum systems 222
high-voltage supplies 222
ion implantation 63
alloy 71
channeling 93
concentration 67
future 236
high dose 169
hydrogen in silicon 145
molecular 226
recoil 183
self 129
sputtering 159
ion-solid simulations
Monte Carlo 72
ion stopping 49
irradiation-enhanced diffusion 124

Joule 6
Junctions
deeper 97
shallow 97

Kinchin-Pease
function 79–80
modified function 81
kinematics
elastic collisions 25

Laboratory coordinates 26
laboratory scattering angle 29
laser annealing 140
latchup 198, 202
lateral spreading of dopants 195
lattice
disorder 94
parameter 5

layer transfer 143
Lennard-Jones
  interatomic potential 13
lifetime spike 88
linac accelerators 219
Lindhard,screening function 17
Lindhard-Scharff
  electronic stopping 60
lightly-doped drain 197, 205
linear cascade sputtering 160
long-range interatomic force 12
low energy electronic stopping 58

Mass
  reduced 28
  number 7
materials integration 143
mean free path 86
medium current beamlines 218
medium current implantation 214
mixing enthalpy 180
modulus, elastic 23
molecular implantation 226
momentum, conservation 25
monolayer 6
Monte Carlo
  dpa 91
  ion-solid simulations 72
Moore's Law 193, 213
MOSFET 110
motion, central force 30

Nearest-neighbor spacing 13
neutron 8
nuclear
  collisions 50
  cross-section 51
nuclear stopping
  channeling 97
  power law 48
  cross-section 51
  ZBL cross-section 54
nucleus
  radius 9
nuclides 7
number
  atomic 2
  mass 7

Orbital angular momentum 32

Path, mean free 86
Pauli exclusion principle 12, 15
planar densities 5
Planck's constant 91
p-n junction 107
polyatomic materials
  range 71
  sputtering 164
polycrystalline 3
potential
  central force 11
  interatomic 13
  mean ionization 57
  minimum energy 13
  screened Coulomb 15
  unscreened Coulomb 101
particle, alpha 8
preferential sputtering 165
primary knock-on
  atom (PKA) 77
  damage energy 81
  displacements produced by 79
projected range 2, 63
  calculation 60
  distribution 65
  straggling 65
proton 8
punch through effect 195
punch-through-stop 200, 203

Radial range 65
radiation-damage 77
radiation-enhanced diffusion 124
radius
  Bohr 9
  nucleus 9
  screening 19
random-walk
  collision cascade 186
  diffusion 186
range 2, 63
  calculations 60–72
  channeling 94
  distributions 2, 65
  polyatomic targets 70
  projected 2, 63, 68
  radial 64
  spreading 64
  SRIM 72
  straggling 2, 65, 70

recoil implantation 183
recombination center 116
  energy 34
  ZBL energy 55
regrowth rate 131
  orientation 137
replacement collision 80, 86
retrograde wells 198, 215
  formation 202
  implants 203
reverse bias 107
RF linac beamlines 219
ribbon beam 234
Rutherford backscattering 130
Rutherford cross-section 101

Scattering
  angle 26, 29
  center-of-mass 27
  classical theory 24
  cross-section 37
screened Coulomb potential 16
screening distance 19
  Thomas-Fermi 19
  universal 18
screening function 16
  Bohr 17
  Lenz-Jensen 171
  Lindhard 17
  Moliere 179
  Sommerfeld asymptotic 16
  Thomas-Fermi 17
  universal 17–18
screening length
  Bohr 19
  Firsov 19
  Lindhard 19
  Thomas-Fermi 19
  universal 18
shadowing 93
shallow dopant impurities 115
shallow junction formation 223
short-channel effect 193, 195, 199
short-range interatomic force 12
simulation
  SRIM 72, 89, 175
  TRIM 72
Si
  amorphous 127
  slicing 143
silicon-on-insulator 144
SIMOX 145
single element targets sputtering 159
Smart-Cut™ 143
SOI 144
solid angle 38, 41
solid solubility 120
source implant 205
space charge effect 207, 211
space charge neutralization 224
space charge region 107
spreading range 64
spike 86
  displacement 86
  quench time 88
  thermal 87
  time 87
sputtering
  alloy 164
  angular dependence 163
  composition changes 166
  computer simulation 175
  deposited energy 160
  ion implantation 159
  linear cascade 160
  materials factor 160
  polyatomic target 164
  preferential 165
  single element targets 159
  steady state 162
  yield 159,
standard deviation
  range distribution 66
stopping
  cross-section 51
  electronic 56
  nuclear 51
  SRIM
stacking faults 117
straggling 2, 65
  polyatomic 70
SUPREM 196
system, ion implantation 2

Table of elements 239
tandem accelerators 222
temperature
  collision cascade 87
  spike 88
thermal spike 87

thermodynamic
  effect ion beam mixing 187
Thomas-Fermi screening
  distance 19
  function 16
  length 19
threshold voltage 193
  adjustment 199, 202, 214
total cross-section 39
two-particle scattering 24
transient enhanced
  diffusion 122, 196
transferred energy 29
transverse projected range 65
TRIM 72
twins 117
twin well 202

Universal screening length 18

Vacancy concentration 133
  charge state 134
vacancy-interstitial defects 78
velocity
  Bohr 8
  growth 131
  of light 8
volume, atomic 6
volt, electron 6

Wafer handling 221
work function 193

Yield, sputtering 160

ZBL
  Nuclear stopping 54
  universal screening function 18